The Dissertation Committee for Dorothy Ann Silbaugh Certifies that this is the approved version of the following dissertation:

Fluorescent Silicon Nanocrystals for Bioimaging

Committee:

Brian A. Korgel, Supervisor

Guihua Yu

John G. Ekerdt

Jennifer A. Maynard

James W. Tunnell

Fluorescent Silicon Nanocrystals for Bioimaging

by

Dorothy Ann Silbaugh

Dissertation

Presented to the Faculty of the Graduate School of

The University of Texas at Austin

in Partial Fulfillment

of the Requirements

for the Degree of

Doctor of Philosophy

The University of Texas at Austin

December 2017

Dedication

For my family

Acknowledgements

I would like to thank the people who have directly and indirectly contributed to my progress these past few years.

First, I would like to thank my advisor Dr. Brian Korgel for all the opportunities he has provided that enabled my growth as a graduate student. He has provided me with guidance, insight, and support in numerous ways. Additionally, I would like to thank Dr. John Ekerdt, Dr. James Tunnell, Dr. Jennifer Maynard, and Dr. Guihua Yu for being a part of my committee.

I would also like to thank all members of the Korgel research group. My lab work was greatly shaped by the instruction of Yixuan Yu, who spent many hours teaching me nanocrystal synthesis reactions. My peers Vikas Reddy Voggu, Adrien Guillaussier, Emily Adkins, and Cherrelle Thomas provided not only support as we learned research techniques together, but also camaraderie through our shared lab experiences. I'd especially like to thank Vikas for providing a steady supply of chocolate treats that made long lab days more bearable. To all the other Korgel group members who I have interacted with, including Xiaotang Lu, Timothy Bogart, Jackson Stolle, Philip Liu, Doug Pernik, Tushti Shah, Taizhi Jiang, Hyun Gyung Kim, Dan Houck, and Tim Siegler, thank you for providing inspiration and influencing my work over the years. Finally, to my undergraduates assistants Kyle Dalal, Richard Paul, and Newton Liu, thank you for all you did to keep our research moving forward.

My collaborators have also played a huge role during my graduate studies. I'd like to thank Lidia Ferrer Tasies for introducing me to quatsome and cryogenic TEM. For my cell work collaborators Xianzhe Wang and Christopher Stevens, thank you for all of your

patience and effort as we worked out the kinks in our experiments. For bioimaging applications, I am indebted to Dr. Arnold Estrada and Dr. Jeremy Jarrett for the time and effort they spent to enable imaging our nanocrystals. Also, I'd like to thank Dwight Romanowitz, with whom I spent many hours as we set up the cryogenic transmission electron microscopy equipment.

I'd also like to thank the people who supported my decision to continue my academic career, including my M.S. advisor Dr. Wayne Giles. His inspiration and belief in me helped me decide that I could return to school and complete my doctorate.

Outside of the lab, I'd like to thank my family for supporting me, even as I moved halfway across the country to pursue my graduate studies. I appreciate all the care packages of cookies and chocolates I've received. I must, of course, express extreme gratitude to my husband who has helped me in many ways that cannot be listed on one page. And finally, to my little man Owen, whose smile makes everything worth it.

Fluorescent Silicon Nanocrystals for Bioimaging

Dorothy Ann Silbaugh, Ph.D.

The University of Texas at Austin, 2017

Supervisor: Brian A. Korgel

Quantum dots have been used as alternatives to organic dyes for fluorescence imaging because they are resistant to photobleaching, exhibit strong response to two-photon excitation, and can be conjugated to a wide variety of targeting molecules. Silicon (Si) nanocrystal quantum dots in particular exhibit bright, size-dependent emission with visible to near infrared wavelengths and are biocompatible, making them potentially interesting for *in vitro* and *in vivo* bioimaging. Here, Si nanocrystals are studied for imaging applications.

The stability of Si nanocrystal dispersibility and photoluminescence (PL) in aqueous solutions was studied. Hydrophobic Si nanocrystals were dispersed with surfactants to produce colloidally stable and brightly fluorescent dispersions, with PL quantum yields in the range of 3.2% - 6.6%. Hydrophilic Si nanocrystals capped with a ligand containing a terminal carboxylic acid group could be directly dispersed in aqueous environments with quantum yields of up to 9.1% in water. The nanocrystal PL was stable in water for at least one week, however there was a significant loss of PL when the particles were dispersed in biological solutions. The drop in PL was accompanied by surface oxidation and degradation of the nanocrystals. Si nanocrystals incubated with mouse macrophage cells were actively taken up by endocytosis. Cell viability assays indicated that the nanocrystals were not toxic to the macrophages. The Si nanocrystals

were bright enough to be imaged within the cells by one-photon and two-photon microscopy. Hydrophilic Si nanocrystals that emit in the near infrared (900-1000 nm) could also be dispersed directly into water, however the emission quantum yields were prohibitively low for imaging applications. Time gated imaging of cells labeled with Si nanocrystals enabled multiplex imaging using optical probes with spectral overlap by separating the PL of organic dyes with short nanosecond lifetimes and Si nanocrystals with long microsecond lifetimes. Finally, biotin bioconjugation was accomplished to Si nanocrystal surfaces, though the conjugation reaction efficiencies were relatively low.

Table of Contents

List of Tables xiv

List of Figures xv

Chapter 1: Introduction 1

1.1 Nanoparticles for Medical Applications 1

1.2 Semiconductor Nanoparticles 2

1.2.1 Quantum Dots 2

1.2.2 Silicon Nanocrystals 3

1.3 Dispersing Nanoparticles in Aqueous Solutions 7

1.3.1 Surfactants and Polymers 8

1.3.2 Hydrophilic Ligands 9

1.4 Bioimaging 10

1.5 Dissertation Overview 12

1.6 References 13

Chapter 2: Assembly of Fluorescent Silicon Nanocrystals with Liposomes and Uptake by Macrophage Cells 22

2.1 Introduction 22

2.2 Experimental Methods 23

2.2.1 Materials 23

2.2.2 Si Nanocrystal Synthesis 24

2.2.3 Incorporation of Si Nanocrystals with Liposomes 25

2.2.4 Si Nanocrystal and Liposome Characterization 26

2.2.5 Liposome-Si Nanocrystal Incubation with Cells 28

2.2.6 Cell Uptake Characterization 29

2.3 Results and Discussion 30

2.3.1 Liposome-Si Nanocrystal Assembly 30

2.3.2 Liposome-Si Nanocrystal Photoluminescence Stability 42

2.3.3 Uptake of Liposome-Si Nanocrystal Assemblies 43

2.3.4 Cytotoxicity of Liposome-Si Nanocrystal Assemblies 49

2.3.5 Two-Photon Imaging of Macrophage Cells....50
2.4 Conclusion....51
2.5 References....52

Chapter 3: Highly Fluorescent Silicon Nanocrystals Stabilized in Water using Quatsomes....56
3.1 Introduction....56
3.2 Experimental Methods....57
3.2.1 Materials....57
3.2.2 Si Nanocrystal Synthesis and Assembly with Quatsomes....58
3.2.3 Characterization....61
3.3 Results and Discussion....62
3.3.1 Incorporation of Si Nanocrystals with Quatsomes....62
3.3.2 Colloidal and Fluorescence Stability of Si Nanocrystal-Quatsome Assemblies....68
3.3.3 Comparison to Liposomal Structures....74
3.3.4 Dispersion Stability of Diluted Assemblies....75
3.3.5 Role of Chloroform in Si Nanocrystal-Quatsome Assemblies....76
3.3.6 Interaction between Dodecanethiol-Capped Gold Nanocrystals and Quatsomes....78
3.3.7 Mechanism of Interaction between Nanocrystals and Quatsomes....81
3.4 Conclusion....84
3.5 References....85

Chapter 4: Stability of Hydrophilic Ligand Passivated Silicon Nanocrystals in Biological Solutions and Uptake by Cells....89
4.1 Introduction....89
4.2 Experimental Methods....90
4.2.1 Materials....90
4.2.2 Si Nanocrystal Synthesis....91
4.2.3 Transfer of Si Nanocrystals into Water and Incubation with Biological Solutions....92

4.2.4 Si Nanocrystal Characterization 93
4.2.5 Si Nanocrystal Incubation with Cells and Characterization 96
4.3 Results and Discussion 99
4.3.1 Si Nanocrystals in Biological Solutions 99
4.3.2 Si Nanocrystal Uptake, Toxicity, and Inflammatory Response in Macrophage Cells 111
4.4 Conclusion 118
4.5 References 119

Chapter 5: Aqueous Dispersibility and Photoluminescence of Near-Infrared Emitting Si Nanocrystals 123
5.1 Introduction 123
5.2 Experimental Methods 124
5.2.1 Materials 124
5.2.2 Si Nanocrystal Synthesis 125
5.2.3 Characterization 127
5.3 Results and Discussion 129
5.3.1 Si Nanocrystal Hydrolysis and Transfer into Water 129
5.3.2 Photoluminescence of NIR Emitting Si Nanocrystals 134
5.4 Conclusion 136
5.5 References 137

Chapter 6: Spectral and Temporal Multiplexing for Colocalization of Silicon Nanocrystals in Mouse Macrophage Cells 142
6.1 Introduction 142
6.2 Experimental Methods 144
6.2.1 Materials 144
6.2.2 Si Nanocrystal Synthesis and Transfer into Water 144
6.2.3 Cell Culture and Incubation with Si Nanocrystals 146
6.2.4 Characterization and Imaging 146
6.3 Results and Discussion 148
6.3.1 Time Gated Imaging Setup 148

6.3.2 Cell Imaging with Si Nanocrystals, CellMask Deep Red, and DAPI 151
6.3.3 Localization of Si Nanocrystals in Macrophage Cells.....156
6.4 Conclusion 161
6.5 References.....161

Chapter 7: Bioconjugation of Si Nanocrystals.....167
7.1 Introduction.....167
7.2 Experimental Methods.....168
7.2.1 Materials 168
7.2.2 Silicon Nanocrystal Synthesis.....168
7.2.3 Bioconjugation.....169
7.2.4 Characterization 170
7.3 Results and Discussion 171
7.3.1 Bioconjugation.....171
7.3.2 Measurement of Bioconjugation Efficiency 174
7.4 Conclusion 178
7.5 References.....179

Chapter 8: Conclusions and Future Directions 181
8.1 Conclusions.....181
8.1.1 Si Nanocrystal-Surfactant Assemblies.....181
8.1.2 Hydrophilic Ligand Passivated Si Nanocrystals.....182
8.1.3 Cell Uptake of Si Nanocrystals and Toxicity 182
8.1.4 Imaging 183
8.1.5 Bioconjugation.....183
8.2 Future Directions 184
8.2.1 Active Targeting through Bioconjugated Molecules.....184
8.2.2 Near Infrared Imaging.....185
8.2.3 *In Vivo* Imaging.....185
8.2.4 Therapy with Si Nanocrystals.....186
8.3 References.....186

References.....189

Vita 207

List of Tables

Table 2.1 DLS and zeta potential measurements for Si nanocrystal and liposome dispersions, measured in triplicate at 25 °C. 36

Table 3.1 Summary of quatsome-Si nanocrystal assembly preparations used in stability testing. 69

Table 4.1 Particle sizes as measured by DLS and zeta potentials. Values reported are mean ± standard deviation, for n=3 measurements. * A secondary population of particles with size 2.7 ± 0.1 nm was identified, and corresponds to free BSA molecules. 111

Table 6.1 Pearson's coefficients for PL colocalization calculated between Si nanocrystals and dextran or lysosomes. 160

Table 6.2 Pearson's coefficients for PL colocalization calculated between Si nanocrystals and DAPI or CellMask Deep Red. 160

Table 7.1 Summary of conditions tested for bioconjugation of Si nanocrystals to amine-PEG11-Biotin 173

Table 7.2 Results of the HABA-avidin assay to measure biotin on Si nanocrystals. 175

List of Figures

Figure 1.1 Illustration of the bandgap (E_g) in bulk semiconductor materials and nanoscale materials. 3

Figure 1.2 Illustration comparing electron-hole recombination and light emission in direct and indirect bandgap semiconductors. 4

Figure 1.3 Absorbance and PL spectra (excited at 320 nm) for 2.8 nm diameter Si nanocrystals passivated with 1-octene and dispersed in chloroform. 4

Figure 1.4 Illustration of the process for forming Si nanocrystals by the thermal annealing of hydrogen silsesquioxane. 6

Figure 1.5 Illustration of liposome showing assembly of hydrophobic particles inside of the lipid bilayer and hydrophilic particles inside the aqueous core. 9

Figure 1.6 (a) Illustration of lifetime gating using a short lived (3 ns) probe and a long lived (60 μs) probe. By gating the emission at short times (region R1) versus long times (region R2), it is possible to separate the contributions from the two probes. (b) Illustration of one-photon and two-photon excitation. 11

Figure 2.1 (a) TEM image of 2.8 nm octene capped Si nanocrystals. Inset shows vial of Si nanocrystals under ambient light and on a 365 nm ultraviolet lamp. (b) XRD pattern confirmed the diamond cubic silicon structure with a=b=c=0.543 nm (PDF # 027-1402). (c) FTIR data for Si nanocrystals passivated with 1-octene confirmed surface passivation with an alkene. 31

Figure 2.2 Illustration of the process used to incorporate Si nanocrystals into liposomes. The chloroform annealing step was performed on some samples.....32

Figure 2.3 CryoTEM images of Lip-NC assemblies synthesized with the chloroform annealing step. Nanocrystal aggregates were observed with sizes and shapes similar to empty liposomes (green arrows), non-spherical shapes (yellow arrows), and large irregular shapes (red arrows). Pictures of the dispersions under ambient light and on a 365 nm ultraviolet lamp. Normalized PL and PLE spectra for each of the dispersions, with black dotted lines indicating peak PL wavelength for Si nanocrystals in chloroform (718 nm).....35

Figure 2.4 Illustration of the formation of Si nanocrystal aggregates. The thin film containing lipids and octene capped Si nanocrystals is hydrated and bath sonication is used to form liposomes. After one Si nanocrystal associates with the hydrophobic core in the bilayer, there is a driving force for nanoparticles to cluster. The cluster may then act as a single large particle and becomes coated with a lipid monolayer. 38

Figure 2.5 Calculated dispersion emission fractions (DEF) for Lip-NC assemblies. Samples were prepared either with (blue bars) or without (yellow bars) the chloroform annealing step. All samples were prepared in triplicate, and error bars represent standard deviation. * DEF for PEG samples were not measured in the absence of the annealing step. 40

Figure 2.6 (a) Normalized emission intensity and (b) PL emission wavelength for samples constructed of DOPC, 1:1 DOPC:DOPG, 1:1 DOPC:DOTAP, and 98:2 DOPC:DOPE-PEG, showing the change in Lip-NC dispersion PL over three weeks. 43

Figure 2.7 Confocal images showing emission captured from Si nanocrystals (false colored red) and DAPI nucleus dye (false colored blue) after incubation of 1:1 DOPC:DOPG Lip-NC assemblies with J774 cells for 3 hours. (a) At 37 °C Lip-NC assemblies incubated with the cells resulted in a visible uptake of Si nanocrystals. Inset shows two cells with brightfield overlay (scale bar 10 μm). (b) At 4 °C the Si nanocrystal signal is significantly lower as active uptake is limited. (c) Cells incubated without Lip-NC assemblies did not show any signal in the silicon nanocrystal emission range. (d) Flow cytometry confirmed higher emission intensity for cells incubated with Lip-NC assemblies at 37 °C as compared to 4 °C. (e) Concentration dependent uptake was measured for Lip-NC assemblies. A linear fit was made to the data ($R^2 = 0.9997$). Error bars are standard deviation (n=2). 46

Figure 2.8 Confocal images of cells showing signal from silicon nanocrystals (false colored red) and DAPI nucleus dye (false colored blue) after incubation with J774 cells at 37 °C for (a) 1 hour, (b) 3 hours, or (c) 6 hours with 1:1 DOPC:DOPG Lip-NC assemblies. (d) Flow cytometry of the cells confirmed the time dependent uptake. 47

Figure 2.9 Flow cytometry results showing Si nanocrystal emission from (a) J774 cells and (b) Caco2 cells incubated with neutral (DOPC), anionic (1:1 DOPC:DOPG), or cationic (1:1 DOPC:DOTAP) Lip-NC assemblies at either 37 °C or 4 °C. Error bars are standard deviation (n=2). * Data was not collected for samples without Lip-NC assemblies at 4 °C. 48

Figure 2.10 Cell viability was measured by (a) LDH assay and (b) MTS assay for J774 cells incubated at 37 °C with 1:1 DOPC:DOPG liposomes assembled with Si nanocrystals, gold nanocrystals, or no nanocrystals. Error bars are standard deviation (n=3). 50

Figure 2.11 Images of macrophages with Si nanocrystals (in 1:1 DOPC:DOPG Lip-NC assemblies) and DAPI taken using one-photon (405 nm) and two-photon (800 nm) excitation. 51

Figure 3.1 (a) TEM images of octene-coated Si nanocrystals. (b) Histogram showing size distribution of Si nanocrystals. (c) TGA results for 1-octene coated Si nanocrystals. 63

Figure 3.2 (a) Schematic representation of the process for incorporating Si nanocrystals into quatsomes through bath sonication. (b-d) CryoTEM or TEM images of 7 mM quatsomes, Si nanocrystals, and their assemblies along with photographs of the dispersions under ambient light (on the left) and a 365 nm UV lamp (on the right), as well as illustrations of the structures. 64

Figure 3.3 CryoTEM images of fluorescent dispersions of Si nanocrystal-quatsome assemblies. The red arrows indicate Si nanocrystal clusters that are not associated with quatsomes; whereas, the green and blue arrows show clusters associated with one or more quatsomes, respectively. 65

Figure 3.4 (a) Absorbance (solid lines), PL (dashed lines), and PLE (dotted lines) spectra for octene capped Si nanocrystals dispersed in chloroform and incorporated into quatsomes in aqueous media. Inset shows photographs of vials of (left) Si nanocrystals in chloroform and (right) quatsome-Si nanocrystal assemblies, each containing the same concentration of Si nanocrystals, under ambient light (top) or on a 365 nm ultraviolet lamp (bottom). (b) Data collected for quantum yield calculation.....66

Figure 3.5 CryoTEM images of the Si nanocrystal-quatsome samples prepared by bath sonication for (a) 1 minute, (b) 5 minutes, (c) 15 minutes, and (d) 30 minutes. (d) DLS data showing smaller size at 15 and 30 minutes of bath sonication. 68

Figure 3.6 Fluorescence stability of Si nanocrystals (SiNCs) dispersed in aqueous solution with quatsomes or CTAB. The five samples shown in (a-e) are summarized in Table 3.1. Photographs of vials under ambient light (top) and on a 365 nm UV lamp (bottom) taken (a) immediately, (b) one day, (c) 2 weeks, (d) 8 weeks, and (e) 12 weeks after preparation. (f) Absorbance measured at 320 nm and (g) average PL wavelength (excited at 320 nm) demonstrate the stability of the nanoparticle fluorescence in quatsomes. 70

Figure 3.7 CryoTEM images of 7 mM quatsome-Si nanocrystal assemblies taken (a)-(c) on the day the sample was prepared and (d)-(f) 2 days, (g)-(i) 7 weeks, and (j)-(l) 12 weeks after the sample was prepared. 71

Figure 3.8 DLS data showing change in size distribution over 8 weeks for (a) 7mM quatsome-Si nanocrystal assemblies (sample (i) from stability trials) and (b) nanocrystal-free quatsomes (sample (v) from stability trials).....72

Figure 3.9 CryoTEM images of 0.7 mM quatsome-Si nanocrystal assemblies. 73

Figure 3.10 CryoTEM images of Si nanocrystals dispersed with 7 mM CTAB..... 74

Figure 3.11 Results from using the quatsome-Si nanocrystal assembly process with DOPC (neutral) and DOPG (anionic) liposomes. Photographs of vials of (a) DOPC and (e) DOPG were taken under ambient light and on a 365 nm UV lamp (i) before bath sonication, (ii) immediately after sonication, (iii) after 1 day, and (iv) after 3 days. CryoTEM images of the liposomes before adding nanocrystals showed that the (b) DOPC and (f) DOPG liposomes formed small, unilamellar vesicles. CryoTEM images (c-d) of the DOPC liposomes after bath sonication showed that Si nanocrystals incorporated with the lipid, however formed large complexes. CryoTEM images (g-h) of the DOPG liposomes after bath sonication showed that the Si nanocrystals aggregated outside of empty liposomes with no incorporation into the liposomes.....75

Figure 3.12 Dilution by dialysis of Si nanocrystals dispersed with (i) 7 mM CTAB and (ii) 7 mM quatsomes. (a) Photographs of vials containing (i) and (ii) prior to dialysis. Top row under ambient light and bottom row illuminated with a 254 nm ultraviolet lamp. (b-c) Photographs of the nanocrystal dispersions after (b) 3 and (c) 6 rounds of dialysis. (d) Photographs of dispersions removed from the dialysis tubing after 6 rounds of dialysis. (e-f) CryoTEM images of the 7 mM quatsome-Si nanocrystals after 6 rounds of dialysis.....76

Figure 3.13 Results of changing chloroform volume to quatsome-Si nanocrystal assembly stability, under ambient light (top row) and on a 254 nm UV lamp (bottom row). In each sample 135 μg of Si nanocrystals was added, though in different concentrations, and thus volumes of chloroform. Samples from left to right are: (i) 10 μl of 13.5 mg/ml Si nanocrystals in chloroform, (ii) 20 μl of 6.75 mg/ml Si nanocrystals in chloroform (typical conditions), (iii) 40 μl of 3.375 mg/ml Si nanocrystals in chloroform, (iv) 80 μl of 1.6875 mg/ml Si nanocrystals in chloroform, (v) 200 μl of 0.675 mg/ml Si nanocrystals in chloroform. (f) Within one day after preparation (vial (i) had orange-brown precipitate consistent with Si nanocrystals. 78

Figure 3.14 (a) TEM images of dodecanethiol-capped Au nanocrystals. (b) Histogram showing size distribution of Au nanocrystals. (c) TGA results for dodecanethiol-capped Au nanocrystals. 79

Figure 3.15 Results of incorporating 1.8 nm dodecanethiol capped Au nanocrystals into quatsomes through 5 minutes of bath sonication. (a) Photographs of vial with Au nanocrystals and quatsomes over 8 weeks showed a gradual change in color from brown-grey to purple (i) before sonication, (ii) immediately after sonication, (iii) after 1 day, (iv) after 2 weeks, (v) after 4 weeks, and (vi) after 8 weeks. (b) UV-Vis data for samples over time showed increase in plasmon peak intensity. (c) Size distribution of Au nanocrystals as measured by TEM. CryoTEM images of quatsome-AuNC dispersions at (d-e) 0 days, (f-g) 1 week, and (h-i) several weeks after preparation. 81

Figure 3.16 Proposed mechanism for the formation of quatsome-nanocrystal assemblies. In the diagram, CTAB is the blue headed structure, cholesterol is the yellow structure. (a) Scheme of the ligand densities on the Si nanocrystals (SiNC) and Au nanocrystals (AuNC). (b) Illustration of the interactions of Au nanocrystals and quatsomes and CTAB molecules. (c) Scheme of the interactions of Si nanocrystals and quatsomes, and the formation of the stable Si nanocrystals covered with a monolayer of chol-CTAB pairs.....83

Figure 4.1 Characterization of 10-undecenoic acid passivated Si nanocrystals. (a) Photoluminescence emission (solid lines) and absorbance (dashed lines) spectra captured for samples dispersed in ethanol (black lines) or water (blue lines) indicate minimal shift in photoluminescence properties. Inset is a photo of Si nanocrystals dispersed in water on an ultraviolet lamp (365 nm), demonstrating emission in the visible range. TEM images of Si nanocrystals in (b) ethanol and (c) water. (d) TGA data for the 10-undecenoic acid capped Si nanocrystals. (e) FTIR data for Si nanocrystals dried out of ethanol or water shows the deprotonation of COOH. (f) XRD data for Si nanocrystals dried out of ethanol or water (reference pattern is PDF 027-1402, with a=b=c=0.543088 nm)...101

Figure 4.2 Photographs of Si nanocrystals stored in water adjusted to pH 2 – pH 12 (as labeled on vials) over three days. 103

Figure 4.3 PL spectra of Si nanocrystals dispersed in (a) pH 7.4 water, (b) 0.1 M phosphate buffer, and (c) cell culture medium. In each figure, the spectra from days 0, 1, 2, 4, and 7 after adding Si nanocrystals into the solution are shown, with day 0 PL shown in black to day 7 PL shown in blue. Red spectra are PL measured for samples containing no Si nanocrystals and indicate solution fluorescence. Insets show normalized intensity over the same 7 day period (color coded as black for day 0 to blue for day 7). 104

Figure 4.4 Summary of changes in PL for Si nanocrystals dispersed in a variety of buffers and cell culture medium components for 7 days (error bars are standard deviation, n=3). PL decrease was measured by comparing PL intensity on day 7 to day 0. Positive values indicate a decrease in PL intensity. Peak wavelength was calculated as the average emission wavelength. A positive peak wavelength shift indicates a blue shift to lower wavelengths. 105

Figure 4.5 Scatter plots showing PL intensity decrease (a-b) and peak emission wavelength (c- d) as a function of concentration or pH.....106

Figure 4.6 XPS Si 2p data for Si nanocrystals dispersed in ethanol, water, cell culture medium, phosphate buffer, vitamin mix, and sodium bicarbonate. Data (black diamonds) was fit (blue line) with the relative contributions (black lines) from oxidized Si states. 108

Figure 4.7 (a) Results of ICP analysis of Si concentration in the filtrate from Si nanocrystals dispersed in various solutions. For each solution, the plots represent measurements taken on days 1, 4, and 7 after adding Si nanocrystals. The maximum possible Si concentration for the preparation was 1.56 mg/L. Comparison of the (b) PL intensity decrease and (c) the emission wavelength shift to the filtrate Si concentration on day 7. 109

Figure 4.8 Summary of changes in PL for Si nanocrystals dispersed in solutions at either 25 °C (blue bars) or 37 °C (orange bars) over 24 hours. 110

Figure 4.9 Confocal images of (a) J774 and (b) CHO cells incubated with Si nanocrystals (SiNC) for 3 hours at either 4 °C or 37 °C. Excitation wavelength of 405 nm was used, and Si nanocrystal signal (false colored red) was captured at 670-740 nm while DAPI nucleus signal (false colored blue) was captured at 417-566 nm. Flow cytometry fluorescence intensity of (c) J774 and (d) CHO cells incubated with either Si nanocrystals or with just water, at either 4 °C or 37 °C, identified that only J774 cells incubated with Si nanocrystals at physiological temperature showed an increase in emission intensity. 113

Figure 4.10 (a) Confocal images showing increase in Si nanocrystal (SiNC) signal throughout the cytoplasm of J774 cells after uptake over a 24 hour period. (b) Time dependent uptake of Si nanocrystals as measured by flow cytometry. (c) Concentration dependent uptake of Si nanocrystals as measured by flow cytometry. Error bars are standard deviation (n=3). 115

Figure 4.11 (a) Uptake of Si nanocrystals (SiNC) in the presence of cytochalasin D (CytD) and nocodazole (Noco) blockers, as measured by flow cytometry (error bars are standard deviation n=3). * indicate P<0.05 between Si nanocrystals with no drug and sample with drug using unpaired Student's t-test. Data normalized to sample with no drug. Confocal images of cells treated with (b) CytD and (c) Noco at 10 μg/ml. ...116

Figure 4.12 Viability assays using LDH and MTS for cells incubated (orange bars) with Si nanocrystals or (blue bars) without Si nanocrystals. 117

Figure 4.13 mRNA expression levels of inflammation markers TNF-α and IL-1β as measured by qPCR. Expression levels are reported as fold expression relative to cells treated with media containing only water. LPS was a positive control. Error bars are standard deviation (n=2). * indicate P<0.1 and ** indicate P<0.05 between LPS control and samples using unpaired Student's t-test. 118

Figure 5.1 Illustration of Si nanocrystal passivation, hydrolysis, and transfer to water. The photograph shows a vial containing 6.3 nm Si nanocrystals dispersed in water. 129

Figure 5.2 Transmission electron microscopy images of Si nanocrystals capped with ethyl 10-undecnocate with diameters of (a) 4.7 nm or (b) 6.3 nm. After one week in water the 6.3 nm nanocrystals (yellow arrows) appeared embedded in larger, amorphous material. 130

Figure 5.3 TGA results for ethyl 10-undecenoic acid Si nanocrystals performed in air atmosphere. 131

Figure 5.4 Characterization results of 6.3 nm Si nanocrystal hydrolysis and transfer into water. (a) FTIR spectra show the hydrolysis of ethyl 10-undecenoate ligands into carboxylic acids. (b) XRD patterns for Si nanocrystals throughout the process show no change to the crystal structure. The reference pattern is for diamond cubic silicon (PDF 027-1402, with a=b=c=0.543088 nm). (c) XPS spectra for Si nanocrystals. Raw data (black diamonds) was fit (blue line) by summing Si peak contributions (black lines).....133

Figure 5.5 Normalized absorbance and PL emission spectra for (a) 4.7 nm and (b) 6.3 nm Si nanocrystals, showing changes in spectra after hydrolysis of ethyl 10-undecenoate and then transfer into water. Si nanocrystals were dispersed in 1:1 v/v ethanol:toluene before hydrolysis, in ethanol after hydrolysis, and in pH 8.5 water after water transfer. Grey dashed lines indicate peak PL wavelength before hydrolysis (952 nm for the 4.7 nm Si nanocrystals and 985 nm for the 6.3 nm Si nanocrystals). 135

Figure 5.6 PL emission quantum yields of 4.7 nm and 6.3 nm Si nanocrystal samples. Si nanocrystals were dispersed in 1:1 v/v ethanol:toluene before hydrolysis, in ethanol after hydrolysis, and in pH 8.5 water after water transfer. 136

Figure 6.1 (a) Schematic depiction of TCSPC microscope setup, showing data capture from two PMTs to enable simultaneous capture of emission from spectrally distinct probes. HWP: half-wave plate, BD: beam dump, PBS: polarizing beam splitter, SM: scanning mirrors, DM: dichroic mirror. (b) Depiction of lifetime gating, showing the regions "R1" (0-2 ns after the PL peak) and "R2" (9.5-11.5 ns after the peak). The difference between the two sums (R1-R2) corresponds to the contribution from the short-lived emitting dye, while R2 corresponds to the contribution from the long-lived Si nanocrystals.....149

Figure 6.2 (a) PL spectrum for 10-undecenoic acid capped Si nanocrystals excited at 320 nm. Inset shows a vial of 10-undecenoic acid capped Si nanocrystals dispersed in water on a 365 nm ultraviolet lamp. (b) Time-resolved PL emission of Si nanocrystals dispersed in water exhibiting microsecond fluorescence decay lifetime; the data are fit to Equation 6.1 (red line). (c) Si nanocrystal PL intensity measured at increasing excitation laser powers. A linear fit (red line) to the log-log plot had a slope close to 2, confirming two-photon absorption.....151

Figure 6.3 One-photon confocal microscopy images of J774 cells after 3 hours of incubation with 10-undecenoic acid capped Si nanocrystals. DAPI emission is false colored blue and Si nanocrystal emission is false colored red. 152

Figure 6.4 (a) Si nanocrystal emission (orange line) shown in relation to peak DAPI emission (blue dotted line) and CellMask Deep Red (red dotted line), with shaded regions showing positions of the blue and red PMT emission filters. For control experiments containing either no probes or just one of the probes, the PL intensity over time for each image was summed in (b) the blue PMT and (c) the red PMT. Samples contained either no probes (cells only, black dots), Si nanocrystals only (red dots), DAPI only (blue dots), or CellMask Deep Red only (green dots). (c) The gating parameters selected were used to analyze images taken of the control samples, and the maximum intensity within each of the defined gating regions was normalized to the highest intensity probe. 154

Figure 6.5 (a) PL decay curves captured by the red and blue PMTs and integrated over all pixels show the fast and slow lifetime components of the fluorescent dyes and the Si nanocrystals. A brief gap in the lifetime data was an artifact of the collection system. (b) Intensity maps for each probe were constructed using the summed PL intensity in regions R1 and R2 at each pixel. (c) Overlaid images of the cells with emission from Si nanocrystals (false colored red), CellMask Deep Red dye (false colored green), and DAPI dye (false colored blue), show that the nanocrystals appear throughout the interior of the cell cytoplasm. The optical sections showing the top, middle, and bottom of the cells were taken 4 μm apart. 156

Figure 6.6 Lifetime-gated images showing overlaid Si nanocrystals (false colored red), lysosomes (false colored green), and dextran (false colored blue). The cells were incubated with the Si nanocrystals for either (a) 30 minutes or (b) 3 hours, and the optical sections were taken 4 μm apart to show the top, middle, and bottom of the cells. Cells selected for colocalization analysis are outlined with white dashed boxes. Insets show intensity scatter plots of the selected cells comparing the (top) green-lysosome and red-Si nanocrystal pixel intensities, and the (bottom) blue-dextran and red-Si nanocrystal pixel intensities, with linear data indicating colocalization. 158

Figure 7.1 Illustration of the bioconjugation of biotin to Si nanocrystals.....172

Figure 7.2 TEM images of Si nanocrystals after conjugation to amine-PEG11-biotin, and pictures of the vials on 365 nm ultraviolet lamp. (a-d) correspond to samples A-D as outlined in Table 7.1. 174

Figure 7.3 Dynamic light scattering data for bioconjugated samples. Measurements were taken in triplicate (error bars are standard deviation, n=3) at 25 °C. 176

Figure 7.4 (a) Photographs of nanocrystal dispersions before and after magnetic bead separation. Left two vials contain Si nanocrystals not conjugated to biotin. Right two vials contain Si nanocrystals conjugated to biotin. Middle two vials have streptavidin magnetic beads added. PL intensity of samples containing Si nanocrystals (SiNC) (b) or Si nanocrystals conjugated to biotin (c), measured before and after separation with magnetic beads. 178

Chapter 1: Introduction

1.1 Nanoparticles for Medical Applications

Nanotechnology advances over the past few decades have led to improved precision in the synthesis of nanoparticles with well characterized size, surface, and physical properties. These improvements have led to the successful application of nanotechnology in a variety of fields, including photovoltaics, light emitting diodes, catalysis, and medicine.[1] At the nanoscale, material physical properties are dominated by features such as high surface area to volume ratios as well as quantum size effects.[2] There has been considerable interest in the use of biocompatible nanotechnology for biomedical applications since the particles are on the same size scale as biomolecules and cells, and unique nanoscale properties can be exploited for use in medical imaging, sensing, and therapy.[3–8] Nanoparticles constructed of various materials have been synthesized extensively over the past few decades for medical applications. For example, the plasmon resonance observed in gold nanoparticles can be useful for photothermal therapy,[9] while iron oxide nanoparticles have been developed for use in magnetic resonance imaging.[4]

Fluorescent particles hold particular interest for medical imaging applications where organic dyes are currently used.[3,6,8,10–12] Compared to dyes, fluorescent nanoparticles typically exhibit favorable properties including improved photostability, broader absorption spectra, narrower emission spectra, and longer fluorescence lifetimes.[11] However, not all fluorescent particles are compatible for use in medical applications. Throughout the process of nanoparticle design, consideration must be given to the intended use of the products: for example, stability and toxicity of nanostructures in biological environments are critical considerations. Nanoparticles ranging from

inorganic nanocrystals to surfactant assemblies have thus been developed and studied for both *in vitro* and *in vivo* applications, including silicon based materials.

1.2 SEMICONDUCTOR NANOPARTICLES

1.2.1 Quantum Dots

Nanoscale semiconductor particles, known as quantum dots, were first reported in the early 1980's.[13,14] When semiconductor materials are scaled down to several nanometers, the electron wavefunctions become constrained, resulting in the energy levels in the conduction and valence bands becoming discrete and the bandgap widening (Figure 1.1).[2,3,14] The effective mass approximation can predict the bandgap for nanoscale materials. The result is composition and size-dependent photoluminescence (PL) emission which spans from the visible to infrared wavelengths for quantum dots constructed of materials including CdSe, CdS, CdTe, InP, InAs, GaAs, ZnSe, ZnS, PbSe, PbS, Si, and Ge.[3,14,15] Extensive research has been conducted to improve size-specific synthesis methods, resulting in particles with wide absorption spectra but narrow emission spectra, thereby making quantum dots ideal for multi-color imaging applications.[10,16–18] Further, the surface chemistries of quantum dots have been engineered with shells and ligands to enhance and stabilize PL emission while also allowing direct dispersion in aqueous solutions.[10,11,19]

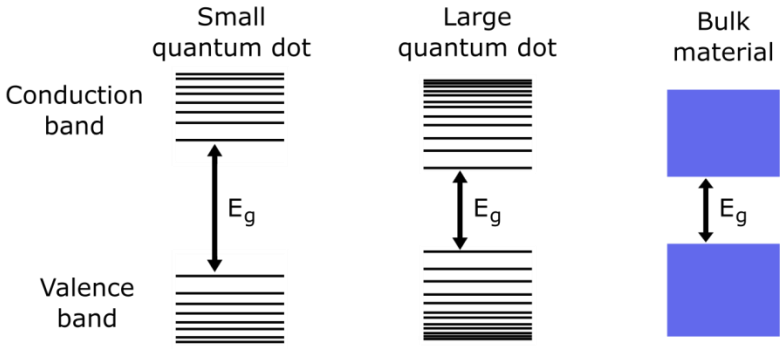

Figure 1.1 Illustration of the bandgap (E_g) in bulk semiconductor materials and nanoscale materials.

Although there has been a tremendous amount of research done on semiconductor quantum dots, much of that research has been based on heavy-metal containing particles, such as CdSe and CdS quantum dots. Because of the necessity for biocompatible and non-toxic materials, there has been a growing interest in silicon nanoparticles.

1.2.2 Silicon Nanocrystals

At the same time that heavy-metal quantum dots were first synthesized, photoluminescence was also observed in silicon (Si) based nanostructures.[14,20,21] Bulk silicon is an indirect bandgap semiconductor, such that the valence band maximum and conduction band minimum do not align in k-space and a phonon is necessary for electron hole recombination (Figure 1.2). While bulk silicon has a bandgap of 1.12 eV, quantum confinement effects at the nanoscale result in size-dependent photoluminescence emission ranging from visible to infrared wavelengths for nanocrystals on the scale of 2-10 nm.[14,22–24] The absorption spectra for Si nanocrystals exhibit no exciton peaks, and a wide apparent Stokes shift is observed (Figure 1.3).

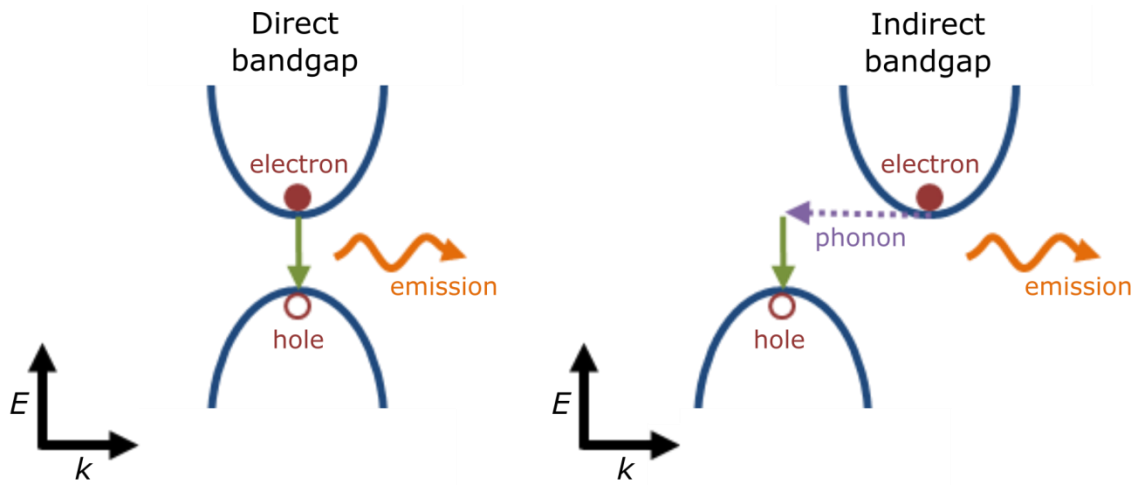

Figure 1.2 Illustration comparing electron-hole recombination and light emission in direct and indirect bandgap semiconductors.

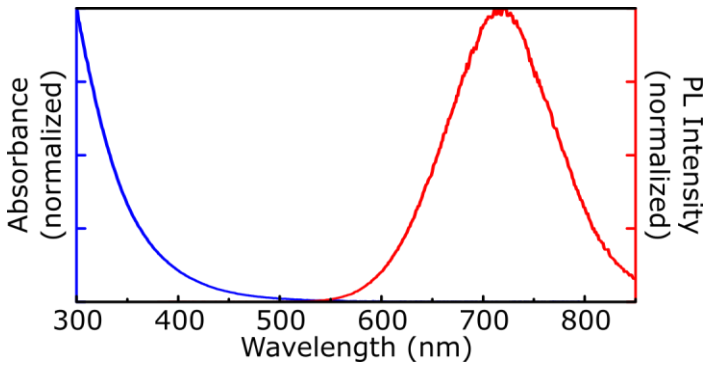

Figure 1.3 Absorbance and PL spectra (excited at 320 nm) for 2.8 nm diameter Si nanocrystals passivated with 1-octene and dispersed in chloroform.

A number of synthesis methods have been developed for Si nanocrystals. Early efforts focused on the formation of Si–rich films by various methods such as ion implantation and co-sputtering which could then be etched with hydrofluoric acid to result in colloidal Si nanocrystals.[25,26] Si nanocrystals have also been formed by the reductive thermolysis of $(HSiO_{1.5})_n$ sol-gel glasses,[27] by solution based methods such as precursor reduction or zintl salt based reactions,[28–31] by preparation in supercritical

fluids,[32,33] and by decomposition of silanes by plasma or heat.[34–36] It should be noted that some of these methods produce blue emitting Si nanocrystals instead of the red emitting particles predicted by the effective mass approximation. These blue emitting nanocrystals tend to display size independent emission. An analysis of the methods that produce blue emitting particles suggests that the introduction of nitrogen or oxygen impurities during synthesis can contribute to the blue emission.[37,38] Ideally, Si nanocrystal emission should remain in red to infrared wavelengths, where tissue penetration is deepest for bioimaging applications.[19,39–41]

A method proposed by Hessel, et al. was developed which addresses challenges encountered with other synthesis methods such as low production yield and poor size control, and reproducibly produces pure nanocrystals which emit in visible to infrared wavelengths (Figure 1.4).[23,42,43] The synthesis starts with a silicon rich flowable oxide (hydrogen silsesquioxane) which is heat in a tube furnace under a reducing atmosphere (forming gas 7% H_2 and 93% N). The result of the annealing is an SiO_2 matrix with embedded Si nanocrystals. The annealing step conditions determine the particle size; for example, annealing at 1100 °C for 1 hour results in Si nanocrystals with diameters of approximately 2.8 nm. After annealing the material can be ground into a fine powder first using a mortar and pestle and then by shaking with borosilicate beads in a wrist action shaker for 9 hours. Etching with HF and HCl in the dark results in liberation of the Si nanocrystals from the SiO_2 matrix, and is typically accomplished over 3-6 hours. The result of the etching is hydrogen terminated Si nanocrystals. This process not only produces size-controlled nanocrystals, but produces them in high quantities (for example, 1 g in a typical synthesis).[43]

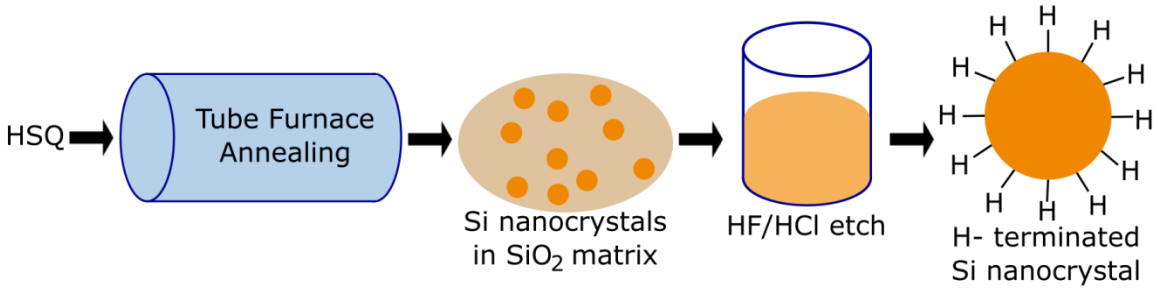

Figure 1.4 Illustration of the process for forming Si nanocrystals by the thermal annealing of hydrogen silsesquioxane.

For all Si nanocrystal synthesis methods, surface chemistry is of critical importance to ensure that the nanocrystals are photoluminescent and stable. Because nanocrystals can contain just a few hundred atoms, a large percentage of the atoms are at the surface. It has been commonly observed that oxidizing Si nanoparticle surfaces results in a PL blue shift, while the introduction of certain functional groups (such as alkyls or amines) can also change emission color.[34,44–46] Hydrogen terminated Si nanocrystals tend to oxidize quickly and surfaces must be protected to maintain photoluminescence. Unlike other quantum dots, adding a semiconductor shell on the Si nanocrystal core is challenging because of the lack of lattice-matched materials that are compatible with crystalline Si. Thus, most preparation methods for colloidal Si nanocrystals use surface passivation through hydrosylilation, resulting in stable Si-C bonds linking ligands to the nanocrystals. Hydrosylilation can be accomplished by thermal processing, UV irradiation, or with the assistance of a platinum catalyst.[23,44,47–49] Si nanocrystals have been passivated with hydrophobic and hydrophilic ligands including, but not limited to, 1-dodecene, 1-octadecence, 10-undecenoic acid, 3-butenoic acid, 1-dodecanethiol, styrene, and diphenylamine.[23,45,50–54] Si nanocrystals passivated with these ligands tend to maintain stable emission for long periods of time (sometimes

on the scale of years). Depending on the ligand, Si nanocrystals may be dispersed in polar or non-polar solvents.

Compared to heavy-metal containing quantum dots, Si nanocrystals developed thus far have slightly lower reported quantum yields (up to 60% vs around 80%), longer PL decay lifetimes (10's of μs vs 10's of ns), wider emission spectra (full width at half maximum on the order of 150-200 nm, Figure 1.3), and, as discussed above, challenges with surface oxidation.[11,23,24,51] However, the biocompatibility of Si, along with emission in the visible to infrared wavelengths, continues to drive the development of these materials for biomedical applications. Silicon is found in trace amounts in the human body, which suggests that if the particles degrade *in vivo* the silicic acid products would not be adverse to patient health.[55,56] Previous work has demonstrated promising results for using Si nanocrystals in *in vitro* and *in vivo* applications,[50,51,56–59] and therefore there is an opportunity to continue investigating their use for bioimaging.

1.3 DISPERSING NANOPARTICLES IN AQUEOUS SOLUTIONS

In order for materials to be useful for biological applications, the particles should remain colloidally dispersed without aggregation in aqueous solutions. Nanoparticle stability in biological solutions can generally be achieved in one of two ways depending on the particle's surface chemistry: (i) hydrophobic nanoparticles can be dispersed with the assistance of amphiphilic molecules, or (ii) hydrophilic nanoparticles can be directly dispersed into water.

1.3.1 Surfactants and Polymers

Amphiphilic molecules have been used to coat the surfaces of individual nanoparticles to allow dispersion in aqueous environments. Molecules used to coat nanoparticles have included polymers such as polyethylene glycol or poly(maleic anhydride), and has included direct conjugation of the polymer to the nanoparticle or surface adsorption.[51,60–63] The use of molecules such as polyethylene glycol can also impact nanoparticle interactions with cells: the layer can provide "stealth" characteristics on the nanoparticles that change how proteins and cells interact with the particle surfaces.[64]

Surfactant molecules can also be used to disperse nanoparticles with hydrophobic surfaces. Micelles and liposomes have been used for decades as delivery vehicles for hydrophobic and hydrophilic drugs, with many formulations in clinical use (Figure 1.5).[65,66] Liposomes have been extensively characterized and thus there is considerable knowledge available for lipids that can, for example, target specific types of cells, or that are responsive to heat.[66,67] Nanoparticles incorporated with surfactants have been shown to be stable and easily dispersible in aqueous solutions.[50,51,68–71] Techniques such as cryogenic transmission electron microscopy can aid in the study of these assemblies since they allow the direct observation of the systems frozen in vitreous ice.[72]

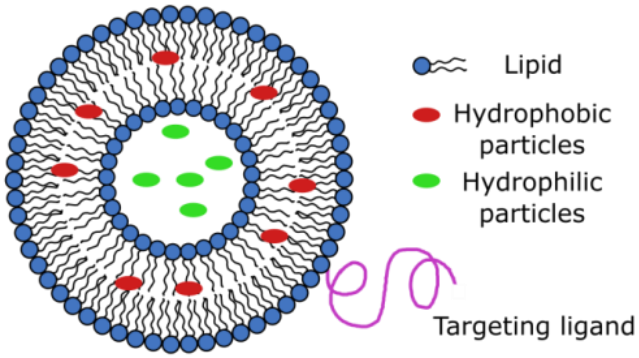

Figure 1.5 Illustration of liposome showing assembly of hydrophobic particles inside of the lipid bilayer and hydrophilic particles inside the aqueous core.

1.3.2 Hydrophilic Ligands

Nanoparticle surfaces have been engineered with shells or surface-conjugated ligands to allow direct dispersion of the particles in water without the need for additional polymers or surfactants. Hydrophilic capping ligands include molecules that can be directly bound to the silicon surface and contain distal polar groups that can interact with an aqueous environment.[49,73,74] Si nanocrystals have been capped with 10-undecenoic acid, which results in distal polar carboxylic acid groups that can enable the nanocrystals to be dispersed in polar solvents such as ethanol or water.[52,75] In aqueous solutions at neutral pH, the carboxylic acids deprotonate, leaving the nanoparticles with negatively charged surfaces that contribute to electrostatic repulsive forces between the nanoparticles to achieve colloidal stability.[76] This stabilization is very sensitive, however, to conditions including the solution pH and ionic content, and thus particles that may be stable in water can aggregate when exposed to biological solutions. In contrast to the methods using polymers and surfactants, ligand-dispersible nanoparticles tend to be much smaller. For example, a Si nanocrystal with 2.8 nm diameter core has a diameter of

around 5 nm when capped with 10-undecenoic acid ligands. This puts the nanocrystals on the same size scale as large proteins or antibodies.

1.4 BIOIMAGING

Fluorescence imaging techniques have been extensively developed and used in applications ranging from the study of *in vitro* biological processes to labeling *in vivo* structures for medical diagnostics.[12,77,78] These techniques can often be performed using simple equipment (such as an ultraviolet lamp) and the results can be evaluated by direct observation or by capturing and processing images, making fluorescence imaging a quick, yet accurate technique to obtain valuable biological information.[12] Imaging relies on the ability for fluorescent probes such as organic dyes to accumulate at the sites of certain biomolecules or tissue. Nanoparticles continue to be explored as fluorescent probes due to favorable attributes such as resistance to photobleaching and adaptable surface chemistries that can enable cell targeting.[11,79]

Fluorescent silicon nanoparticles have been demonstrated for use in bioimaging at the cellular, tissue, and animal scales, with no toxicity observed.[50,51,56–59,74,80–82] The ability to reproducibly synthesize Si nanocrystals with specific emission wavelengths that span the near-infrared imaging window make them potential candidates for spectrally multiplexed imaging, where one excitation wavelength can be used to excite probes that emit at different wavelengths, and which has been demonstrated with quantum dots.[16–18] Unfortunately, spectral multiplexing with Si nanocrystals has been difficult to achieve due to the broad emission spectra, with full width at half maximum in the range of 150-200 nm. Beyond spectral multiplexing, temporal multiplexing has also been investigated for imaging with multiple fluorescent probes. Time-correlated single photon counting

(TCSPC) allows for the measurement of fluorescence decay in biological samples, and thus can discern between probes that have different fluorescent lifetimes (Figure 1.6a).[83] Because of the unique time scales typically observed for organic dyes (< 10 ns), quantum dots (10-100 ns, depending on the material), and Si nanocrystals (10-100 µs), lifetime imaging can enable temporal multiplexing of multiple probes, even when they have overlapping emission spectra.[11,84–86]

Multi-photon imaging has also been explored with quantum dots since they efficiently undergo two-photon absorption (Figure 1.6b).[87] Because the two photons have lower energy than photons used for single photon excitation, pulsed infrared lasers are typically used, which enables imaging deep into tissue samples.[39,87,88] Additionally, because two-photon absorption depends on the simultaneous presence of two photons the excitation probability is localized to a small focal volume and thus allows for three-dimensional resolution.[77,87] Si nanocrystals have been shown to exhibit efficient two photon absorption.[80,81,89]

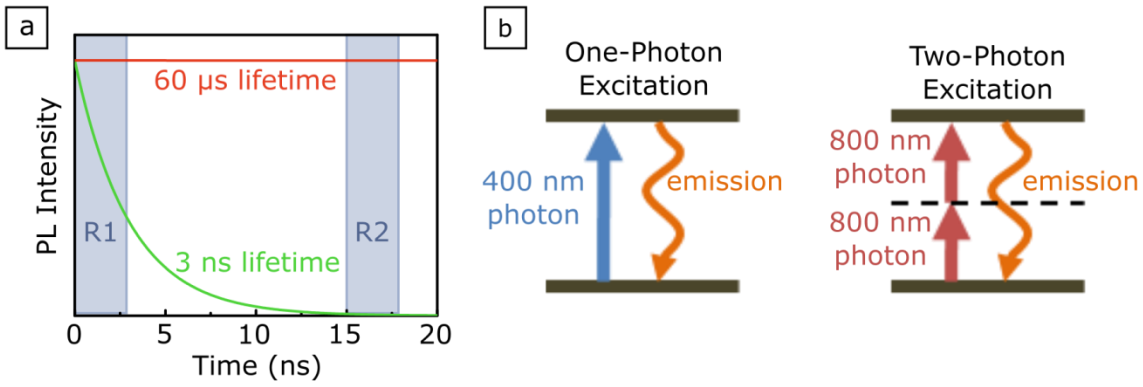

Figure 1.6 (a) Illustration of lifetime gating using a short lived (3 ns) probe and a long lived (60 µs) probe. By gating the emission at short times (region R1) versus long times (region R2), it is possible to separate the contributions from the two probes. (b) Illustration of one-photon and two-photon excitation.

In the development of new probes for bioimaging, it is necessary to consider the interactions between nanoparticles and biomolecules or cells. Previous work has identified that nanoparticle characteristics such as their size, shape, and surface chemistry can impact how particles are taken up by cells, as well as how nanoparticles are cleared from the body.[56,90–94] If the intent is to use a probe for imaging inside of cells it is necessary to study the uptake mechanism used by the cells to ensure the probe can reach its target.[93] The fate of the material after imaging is another important factor in the design of new fluorescent probes. Since silicon is found in the human body in trace amounts and the body is able to process and clear silicic acids,[55,95] it is expected that silicon based probes can degrade over time and be removed from patients without the accumulation of toxic materials.

Additionally, the fluorescence stability of probes is a critical consideration for *in vivo* and *in vitro* imaging. Probes must be able to retain their fluorescence when exposed to the biological environment, and should maintain their fluorescence for a sufficiently long enough period for the particles to accumulate in the target cell or tissue. Considering that nanoparticles may accumulate in tissues or organelles with low pH or high concentrations of biomolecules, characterization of the particle fluorescence stability in those environments will guide the use of Si nanocrystals for *in vivo* and *in vitro* imaging applications.

1.5 DISSERTATION OVERVIEW

The need for biocompatible and non-toxic particles has continued to be of primary interest for the development of new fluorescent probes for bioimaging. Si nanocrystals synthesis methods have been greatly improved to produce passivated particles with size-

dependent photoluminescence, and thus the goal of this work is to move Si nanocrystals toward practical use in fluorescence imaging. Chapter 2 presents the results of using liposomal assemblies to disperse hydrophobic Si nanocrystals, and also examines the uptake of the fluorescent Si nanocrystal-liposome assemblies by macrophage cells. Chapter 3 studies the incorporation of Si nanocrystals into "quatsomes," which are stable surfactant assemblies composed of cetyl trimethylammonium bromide and cholesterol. Chapter 4 explores the stability of 10-undecenoic acid capped Si nanocrystals in aqueous biological solutions and characterizes the uptake of the Si nanocrystals in cells using flow cytometry and confocal microscopy, as well as assesses the toxicity of the nanoparticles. Chapter 5 presents data for water dispersible Si nanocrystals that emit in the near infrared. Chapter 6 demonstrates the use of 10-undecenoic acid capped Si nanocrystals for two-photon and lifetime gated *in vitro* imaging. Chapter 7 presents data on the bioconjugation of biotin to 10-undecenoinc acid capped Si nanocrystals. Chapter 8 provides final conclusions and proposed future research.

1.6 REFERENCES

(1) Kovalenko, M. V.; Manna, L.; Cabot, A.; Hens, Z.; Talapin, D. V.; Kagan, C. R.; Klimov, V. I.; Rogach, A. L.; Reiss, P.; Milliron, D. J.; Guyot-Sionnest, P.; Konstantatos, G.; Park, W. J.; Hyeon, T.; Korgel, B. A.; Murray, C. B.; Heiss, W. Prospects of Nanoscience with Nanocrystals. *ACS Nano* **2015**, *9*, 1012–1057.

(2) Alivisatos, A. P. Perspectives on the Physical Chemistry of Semiconductor Nanocrystals. *J. Phys. Chem*. **1996**, *100*, 13226–13239.

(3) Bruchez, M.; Moronne, M.; Gin, P.; Weiss, S.; Alivisatos, A. P. Semiconductor Nanocrystals as Fluorescent Biological Labels. *Science* **1998**, *281*, 2013–2016.

(4) Pankhurst, Q. A.; Connolly, J.; Jones, S. K.; Dobson, J. Applications of Magnetic Nanoparticles in Biomedicine. *J. Phys. Appl. Phys.* **2003**, *36*, R167.

(5) Salata, O. Applications of Nanoparticles in Biology and Medicine. *J. Nanobiotechnology* **2004**, *2*, 3.

(6) Medintz, I. L.; Uyeda, H. T.; Goldman, E. R.; Mattoussi, H. Quantum Dot Bioconjugates for Imaging, Labelling and Sensing. *Nat. Mater*. **2005**, *4*, 435–446.

(7) Luo, X.; Morrin, A.; Killard, A. J.; Smyth, M. R. Application of Nanoparticles in Electrochemical Sensors and Biosensors. *Electroanalysis* **2006**, *18*, 319–326.

(8) Yao, J.; Yang, M.; Duan, Y. Chemistry, Biology, and Medicine of Fluorescent Nanomaterials and Related Systems: New Insights into Biosensing, Bioimaging, Genomics, Diagnostics, and Therapy. *Chem. Rev*. **2014**, *114*, 6130–6178.

(9) Hu, M.; Chen, J.; Li, Z.-Y.; Au, L.; Hartland, G. V.; Li, X.; Marquez, M.; Xia, Y. Gold Nanostructures: Engineering Their Plasmonic Properties for Biomedical Applications. *Chem. Soc. Rev*. **2006**, *35*, 1084–1094.

(10) Pinaud, F.; Michalet, X.; Bentolila, L. A.; Tsay, J. M.; Doose, S.; Li, J. J.; Iyer, G.; Weiss, S. Advances in Fluorescence Imaging with Quantum Dot Bio-Probes. *Biomaterials* **2006**, *27*, 1679–1687.

(11) Resch-Genger, U.; Grabolle, M.; Cavaliere-Jaricot, S.; Nitschke, R.; Nann, T. Quantum Dots versus Organic Dyes as Fluorescent Labels. *Nat. Methods* **2008**, *5*, 763–775.

(12) Kobayashi, H.; Ogawa, M.; Alford, R.; Choyke, P. L.; Urano, Y. New Strategies for Fluorescent Probe Design in Medical Diagnostic Imaging. *Chem. Rev*. **2010**, *110*, 2620–2640.

(13) Brus, L. E. Electron–electron and Electron-hole Interactions in Small Semiconductor Crystallites: The Size Dependence of the Lowest Excited Electronic State. *J. Chem. Phys.* **1984**, *80*, 4403–4409.

(14) Brus, L. E.; Szajowski, P. F.; Wilson, W. L.; Harris, T. D.; Schuppler, S.; Citrin, P. H. Electronic Spectroscopy and Photophysics of Si Nanocrystals: Relationship to Bulk c-Si and Porous Si. *J. Am. Chem. Soc*. **1995**, *117*, 2915–2922.

(15) Murray, C. B.; Norris, D. J.; Bawendi, M. G. Synthesis and Characterization of Nearly Monodisperse CdE (E = Sulfur, Selenium, Tellurium) Semiconductor Nanocrystallites. *J. Am. Chem. Soc*. **1993**, *115*, 8706–8715.

(16) Jaiswal, J. K.; Mattoussi, H.; Mauro, J. M.; Simon, S. M. Long-Term Multiple Color Imaging of Live Cells Using Quantum Dot Bioconjugates. *Nat. Biotechnol*. **2003**, *21*, 47–51.

(17) Wu, X.; Liu, H.; Liu, J.; Haley, K. N.; Treadway, J. A.; Larson, J. P.; Ge, N.; Peale, F.; Bruchez, M. P. Immunofluorescent Labeling of Cancer Marker Her2 and Other Cellular Targets with Semiconductor Quantum Dots. *Nat. Biotechnol*. **2003**, *21*, 41–46.

(18) Kang, W. J.; Chae, J. R.; Cho, Y. L.; Lee, J. D.; Kim, S. Multiplex Imaging of Single Tumor Cells Using Quantum-Dot-Conjugated Aptamers. *Small* **2009**, *5*, 2519–2522.

(19) Michalet, X.; Pinaud, F. F.; Bentolila, L. A.; Tsay, J. M.; Doose, S.; Li, J. J.; Sundaresan, G.; Wu, A. M.; Gambhir, S. S.; Weiss, S. Quantum Dots for Live Cells, in Vivo Imaging, and Diagnostics. *Science* **2005**, *307*, 538–544.

(20) Canham, L. T. Silicon Quantum Wire Array Fabrication by Electrochemical and Chemical Dissolution of Wafers. *Appl. Phys. Lett*. **1990**, *57*, 1046–1048.

(21) Cullis, A. G.; Canham, L. T.; Calcott, P. D. J. The Structural and Luminescence Properties of Porous Silicon. *J. Appl. Phys*. **1997**, *82*, 909–965.

(22) Takagahara, T.; Takeda, K. Theory of the Quantum Confinement Effect on Excitons in Quantum Dots of Indirect-Gap Materials. *Phys. Rev. B* **1992**, *46*, 15578–15581.

(23) Hessel, C. M.; Reid, D.; Panthani, M. G.; Rasch, M. R.; Goodfellow, B. W.; Wei, J.; Fujii, H.; Akhavan, V.; Korgel, B. A. Synthesis of Ligand-Stabilized Silicon Nanocrystals with Size-Dependent Photoluminescence Spanning Visible to Near-Infrared Wavelengths. *Chem. Mater*. **2012**, *24*, 393–401.

(24) Yu, Y.; Fan, G.; Fermi, A.; Mazzaro, R.; Morandi, V.; Ceroni, P.; Smilgies, D.-M.; Korgel, B. A. Size-Dependent Photoluminescence Efficiency of Silicon Nanocrystal Quantum Dots. *J. Phys. Chem. C* **2017**, *121*, 23240-23248.

(25) Hayashi, S.; Nagareda, T.; Kanzawa, Y.; Yamamoto, K. Photoluminescence of Si-Rich SiO2 Films: Si Clusters as Luminescent Centers. *Jpn. J. Appl. Phys*. **1993**, *32*, 3840.

(26) Pavesi, L.; Negro, L. D.; Mazzoleni, C.; Franzo, G.; Priolo, F. Optical Gain in Silicon Nanocrystals. *Nature* **2000**, *408*, 440–444.

(27) Henderson, E. J.; Kelly, J. A.; Veinot, J. G. C. Influence of HSiO1.5 Sol−Gel Polymer Structure and Composition on the Size and Luminescent Properties of Silicon Nanocrystals. *Chem. Mater*. **2009**, *21*, 5426–5434.

(28) Heath, J. R. A Liquid-Solution-Phase Synthesis of Crystalline Silicon. *Science* **1992**, *258*, 1131.

(29) Dhas, N. A.; Raj, C. P.; Gedanken, A. Preparation of Luminescent Silicon Nanoparticles: A Novel Sonochemical Approach. *Chem. Mater*. **1998**, *10*, 3278–3281.

(30) Bley, R. A.; Kauzlarich, S. M. A Low-Temperature Solution Phase Route for the Synthesis of Silicon Nanoclusters. *J. Am. Chem. Soc*. **1996**, *118*, 12461–12462.

(31) Yang, C.-S.; Bley, R. A.; Kauzlarich, S. M.; Lee, H. W. H.; Delgado, G. R. Synthesis of Alkyl-Terminated Silicon Nanoclusters by a Solution Route. *J. Am. Chem. Soc*. **1999**, *121*, 5191–5195.

(32) Holmes, J. D.; Ziegler, K. J.; Doty, R. C.; Pell, L. E.; Johnston, K. P.; Korgel, B. A. Highly Luminescent Silicon Nanocrystals with Discrete Optical Transitions. *J. Am. Chem. Soc*. **2001**, *123*, 3743–3748.

(33) English, D. S.; Pell, L. E.; Yu, Z.; Barbara, P. F.; Korgel, B. A. Size Tunable Visible Luminescence from Individual Organic Monolayer Stabilized Silicon Nanocrystal Quantum Dots. *Nano Lett*. **2002**, *2*, 681–685.

(34) Li, X.; He, Y.; Talukdar, S. S.; Swihart, M. T. Process for Preparing Macroscopic Quantities of Brightly Photoluminescent Silicon Nanoparticles with Emission Spanning the Visible Spectrum. *Langmuir* **2003**, *19*, 8490–8496.

(35) Cannon, W. r.; Danforth, S. c.; Flint, J. h.; Haggerty, J. s.; Marra, R. a. Sinterable Ceramic Powders from Laser-Driven Reactions: I, Process Description and Modeling. *J. Am. Ceram. Soc*. **1982**, *65*, 324–330.

(36) Mangolini, L.; Thimsen, E.; Kortshagen, U. High-Yield Plasma Synthesis of Luminescent Silicon Nanocrystals. *Nano Lett*. **2005**, *5*, 655–659.

(37) Fuzell, J.; Thibert, A.; Atkins, T. M.; Dasog, M.; Busby, E.; Veinot, J. G. C.; Kauzlarich, S. M.; Larsen, D. S. Red States versus Blue States in Colloidal Silicon Nanocrystals: Exciton Sequestration into Low-Density Traps. *J. Phys. Chem. Lett*. **2013**, *4*, 3806–3812.

(38) Dasog, M.; Yang, Z.; Regli, S.; Atkins, T. M.; Faramus, A.; Singh, M. P.; Muthuswamy, E.; Kauzlarich, S. M.; Tilley, R. D.; Veinot, J. G. C. Chemical Insight into the Origin of Red and Blue Photoluminescence Arising from Freestanding Silicon Nanocrystals. *ACS Nano* **2013**, *7*, 2676–2685.

(39) Bashkatov, A. N.; Genina, E. A.; Kochubey, V. I.; Tuchin, V. V. Optical Properties of Human Skin, Subcutaneous and Mucous Tissues in the Wavelength Range from 400 to 2000 nm. *J. Phys. Appl. Phys*. **2005**, *38*, 2543.

(40) Weissleder, R. A Clearer Vision for in Vivo Imaging. *Nat. Biotechnol*. **2001**, *19*, 316–317.

(41) Frangioni, J. V. In Vivo Near-Infrared Fluorescence Imaging. *Curr. Opin. Chem. Biol*. **2003**, *7*, 626–634.

(42) Hessel, C. M.; Henderson, E. J.; Veinot, J. G. C. Hydrogen Silsesquioxane: A Molecular Precursor for Nanocrystalline Si−SiO2 Composites and Freestanding Hydride-Surface-Terminated Silicon Nanoparticles. *Chem. Mater*. **2006**, *18*, 6139–6146.

(43) Clark, R. J.; Aghajamali, M.; Gonzalez, C. M.; Hadidi, L.; Islam, M. A.; Javadi, M.; Mobarok, M. H.; Purkait, T. K.; Robidillo, C. J. T.; Sinelnikov, R.; Thiessen, A. N.; Washington, J.; Yu, H.; Veinot, J. G. C. From Hydrogen Silsesquioxane to Functionalized Silicon Nanocrystals. *Chem. Mater*. **2017**, *29*, 80–89.

(44) Gupta, A.; Swihart, M. T.; Wiggers, H. Luminescent Colloidal Dispersion of Silicon Quantum Dots from Microwave Plasma Synthesis: Exploring the Photoluminescence Behavior Across the Visible Spectrum. *Adv. Funct. Mater*. **2009**, *19*, 696–703.

(45) Dasog, M.; De los Reyes, G. B.; Titova, L. V.; Hegmann, F. A.; Veinot, J. G. C. Size vs Surface: Tuning the Photoluminescence of Freestanding Silicon Nanocrystals Across the Visible Spectrum via Surface Groups. *ACS Nano* **2014**, *8*, 9636–9648.

(46) Sinelnikov, R.; Dasog, M.; Beamish, J.; Meldrum, A.; Veinot, J. G. C. Revisiting an Ongoing Debate: What Role Do Surface Groups Play in Silicon Nanocrystal Photoluminescence? *ACS Photonics* **2017**, *4*, 1920–1929.

(47) Dohnalová, K.; Poddubny, A. N.; Prokofiev, A. A.; De Boer, W. D.; Umesh, C. P.; Paulusse, J. M.; Zuilhof, H.; Gregorkiewicz, T. Surface Brightens up Si Quantum Dots: Direct Bandgap-like Size-Tunable Emission. *Light Sci. Appl*. **2013**, I, e47.

(48) Dohnalová, K.; Gregorkiewicz, T.; Kůsová, K. Silicon Quantum Dots: Surface Matters. *J. Phys. Condens. Matter* **2014**, *26*, 173201.

(49) Warner, J. H.; Hoshino, A.; Yamamoto, K.; Tilley, R. D. Water-Soluble Photoluminescent Silicon Quantum Dots. *Angew. Chem*. **2005**, *117*, 4626–4630.

(50) Erogbogbo, F.; Yong, K.-T.; Roy, I.; Hu, R.; Law, W.-C.; Zhao, W.; Ding, H.; Wu, F.; Kumar, R.; Swihart, M. T.; Prasad, P. N. In Vivo Targeted Cancer Imaging, Sentinel Lymph Node Mapping and Multi-Channel Imaging with Biocompatible Silicon Nanocrystals. *ACS Nano* **2010**, *5*, 413–423.

(51) Henderson, E. J.; Shuhendler, A. J.; Prasad, P.; Baumann, V.; Maier-Flaig, F.; Faulkner, D. O.; Lemmer, U.; Wu, X. Y.; Ozin, G. A. Colloidally Stable Silicon Nanocrystals with Near-Infrared Photoluminescence for Biological Fluorescence Imaging. *Small* **2011**, *7*, 2507–2516.

(52) Yu, Y.; Hessel, C. M.; Bogart, T. D.; Panthani, M. G.; Rasch, M. R.; Korgel, B. A. Room Temperature Hydrosilylation of Silicon Nanocrystals with Bifunctional Terminal Alkenes. *Langmuir* **2013**, *29*, 1533–1540.

(53) Yu, Y.; Rowland, C. E.; Schaller, R. D.; Korgel, B. A. Synthesis and Ligand Exchange of Thiol-Capped Silicon Nanocrystals. *Langmuir* **2015**, *31*, 6886–6893.

(54) Yu, Y.; Korgel, B. A. Controlled Styrene Monolayer Capping of Silicon Nanocrystals by Room Temperature Hydrosilylation. *Langmuir* **2015**, *31*, 6532–6537.

(55) Iler, R. K. *The Chemistry of Silica: Solubility, Polymerization, Colloid and Surface Properties, and Biochemistry*; Wiley: New York, 1979.

(56) Park, J.-H.; Gu, L.; Maltzahn, G. von; Ruoslahti, E.; Bhatia, S. N.; Sailor, M. J. Biodegradable Luminescent Porous Silicon Nanoparticles for in Vivo Applications. *Nat. Mater*. **2009**, *8*, 331–336.

(57) Erogbogbo, F.; Yong, K.-T.; Roy, I.; Xu, G.; Prasad, P. N.; Swihart, M. T. Biocompatible Luminescent Silicon Quantum Dots for Imaging of Cancer Cells. *ACS Nano* **2008**, *2*, 873–878.

(58) Bhattacharjee, S.; Rietjens, I. M. C. M.; Singh, M. P.; Atkins, T. M.; Purkait, T. K.; Xu, Z.; Regli, S.; Shukaliak, A.; Clark, R. J.; Mitchell, B. S.; Alink, G. M.; Marcelis, A. T. M.; Fink, M. J.; Veinot, J. G. C.; Kauzlarich, S. M.; Zuilhof, H. Cytotoxicity of Surface-Functionalized Silicon and Germanium Nanoparticles: The Dominant Role of Surface Charges. *Nanoscale* **2013**, *5*, 4870–4883.

(59) Liu, J.; Erogbogbo, F.; Yong, K.-T.; Ye, L.; Liu, J.; Hu, R.; Chen, H.; Hu, Y.; Yang, Y.; Yang, J.; Roy, I.; Karker, N. A.; Swihart, M. T.; Prasad, P. N. Assessing Clinical Prospects of Silicon Quantum Dots: Studies in Mice and Monkeys. *ACS Nano* **2013**, *7*, 7303–7310.

(60) Gao, X.; Cui, Y.; Levenson, R. M.; Chung, L. W. K.; Nie, S. In Vivo Cancer Targeting and Imaging with Semiconductor Quantum Dots. *Nat. Biotechnol*. **2004**, *22*, 969–976.

(61) Clark, R. J.; Dang, M. K. M.; Veinot, J. G. C. Exploration of Organic Acid Chain Length on Water-Soluble Silicon Quantum Dot Surfaces. *Langmuir* **2010**, *26*, 15657–15664.

(62) Jokerst, J. V.; Lobovkina, T.; Zare, R. N.; Gambhir, S. S. Nanoparticle PEGylation for Imaging and Therapy. *Nanomed*. **2011**, *6*, 715–728.

(63) Hessel, C. M.; Rasch, M. R.; Hueso, J. L.; Goodfellow, B. W.; Akhavan, V. A.; Puvanakrishnan, P.; Tunnel, J. W.; Korgel, B. A. Alkyl Passivation and Amphiphilic Polymer Coating of Silicon Nanocrystals for Diagnostic Imaging. *Small* **2010**, *6*, 2026–2034.

(64) Gref, R.; Lück, M.; Quellec, P.; Marchand, M.; Dellacherie, E.; Harnisch, S.; Blunk, T.; Müller, R. H. 'Stealth' Corona-Core Nanoparticles Surface Modified by Polyethylene Glycol (PEG): Influences of the Corona (PEG Chain Length and Surface Density) and of the Core Composition on Phagocytic Uptake and Plasma Protein Adsorption. *Colloids Surf. B Biointerfaces* **2000**, *18*, 301–313.

(65) Chang, H.-I.; Yeh, M.-K. Clinical Development of Liposome-Based Drugs: Formulation, Characterization, and Therapeutic Efficacy. *Int. J. Nanomedicine* **2012**, *7*, 49–60.

(66) Allen, T. M.; Cullis, P. R. Liposomal Drug Delivery Systems: From Concept to Clinical Applications. *Adv. Drug Deliv. Rev*. **2013**, *65*, 36–48.

(67) Manzoor, A. A.; Lindner, L. H.; Landon, C. D.; Park, J.-Y.; Simnick, A. J.; Dreher, M. R.; Das, S.; Hanna, G.; Park, W.; Chilkoti, A.; Koning, G. A.; Hagen, T. L. M. T.; Needham, D.; Dewhirst, M. W. Overcoming Limitations in Nanoparticle Drug Delivery: Triggered, Intravascular Release to Improve Drug Penetration into Tumors. *Cancer Res*. **2012**, *72*, 5566–5575.

(68) Dubertret, B.; Skourides, P.; Norris, D. J.; Noireaux, V.; Brivanlou, A. H.; Libchaber, A. In Vivo Imaging of Quantum Dots Encapsulated in Phospholipid Micelles. *Science* **2002**, *298*, 1759–1762.

(69) Al-Jamal, W. T.; Al-Jamal, K. T.; Tian, B.; Lacerda, L.; Bomans, P. H.; Frederik, P. M.; Kostarelos, K. Lipid−Quantum Dot Bilayer Vesicles Enhance Tumor Cell Uptake and Retention in Vitro and in Vivo. *ACS Nano* **2008**, *2*, 408–418.

(70) Rasch, M. R.; Rossinyol, E.; Hueso, J. L.; Goodfellow, B. W.; Arbiol, J.; Korgel, B. A. Hydrophobic Gold Nanoparticle Self-Assembly with Phosphatidylcholine Lipid: Membrane-Loaded and Janus Vesicles. *Nano Lett*. **2010**, *10*, 3733–3739.

(71) Derfus, A. M.; Chan, W. C. W.; Bhatia, S. N. Intracellular Delivery of Quantum Dots for Live Cell Labeling and Organelle Tracking. *Adv. Mater*. **2004**, *16*, 961–966.

(72) Dubochet, J. Cryo-Electron Microscopy of Vitrified Specimens. *Q. Rev. Biophys*. **1988**, *21*, 129–228.

(73) Sato, S.; Swihart, M. T. Propionic-Acid-Terminated Silicon Nanoparticles: Synthesis and Optical Characterization. *Chem. Mater*. **2006**, *18*, 4083–4088.

(74) Li, Z. F.; Ruckenstein, E. Water-Soluble Poly(Acrylic Acid) Grafted Luminescent Silicon Nanoparticles and Their Use as Fluorescent Biological Staining Labels. *Nano Lett*. **2004**, *4*, 1463–1467.

(75) Erogbogbo, F.; Tien, C.-A.; Chang, C.-W.; Yong, K.-T.; Law, W.-C.; Ding, H.; Roy, I.; Swihart, M. T.; Prasad, P. N. Bioconjugation of Luminescent Silicon Quantum Dots for Selective Uptake by Cancer Cells. *Bioconjug. Chem*. **2011**, *22*, 1081–1088.

(76) Glendinning, A. B.; Russel, W. B. The Electrostatic Repulsion between Charged Spheres from Exact Solutions to the Linearized Poisson-Boltzmann Equation. *J. Colloid Interface Sci*. **1983**, *93*, 95–104.

(77) *Handbook of Biological Confocal Microscopy*; Pawley, J. B., Ed.; 3rd ed.; Springer US: Boston, MA, 2006.

(78) *Biomedical Optical Imaging*; Fujimoto, J. G.; Farkas, D., Eds.; Oxford University Press, 2009.

(79) Brannon-Peppas, L.; Blanchette, J. O. Nanoparticle and Targeted Systems for Cancer Therapy. *Adv. Drug Deliv. Rev*. **2004**, *56*, 1649–1659.

(80) Kim, D.; Kang, J.; Wang, T.; Ryu, H. G.; Zuidema, J. M.; Joo, J.; Kim, M.; Huh, Y.; Jung, J.; Ahn, K. H.; Kim, K. H.; Sailor, M. J. Two-Photon In Vivo Imaging with Porous Silicon Nanoparticles. *Adv. Mater*. **2017**, 1703309.

(81) Tu, C.; Ma, X.; Pantazis, P.; Kauzlarich, S. M.; Louie, A. Y. Paramagnetic, Silicon Quantum Dots for Magnetic Resonance and Two-Photon Imaging of Macrophages. *J. Am. Chem. Soc*. **2010**, *132*, 2016–2023.

(82) He, Y.; Zhong, Y.; Peng, F.; Wei, X.; Su, Y.; Lu, Y.; Su, S.; Gu, W.; Liao, L.; Lee, S.-T. One-Pot Microwave Synthesis of Water-Dispersible, Ultraphoto- and PH-Stable, and Highly Fluorescent Silicon Quantum Dots. *J. Am. Chem. Soc*. **2011**, *133*, 14192–14195.

(83) Berezin, M. Y.; Achilefu, S. Fluorescence Lifetime Measurements and Biological Imaging. *Chem. Rev*. **2010**, *110*, 2641–2684.

(84) Dahan, M.; Laurence, T.; Pinaud, F.; Chemla, D. S.; Alivisatos, A. P.; Sauer, M.; Weiss, S. Time-Gated Biological Imaging by Use of Colloidal Quantum Dots. *Opt. Lett*. **2001**, *26*, 825–827.

(85) Bouccara, S.; Fragola, A.; Giovanelli, E.; Sitbon, G.; Lequeux, N.; Pons, T.; Loriette, V. Time-Gated Cell Imaging Using Long Lifetime near-Infrared-Emitting Quantum Dots for Autofluorescence Rejection. *J. Biomed. Opt*. **2014**, *19*, 051208.

(86) Gu, L.; Hall, D. J.; Qin, Z.; Anglin, E.; Joo, J.; Mooney, D. J.; Howell, S. B.; Sailor, M. J. In Vivo Time-Gated Fluorescence Imaging with Biodegradable Luminescent Porous Silicon Nanoparticles. *Nat. Commun*. **2013**, 4.

(87) Zipfel, W. R.; Williams, R. M.; Webb, W. W. Nonlinear Magic: Multiphoton Microscopy in the Biosciences. *Nat. Biotechnol*. **2003**, *21*, 1369–1377.

(88) Denk, W.; Strickler, J. H.; Webb, W. W. Two-Photon Laser Scanning Fluorescence Microscopy. *Science* **1990**, *248*, 73–76.

(89) He, G. S.; Zheng, Q.; Yong, K.-T.; Erogbogbo, F.; Swihart, M. T.; Prasad, P. N. Two- and Three-Photon Absorption and Frequency Upconverted Emission of Silicon Quantum Dots. *Nano Lett*. **2008**, *8*, 2688–2692.

(90) Hsu, M. J.; Juliano, R. L. Interactions of Liposomes with the Reticuloendothelial System: II. Nonspecific and Receptor-Mediated Uptake of Liposomes by Mouse Peritoneal Macrophages. *Biochim. Biophys. Acta BBA - Mol. Cell Res*. **1982**, *720*, 411–419.

(91) Albanese, A.; Tang, P. S.; Chan, W. C. W. The Effect of Nanoparticle Size, Shape, and Surface Chemistry on Biological Systems. *Annu. Rev. Biomed. Eng*. **2012**, *14*, 1–16.

(92) Elias, D. R.; Poloukhtine, A.; Popik, V.; Tsourkas, A. Effect of Ligand Density, Receptor Density, and Nanoparticle Size on Cell Targeting. *Nanomedicine Nanotechnol. Biol. Med*. **2013**, *9*, 194–201.

(93) Oh, N.; Park, J.-H. Endocytosis and Exocytosis of Nanoparticles in Mammalian Cells. *Int. J. Nanomedicine* **2014**, *9*, 51–63.

(94) Choi, H. S.; Liu, W.; Misra, P.; Tanaka, E.; Zimmer, J. P.; Itty Ipe, B.; Bawendi, M. G.; Frangioni, J. V. Renal Clearance of Quantum Dots. *Nat. Biotechnol*. **2007**, *25*, 1165–1170.

(95) Popplewell, J. F.; King, S. J.; Day, J. P.; Ackrill, P.; Fifield, L. K.; Cresswell, R. G.; di Tada, M. L.; Liu, K. Kinetics of Uptake and Elimination of Silicic Acid by a Human Subject: A Novel Application of 32Si and Accelerator Mass Spectrometry. *J. Inorg. Biochem*. **1998**, *69*, 177–180.

Chapter 2: Assembly of Fluorescent Silicon Nanocrystals with Liposomes and Uptake by Macrophage Cells

2.1 INTRODUCTION

The ability to use nanoparticles in place of traditional fluorescent molecules for biomedical imaging has led to the development of contrast agents with broad excitation and emission spectra, long fluorescence lifetimes, high quantum yields, and high stability against photobleaching.[1–3] Silicon (Si) based nanoparticles in particular are attractive probes for bioimaging because the material is considered non-toxic and biocompatible, and methods to synthesize Si nanocrystals can produce alkene capped particles with narrow size distributions.[4–9] Various methods have been proposed for stabilizing hydrophobic Si nanocrystals in aqueous environments, including the use of surfactants or polymer coatings.[3,5,7,10,11] The optimization of bright photoluminescence from Si nanocrystal-surfactant assemblies is important for the use of these assemblies *in vitro* and *in vivo*, and depends on both the capacity for nanocrystals to load into the surfactant dispersion as well as the photoluminescence stability.

Liposomes have hydrophobic and hydrophilic regions that can be loaded with particles and have found use as targeted and non-targeted carriers for drugs, molecules, genes, SiRNA, and nanoparticles.[12–16] The lipids in liposome assemblies can vary in their net charge, headgroup composition, hydrocarbon chain length, and hydrocarbon saturation, and these factors can affect how particles incorporate into the liposomes as well as how the assemblies interact with cells.[13,16–18] Additionally, preparation procedures for nanoparticle-liposome assemblies such as chloroform annealing can affect loading capacity.[19] Here, we examined the assembly of 2.8 nm hydrophobic Si nanocrystals into liposomes ("Lip-NC assemblies") constructed from various lipids to maximize dispersion emission. The ability for Si nanocrystals to incorporate into liposomes was examined

using cryogenic transmission electron microscopy (cryoTEM). The nanocrystals incorporated as aggregates into the assemblies, with the highest loading in anionic liposome formulations with quantum yields of 3.2%.

The Lip-NC dispersions assemblies were also evaluated for bioimaging with live cells. It was possible to capture Si nanocrystal emission in the interior of macrophage cells using confocal microscopy after incubating Lip-NC assemblies with the cells. One-photon and two-photon imaging of Si nanocrystals could be achieved. Additionally, the assemblies did not show any toxicity towards the cells, demonstrating the potential for using the Lip-NC assemblies as bioimaging probes.

2.2 EXPERIMENTAL METHODS

2.2.1 Materials

Hydrogen silsesquioxane (HSQ) was obtained from Dow Corning. Hydrochloric acid (HCl, 37%), hexanes (≥98.5%), chloroform (≥99.8%), toluene (≥99.5%), and sodium chloride were purchased from Fisher. 4-(2-hydroxyethyl)-1-piperazineethanesulfonic acid) (HEPES), sodium hydroxide, hydrofluoric acid (HF, 48%), 1-octene (98%), 1-dodecene (95%), and 1-hexene (97%) were purchased from Sigma. Ethanol was purchased from Pharmco-Aaper. Cholesterol was obtained from Anatrace. All lipids were purchased from Avanti Polar Lipids. DAPI-Fluoromount-G was purchased from SouthernBiotech, while sodium pyruvate was purchased from Hyclone. Dulbecco's Modified Eagle Medium (DMEM) and phosphate buffered saline (PBS) were purchased from Gibco. Fetal bovine serum (FBS) and penicillin/streptomycin were purchased from Life Technologies. Non-essential amino acids were purchased from Lonza. The CytoTox 96® Non-Radioactive Cytotoxicity Assay and CellTiter 96®

AQueous Non-Radioactive Cell Proliferation Assay kits were purchased from Promega. Ultrapure water was obtained from a Millipore Synergy Ultrapure water system operating at 18.2 MΩ/cm.

2.2.2 Si Nanocrystal Synthesis

Silicon nanocrystals capped with alkenes were synthesized from HSQ as previously reported.[7] Solvent was removed from HSQ and the material was placed in a tube furnace for 1 hour at 1100 °C under forming gas (93% nitrogen and 7% hydrogen) flow. A mortar and pestle were used to grind the resulting material. The particle size was further reduced using 9 hours of mechanical shaking in a wrist action shaker with borosilicate beads. From the resulting material, 300 mg of the powder was etched with 1 ml HCl and 10 ml HF for 3.5 hours in the dark. The hydrogen terminated silicon nanocrystals were then washed by centrifugation: first the solution was centrifuged and the precipitated material was retained, then two washes with ethanol and one wash with chloroform were used to remove any trace acids. The nanocrystals were then dispersed in 15 ml of 1-octene and injected into a 3-neck flask under vacuum. Three freeze-thaw cycles were performed to remove residual oxygen with the freeze being done under vacuum and the thaw under nitrogen gas. The flask was then left stirring at 120 °C for 12 hours. The solution was then transferred to a centrifuge tube and centrifuged for 5 min at 8000 rpm and the precipitate containing poorly passivated nanocrystals was discarded. Ethanol (antisolvent) was added until the solution became turbid and the sample was centrifuged. The supernatant was removed and the nanocrystals were redispersed in hexanes. Three additional cycles of solvent-antisolvent washing were used before finally dispersing the nanocrystals in chloroform for storage.

For the nanocrystal size experiments, size selective precipitation was used to separate a sample of 1-octene capped Si nanocrystals into subsets of smaller and larger particles. By adding a small amount of anti-solvent (ethanol) to a solution of Si nanocrystals dispersed in hexane, the largest nanocrystals were precipitated out by centrifuging at 8000 rpm for 5 minutes. The supernatant containing smaller nanocrystals was then transferred to a new centrifuge tube and a small amount of ethanol was added before centrifuging, causing the next largest nanocrystals to precipitate out. This process was repeated until five size fractions were produced, of which the largest (3.0 ± 0.6 nm) and smallest (2.7 ± 0.6 nm) were used for experiments with liposomes.

2.2.3 Incorporation of Si Nanocrystals with Liposomes

In a typical preparation, a total of 15 μmol of lipid and 0.75 mg of silicon nanocrystals were dispersed in 1 ml of chloroform in a 50 ml round bottom glass flask. The solution was then dried into a film using a rotary evaporator (Rotavapor R-3000 connected to a Welch dry vacuum system, model 2025) for 15 minutes at 25 °C, followed by 3 hours under vacuum in a vacuum oven (Isotemp Vacuum Oven Model 281A) set to 25° C at -760 mmHg vacuum. Where chloroform annealing was used, the dried film was inverted and placed over a glass bottle filled with chloroform for 1 hour, as previously reported.[19] The film was then hydrated using 1 ml of either water (for neutral liposomes) or a solution of 10 mM HEPES and 10 mM NaCl (for charged liposomes) adjusted to pH 7.2 using NaOH. The flask was bath sonicated for 5 minutes to disperse the lipids and nanoparticles into solution before transferring the solution to a 20 ml glass vial for another 30 minutes of bath sonication (Bransonic M1800 bath sonicator, 40kHz, half gallon tank). The dispersion was then transferred to a 1.5 ml centrifuge tube and

centrifuged for 5 minutes at 600 G to separate any silicon nanocrystals that were not incorporated into liposomes. The supernatant was removed and transferred to a new 1.5 ml centrifuge tube and centrifuged for 5 minutes at 900 G. The supernatant containing the Lip-NC assemblies was transferred to a new vial and stored at 25 °C.

2.2.4 Si Nanocrystal and Liposome Characterization

Silicon nanoparticles were characterized with Transmission Electron Microscopy (TEM) using an FEI Tecnai Biotwin TEM operated at 80 kV accelerating voltage. Samples were prepared by drop casting silicon nanocrystals onto 200 mesh carbon-coated copper grids (Electron Microscopy Science) and images were acquired digitally. Si nanocrystal diameters were estimated from TEM issues by measuring 100 particles.

X-ray diffraction (XRD) data was acquired on a Rigaku R-Axis Spider diffractometer using Cu Kα radiation (λ = 0.15418 nm) and an image plate detector. Dried nanocrystals were positioned onto a nylon loop using mineral oil (a background scan was complete without nanocrystals added). The sample was then rotated at 10° per second for 20 minutes. The two dimensional diffraction data was then integrated using 2DP Spider software (version 1.0, Rigaku).

Fourier transform infrared spectroscopy (FTIR) data was acquired on a Thermo Mattson Infinity Gold FTIR spectrometer with a Spectra-Tech Thermal ARK attenuated total reflectance module. The chamber was purged with nitrogen gas for 15 minutes before the background signal was collected. The nanocrystal sample was then drop cast onto the ARK crystal plate and allowed to dry under a nitrogen gas purge for 15 minutes. Measurements were taken by acquiring 512 scans at a resolution of 4 cm^{-1} and background was subtracted.

Cryogenic TEM (cryoTEM) samples were prepared on lacey carbon coated copper 200 mesh grids (Electron Microscopy Science) using a Leica EM GP. The environmentally controlled chamber was set to 25 °C and 90% humidity, and the sample was blotted for 3 seconds on one side and 1 second on the other side before being plunged into liquid ethane at -182 °C. The grid was then transferred under liquid nitrogen into a Gatan 626 Cryo-Transfer Holder, which was then inserted into an FEI Tecnai Biotwin TEM. The TEM was operated at 80 kV accelerating voltage with FEI low dose software used for imaging.

Dynamic Light Scattering (DLS) data were acquired with a Zetasizer Nano ZS (Malvern Instruments) at an angle of 173° and temperature of 25 °C. Sample sizes were measured in triplicate in 40 µl disposable cuvettes. Zeta potential data were captured in triplicate with the same instrument using disposable folded capillary zeta cells. Zetasizer software (Malvern Instruments) was used to analyze sample average size (z-average), polydispersity index (PDI), and zeta potential.

Spectroscopy data was collected for samples after 20 times dilution into water using glass cuvettes. Absorbance spectra were acquired on a Varian Cary 50 Bio ultraviolet-visible spectrophotometer. Photoluminescence emission (PL) and photoluminescence excitation (PLE) spectra were captured on a Varian Cary Eclipse fluorescence spectrophotometer. All PL spectra were captured using an excitation wavelength of 320 nm while PLE spectra were captured using an emission wavelength of 665 nm. PL peak wavelength position was calculated by determining the average emission wavelength. Rhodamine B was used as a standard for quantum yield measurements (quantum yield of 0.49 in ethanol).[20] Quantum yield was calculated according to the relation: $QY_{Si}=(QY_{ref})\ (A_{ref}/A_{Si})(I_{si}/I_{ref})(\eta_{Si}/\eta_{ref})^2$, where QY is the quantum yield, A is the absorbance at 350 nm, I is the PL intensity upon excitation at 350

nm, η is the solvent refractive index, and the subscripts *Si* and *ref* refer to the Si nanocrystal samples and Rhodamine B reference, respectively.

2.2.5 Liposome-Si Nanocrystal Incubation with Cells

J774A.1 macrophage cells were grown in DMEM supplemented with 10% fetal bovine serum, 100 U/mL penicillin-streptomycin, and 1 mM sodium pyruvate. Caco-2 epithelial cells were grown in the same medium with the addition of 0.1 mM non-essential amino acids. All cells were maintained in a humidified 37 °C incubator with an atmosphere of 5% CO_2, unless otherwise indicated.

For confocal microscopy experiments cells were seeded on glass coverslips in 6-well plates at a density of 2 x 10^4 /cm^2 two days before the assay. Culture medium was replaced with Lip-NC dispersions diluted 5-fold in growth medium, and incubated for 3 hours at 37 °C unless otherwise indicated. At the end of the incubation the coverslips were washed 4 times with PBS to remove Lip-NC assemblies not taken up by the cells. The cells were then fixed with 4% formaldehyde for 10 minutes at 37 °C. The coverslips were then washed three times with PBS, mounted on glass slides with DAPI Fluoromount-G. For experiments performed at 4 °C the cell culture plate was maintained on ice for 30 minutes before and during the assay.

For flow cytometry experiments cells were seeded in 6-well or 24-well plates at a density of 2 x 10^4 /cm^2 two days before the assay. Culture medium was replaced with Lip-NC dispersions diluted 5-fold in growth medium, and incubated for 3 hours at 37 °C unless otherwise indicated. At the end of the incubation the cells were washed 4 times with PBS to remove Lip-NC assemblies not taken up by the cells. The cells were then mechanically scraped from the wells for flow cytometry.

2.2.6 Cell Uptake Characterization

Confocal imaging was conducted on a Zeiss LSM 710 confocal microscope. DAPI was excited at a wavelength of 405 nm and emission was captured at 417-566 nm. Silicon nanocrystals were excited at a wavelength of 405 nm and emission was captured at 670-740 nm. Images were taken at the center plane of the cells using the DAPI stained nucleus as a guide. Zeiss confocal software was used to overlay images with the DAPI channel in blue and the silicon nanocrystal channel in red.

Two-photon microscopy was conducted on a commercial two-photon/confocal microscopy system (Prairie Technologies, Ultima Intravital). The microscope objective used was an Olympus XLUMPLFLN 20x 1.0 NA, water immersion lens. The two-photon excitation source was a Ti:sapphire laser (Spectra-Physics Tsunami) with 150 fs pulses while the single photon excitation source was a diode laser. Both Si nanocrystals and DAPI were excited at either 405 nm (for one photon images) or 800 nm (for two photon images). Si nanocrystal fluorescence was captured using a 690 ± 30 nm filter, while DAPI fluorescence was captured using a 460 ± 25 nm filter. Images were false colored red for Si nanocrystals and blue for DAPI.

Flow cytometry was conducted on a BD Biosciences LSR Fortessa Flow Cytometer. Silicon nanocrystals were excited at 405 nm and emission was captured using a 670 nm long pass filter for 10,000 live cells. FlowJo software was used for data analysis.

Two assays were used to test the effect of Lip-NC assemblies on cell viability: the lactate dehydrogenase (LDH) assay using CytoTox 96® Non-Radioactive Cytotoxicity Assay kit and 3-(4,5-dimethylthiazol-2-yl)-5-(3-carboxymethoxyphenyl)-2-(4-sulfophenyl)-2H-tetrazolium (MTS) assay using CellTiter 96® AQueous Non-Radioactive Cell Proliferation Assay kit. Both assays were performed according to the

manufacturer's instructions. Briefly, cells were seeded and grown as for the flow cytometry experiments. Lip-NC assemblies were incubated with the cells at 37 °C for 1, 3, or 6 hours. Next, the culture supernatants were transferred to microcentrifuge tubes and centrifuged at 13,000 g for 10 minutes. 50 µl of each clarified supernatant was transferred to a flat-bottom 96-well plate and mixed with 50 µl of LDH substrate using a multichannel pipette. After 30 minutes of incubation at room temperature in the dark, the absorbance was read at 490 nm. The viability % is calculated as follows: [1-(Sample A490 - Cells without treatment A490)/(100% lysis A490 - Cells without treatment A490)] X 100%. 100% lysis was from cells lysed with 0.9% Triton X-100.

The remaining cells in the plate were immediately washed three times with PBS to remove residual Lip-NC assemblies, and medium containing 6-fold dilution of MTS and phenazine methosulfate (PMS) solution was added into each well and incubated in 37 °C incubator with 5% CO_2 for 1 hour. Then the supernatants were transferred to a flat-bottom 96-well plate to be read at 490 nm. The viability % was calculated as follows: (Sample A490 – No cell A490)/(Cells without treatment A490– No cell A490) X 100%. Wells without cells were used as the blank to account for automatic coloration.

2.3 RESULTS AND DISCUSSION

2.3.1 Liposome-Si Nanocrystal Assembly

Figure 2.1 shows the 1-octene passivated Si nanocrystals used in the liposome assembly experiments. Nanocrystals were synthesized by thermal decomposition of hydrogen silsesquioxane (HSQ) as previously reported by Hessel et al.[7] using an annealing temperature of 1100 °C to produce nanocrystals with diameters of 2.8 ± 0.5 nm. Figure 2.1b shows the x-ray diffraction pattern confirming a diamond cubic lattice

structure. The nanocrystals were passivated with 1-octene to prevent surface oxidation and confer dispersibility in non-polar solvents such as chloroform. Figure 2.1c shows FTIR data indicating peaks associated with hydrosylilation of an alkene to the Si surface, including C-H stretching (2800-3000 cm^{-1}), Si-H stretching (~2200 cm^{-1}), C-CH_3 stretching (1300-1500 cm^{-1}), and Si-O-Si stretching (~1100 cm^{-1}). The absence of C=C stretching (~1640 cm^{-1}) indicates that all 1-octene was either bound to the silicon nanocrystal surface or washed away.

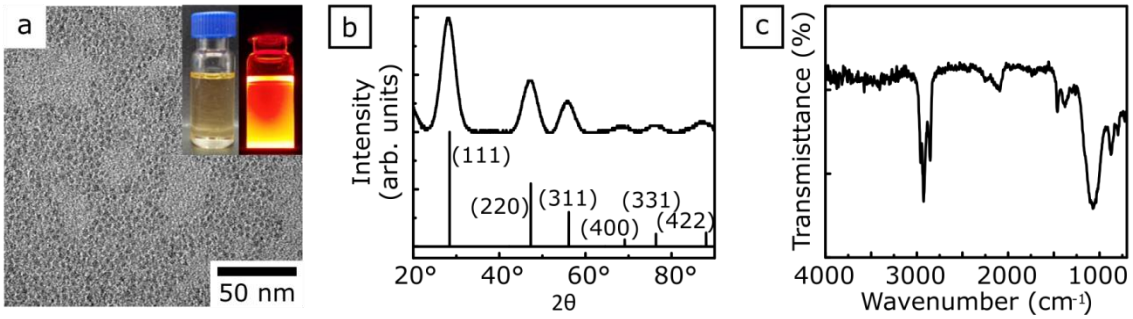

Figure 2.1 (a) TEM image of 2.8 nm octene capped Si nanocrystals. Inset shows vial of Si nanocrystals under ambient light and on a 365 nm ultraviolet lamp. (b) XRD pattern confirmed the diamond cubic silicon structure with a=b=c=0.543 nm (PDF # 027-1402). (c) FTIR data for Si nanocrystals passivated with 1-octene confirmed surface passivation with an alkene.

Figure 2.2 illustrates the process used to incorporate Si nanocrystals into liposomes, which was similar to the methods previously reported for loading hydrophobic drugs and particles into liposomes.[17,21,22] 0.75 mg of octene coated Si nanocrystals were dispersed with 15 μmol of lipid in 1 ml of chloroform and then dried into a thin film. In some preparations, the thin film underwent a chloroform annealing step, which has previously been identified as improving the incorporation of nanoparticles into liposomes by allowing rearrangement of the particles in the film.[19] The film was then hydrated to a

final volume of 1 ml and bath sonicated to form liposomes. The samples were centrifuged to precipitate nanocrystals not incorporated into liposomes.

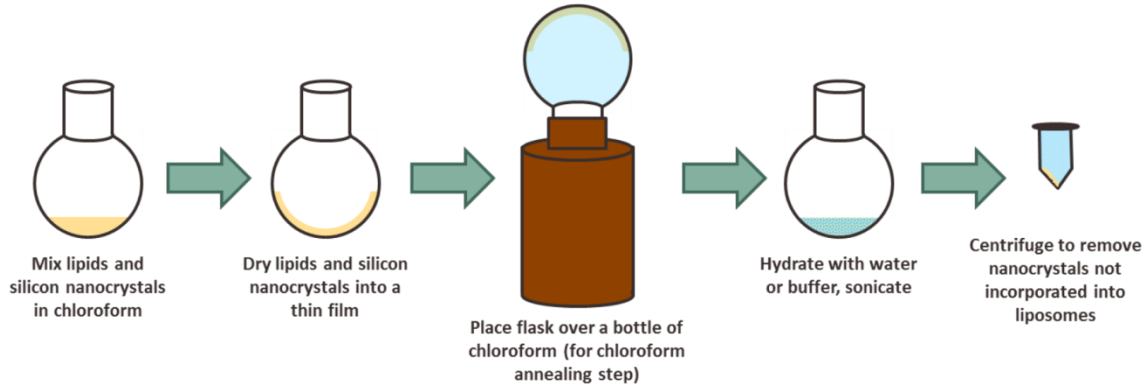

Figure 2.2 Illustration of the process used to incorporate Si nanocrystals into liposomes. The chloroform annealing step was performed on some samples.

Liposomes assembled with Si nanocrystals were composed of the following lipids and molecules:

(i) Zwitterionic, unsaturated lipids. 1,2-dioleoyl-sn-glycero-3-phosophocholine (DOPC), an 18:1(Δ9-cis) unsaturated lipid was used. Unsaturated lipids have higher membrane fluidity than saturated lipids,[17] and DOPC liposomes have a bilayer thickness of 4.6 nm[23] that should be able to accommodate the 2.8 nm Si nanocrystals. DOPC has previously been shown to incorporate gold nanocrystals into the lipid bilayer.[19] DOPC is considered a helper lipid in many liposome formulations as it can be used to control surface charge density.[15]

(ii) Zwitterionic, saturated lipids. 1,2-dilauroyl-sn-glycero-3-phosphocholine (DLPC), an 12:0 saturated lipid was used. While saturated lipids have less membrane fluidity, DLPC has a shorter hydrocarbon chain than DOPC and is in the disordered liquid crystalline phase at room temperature.

(iii) Anionic lipids. 1,2-dioleoyl-sn-glycero-3-phospho-(1'-rac-glycerol) (DOPG), an 18:1(Δ9-cis) unsaturated lipid was used.

(iv) Cationic lipids. 1,2-dioleoyl-3-trimethylammonium-propane (DOTAP), an 18:1(Δ9-cis) unsaturated lipid was used.

(v) Zwitterionic, unsaturated lipids with conical structure. 1,2-dioleoyl-sn-glycero-3-phosphoethanolamine (DOPE), an 18:1(Δ9-cis) unsaturated lipid that can form an inverted hexagonal phase was used. DOPE is frequently used as the zwitterionic lipid in formulations for drug release applications.[13,15,24]

(vi) Polyethylene glycol (PEG) conjugated lipids. DOPE-PEG2000 was used, which has a 2,000 molecular weight PEG molecule conjugated to DOPE. Adding PEG to liposome surfaces can improve liposome stability, increase *in vivo* circulation time, and alter how liposomes are taken up by cells.[12,16,25]

(vii) Cholesterol. Cholesterol inserts into the membrane bilayer structure and changes membrane fluidity.[15,16,26]

Figure 2.3 shows cryoTEM images, vial photographs, and photoluminescence data for the Lip-NC formulations prepared with the chloroform annealing step. In all samples the Si nanocrystals appeared as aggregates that exhibited different shapes and sizes depending on the formulation. Formulations containing only DOPC or DOPC with DOPG had Si nanocrystal aggregates that were approximately the same size and shape as empty liposomes (green arrows). In other dispersions the aggregates appeared at similar sizes as the empty liposomes, however they had non-spherical shapes (yellow arrows). Finally, some dispersions appeared to contain irregularly shaped, large aggregates (red arrows). The photoluminescence data indicates either no blue shift or a very small blue shift in the emission wavelengths (<10 nm) compared to the Si nanocrystals dispersed in

chloroform, which may correspond to either slight surface oxidation of the Si nanocrystals or a higher percentage of smaller Si nanocrystals incorporated in the liposomes.

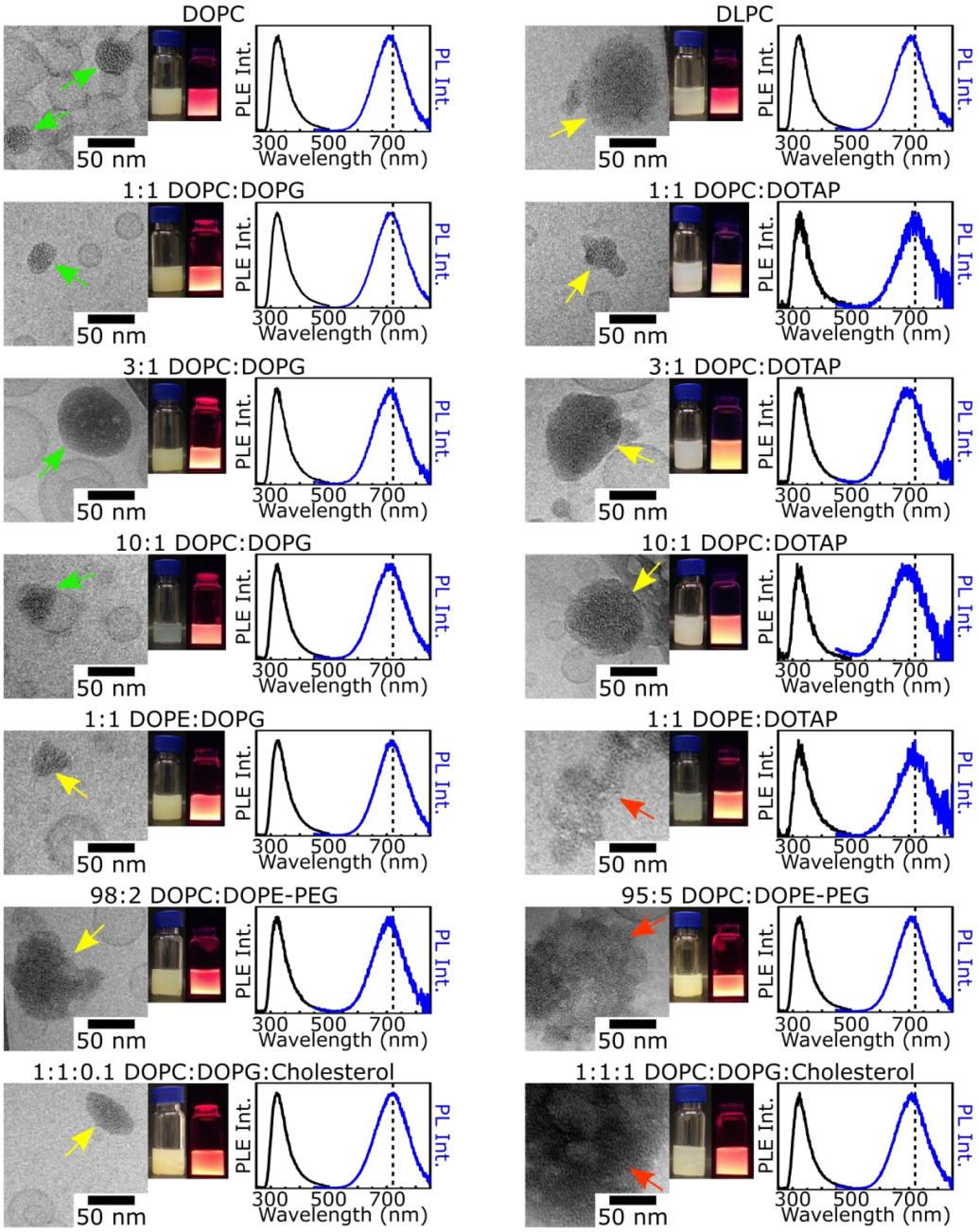

Figure 2.3 CryoTEM images of Lip-NC assemblies synthesized with the chloroform annealing step. Nanocrystal aggregates were observed with sizes and shapes similar to empty liposomes (green arrows), non-spherical shapes (yellow arrows), and large irregular shapes (red arrows). Pictures of the dispersions under ambient light and on a 365 nm ultraviolet lamp. Normalized PL and PLE spectra for each of the dispersions, with black dotted lines indicating peak PL wavelength for Si nanocrystals in chloroform (718 nm).

Table 2.1 presents the dynamic light scattering and zeta potential data for the chloroform annealed samples. The assembly sizes ranged from 128-322 nm, which are typical sizes for small unilamellar liposomes and on the same scale as liposomal formulations used for drug delivery.[15] The polydispersity index (PDI) values for Lip-NC assemblies were in the range (0.1-0.5) expected for samples that have a low level of polydispersity.[27] A comparison of the sizes for liposomes constructed in the absence of Si nanocrystals but using the same preparation process (including the chloroform annealing step) found that the formulations with Si nanocrystals had slightly larger sizes.

Liposome – Si nanocrystal assemblies			
Composition	Size (nm)	Polydispersity Index	Zeta Potential (mV)
Liposome – Si nanocrystal assemblies			
DOPC	205.3 ± 6.2	0.304 ± 0.002	-23.9 ± 0.6
DLPC	165.7 ± 1.4	0.236 ± 0.015	-1.2 ± 0.3
1:1 DOPC:DOPG	184.7 ± 4	0.227 ± 0.019	-49.5 ± 0.8
3:1 DOPC:DOPG	159.1 ± 2.8	0.238 ± 0.009	-54.0 ± 2.8
10:1 DOPC:DOPG	128.4 ± 3.2	0.256 ± 0.006	-30.5 ± 0.6
1:1 DOPC:DOTAP	135.5 ± 4	0.265 ± 0.007	58.6 ± 3.4
3:1 DOPC:DOTAP	314.7 ± 27.2	0.242 ± 0.129	49.5 ± 1.0
10:1 DOPC:DOTAP	236.1 ± 21	0.439 ± 0.065	37.6 ± 0.8
1:1 DOPE:DOPG	192.7 ± 2.6	0.252 ± 0.018	-63.6 ± 0.5
1:1 DOPE:DOTAP	147.5 ± 4.5	0.299 ± 0.005	56.5 ± 0.6
98:2 DOPC:DOPE-PEG	154.4 ± 2.3	0.261 ± 0.012	-47.8 ± 2.3
95:5 DOPC:DOPE-PEG	160.4 ± 2.2	0.256 ± 0.003	-29.9 ± 0.5
1:1:0.1 DOPC:DOPG:Cholesterol	156.9 ± 3.4	0.246 ± 0.012	-67.0 ± 0.4
1:1:1 DOPC:DOPG:Cholesterol	322.4 ± 3.3	0.347 ± 0.052	-69.1 ± 1.4
Liposomes prepared without Si nanocrystals			
DOPC	149.4 ± 2.2	0.195 ± 0.011	-13.6 ± 1.1
1:1 DOPC:DOPG	98.1 ± 1.8	0.219 ± 0.008	-86.4 ± 3.0
1:1 DOPC:DOTAP	182.7 ± 3.3	0.294 ± 0.006	82.5 ± 0.5

Table 2.1 DLS and zeta potential measurements for Si nanocrystal and liposome dispersions, measured in triplicate at 25 °C.

The shapes and sizes attained by the various lipid constructs indicate that lipid chemistry plays a role in how the nanocrystals assemble, likely through differences in membrane fluidity. Liposomes constructed with saturated lipids (DLPC) or cholesterol have less membrane fluidity, and the Si nanocrystal assemblies appeared non-spherical. Samples containing DOPE, which can attain inverted hexagonal phases, displayed irregular shapes as well. It also appears that headgroup charge can affect Si nanocrystal incorporation: within the series of charged liposomes with the same hydrocarbon chain configurations (DOPC with either DOPG or DOTAP) the Si nanocrystals assembled either as round aggregates or with irregular shapes. Charged headgroups interact with the surrounding aqueous solution, and examinations of charged lipid bilayers have identified that local solvent ionic content can impact membrane fluidity.[28] The interaction between DOPC, DOPG, and DOTAP with the HEPES buffer solution can result in membrane fluidity changes that result in differences in aggregate shape, such as the irregular shapes observed with the DOTAP formulations.

Figure 2.4 illustrates the likely assembly process for the Si nanocrystal aggregates. Hydrophobic nanoparticles in aqueous environments are known to cluster to minimize free energy in the system, as well as to associate with the hydrophobic hydrocarbon chains on lipids.[29] In order for nanocrystals to enter into a liposome bilayer, there must be sufficient energy to cause the lipid bilayer to unzip and make space for the particles.[22] The hydrophobic pocket inside the bilayer then has void space surrounding it, and adding new nanoparticles to the cluster causes a further decrease in the system free energy. Thus, once one bilayer accommodates some nanoparticles, it is likely that the cluster will grow. This can explain why the cryoTEM images show either completely empty liposomes or clusters of nanoparticles. A recent study analyzing the effect of hydrophobic nanoparticle size on the ability to incorporate into lipid bilayers found that

there is a threshold in lipid behavior for nanoparticles with diameters above 6 nm.[30] Below this threshold, small nanoparticles can incorporate into the bilayer. However, larger particles disrupt the bilayer structure and a lipid monolayer wraps around the particle surface. While the Si nanocrystals used here are small (2.8 nm), if they become aggregated into clusters > 6nm, there will be a driving force for the lipids to form monolayers over the clusters. The fact that the Lip-NC assemblies remain dispersed for at least several days (see stability testing below) supports the scenario of a lipid monolayer coating the Si nanocrystals.

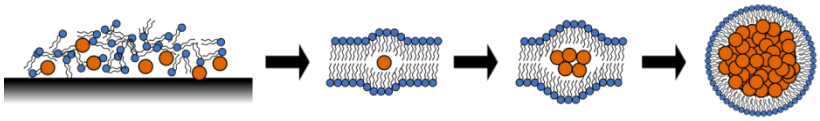

Figure 2.4 Illustration of the formation of Si nanocrystal aggregates. The thin film containing lipids and octene capped Si nanocrystals is hydrated and bath sonication is used to form liposomes. After one Si nanocrystal associates with the hydrophobic core in the bilayer, there is a driving force for nanoparticles to cluster. The cluster may then act as a single large particle and becomes coated with a lipid monolayer.

From a visual inspection of the Lip-NC assemblies presented in Figure 2.3, the brightest dispersion appeared to be 1:1 DOPC:DOPG. The quantum yield for a 1:1 DOPC:DOPG Lip-NC dispersion was 3.2%. While this is lower than the quantum yield calculated for the 1-octene capped Si nanocrystals in chloroform (14.6%), it is comparable to fluorophores currently used in bioimaging.[31]

The loading capacity of Si nanocrystals into the liposome dispersions was quantitatively assessed using a variation of a calculation used for pharmaceutical liposomes. The encapsulation efficiency measures the percentage of drug encapsulated in liposomes for drugs delivered using liposomal assemblies (as opposed to drug material

that is lost during the assembly procedure and thus is not available for delivery to the patient).[17] Here, the loading capacity for Si nanocrystals in liposomes was estimated as the dispersion emission fraction (DEF) which was defined according to Equation 2.1:

$$DEF = 100 \times \frac{I_{Lip-NC}}{I_{SiNC}} \qquad \text{Equation 2.1}$$

where $I_{Lip\text{-}NC}$ is the measured emission intensity from a Lip-NC dispersion and I_{SiNC} is the measured emission intensity from Si nanocrystals dispersed in chloroform at the maximum concentration possible according to the synthesis methods (0.75 mg Si nanocrystals in 1 ml chloroform). This relation uses PL emission as a measure of nanocrystal loading and thus takes into consideration not only the amount of Si nanocrystals incorporated, but also any loss of PL that results from dispersing the nanocrystals with liposomes. Figure 2.5 shows the DEF for samples prepared with or without the chloroform annealing step. The measured DEF values agreed with the visual appearance of the nanocrystal samples: the samples with the highest DEF values displayed visibly brighter fluorescence when excited by ultraviolet light.

The highest DEF values were close to 50%, indicating that half of the Si nanocrystals introduced into the Lip-NC assembly synthesis were incorporated into the dispersions. The results show that while the chloroform annealing step had some effect on the loading (often to increase the emission), the difference between annealed and non-annealed samples is not significant in most formulations. CryoTEM images of assemblies prepared without the chloroform annealing step showed that in all cases the nanocrystals assembled as aggregates, and thus it appears that the annealing step does not have an impact on Lip-NC assembly formation.

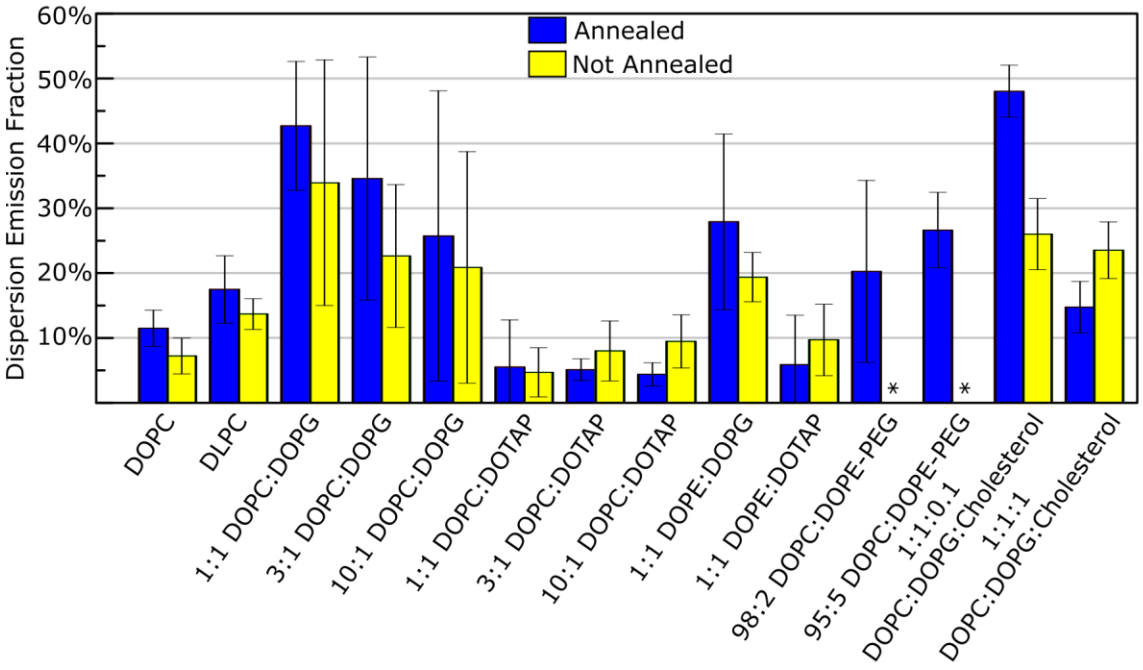

Figure 2.5 Calculated dispersion emission fractions (DEF) for Lip-NC assemblies. Samples were prepared either with (blue bars) or without (yellow bars) the chloroform annealing step. All samples were prepared in triplicate, and error bars represent standard deviation. * DEF for PEG samples were not measured in the absence of the annealing step.

The charged liposomes displayed a trend between surface charge and DEF: compared to the neutral DOPC Lip-NC assemblies, as the proportion of anionic lipid (DOPG) was increased the DEF increased; while conversely as the proportion of cationic lipid (DOTAP) was increased the DEF decreased. These results suggest that although the octene coated Si nanocrystals are lipophilic and interact with the lipid hydrocarbon chains, the headgroup charge and/or composition impact the ability of the lipids to assemble with the silicon nanocrystals, as previously discussed.

The data indicated that for the liposomes with PEG, increasing the fraction of PEG correlated with a higher DEF. Although from cryo-TEM images (Figure 2.3) the PEGylated liposomes associated with nanoparticles appeared in non-spherical shapes, it

is possible that the dispersions still held more nanocrystals due to the increased steric stabilization between liposomes that PEG provides. For samples containing cholesterol, it was found that a ratio of 1:1:0.1 DOPC:DOPG:cholesterol did not affect the ability for Si nanocrystals to incorporate with the lipids (as compared to 1:1 DOPC:DOPG Lip-NC assemblies). However, when the amount of cholesterol was increased to a ratio of 1:1:1 DOPC:DOPG:Cholesterol the DEF decreased significantly. This formulation was also seen to have irregular shapes (Figure 2.3) and large size as measured by DLS, suggesting that the Si nanocrystals disrupted the formation of stable liposomes. The positioning of cholesterol within the lipid bilayer may compete with the ability for silicon nanocrystals to associate with the hydrophobic regions of the lipids, or the membrane may become less fluid, both of which can result in lower levels of Si nanocrystal incorporation.

The effect of Si nanocrystal size on loading into liposomes was evaluated by size selecting the octene capped nanocrystals into smaller and larger subsets before incorporating them into 1:1 DOPC:DOPG liposomes. Although the particles were still very close in size (3.0 ± 0.6 nm and 2.7 ± 0.6 nm for the larger and smaller nanocrystal subsets, respectively), measurement of their loading into 1:1 DOPC:DOPG liposomes found that the larger nanocrystals resulted in a DEF of 24.2%, while the smaller nanocrystals resulted in a DEF of 70.6%, demonstrating a considerable increase in Si nanocrystal loading with decreasing particle size. These results can also explain the slight blue shift observed after incorporating Si nanocrystals into liposome assemblies, since the smallest particles are more likely to be included in the dispersion. CryoTEM images taken of the samples prepared with the size-selected Si nanocrystals (data not shown) confirmed that the assemblies appeared similar to the 1:1 DOPC:DOPG Lip-NC assemblies prepared without size selection.

The loading capacity was also investigated by increasing the total amount of lipid used to disperse the Si nanocrystals, from 15 μmol up to 60 μmol. The DEF only increased by 7% with the additional lipids.

2.3.2 Liposome-Si Nanocrystal Photoluminescence Stability

Lip-NC dispersions were assessed for photoluminescence stability by monitoring the PL emission intensity and wavelength over three weeks. Figure 2.6 shows the stability for Lip-NC assemblies prepared with DOPC, 1:1 DOPC:DOPG, 1:1 DOPC:DOTAP, and 98:2 DOPC:DOPE-PEG. The emission of DOPC, 1:1 DOPC:DOPG, and 98:2 DOPC:DOPE-PEG appeared to drop off after the first week to around 70% of the original dispersion emission intensity, and then leveled off close to 60% after three weeks. In contrast, the sample constructed with 1:1 DOPC:DOTAP had a sharp decrease in PL intensity after 1 week and only maintained 20% of the original emission intensity after three weeks. Additionally, the 1:1 DOPC:DOTAP sample was the only sample to see a significant blue shift in the PL wavelength (drop of approximately 50 nm), suggesting that the cationic formulation did provide as much stability as the other formulations.

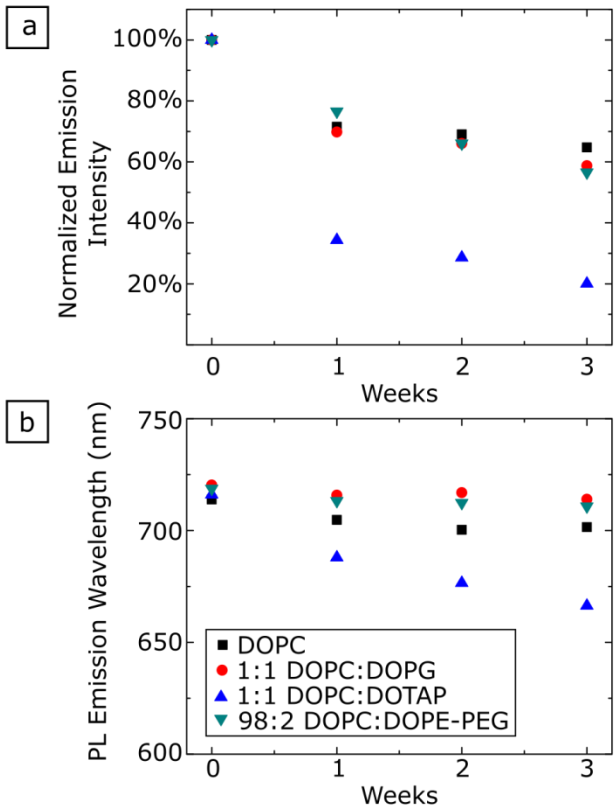

Figure 2.6 (a) Normalized emission intensity and (b) PL emission wavelength for samples constructed of DOPC, 1:1 DOPC:DOPG, 1:1 DOPC:DOTAP, and 98:2 DOPC:DOPE-PEG, showing the change in Lip-NC dispersion PL over three weeks.

2.3.3 Uptake of Liposome-Si Nanocrystal Assemblies

The uptake of anionic 1:1 DOPC:DOPG Lip-NC assemblies was studied in J77A.1 mouse macrophage cells. We selected this combination because the 1:1 DOPC:DOPG Lip-NC assemblies exhibited bright PL (close to 50% DEF) and anionic liposomes have been found to be readily taken up by mouse macrophage cells.[18,32,33] After incubating the Lip-NC assemblies with the cells for 3 hours at 37 °C, the cells were rinsed to remove any Lip-NC assemblies not taken up. Confocal microscopy was used to

image Si nanocrystals with an excitation wavelength of 405 nm and emission was captured at 670-740 nm. Figure 2.7a shows the confocal microscopy images of the cells, with Si nanocrystals false colored red and DAPI nucleus dye false colored blue. The Si nanocrystals appear to spread through the cell interior. Figure 2.7b shows that incubation at 4 °C resulted in considerably less nanocrystal signal observed. Endocytosis is an energy dependent process, and since macrophage cells are not metabolically active at 4 °C, the attenuated signal may be attributed to adsorption of Lip-NC assemblies to the cell surfaces rather than active take up of the Lip-NC assemblies.[33,34]

Figure 2.7d shows flow cytometry data for Si nanocrystal emission from the macrophage cells. Flow cytometry can measure the emission intensity for a sample of cells, and higher emission intensities are expected when nanocrystals have been taken up by cells.[35] After incubating the cells with Lip-NC assemblies, the cells were rinsed and then mechanically scraped from the wells. A 405 nm excitation wavelength and 670 nm longpass filter were used to capture emission from the Si nanocrystals. Flow cytometry confirmed higher emission intensity at 37 °C (4605 ± 14, mean emission intensity ± standard deviation with n=2) as compared to 4 °C (1347 ± 15), indicating that more nanocrystals were taken up at the higher temperature. The background fluorescence signals for cells without any liposomes (382 ± 1) or with liposomes that didn't have any nanocrystals (402 ± 2) were significantly lower. Thus, the flow cytometry data confirms the increased signal from silicon nanocrystals that was observed under confocal microscopy.

Figure 2.7e plots the relationship between Lip-NC concentration and the amount of emission observed from cells. A series of dilutions were made to 1:1 DOPC:DOPG Lip-NC assemblies and the relative emissions were measured. Flow cytometry was then used to measure the emission of Si nanocrystals from cells incubated with the dilutions.

The data fits a linear regression and suggests that in the concentration range tested the point of saturation was not reached, which is consistent with macrophage uptake by non-receptor mediated processes or by receptors that were not saturated with the Lip-NC assemblies.[33,34]

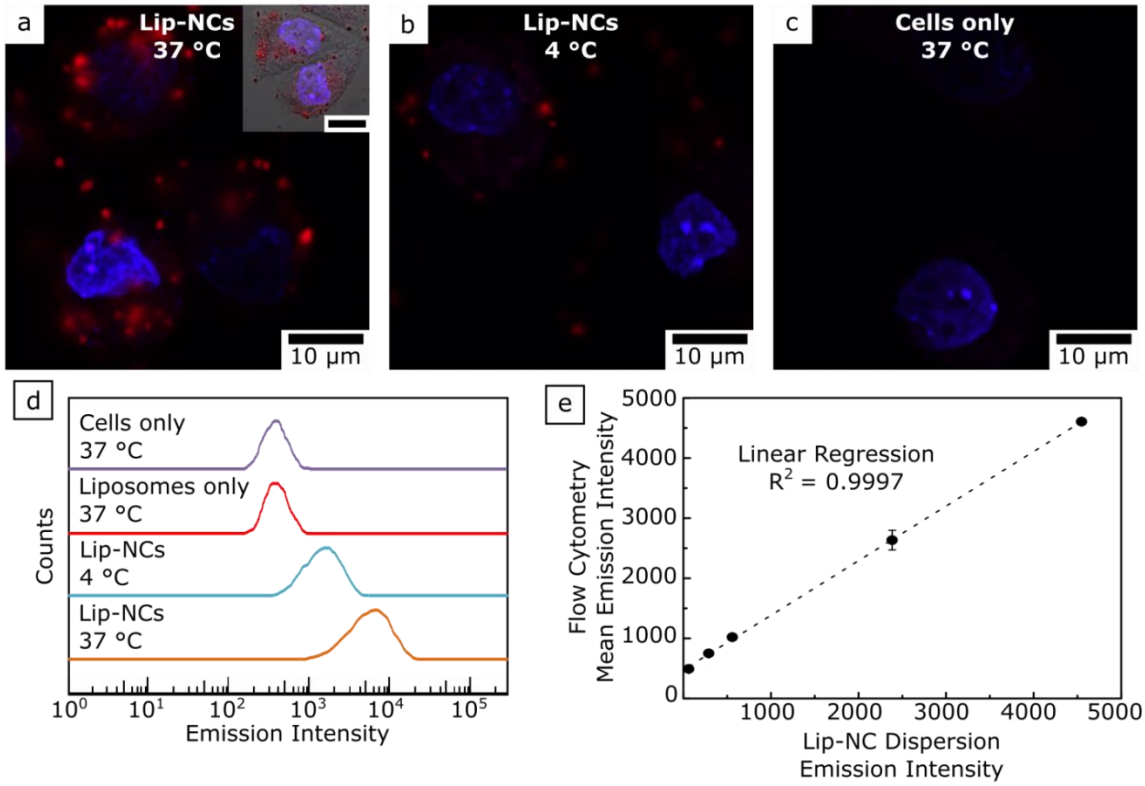

Figure 2.7 Confocal images showing emission captured from Si nanocrystals (false colored red) and DAPI nucleus dye (false colored blue) after incubation of 1:1 DOPC:DOPG Lip-NC assemblies with J774 cells for 3 hours. (a) At 37 °C Lip-NC assemblies incubated with the cells resulted in a visible uptake of Si nanocrystals. Inset shows two cells with brightfield overlay (scale bar 10 µm). (b) At 4 °C the Si nanocrystal signal is significantly lower as active uptake is limited. (c) Cells incubated without Lip-NC assemblies did not show any signal in the silicon nanocrystal emission range. (d) Flow cytometry confirmed higher emission intensity for cells incubated with Lip-NC assemblies at 37 °C as compared to 4 °C. (e) Concentration dependent uptake was measured for Lip-NC assemblies. A linear fit was made to the data ($R^2 = 0.9997$). Error bars are standard deviation (n=2).

Figure 2.8 shows confocal images and flow cytometry data for 1:1 DOPC:DOPG Lip-NC assemblies incubated with J774 cells for 1, 3, or 6 hours. At longer incubation times there was more Si nanocrystal emission visible in the confocal images. Flow cytometry of the cells (Figure 2.8d) confirmed that over time the mean fluorescence

emission intensity increased from 1 hour (4,694 ± 5, mean emission intensity ± standard deviation, n=2), to 3 hours (10,107 ± 730), to 6 hours (12,545 ± 774), with a minimal signal from cells incubated without Lip-NC assemblies for 3 hours as a control (744 ± 7).

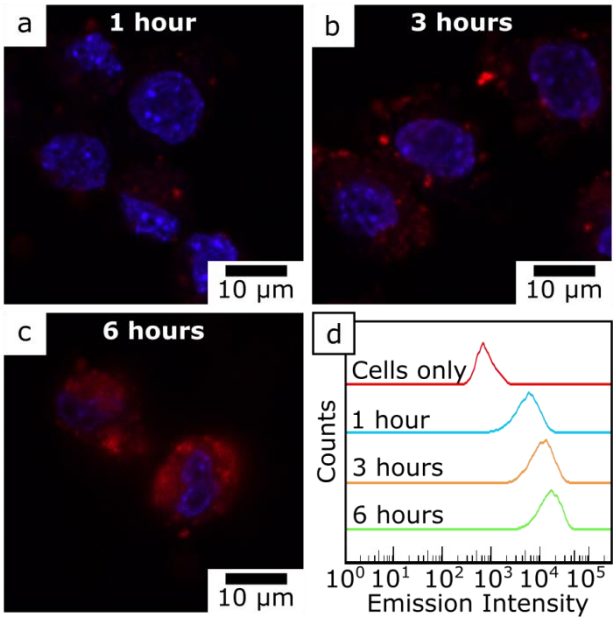

Figure 2.8 Confocal images of cells showing signal from silicon nanocrystals (false colored red) and DAPI nucleus dye (false colored blue) after incubation with J774 cells at 37 °C for (a) 1 hour, (b) 3 hours, or (c) 6 hours with 1:1 DOPC:DOPG Lip-NC assemblies. (d) Flow cytometry of the cells confirmed the time dependent uptake.

Figure 2.9 presents the flow cytometry results for nanocrystal uptake measured for different liposome compositions and with different cell types. Lip-NC assemblies were prepared with either neutral (DOPC), anionic (1:1 DOPC:DOPG), or cationic (1:1 DOPC:DOTAP) lipids, and the dispersions were diluted to have identical emission intensities. The fluorescent dispersions were then incubated for 3 hours at 4 °C or 37 °C with either J774 mouse macrophage cells or Caco2 epithelial cells. For the J774 cells all formulations resulted in more silicon nanocrystal emission at 37 °C as compared to the

emission observed at 4 °C, suggesting that the Lip-NC assemblies were actively taken up by the cells. The most significant uptake at 37 °C was observed with the anionic Lip-NC formulation and is consistent with previous reports for macrophage cells.[18,32] For the Caco2 cells, the emission was nearly constant regardless of liposome formulation or incubation temperature, and was at the same intensity of the sample incubated without any Si nanocrystals. Confocal microscopy performed on the Caco2 cells also was not able to identify any Si nanocrystal emission from the cells. The failure of Caco2 cells to take up silicon nanocrystals is likely related to the non-specific surface chemistry on the Lip-NC assemblies. Caco2 cells exhibit low levels of non-specific particle uptake and preferentially take up particles displaying specific recognition groups such as folic acid or vitamin E polyethylene glycol succinate.[36–38]

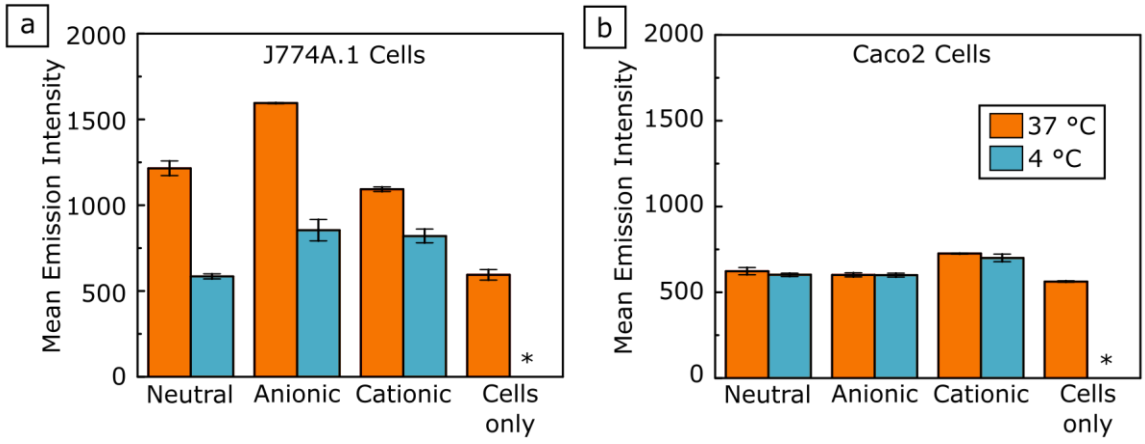

Figure 2.9 Flow cytometry results showing Si nanocrystal emission from (a) J774 cells and (b) Caco2 cells incubated with neutral (DOPC), anionic (1:1 DOPC:DOPG), or cationic (1:1 DOPC:DOTAP) Lip-NC assemblies at either 37 °C or 4 °C. Error bars are standard deviation (n=2). * Data was not collected for samples without Lip-NC assemblies at 4 °C.

2.3.4 Cytotoxicity of Liposome-Si Nanocrystal Assemblies

Figure 2.10 shows the results of cytotoxicity assays performed for 1:1 DOPC:DOPG Lip-NC assemblies incubated with J774 cells for 1, 3, or 6 hours. Two different assays were selected to assess viability: (i) a lactate dehydrogenase (LDH) enzyme assay to measure the release of the LDH enzyme upon damage to the cellular plasma membrane which accompanies cell death and (ii) an 3-(4,5-dimethylthiazol-2-yl)-5-(3-carboxymethoxyphenyl)-2-(4-sulfophenyl)-2H-tetrazolium (MTS) assay to measure the metabolic activity of the cells. Neither toxicity assay showed significant cellular toxicity over the 6 hour incubation with the Lip-NC assemblies (Figure 10). For comparison, cells were also incubated with liposome-gold nanocrystal assemblies (since gold is considered biocompatible)[39] and liposomes that did not contain any nanoparticles, and all three samples resulted in similar cytotoxicity results. It should be noted that the >100% viability rates measured for the MTS assay may have been the result of increased metabolic activity from Lip-NC uptake through the energy-dependent endocytosis pathway. Overall, the low toxicity observed with J774 cells over a 6 hour period suggest that the 1:1 DOPC:DOPG Lip-NC assemblies can be useful for medical imaging.

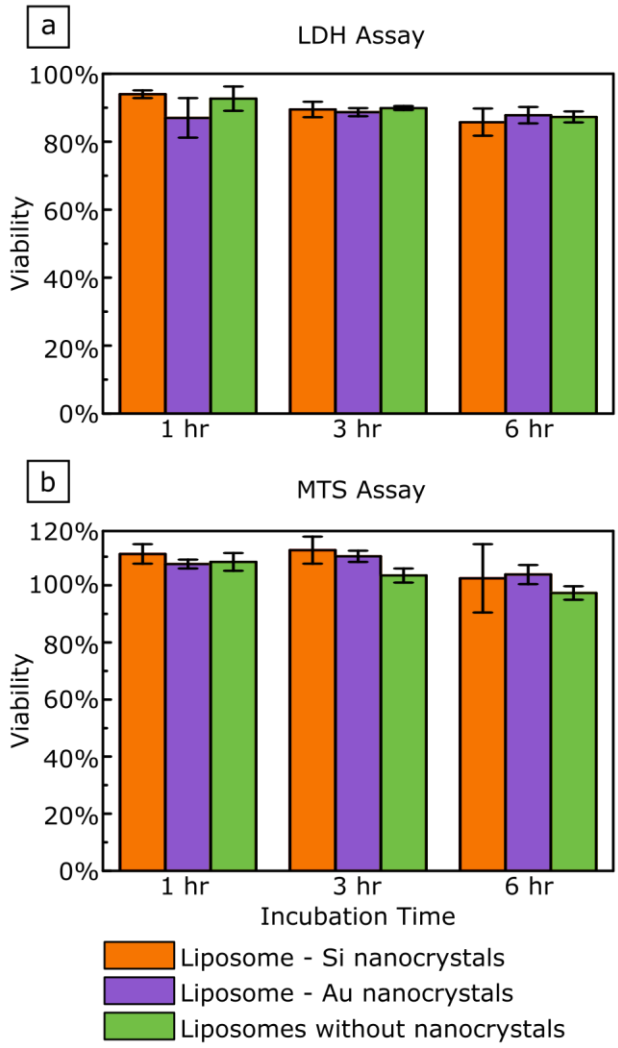

Figure 2.10 Cell viability was measured by (a) LDH assay and (b) MTS assay for J774 cells incubated at 37 °C with 1:1 DOPC:DOPG liposomes assembled with Si nanocrystals, gold nanocrystals, or no nanocrystals. Error bars are standard deviation (n=3).

2.3.5 Two-Photon Imaging of Macrophage Cells

Figure 2.11 shows the results of imaging macrophage cells with 1:1 DOPC:DOPG Lip-NC assemblies and DAPI using either one-photon or two-photon microscopy. A

pinhole is typically used to exclude out of focus light in one-photon microscopy.[31] Here a large pinhole (2000 μm) was used, resulting in images that appear blurry. In contrast, two-photon microscopy requires the simultaneous absorption of two photons from a pulsed laser source, such that the probability of excitation is localized to a small focal volume.[44] Thus, the two-photon images in Figure 2.11 appear to have better spatial resolution without the use of a pinhole.

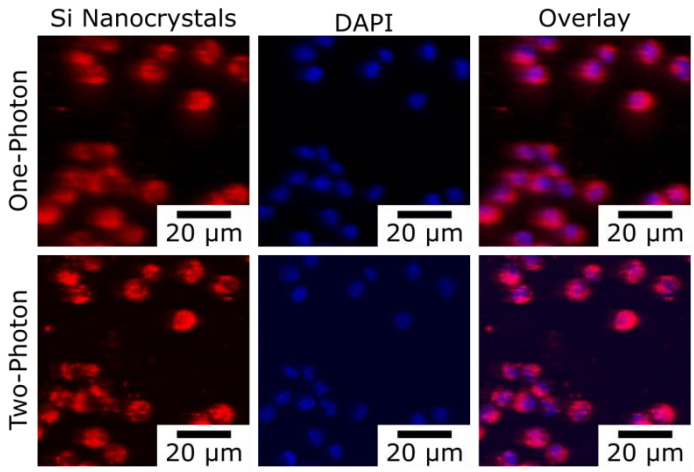

Figure 2.11 Images of macrophages with Si nanocrystals (in 1:1 DOPC:DOPG Lip-NC assemblies) and DAPI taken using one-photon (405 nm) and two-photon (800 nm) excitation.

2.4 CONCLUSION

The experiments presented here demonstrate the assembly of hydrophobic Si nanocrystals with lipids, and the subsequent use of the Lip-NC assemblies to traffic fluorescent nanoparticles into cells for confocal imaging. In all Lip-NC formulations we observed that the nanocrystals appeared as aggregates rather than loading into liposome bilayers (Figure 2.3). Previous studies on the incorporation of nanoparticles into

liposomes often observed small inclusions of <5 nanoparticles per liposome, which would limit the efficacy of using liposomes as nanoparticle delivery vehicles.[40–43] We have demonstrated high loading (up to 50% dispersion emission fraction) for Lip-NC assemblies and have confirmed that the dispersions are bright enough to be imaged using confocal microscopy. Lip-NC assembly uptake was consistent with previous reports of charged liposome uptake by macrophages, where liposomes interact with cell surfaces before being taken up by endocytosis.[18,33,34] Liposomal carriers can be tagged with specific biomolecules that allow targeted interactions with cells,[16] and future work may investigate the uptake of tagged Lip-NC assemblies by cells.

2.5 REFERENCES

(1) Dubertret, B.; Skourides, P.; Norris, D. J.; Noireaux, V.; Brivanlou, A. H.; Libchaber, A. In Vivo Imaging of Quantum Dots Encapsulated in Phospholipid Micelles. *Science* **2002**, *298*, 1759–1762.

(2) Resch-Genger, U.; Grabolle, M.; Cavaliere-Jaricot, S.; Nitschke, R.; Nann, T. Quantum Dots versus Organic Dyes as Fluorescent Labels. *Nat. Methods* **2008**, *5*, 763–775.

(3) Wegner, K. D.; Hildebrandt, N. Quantum Dots: Bright and Versatile in Vitro and in Vivo Fluorescence Imaging Biosensors. *Chem. Soc. Rev*. **2015**, *44*, 4792–4834.

(4) Warner, J. H.; Hoshino, A.; Yamamoto, K.; Tilley, R. D. Water-Soluble Photoluminescent Silicon Quantum Dots. *Angew. Chem*. **2005**, *117*, 4626–4630.

(5) Erogbogbo, F.; Yong, K.-T.; Roy, I.; Xu, G.; Prasad, P. N.; Swihart, M. T. Biocompatible Luminescent Silicon Quantum Dots for Imaging of Cancer Cells. *ACS Nano* **2008**, *2*, 873–878.

(6) Park, J.-H.; Gu, L.; Maltzahn, G. von; Ruoslahti, E.; Bhatia, S. N.; Sailor, M. J. Biodegradable Luminescent Porous Silicon Nanoparticles for in Vivo Applications. *Nat. Mater*. **2009**, *8*, 331–336.

(7) Hessel, C. M.; Reid, D.; Panthani, M. G.; Rasch, M. R.; Goodfellow, B. W.; Wei, J.; Fujii, H.; Akhavan, V.; Korgel, B. A. Synthesis of Ligand-Stabilized Silicon Nanocrystals with Size-Dependent Photoluminescence Spanning Visible to Near-Infrared Wavelengths. *Chem. Mater*. **2012**, *24*, 393–401.

(8) Bhattacharjee, S.; Rietjens, I. M. C. M.; Singh, M. P.; Atkins, T. M.; Purkait, T. K.; Xu, Z.; Regli, S.; Shukaliak, A.; Clark, R. J.; Mitchell, B. S.; Alink, G. M.; Marcelis, A. T. M.; Fink, M. J.; Veinot, J. G. C.; Kauzlarich, S. M.; Zuilhof, H. Cytotoxicity of Surface-Functionalized Silicon and Germanium Nanoparticles: The Dominant Role of Surface Charges. *Nanoscale* **2013**, *5*, 4870–4883.

(9) Yu, Y.; Fan, G.; Fermi, A.; Mazzaro, R.; Morandi, V.; Ceroni, P.; Smilgies, D.-M.; Korgel, B. A. Size-Dependent Photoluminescence Efficiency of Silicon Nanocrystal Quantum Dots. *J. Phys. Chem. C* **2017**, *121*, 23240–23248.

(10) Jang, H.; Pell, L. E.; Korgel, B. A.; English, D. S. Photoluminescence Quenching of Silicon Nanoparticles in Phospholipid Vesicle Bilayers. *J. Photochem. Photobiol. Chem*. **2003**, *158*, 111–117.

(11) Henderson, E. J.; Shuhendler, A. J.; Prasad, P.; Baumann, V.; Maier-Flaig, F.; Faulkner, D. O.; Lemmer, U.; Wu, X. Y.; Ozin, G. A. Colloidally Stable Silicon Nanocrystals with Near-Infrared Photoluminescence for Biological Fluorescence Imaging. *Small* **2011**, *7*, 2507–2516.

(12) Wang, M.; Thanou, M. Targeting Nanoparticles to Cancer. *Pharmacol. Res*. **2010**, *62*, 90–99.

(13) Balazs, D. A.; Godbey, W. T. Liposomes for Use in Gene Delivery. *J. Drug Deliv*. **2010**, *2011*, e326497.

(14) Al-Jamal, W. T.; Kostarelos, K. Liposomes: From a Clinically Established Drug Delivery System to a Nanoparticle Platform for Theranostic Nanomedicine. *Acc. Chem. Res*. **2011**, *44*, 1094–1104.

(15) Chang, H.-I.; Yeh, M.-K. Clinical Development of Liposome-Based Drugs: Formulation, Characterization, and Therapeutic Efficacy. *Int. J. Nanomedicine* **2012**, *7*, 49–60.

(16) Allen, T. M.; Cullis, P. R. Liposomal Drug Delivery Systems: From Concept to Clinical Applications. *Adv. Drug Deliv. Rev*. **2013**, *65*, 36–48.

(17) Kulkarni, S. B.; Betageri, G. V.; Singh, M. Factors Affecting Microencapsulation of Drugs in Liposomes. *J. Microencapsul*. **1995**, *12*, 229–246.

(18) Miller, C. R.; Bondurant, B.; McLean, S. D.; McGovern, K. A.; O'Brien, D. F. Liposome−Cell Interactions in Vitro: Effect of Liposome Surface Charge on the Binding and Endocytosis of Conventional and Sterically Stabilized Liposomes. *Biochemistry* **1998**, *37*, 12875–12883.

(19) Rasch, M. R.; Yu, Y.; Bosoy, C.; Goodfellow, B. W.; Korgel, B. A. Chloroform-Enhanced Incorporation of Hydrophobic Gold Nanocrystals into Dioleoylphosphatidylcholine (DOPC) Vesicle Membranes. *Langmuir* **2012**, *28*, 12971–12981.

(20) Casey, K. G.; Quitevis, E. L. Effect of Solvent Polarity on Nonradiative Processes in Xanthene Dyes: Rhodamine B in Normal Alcohols. *J. Phys. Chem*. **1988**, *92*, 6590–6594.

(21) Paasonen, L.; Laaksonen, T.; Johans, C.; Yliperttula, M.; Kontturi, K.; Urtti, A. Gold Nanoparticles Enable Selective Light-Induced Contents Release from Liposomes. *J. Controlled Release* **2007**, *122*, 86–93.

(22) Rasch, M. R.; Rossinyol, E.; Hueso, J. L.; Goodfellow, B. W.; Arbiol, J.; Korgel, B. A. Hydrophobic Gold Nanoparticle Self-Assembly with Phosphatidylcholine Lipid: Membrane-Loaded and Janus Vesicles. *Nano Lett*. **2010**, *10*, 3733–3739.

(23) Gallová, J.; Uhríková, D.; Islamov, A.; Kuklin, A.; Balgavý, P. Effect of Cholesterol on the Bilayer Thickness in Unilamellar Extruded DLPC and DOPC Liposomes: SANS Contrast Variation Study. *Gen. Physiol. Biophys*. **2004**, *23*, 113–128.

(24) Du, Z.; Munye, M. M.; Tagalakis, A. D.; Manunta, M. D. I.; Hart, S. L. The Role of the Helper Lipid on the DNA Transfection Efficiency of Lipopolyplex Formulations. *Sci. Rep*. **2014**, *4*.

(25) Papahadjopoulos, D.; Allen, T. M.; Gabizon, A.; Mayhew, E.; Matthay, K.; Huang, S. K.; Lee, K. D.; Woodle, M. C.; Lasic, D. D.; Redemann, C. Sterically Stabilized Liposomes: Improvements in Pharmacokinetics and Antitumor Therapeutic Efficacy. *Proc. Natl. Acad. Sci*. **1991**, *88*, 11460–11464.

(26) Briuglia, M.-L.; Rotella, C.; McFarlane, A.; Lamprou, D. A. Influence of Cholesterol on Liposome Stability and on in Vitro Drug Release. *Drug Deliv. Transl. Res*. **2015**, *5*, 231–242.

(27) Stetefeld, J.; McKenna, S. A.; Patel, T. R. Dynamic Light Scattering: A Practical Guide and Applications in Biomedical Sciences. *Biophys. Rev*. **2016**, *8*, 409–427.

(28) Dickey, A.; Faller, R. Examining the Contributions of Lipid Shape and Headgroup Charge on Bilayer Behavior. *Biophys. J*. **2008**, *95*, 2636–2646.

(29) Chandler, D. Interfaces and the Driving Force of Hydrophobic Assembly. *Nature* **2005**, *437*, 640–647.

(30) Guo, Y.; Terazzi, E.; Seemann, R.; Fleury, J. B.; Baulin, V. A. Direct Proof of Spontaneous Translocation of Lipid-Covered Hydrophobic Nanoparticles through a Phospholipid Bilayer. *Sci. Adv*. **2016**, *2*, e1600261.

(31) *Handbook of Biological Confocal Microscopy*; Pawley, J. B., Ed.; 3rd ed.; Springer US: Boston, MA, 2006.

(32) Hsu, M. J.; Juliano, R. L. Interactions of Liposomes with the Reticuloendothelial System: II. Nonspecific and Receptor-Mediated Uptake of Liposomes by Mouse Peritoneal Macrophages. *Biochim. Biophys. Acta BBA - Mol. Cell Res*. **1982**, *720*, 411–419.

(33) Lee, K. D.; Nir, S.; Papahadjopoulos, D. Quantitative Analysis of Liposome-Cell Interactions in Vitro: Rate Constants of Binding and Endocytosis with Suspension and Adherent J774 Cells and Human Monocytes. *Biochemistry* **1993**, *32*, 889–899.

(34) Oh, N.; Park, J.-H. Endocytosis and Exocytosis of Nanoparticles in Mammalian Cells. *Int. J. Nanomedicine* **2014**, *9*, 51–63.

(35) Derfus, A. M.; Chan, W. C. W.; Bhatia, S. N. Intracellular Delivery of Quantum Dots for Live Cell Labeling and Organelle Tracking. *Adv. Mater*. **2004**, *16*, 961–966.

(36) Win, K. Y.; Feng, S.-S. Effects of Particle Size and Surface Coating on Cellular Uptake of Polymeric Nanoparticles for Oral Delivery of Anticancer Drugs. *Biomaterials* **2005**, *26*, 2713–2722.

(37) Cartiera, M. S.; Johnson, K. M.; Rajendran, V.; Caplan, M. J.; Saltzman, W. M. The Uptake and Intracellular Fate of PLGA Nanoparticles in Epithelial Cells. *Biomaterials* **2009**, *30*, 2790–2798.

(38) Roger, E.; Kalscheuer, S.; Kirtane, A.; Guru, B. R.; Grill, A. E.; Whittum-Hudson, J.; Panyam, J. Folic Acid Functionalized Nanoparticles for Enhanced Oral Drug Delivery. *Mol. Pharm*. **2012**, *9*, 2103–2110.

(39) Connor, E. E.; Mwamuka, J.; Gole, A.; Murphy, C. J.; Wyatt, M. D. Gold Nanoparticles Are Taken Up by Human Cells but Do Not Cause Acute Cytotoxicity. *Small* **2005**, *1*, 325–327.

(40) Al-Jamal, W. T.; Al-Jamal, K. T.; Tian, B.; Lacerda, L.; Bomans, P. H.; Frederik, P. M.; Kostarelos, K. Lipid−Quantum Dot Bilayer Vesicles Enhance Tumor Cell Uptake and Retention in Vitro and in Vivo. *ACS Nano* **2008**, *2*, 408–418.

(41) Paasonen, L.; Sipilä, T.; Subrizi, A.; Laurinmäki, P.; Butcher, S. J.; Rappolt, M.; Yaghmur, A.; Urtti, A.; Yliperttula, M. Gold-Embedded Photosensitive Liposomes for Drug Delivery: Triggering Mechanism and Intracellular Release. *J. Controlled Release* **2010**, *147*, 136–143.

(42) De Leo, V.; Catucci, L.; Falqui, A.; Marotta, R.; Striccoli, M.; Agostiano, A.; Comparelli, R.; Milano, F. Hybrid Assemblies of Fluorescent Nanocrystals and Membrane Proteins in Liposomes. *Langmuir* **2014**, *30*, 1599–1608.

(43) Tahara, K.; Fujimoto, S.; Fujii, F.; Tozuka, Y.; Jin, T.; Takeuchi, H. Quantum Dot-Loaded Liposomes to Evaluate the Behavior of Drug Carriers after Oral Administration. *J. Pharm*. **2013**, *2013*.

(44) Zipfel, W. R.; Williams, R. M.; Webb, W. W. Nonlinear Magic: Multiphoton Microscopy in the Biosciences. *Nat. Biotechnol.* **2003**, *21*, 1369–1377.

Chapter 3: Highly Fluorescent Silicon Nanocrystals Stabilized in Water using Quatsomes

3.1 INTRODUCTION

Semiconductor nanocrystals, or quantum dots, have been used extensively to study biological systems due to their fluorescence properties and photostability.[1–5] Silicon nanoparticles offer biocompatibility and photoluminescence that is well-suited for medical imaging using near-infrared (NIR) or long-wavelength visible light.[3,6–8] For these applications, Si nanocrystals must be dispersed in aqueous media and retain their fluorescence. This has been accomplished by capping Si nanocrystals with organic ligands bearing polar functional groups or by coating hydrophobic nanocrystals with surfactant or amphiphilic polymer.[3,7–10] By incorporating nanocrystals into surfactant assemblies, such as micelles or vesicles, additional functionality might be achieved.[1,7,10–17] For example, liposomal vesicles are especially interesting since they are medically-accepted pharmaceutical carriers and could provide a therapeutic delivery vehicle combined with the imaging capabilities of the nanocrystals.[18–20] However, liposomes can suffer from aggregation and non-uniformity, which can negatively impact pharmacological properties and pharmaceutical properties.

Here, we show that non-liposomal vesicular structures, called quatsomes, can be highly effective dispersing agents and carriers for Si nanocrystals, with long-term dispersion stability and fluorescence. Quatsomes are composed of sterols and quaternary ammonium surfactants that self-assemble into vesicular bilayers.[21] Quatsomes are extremely stable and have been shown to remain dispersed for several years with high uniformity in size and lamellarity.[22–24] Quatsomes have antibacterial and anti-biofilm properties, and have been used successfully to prepare stable multifunctional vesicle-biomolecule conjugates, to incorporate water insoluble fluorene-based probes, and to

protect excited state intramolecular proton transfer (ESIPT) fluorophores in aqueous media.[23,25–27] Furthermore, quatsomes are largely unaffected by changes in temperature or dilution, making them ideal candidates for use *in vivo*.[21,24] Here, we demonstrate that the integration of Si nanocrystals with orange fluorescence (2.8 nm diameter, photoluminescence quantum yields of about 15%) into quatsomes composed of cholesterol (chol) and cetyl trimethyl ammonium bromide (CTAB) provides stable nanocrystal dispersions in aqueous media with quantum yields of 6.6%.

3.2 EXPERIMENTAL METHODS

3.2.1 Materials

Hydrogen silsesquioxane (HSQ) was purchased from Dow Corning. Hydrofluoric acid (HF, 48%) was purchased from Macron Fine Chemicals. Ethanol was purchased from Pharmco-Aaper. CTAB (high purity grade) was purchased from Amresco. Chol was purchased from Anatrace. 1-Dodecanethiol (98%) was purchased from Acros Organics. 1-octene (98%), gold(III) chloride trihydrate (≥99.9%), tetraoctylammonium bromide (TOAB, 98%), and sodium borohydride (≥98.0%) were purchased from Sigma-Aldrich. Hydrochloric Acid (HCl), hexanes (≥98.5%), chloroform (≥99.8%), and toluene (≥99.5%) were purchased from Fisher. 1,2-dioleoyl-sn-glycero-3-phosophocholine (DOPC) and 1,2-dioleoyl-sn-glycero-3-(1'-rac-glycerol) (DOPG) in chloroform were purchased from Avanti Polar Lipids. Carbon dioxide was obtained from Matheson and nitrogen was obtained from the University of Texas Department of Physics Cryolab. Water used in all experiments was high purity water (18.2 MΩ/cm) and was obtained from a Millipore Synergy Ultrapure water system.

3.2.2 Si Nanocrystal Synthesis and Assembly with Quatsomes

Silicon nanocrystals were synthesized following procedures reported in Hessel, et al.[8] 40 ml of HSQ was degassed and then heated to 1100 °C for 60 min in a tube furnace under forming gas (90% N_2/10% H_2) flow. The resulting brown reaction product was then ground with a mortar and pestle, followed by further size reduction by mechanical shaking in a wrist action shaker with borosilicate beads for 9 hr. The final brown powder consists of Si nanocrystals embedded in an SiO_2 matrix. To liberate the nanocrystals from the matrix, 0.6 g of powder was etched in the dark with 2 ml HCl and 20 ml HF for 3.5 hr. After etching, the material was precipitated by centrifugation for 5 min at 8000 rpm. The supernatant containing HF was removed with a pipette, and the precipitate was redispersed in 20 ml of ethanol and then centrifuged again. This washing process was repeated again with 20 ml of ethanol and once more with 20 ml of chloroform. The resulting H-terminated nanocrystals were redispersed in 20 ml of 1-octene and then injected with a syringe into a 3-neck flask connected to a Schlenk line under vacuum. Liquid nitrogen was used to immediately cool the flask contents under vacuum, and then the dispersion was thawed to room temperature under nitrogen flow. The freeze-thaw process was repeated three more times. The dispersion was stirred under nitrogen flow at 120°C for 12 hr. The unpassivated nanocrystals were precipitated by centrifugation at 8000 rpm for 5 min. The passivated nanocrystals in octene were placed on a rotary evaporator under vacuum at 60°C to evaporate the octene. The nanocrystals were then redispersed in 3 ml of hexanes. The Si nanocrystals were then purified by four washing steps using hexanes/ethanol as the solvent/antisolvent pair. The nanocrystals were redispersed in chloroform at a concentration of 6.75 mg/ml for use.

Gold nanocrystals were synthesized using the procedures described in Rasch, et al.[13] 33 mg of gold (III) chloride trihydrate was dissolved in 20 ml of deionized water. A

separate solution of 6 g of TOAB dissolved in 80 ml toluene was prepared. The aqueous and toluene solutions were mixed and stirred for 1 hr. The aqueous phase was discarded. 0.6 ml of 1-dodecanethiol was added to the toluene solution and stirred for 15 min. An aqueous solution of 378 mg of sodium borohydride in 20 ml of water at 0°C was prepared and added to the toluene solution. After stirring overnight, the aqueous phase was discarded. The nanocrystals were precipitated by adding 5 ml of the gold nanocrystal dispersion to a glass centrifuge tube and 20 ml of ethanol and centrifuging for 5 min at 8000 rpm. The supernatant was discarded and the precipitate was redispersed in toluene. This washing procedure was repeated until the entire gold solution had been washed with ethanol. Finally, the nanocrystals were redispersed and stored in toluene. Prior to use, the nanocrystals were dried and redispersed in chloroform at a concentration of 3 mg/ml.

Quatsomes were made by DELOS-SUSP (depressurization of an expanded liquid organic solution-suspension) as previously described.[23] CO_2-expanded ethanol was used to dissolve cholesterol (chol). A 7.5 ml high-pressure vessel was loaded with a solution of 76 mg of chol in 2.88 ml of ethanol at atmospheric pressure and 35°C. CO_2 was then added by syringe pump until reaching a working pressure of 10 MPa and a CO_2 molar fraction of XCO_2= 0.62. The system was kept at 35°C and 10 MPa for approximately 1 hr. Finally, the CO_2-expanded chol solution was removed from the reactor through a depressurization valve and collected in 24 ml of water with 72 mg of dissolved CTAB to produce the chol-CTAB quatsomes. In this final step, a flow of N_2 is used as a plunger to push down the CO_2-expanded solution from the vessel and to maintain a constant pressure inside the vessel during depressurization. The molar ratio between the CTAB and the chol in the final formulation was 1 to 1, which has been shown to be the correct proportion in order to have a pure vesicular phase.[21] The final quatsome dispersions were composed of 7 mM each of chol and CTAB in water containing 10% ethanol. This

quatsome formulation is referred to throughout as "7 mM quatsomes." A more diluted quatsome formulation composed of 0.7 mM chol and CTAB was prepared by dilution of 7 mM quatsomes with water with 10% ethanol. These are referred to as "0.7 mM quatsomes."

Nanocrystals were incorporated into quatsomes by adding 750 μL of 7 mM or 0.7 mM quatsomes to a 2 ml glass vial. 20 μl of a dispersion of Si nanocrystals in chloroform with a concentration of 6.75 mg/ml were added (corresponding to 0.135 mg Si nanocrystals). The vial was bath-sonicated for 5 min at room temperature (Misonix 1510R-MT or Bransonic M1800 bath sonicator, 40kHz, 1/2 gallon tank). In experiments performed with only CTAB in place of the quatsomes, 7 mM CTAB in water was bath sonicated with the same quantity of Si nanocrystals as above.

DOPC (neutral) liposomes were prepared using the DELOS-susp process.[22,23] 35 mg of DOPC were dissolved in 1.9 ml of ethanol and loaded into a 7.5 ml high-pressure vessel at atmospheric pressure and 35 °C. The solution was then expanded with compressed CO_2 until reaching a molar fraction of CO_2 of XCO_2= 0.76 at a working pressure of 10 MPa. The system was kept at 35 °C and 10 MPa for 1 hr. Finally, the CO_2-expanded DOPC solution was removed from the reactor through a depressurization valve and collected in 9 ml of an aqueous solution to create the liposomes. The final concentration of DOPC in the liposomal system was 3.6 mM in high purity water containing 17% ethanol.

DOPG (anionic) liposomes were prepared by thin film hydration and extrusion. 7 μmol DOPG in chloroform were dried into a film on a rotary evaporator for 15 min. Residual solvent was removed by placing the film in a vacuum oven for 2 hr. The lipid film was then hydrated with 1 ml of 10 mM HEPES, 10 mM NaCl and bath sonicated for

30 min. Finally, the suspension was extruded 21 times through a polycarbonate filter (100 nm pore size) on an Avanti MiniExtruder (Avanti Polar Lipids).

Dialysis was performed using SnakeSkin Dialysis Tubing with 10 kDa molecular weight cutoff (Life Technologies). Six rounds of dialysis into water, each lasting 24 hours, were performed.

3.2.3 Characterization

Transmission electron microscopy (TEM) and cryogenic transmission electron microscopy (cryoTEM) images were acquired digitally using an FEI Tecnai Biotwin TEM operated at 80 kV accelerating voltage. For imaging, Si nanocrystals were drop cast from chloroform onto 200 mesh carbon-coated copper grids (Electron Microscopy Science). CryoTEM samples were prepared using a Leica EM GP by dropping 3 μL of sample onto Quantifoil R1.2/1.3 holey carbon on 300 mesh copper grids (Electron Microscopy Science) inside the environmental control chamber set to 25°C and 90% humidity. After a blotting time of 3.5 sec, the grid was plunged into liquid ethane to vitrify the sample. The grid was transferred to a Gatan 626 Cryo-Transfer Holder under liquid nitrogen. FEI low dose software was used to obtain images of cryoTEM samples using a reduced electron beam dose.

Optical absorbance spectra were acquired on a Varian Cary 50 Bio UV-vis spectrophotometer or a Varian Cary 500 ultraviolet-visible-near infrared spectrophotometer. Photoluminescence (PL) emission and excitation (PLE) spectra were acquired on a Varian Cary Eclipse fluorescence spectrophotometer. Samples were diluted 1/20 prior to measurement. PL quantum yields were determined using Rhodamine B as a PL dye standard, which has a quantum yield of 49% in ethanol.[28] Quantum yield was

calculated according to the equation: $QY_{sample}=(QY_{ref})(A_{ref}/A_{sample})(I_{sample}/I_{ref})(\eta_{sample}/\eta_{ref})^2$, where QY is the quantum yield, A is the absorbance at 350 nm, I is the PL intensity (excited at 350 nm), η is the solvent refractive index, and the subscripts *sample* and *ref* refer to the Si nanocrystal samples and Rhodamine B reference, respectively.

Dynamic light scattering (DLS) data were acquired on a Zetasizer Nano ZS (Malvern Instruments). Samples were measured in 40 µl disposable cuvettes at 173°, with temperature set to 25°C. All measurements were conducted in triplicate. Zetasizer software (Malvern Instruments) was used to analyze data and determine the average size (z-ave) and polydispersity index (PDI), with the dispersant set depending on the medium, as follows: 10% ethanol in water by volume had 8.06% by weight ethanol in water with viscosity of 1.28 cP and refractive index of 1.34, while 17% ethanol in water by volume had 13.9% by weight ethanol in water with a viscosity of 1.66 cP and refractive index of 1.34.

Thermal gravimetric analysis (TGA) was performed using a Mettler Toledo TGA/DSC 1. Nanocrystals dispersed in chloroform were dried in a 70 µl alumina crucible (Mettler Toledo). Sample were heated under 50 ml min^{-1} of air flow at a rate of 10°C min^{-1} from 25°C to 800°C and then held at 800°C for 30 min.

3.3 RESULTS AND DISCUSSION

3.3.1 Incorporation of Si Nanocrystals with Quatsomes

Figures 3.1a shows TEM images of the Si nanocrystals prepared with 1-octene as a ligand and used for the quatsomes experiment. Figure 3.1b shows a size histogram determined from TEM: the average diameter is 2.8±0.6 nm (n=150). TGA was conducted to determine the mass of ligand per Si nanocrystals (Figure 3.1c). At the beginning of the

TGA cycle, the sample consists of Si cores and octene ligand, while at the end of the cycle there was no remaining ligand and all the Si converts to SiO_2. Based on the measured size of the Si core (2.8 nm) and the fractional mass loss, the sample is composed of 37% Si by mass and 63% ligand, corresponding to a ligand coverage density of 9.9 ligands/nm^2.

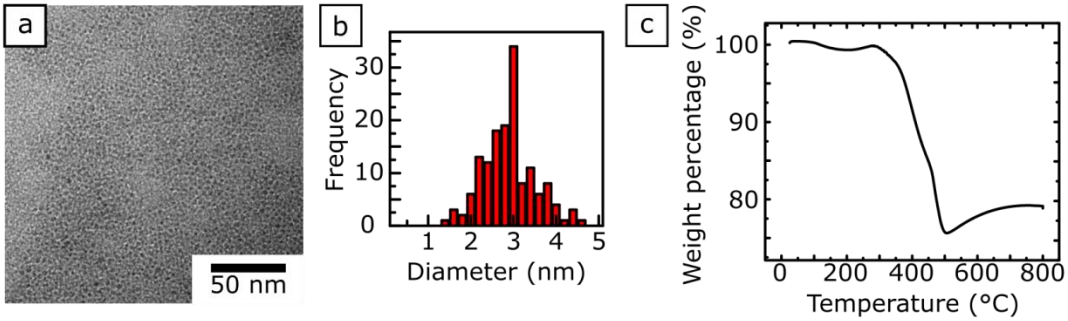

Figure 3.1 (a) TEM images of octene-coated Si nanocrystals. (b) Histogram showing size distribution of Si nanocrystals. (c) TGA results for 1-octene coated Si nanocrystals.

Silicon nanocrystals dispersed in chloroform were incorporated into pre-formed aqueous 7 mM quatsomes using a 5 minute bath sonication procedure, as outlined in Figure 3.2a. The quatsome dispersions initially have a cloudy blue/grey appearance and then become light yellow following the addition of the Si nanocrystals and bath sonication. There is no visible precipitation or phase separation after addition of the nanocrystals to the quatsomes. Figures 3.2b-3.2d show photographs of the quatsome and nanocrystal dispersions before and after they are combined, along with TEM images. The nanocrystal quatsome assemblies dispersed in water exhibit orange fluorescence characteristic of Si nanocrystals dispersed in chloroform, as shown in Figures 3.2c and 3.2d.

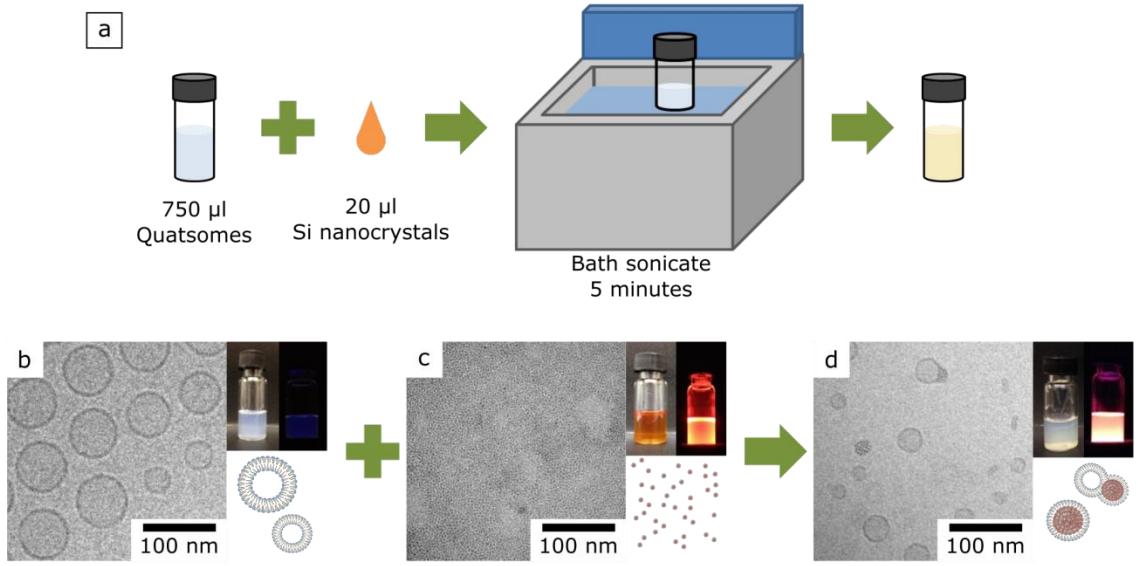

Figure 3.2 (a) Schematic representation of the process for incorporating Si nanocrystals into quatsomes through bath sonication. (b-d) CryoTEM or TEM images of 7 mM quatsomes, Si nanocrystals, and their assemblies along with photographs of the dispersions under ambient light (on the left) and a 365 nm UV lamp (on the right), as well as illustrations of the structures.

Figure 3.3 shows additional cryoTEM images of the fluorescent Si nanocrystal-quatsome assemblies. The Si nanocrystals appear as clusters of similar size as the quatsomes. The nanocrystals do not distribute in the surfactant bilayers of the quatsomes as dodecanethiol-capped gold nanocrystals have been observed in other liposomal vesicles.[13,17] The Si nanocrystal clusters are attached to one (green arrow) or more quatsomes (blue arrow), or in some cases not attached to any quatsomes (red arrow).

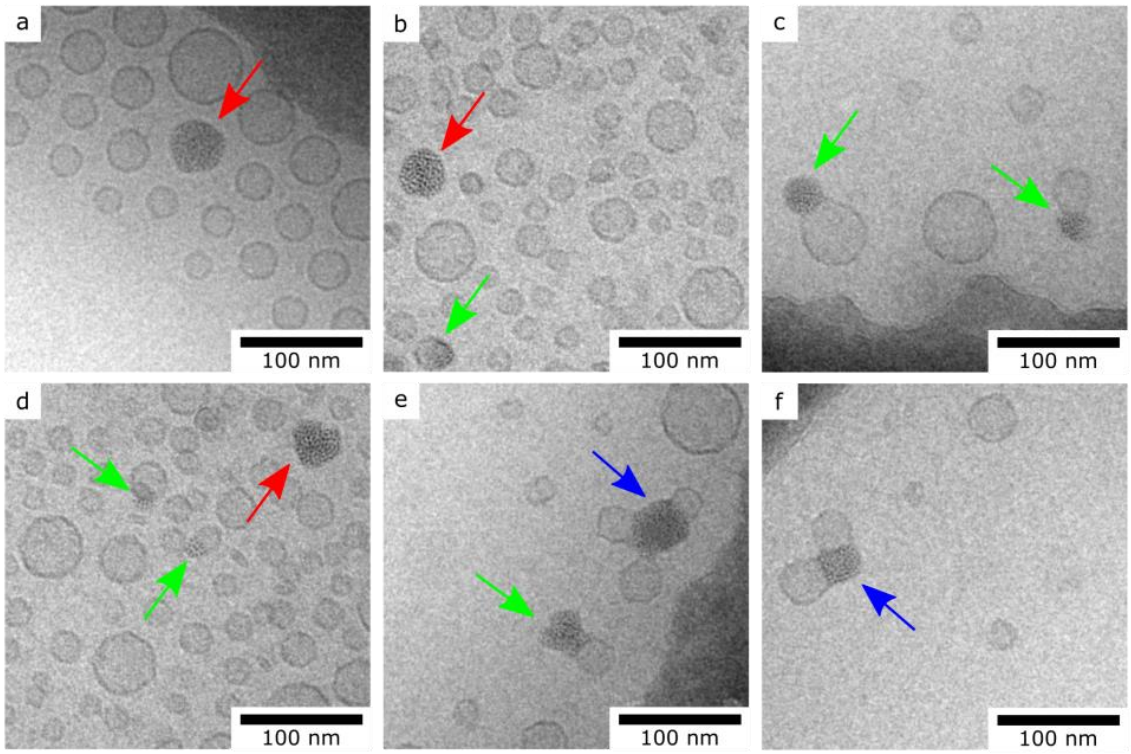

Figure 3.3 CryoTEM images of fluorescent dispersions of Si nanocrystal-quatsome assemblies. The red arrows indicate Si nanocrystal clusters that are not associated with quatsomes; whereas, the green and blue arrows show clusters associated with one or more quatsomes, respectively.

Figure 3.4a compares the optical absorbance, PLE and PL spectra collected from Si nanocrystals either dispersed in chloroform or associated with quatsomes in aqueous media, with constant Si nanocrystal concentration. PL was measured upon excitation at 320 nm, while PLE was measured at an emission of 660 nm. The spectra are nearly identical, indicating that the optical properties of the nanocrystals are successfully transferred to aqueous media using quatsomes as a dispersing vehicle. The quatsome-Si nanocrystal preparations have slightly higher absorbance, which results from additional light scattering of the quatsomes (see, for example, the turbidity of the quatsome dispersions in Figure 3.4). The PL intensity of the quatsome-Si nanocrystal assemblies

was lower than the Si nanocrystals dispersed in chloroform, although the samples still exhibit relatively bright fluorescence when placed over a UV lamp. The decreased PL is partly due to the light scattering of the quatsomes. The PL peak positions of both samples were also nearly identical. Figure 3.4b shows the quantum yield data for the samples. The PL quantum yields of the Si nanocrystals in chloroform and in the quatsome assemblies in water were 16.1% and 6.6%, respectively.

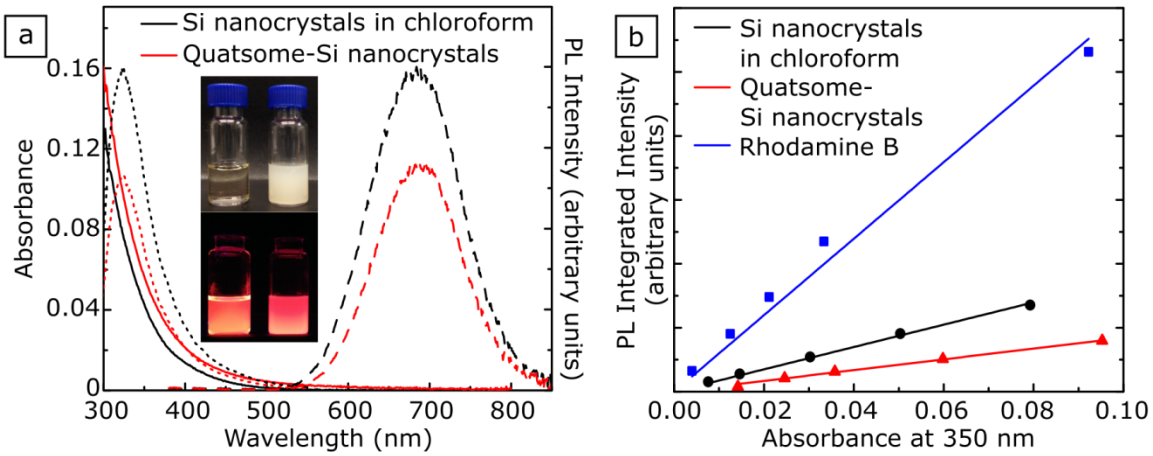

Figure 3.4 (a) Absorbance (solid lines), PL (dashed lines), and PLE (dotted lines) spectra for octene capped Si nanocrystals dispersed in chloroform and incorporated into quatsomes in aqueous media. Inset shows photographs of vials of (left) Si nanocrystals in chloroform and (right) quatsome-Si nanocrystal assemblies, each containing the same concentration of Si nanocrystals, under ambient light (top) or on a 365 nm ultraviolet lamp (bottom). (b) Data collected for quantum yield calculation.

The ratio of Si nanocrystals per quatsome could be estimated based on the preparation conditions. The TGA results provide information on the number of Si nanocrystals per mg of material, and thus it could be deduced that when 135 µg of Si nanocrystals are used in a preparation with 5.25 µmol each of CTAB and chol (750 µl of 7 mM solution), the molar ratio of CTAB : Cholesterol : Si nanocrystal is 1695 : 1695 : 1.

Furthermore, by estimating the diameter of a quatsome from DLS data as 79.3 nm, assuming a bilayer thickness of 4.4 nm,[21] and assuming a CTAB head group area of 0.64 nm^2, it was possible to estimate that there are approximately 55,000 chol-CTAB pairs in each quatsome. In combination with the known amount of Si nanocrystals added to the preparation, it was determined that there are approximately 32 Si nanocrystals per quatsome. CryoTEM images show that not all quatsomes have Si nanocrystals associated with them, though when the Si nanocrystals do assemble into quatsomes they form aggregates with many nanoparticles, so this estimate appears to be reasonable.

The sonication parameters were found to influence the Si nanocrystal-quatsome assembly size and polydispersity (Figure 3.5). Both cryoTEM images and DLS data indicated that while the quatsomes maintained similar size distributions after bath sonication for 1 or 5 minutes, sonication times of 15 or 30 minutes decreased the size of the quatsomes in solution (sizes measured by DLS (each measured in triplicate) were: 1 min z-ave 82 ± 3 nm, PDI 0.248 ± 0.003; 5 min z-ave 69 ± 2 nm, PDI 0.232 ± 0.007; 15 min z-ave 61 ± 2 nm, PDI 0.15 ± 0.02; 30 min z-ave 65 ± 3 nm, PDI 0.139 ± 0.008). Other approaches to loading Si nanocrystals into the quatsomes were also explored, but bath sonication of a mixture of Si nanocrystals dispersed in chloroform added to a quatsome dispersion was found to be the only way to obtain fluorescent assemblies in the same size range as quatsomes. For example, direct addition of Si nanocrystals into the DELOS-susp quatsome formation process did not yield fluorescent dispersions. Probe sonication and vortexing of Si nanocrystals added to quatsome dispersions also did not yield fluorescent dispersions. Probe sonication led to aggregation, while the vortexed sample lost fluorescence.

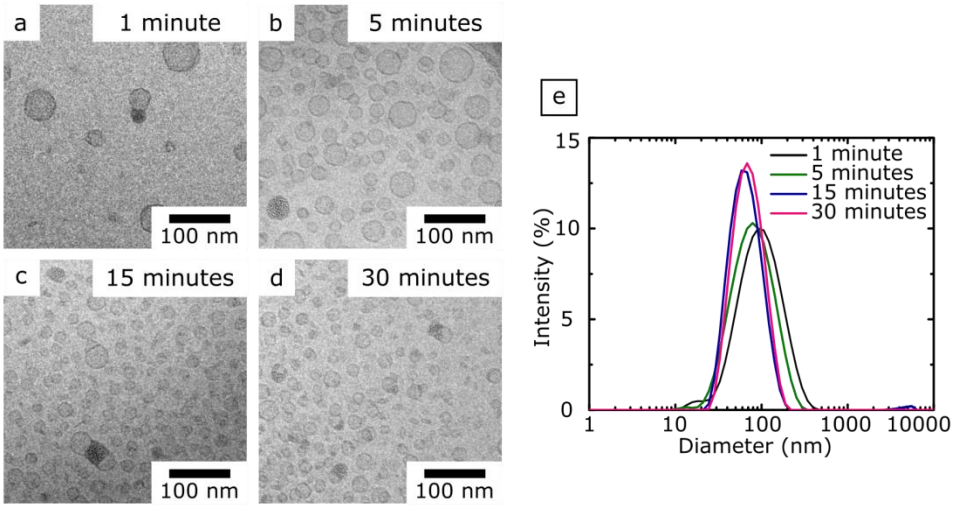

Figure 3.5 CryoTEM images of the Si nanocrystal-quatsome samples prepared by bath sonication for (a) 1 minute, (b) 5 minutes, (c) 15 minutes, and (d) 30 minutes. (d) DLS data showing smaller size at 15 and 30 minutes of bath sonication.

3.3.2 Colloidal and Fluorescence Stability of Si Nanocrystal-Quatsome Assemblies

The colloidal and fluorescence stability of the quatsome-Si nanocrystal assemblies was tested. Table 3.1 summarizes the samples prepared for the stability testing. Figure 3.6 shows photographs of 7 mM quatsome-Si nanocrystal dispersions over the course of 12 weeks. The dispersions were visibly stable during this time period and retained their fluorescence. The optical absorbance did decrease during the first two weeks, but then appeared to stabilize. Perhaps the system is not completely at equilibrium initially, or perhaps there is some oxidation of poorly capped nanocrystals during this time period. Surface oxidation as a result of the aqueous environment may also contribute to the decrease in the average PL wavelength as the nanocrystal core size shrinks. For comparison, over 8 weeks the average PL wavelength blue shifted by 40 nm for the quatsome-Si nanocrystal assemblies but only by 3 nm for Si nanocrystals in chloroform,

suggesting that the aqueous environment and/or CTAB and cholesterol molecules contribute to the observed blue shift. There is no observable change in the morphology of the assemblies imaged by CryoTEM (Figure 3.7).

Sample	Si nanocrystals	Dispersant	Molar ratio of components
i – typical preparation	20 µl of 6.75 mg/ml Si nanocrystals in chloroform	750 µl of 7 mM chol-CTAB quatsomes (7 mM CTAB and 7 mM cholesterol) in 10% ethanol in water	1 Si nanocrystal : 1695 CTAB : 1695 cholesterol
ii – low chol-CTAB	20 µl of 6.75 mg/ml Si nanocrystals in chloroform	750 µl of 0.7 mM chol-CTAB quatsomes (0.7 mM CTAB and 0.7 mM cholesterol) in 10% ethanol in water	1 Si nanocrystal : 170 CTAB : 170 cholesterol
iii – CTAB only	20 µl of 6.75 mg/ml Si nanocrystals in chloroform	750 µl of 7 mM CTAB in 10% ethanol in water	1 Si nanocrystal : 1695 CTAB
iv – water only	20 µl of 6.75 mg/ml Si nanocrystals in chloroform	750 µl of 10% ethanol in water	-
v – no Si nanocrystals	20 µl of chloroform	750 µl of 7 mM chol-CTAB quatsomes (7 mM CTAB and 7 mM cholesterol) in 10% ethanol in water	-

Table 3.1 Summary of quatsome-Si nanocrystal assembly preparations used in stability testing.

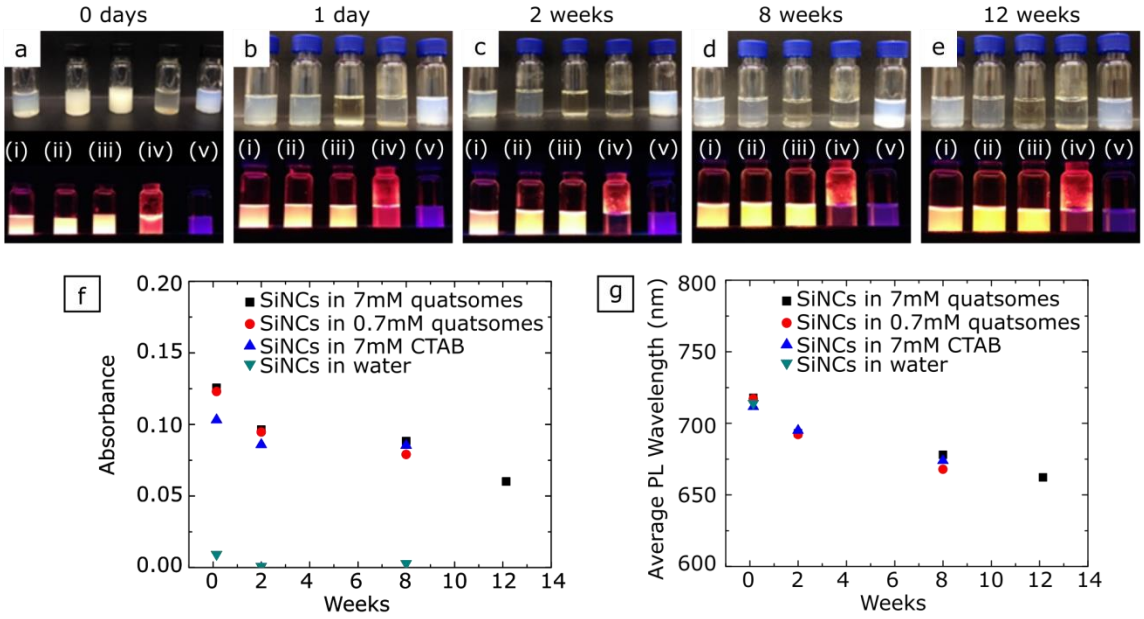

Figure 3.6 Fluorescence stability of Si nanocrystals (SiNCs) dispersed in aqueous solution with quatsomes or CTAB. The five samples shown in (a-e) are summarized in Table 3.1. Photographs of vials under ambient light (top) and on a 365 nm UV lamp (bottom) taken (a) immediately, (b) one day, (c) 2 weeks, (d) 8 weeks, and (e) 12 weeks after preparation. (f) Absorbance measured at 320 nm and (g) average PL wavelength (excited at 320 nm) demonstrate the stability of the nanoparticle fluorescence in quatsomes.

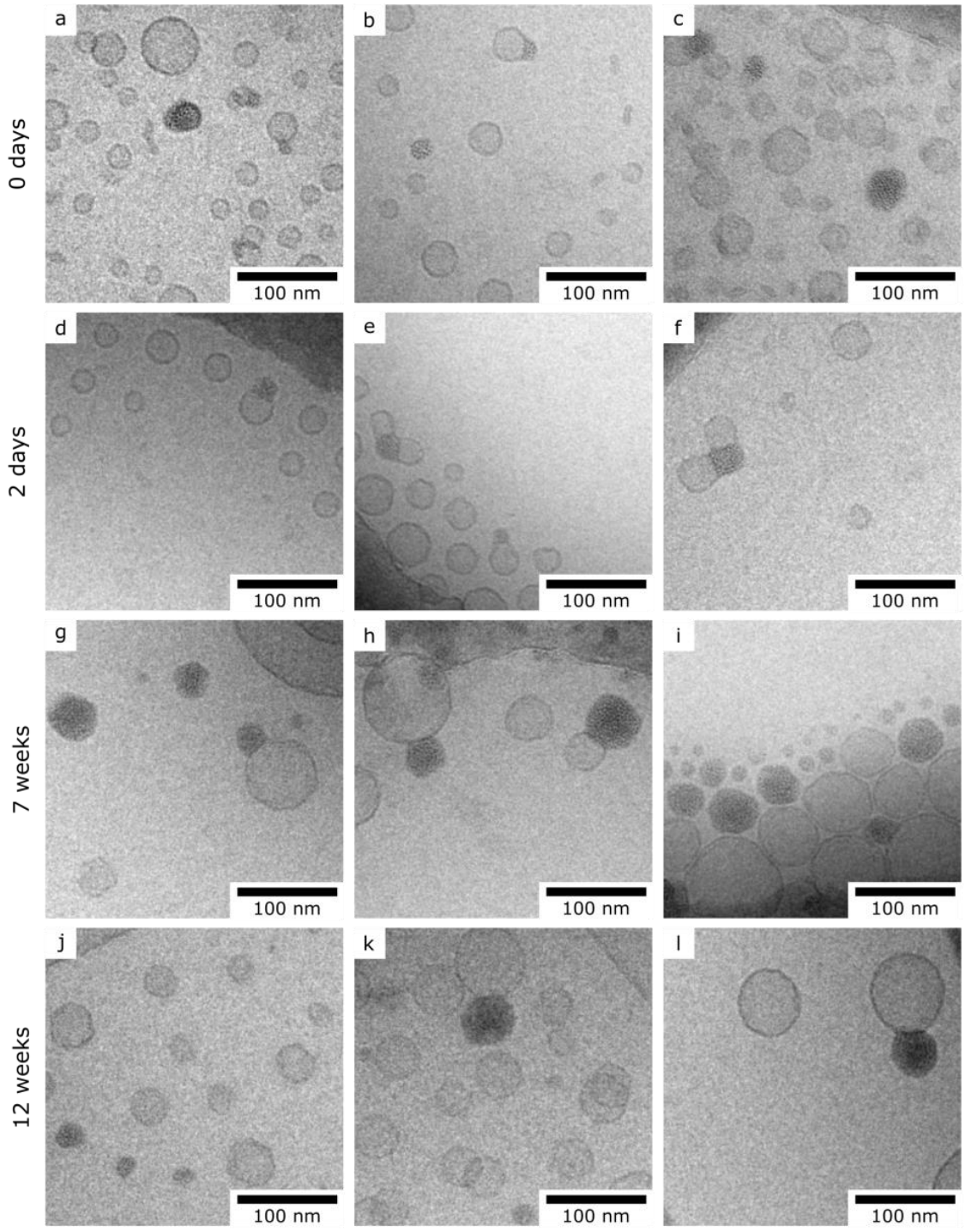

Figure 3.7 CryoTEM images of 7 mM quatsome-Si nanocrystal assemblies taken (a)-(c) on the day the sample was prepared and (d)-(f) 2 days, (g)-(i) 7 weeks, and (j)-(l) 12 weeks after the sample was prepared.

Figure 3.8 shows DLS data for 7 mM quatsome-Si nanocrystal assemblies monitored over 8 weeks (for quatsome-Si nanocrystal assemblies, sizes measured by DLS were: week 0 z-ave 54.3 ± 0.4 nm, PDI 0.262 ± 0.006; week 8 z-ave 65.2 ± 0.2 nm, PDI 0.157 ± 0.008; for quatsomes alone sizes measured by DLS: week 0 z-ave 58.4 ± 0.7 nm, PDI 0.235 ± 0.008; week 8 z-ave 79.3 ± 0.3 nm, PDI 0.10 ± 0.02). There was no observable change in the mean size of the assemblies, but the size distribution became narrower, with the polydispersity index (PDI) decreasing from 0.262 ± 0.006 to 0.157 ± 0.008 over 8 weeks. A similar narrowing of the size distribution was also observed for quatsomes that were bath-sonicated without any nanocrystals (sample v), indicating that this narrowing of the size distribution is inherent to the quatsomes and not related to the presence of the nanocrystals. A similar peak narrowing phenomena was observed in vesicle assemblies formed by cholesterol and zwitterionic surfactants.[29,30] Over time the distribution narrows as the quatsomes return to a thermodynamically stable size range, as expected for stable vesicular assemblies.[31]

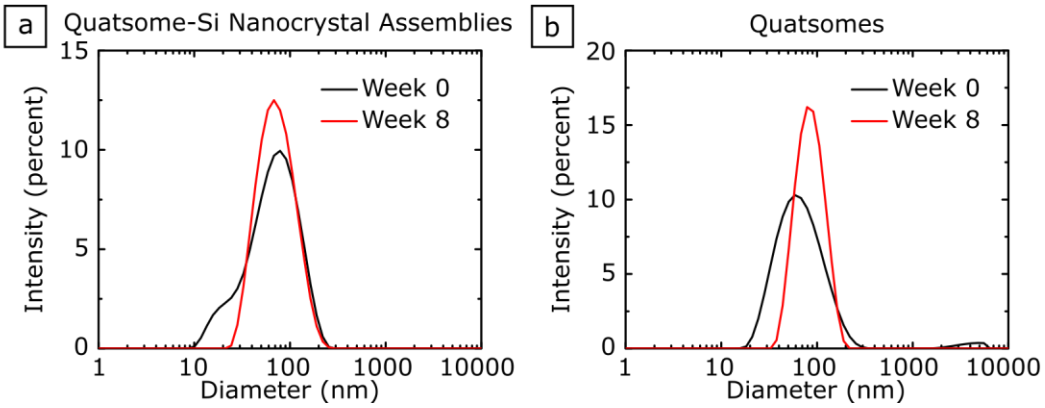

Figure 3.8 DLS data showing change in size distribution over 8 weeks for (a) 7mM quatsome-Si nanocrystal assemblies (sample (i) from stability trials) and (b) nanocrystal-free quatsomes (sample (v) from stability trials).

The stability of the quatsome-Si nanocrystal assemblies was also tested after dilution. As shown in Figure 3.6 sample ii, the assemblies were still stable after a 10X dilution, i.e., 0.7 mM quatsome-Si nanocrystals. This is an important result, as it indicates that there is no loss of integrity of the assemblies even when the CTAB concentration is below the CMC of free CTAB. Figure 3.9 shows cryoTEM images of the 0.7 mM quatsome-Si nanocrystal assemblies, which exhibit similar morphology as the 7 mM quatsome-nanocrystal assemblies. Indeed in many medical applications, dilution is required and it is important that the quatsome-nanocrystal assemblies retain their colloidal stability under these conditions. This is not the case when Si nanocrystals are dispersed only with CTAB. As shown in Figure 3.6 sample iii, CTAB could also be used to form stable dispersions of Si nanocrystals in aqueous media; however, with pure CTAB it is not possible to stabilize Si nanocrystals below the CMC. The CTAB-dispersed Si nanocrystals also tended to produce very polydisperse aggregates of nanocrystals, as observed by CryoTEM (Figure 3.10). Again, for medical applications, consistent size and concentration of load delivery is important, and thus the wide size distribution observed with CTAB micelles would not be ideal for those applications. This is discussed in more detail below.

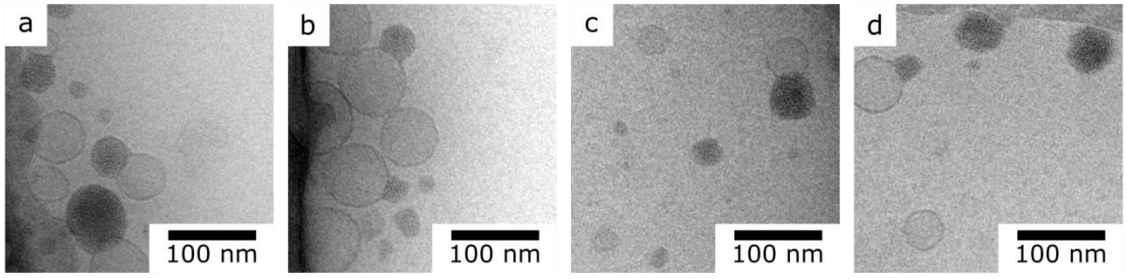

Figure 3.9 CryoTEM images of 0.7 mM quatsome-Si nanocrystal assemblies.

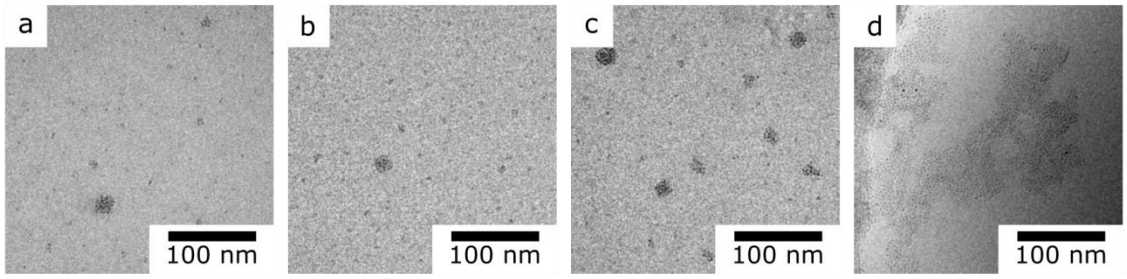

Figure 3.10 CryoTEM images of Si nanocrystals dispersed with 7 mM CTAB.

3.3.3 Comparison to Liposomal Structures

For comparison to liposomal vesicles, Si nanocrystals were combined with charge-neutral DOPC and anionic DOPG lipids—systems that have been used in the past to disperse dodecanethiol-capped gold nanocrystals.[13,17] The same bath sonication used to make the nanocrystal-quatsome assemblies was applied to Si nanocrystal incorporation into the DOPC and DOPG liposomes. Figure 3.11 shows cryoTEM images of these nanocrystal-liposome assemblies. The charge-neutral DOPC liposomes become multilamellar and mixed with large aggregates of Si nanocrystals (Figures 3.11a-3.11d). DLS of the DOPC liposomes showed that they had a z-average size of 58 ± 2 nm (PDI 0.230 ± 0.008) before sonication and grew to a z-average of 464 ± 28 nm (PDI 0.135 ± 0.143) after sonication in the presence of the Si nanocrystals. The vial containing the DOPC and Si nanocrystals also had a white precipitate of lipid at the bottom after sonication. The anionic DOPG liposomes retained their initial size, but no Si nanocrystals were observed to associate with the liposomes (Figures 3.11e-3.11h). The dispersion, however, was fluorescent and separate lipid-stabilized aggregates of Si nanocrystals were observed in the cryoTEM images. The fluorescence of these dispersions however was poor and the DOPG-dispersed nanocrystals no longer fluoresce after only 3 days.

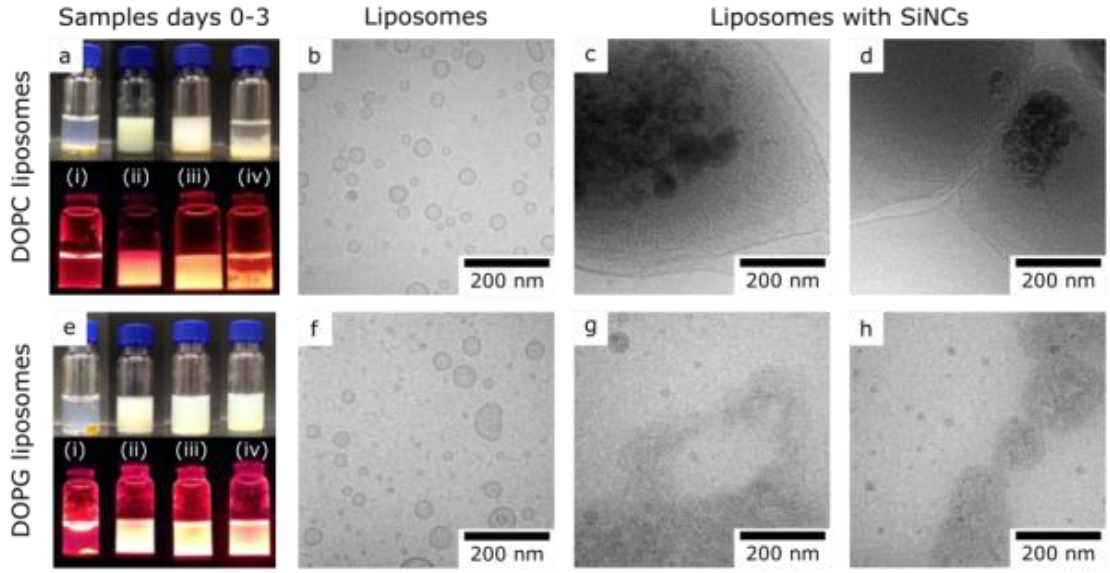

Figure 3.11 Results from using the quatsome-Si nanocrystal assembly process with DOPC (neutral) and DOPG (anionic) liposomes. Photographs of vials of (a) DOPC and (e) DOPG were taken under ambient light and on a 365 nm UV lamp (i) before bath sonication, (ii) immediately after sonication, (iii) after 1 day, and (iv) after 3 days. CryoTEM images of the liposomes before adding nanocrystals showed that the (b) DOPC and (f) DOPG liposomes formed small, unilamellar vesicles. CryoTEM images (c-d) of the DOPC liposomes after bath sonication showed that Si nanocrystals incorporated with the lipid, however formed large complexes. CryoTEM images (g-h) of the DOPG liposomes after bath sonication showed that the Si nanocrystals aggregated outside of empty liposomes with no incorporation into the liposomes.

3.3.4 Dispersion Stability of Diluted Assemblies

Medical diagnostic or theranostic applications that use fluorescent nanocrystals as contrast agents usually require dilution. Si nanocrystals were dispersed in CTAB micelles with CTAB at the same concentration as in the 7 mM quatsome-Si nanocrystal dispersions. Both dispersions were then dialyzed to test their stability against dilution. Figure 3.12 compares the stability of the dispersions. Both dispersions are initially fluorescent, but only the quatsome dispersion remains fluorescent after dialysis. The

CTAB surfactant is only weakly associated with the Si nanocrystals in the micelles, and repeated dilutions lead to loss of dispersibility of the nanocrystals, which precipitate out of the solution. CryoTEM images (Figures 3.12e-3.12f) of the quatsome assemblies show that the dialysis has little effect on the structure of the assemblies. This shows the benefit of the quatsome assemblies compared to CTAB micellar dispersions of the nanocrystals: while both maintain fluorescence for 12 weeks (Figure 3.6), only the quatsome assemblies are stable under dilution.

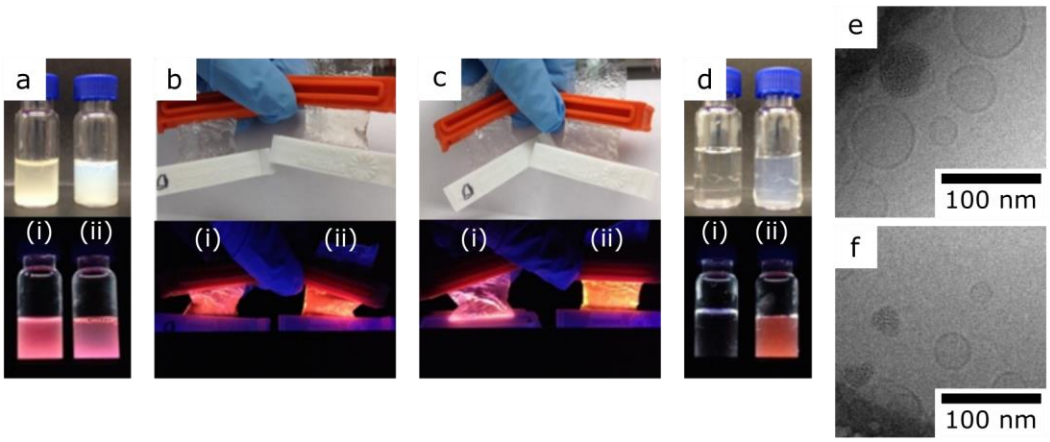

Figure 3.12 Dilution by dialysis of Si nanocrystals dispersed with (i) 7 mM CTAB and (ii) 7 mM quatsomes. (a) Photographs of vials containing (i) and (ii) prior to dialysis. Top row under ambient light and bottom row illuminated with a 254 nm ultraviolet lamp. (b-c) Photographs of the nanocrystal dispersions after (b) 3 and (c) 6 rounds of dialysis. (d) Photographs of dispersions removed from the dialysis tubing after 6 rounds of dialysis. (e-f) CryoTEM images of the 7 mM quatsome-Si nanocrystals after 6 rounds of dialysis.

3.3.5 Role of Chloroform in Si Nanocrystal-Quatsome Assemblies

Figure 3.13 shows the results of changing the amount of chloroform used in the assembly of Si nanocrystals with quatsomes. Using the standard preparation conditions of

750 μl of quatsomes combined with 20 μl of 6.75 mg/ml Si nanocrystals in chloroform resulted in stable, fluorescent dispersions (Figure 3.13, sample ii). If a larger volume of chloroform was used in the preparation, a white precipitate formed (Figure 3.13, samples iii-v). The larger volume of chloroform destabilized the quatsomes. Conversely, if a smaller volume of chloroform was added, not all of the nanocrystals incorporated into the quatsomes and there was visible nanocrystal precipitation (Figure 3.13, sample i). A small amount of chloroform enhances the uptake of dodecanethiol-capped Au nanocrystals into the lipid bilayer of DOPC liposomes.[17] A similar role for chloroform might be occurring here in the Si nanocrystal-quatsome assemblies.

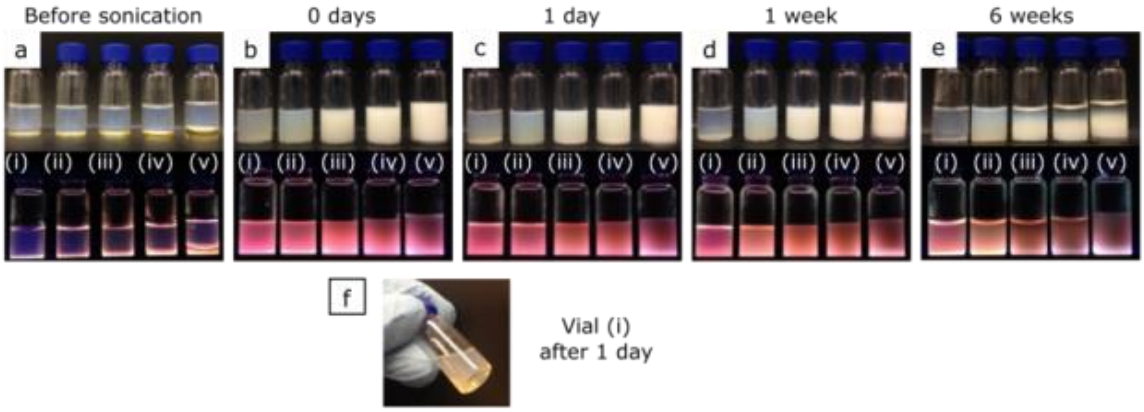

Figure 3.13 Results of changing chloroform volume to quatsome-Si nanocrystal assembly stability, under ambient light (top row) and on a 254 nm UV lamp (bottom row). In each sample 135 µg of Si nanocrystals was added, though in different concentrations, and thus volumes of chloroform. Samples from left to right are: (i) 10 µl of 13.5 mg/ml Si nanocrystals in chloroform, (ii) 20 µl of 6.75 mg/ml Si nanocrystals in chloroform (typical conditions), (iii) 40 µl of 3.375 mg/ml Si nanocrystals in chloroform, (iv) 80 µl of 1.6875 mg/ml Si nanocrystals in chloroform, (v) 200 µl of 0.675 mg/ml Si nanocrystals in chloroform. (f) Within one day after preparation (vial (i) had orange-brown precipitate consistent with Si nanocrystals.

3.3.6 Interaction between Dodecanethiol-Capped Gold Nanocrystals and Quatsomes

To characterize the interaction of quatsomes with hydrophobic metal nanoparticles, gold nanocrystals were prepared. The Au nanocrystals were capped with 1-dodecanethiol and could be dispersed in chloroform. Figure 3.14 shows TEM images of the gold nanocrystals used in the quatsome studies. The average Au nanocrystal size was 1.8±0.4 nm (n=150), as measured by TEM (Figure 3.14b). TGA conducted on the Au nanocrystals determined that the sample was 28.5% ligand by mass and 71.5% Au by mass, which corresponds to a ligand coverage density of 6.9 ligands/nm^2.

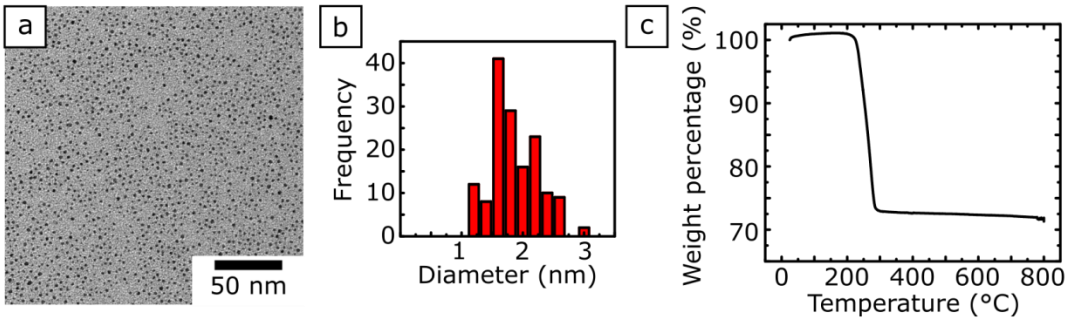

Figure 3.14 (a) TEM images of dodecanethiol-capped Au nanocrystals. (b) Histogram showing size distribution of Au nanocrystals. (c) TGA results for dodecanethiol-capped Au nanocrystals.

It was not possible to make assemblies of dodecanethiol-capped Au nanocrystals and quatsomes. Dispersions of 1.8 nm diameter dodecanethiol-capped gold nanocrystals in 20 µl of chloroform (3 mg/ml Au nanocrystals) were combined with 750 µl of 7mM quatsomes and bath sonicated for 5 min. Immediately after sonication, the dispersion became cloudy with a grey hue, indicating that the nanocrystals were initially dispersed by the presence of quatsomes (Figures 3.15a). The nanocrystals appeared as aggregates (Figures 3.15d-3.15e), similar to what was observed for Si nanocrystals. In contrast, Au nanocrystals of this size have previously been shown to readily incorporate into the lipid bilayer of phosphatidylcholine liposomes.[13,17] The dispersions of Au nanocrystals with quatsomes, however, were unstable and the color changed from grey to purple after a few days (Figure 3.15a). A plasmon peak at around 520 nm emerged in the absorbance spectra, indicating that nanocrystals had aggregated or coalesced.[17] CryoTEM of the purple solution at one week showed that the Au nanocrystal aggregates had decreased in size, with some larger coalesced particles observed both inside the aggregates (Figure 3.15f) and separate from empty quatsomes (Figure 3.15g). Additional cryoTEM (Figures 3.15h-3.15i) of the purple dispersion after several weeks showed that the nanocrystals had coalesced to form large particles (6.7 ±3.0 nm (n=150) as measured by TEM, Figure

3.15c) that were not associated with quatsomes. It is possible that—similar to Si nanocrystals dispersed with CTAB (Figure 3.10)—the coalesced gold nanoparticles remain dispersed due to an interaction with CTAB micelles. CTAB is commonly used in the synthesis of gold nanocrystals in various sizes and shapes,[32–34] and is known to disperse and interact with Au colloids.

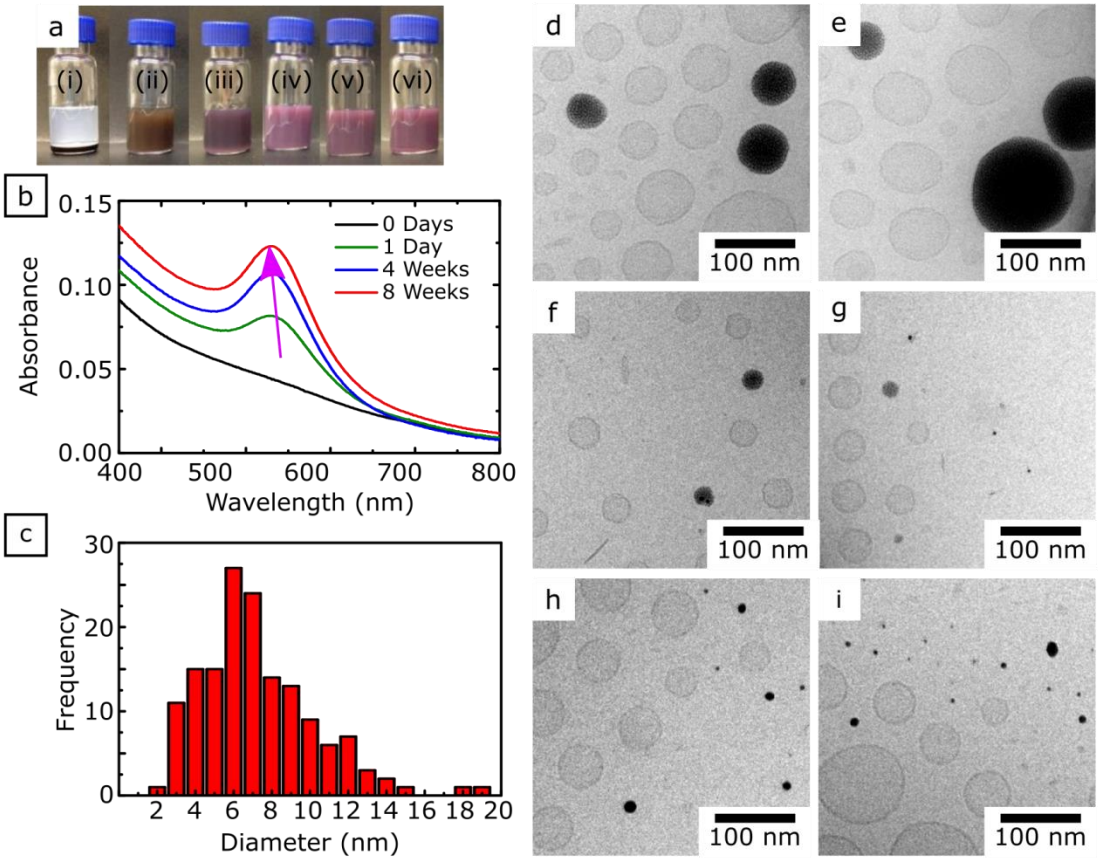

Figure 3.15 Results of incorporating 1.8 nm dodecanethiol capped Au nanocrystals into quatsomes through 5 minutes of bath sonication. (a) Photographs of vial with Au nanocrystals and quatsomes over 8 weeks showed a gradual change in color from brown-grey to purple (i) before sonication, (ii) immediately after sonication, (iii) after 1 day, (iv) after 2 weeks, (v) after 4 weeks, and (vi) after 8 weeks. (b) UV-Vis data for samples over time showed increase in plasmon peak intensity. (c) Size distribution of Au nanocrystals as measured by TEM. CryoTEM images of quatsome-AuNC dispersions at (d-e) 0 days, (f-g) 1 week, and (h-i) several weeks after preparation.

3.3.7 Mechanism of Interaction between Nanocrystals and Quatsomes

The difference in experimentally observed interactions between the quatsomes and the Si and Au nanocrystals may result from the qualitatively different structure of the

ligand shells on the nanocrystals. Figures 3.16b-3.16c illustrate a proposed mechanism for the interactions between nanocrystals and quatsomes. Both Au and Si nanocrystals aggregate in water due to their hydrophobic coating. As the nanocrystal aggregates or clusters form, they interact with other clusters of particles and with the quatsomes. In the case of Au nanocrystals (Figure 3.16b), the less dense capping ligands (6.9 ligands/nm^2) can be repulsed from quatsomes due to entropic repulsive interactions from the "hairy" ligand layer, which play a substantial role in self-assembly processes of nanoparticles.[35] As a result, the Au particles aggregate into large clusters, without incorporation into the quatsomes. These Au aggregates may then become smaller as they stabilize in the aqueous solution, perhaps with a CTAB coating, which can contribute to the observed particle coalescence.[32,33] In the case of Si particles (Figure 3.16c), the denser capping ligand coverage (9.9 ligands/nm^2) may result in an interaction reminiscent of that between vesicles and hydrophobic solid surfaces. In this case, the layers of the quatsome vesicles spread over the surface of the clusters of Si particles. This spreading process requires first the breaking of vesicles and the input of energy. Vesicles are dynamic structures that can be reformed or reduced in size with the addition of sonication energy.[36,37] It was observed that when chol-CTAB quatsomes with Si nanocrystals were sonicated for 15 or 30 min, they were smaller than those sonicated for 1 minute or 5 minutes (Figure 3.5). Thus, it can be hypothesized that when quatsomes are sonicated they are broken down through a redistribution of membrane molecules. When the sonication is performed in the presence of hydrophobic Si nanocrystals with dense capping ligand coverage, this redistribution would allow small aggregates of Si nanocrystals to become stabilized by the hydrophobic part of cholesterol-CTAB monolayers (Figure 3.16c). The resulting self-assembled structure (clusters of Si particles covered by a quatsome monolayer) is now stable in water and acquires the radius

corresponding to the spontaneous curvature of the quatsome building blocks (the bimolecular entities made by the association between CTAB and cholesterol).[21] The result of this process is the coexistence between quatsome vesicles and these self-assembled clusters of Si covered by CTAB and cholesterol with a diameter similar to that of quatsome vesicles. Further, the lack of coalesced Si nanocrystals was likely due to the stable Si-C surface bonds formed upon passivating the surfaces with 1-octene, which prevents the oxidation and degradation of the Si nanocrystals.[38]

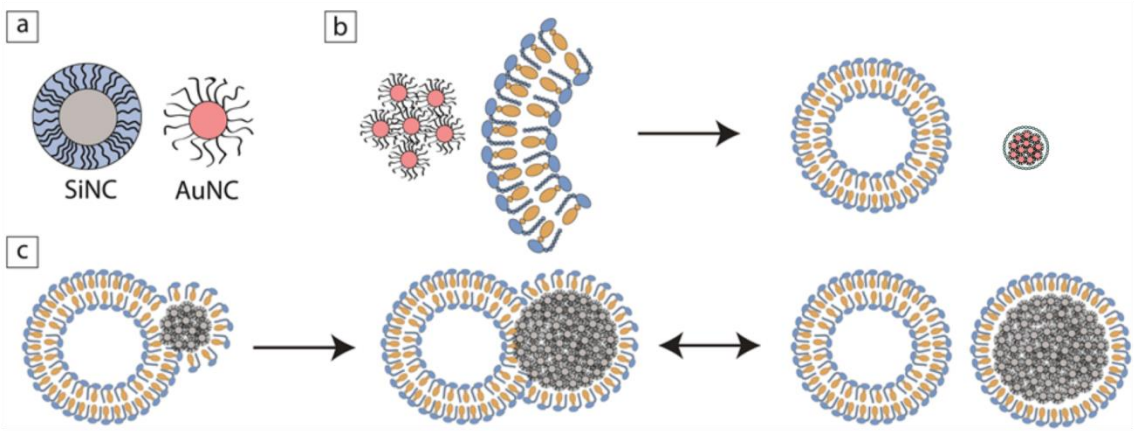

Figure 3.16 Proposed mechanism for the formation of quatsome-nanocrystal assemblies. In the diagram, CTAB is the blue headed structure, cholesterol is the yellow structure. (a) Scheme of the ligand densities on the Si nanocrystals (SiNC) and Au nanocrystals (AuNC). (b) Illustration of the interactions of Au nanocrystals and quatsomes and CTAB molecules. (c) Scheme of the interactions of Si nanocrystals and quatsomes, and the formation of the stable Si nanocrystals covered with a monolayer of chol-CTAB pairs.

Although the Si nanocrystals are aggregated in quatsomes, it is still apparent that the synergy between cholesterol and CTAB, observed before in plain quatsomes,[21] leads to the stable interaction between quatsomes and Si nanocrystals. When CTAB micelles were sonicated with Si nanocrystals, the Si nanocrystals appeared as either very small or

very large, irregularly shaped clusters (Figure 3.10). Additionally, cryoTEM images of Si nanocrystals incorporated into quatsomes in Figure 3.3 show that the Si nanocrystal aggregates are approximately the same size as quatsomes without any Si nanocrystals. Since the size of quatsomes is influenced by the interaction between cholesterol and CTAB, the size of Si nanocrystals aggregated suggests that they are associated with the same chol-CTAB units. Further, as shown in the dilution experiment in Figure 3.12, only Si nanocrystals dispersed in quatsomes remain stable after several rounds of dilution, while Si nanocrystals dispersed in CTAB micelles result in precipitation of the Si nanocrystals after multiple dilutions. Thus, it is specifically the quatsomes where cholesterol and CTAB interact as bimolecular building blocks that contribute to stabilizing the Si nanocrystals.

3.4 CONCLUSION

A method to disperse fluorescent Si nanocrystals in aqueous media with long-term stability was developed, utilizing chol-CTAB quatsomes, which are into non-liposomal vesicular structures. The stable Si nanocrystal aqueous dispersions can be made with five minutes of bath sonication. The nanocrystals remain dispersed in water and maintain the fluorescence properties of the Si nanocrystals for several weeks and after dilution with additional water. The experimental data show that the association of Si nanocrystals with chol-CTAB quatsomes is unique to the nanocrystal type (as compared to Au nanocrystals) as well as the method of preparation. Quatsomes, which have been shown to have extremely long term stability of at least three years in aqueous solutions,[21] provide a vehicle for the dispersion of hydrophobic Si nanocrystals into *in vitro* or *in vivo* environments, even under dilute conditions. The biocompatibility of both quatsomes and

near infrared emitting Si nanocrystals make these structures excellent candidates for biomedical imaging applications. Furthermore, quatsomes have been shown to enhance protein activity and to protect proteins against premature degradation in topical pharmaceutical formulations, as well as to treat biofilms.[25,26] Therefore, the incorporation of both biomolecules and Si nanocrystals into quatsome structures offers the possibility to explore the behavior of these systems in biological environments and their use for theranostics.

3.5 REFERENCES

(1) Dubertret, B.; Skourides, P.; Norris, D. J.; Noireaux, V.; Brivanlou, A. H.; Libchaber, A. In Vivo Imaging of Quantum Dots Encapsulated in Phospholipid Micelles. *Science* **2002**, *298*, 1759–1762.

(2) Michalet, X.; Pinaud, F. F.; Bentolila, L. A.; Tsay, J. M.; Doose, S.; Li, J. J.; Sundaresan, G.; Wu, A. M.; Gambhir, S. S.; Weiss, S. Quantum Dots for Live Cells, in Vivo Imaging, and Diagnostics. *Science* **2005**, *307*, 538–544.

(3) O'Farrell, N.; Houlton, A.; Horrocks, B. R. Silicon Nanoparticles: Applications in Cell Biology and Medicine. *Int. J. Nanomedicine* **2006**, *1*, 451–472.

(4) Panthani, M. G.; Khan, T. A.; Reid, D. K.; Hellebusch, D. J.; Rasch, M. R.; Maynard, J. A.; Korgel, B. A. In Vivo Whole Animal Fluorescence Imaging of a Microparticle-Based Oral Vaccine Containing (CuInSexS2–x)/ZnS Core/Shell Quantum Dots. *Nano Lett*. **2013**, *13*, 4294–4298.

(5) Kovalenko, M. V.; Manna, L.; Cabot, A.; Hens, Z.; Talapin, D. V.; Kagan, C. R.; Klimov, V. I.; Rogach, A. L.; Reiss, P.; Milliron, D. J.; Guyot-Sionnest, P.; Konstantatos, G.; Park, W. J.; Hyeon, T.; Korgel, B. A.; Murray, C. B.; Heiss, W. Prospects of Nanoscience with Nanocrystals. *ACS Nano* **2015**, *9*, 1012–1057.

(6) Park, J.-H.; Gu, L.; Maltzahn, G. von; Ruoslahti, E.; Bhatia, S. N.; Sailor, M. J. Biodegradable Luminescent Porous Silicon Nanoparticles for in Vivo Applications. *Nat. Mater*. **2009**, *8*, 331–336.

(7) Henderson, E. J.; Shuhendler, A. J.; Prasad, P.; Baumann, V.; Maier-Flaig, F.; Faulkner, D. O.; Lemmer, U.; Wu, X. Y.; Ozin, G. A. Colloidally Stable Silicon Nanocrystals with Near-Infrared Photoluminescence for Biological Fluorescence Imaging. *Small* **2011**, *7*, 2507–2516.

(8) Hessel, C. M.; Reid, D.; Panthani, M. G.; Rasch, M. R.; Goodfellow, B. W.; Wei, J.; Fujii, H.; Akhavan, V.; Korgel, B. A. Synthesis of Ligand-Stabilized Silicon Nanocrystals with Size-Dependent Photoluminescence Spanning Visible to Near-Infrared Wavelengths. *Chem. Mater*. **2012**, *24*, 393–401.

(9) Yu, Y.; Hessel, C. M.; Bogart, T. D.; Panthani, M. G.; Rasch, M. R.; Korgel, B. A. Room Temperature Hydrosilylation of Silicon Nanocrystals with Bifunctional Terminal Alkenes. *Langmuir* **2013**, *29*, 1533–1540.

(10) Erogbogbo, F.; Yong, K.-T.; Roy, I.; Xu, G.; Prasad, P. N.; Swihart, M. T. Biocompatible Luminescent Silicon Quantum Dots for Imaging of Cancer Cells. *ACS Nano* **2008**, *2*, 873–878.

(11) Jang, H.; Pell, L. E.; Korgel, B. A.; English, D. S. Photoluminescence Quenching of Silicon Nanoparticles in Phospholipid Vesicle Bilayers. *J. Photochem. Photobiol. Chem*. **2003**, *158*, 111–117.

(12) Paasonen, L.; Laaksonen, T.; Johans, C.; Yliperttula, M.; Kontturi, K.; Urtti, A. Gold Nanoparticles Enable Selective Light-Induced Contents Release from Liposomes. *J. Controlled Release* **2007**, *122*, 86–93.

(13) Rasch, M. R.; Rossinyol, E.; Hueso, J. L.; Goodfellow, B. W.; Arbiol, J.; Korgel, B. A. Hydrophobic Gold Nanoparticle Self-Assembly with Phosphatidylcholine Lipid: Membrane-Loaded and Janus Vesicles. *Nano Lett*. **2010**, *10*, 3733–3739.

(14) Hessel, C. M.; Rasch, M. R.; Hueso, J. L.; Goodfellow, B. W.; Akhavan, V. A.; Puvanakrishnan, P.; Tunnel, J. W.; Korgel, B. A. Alkyl Passivation and Amphiphilic Polymer Coating of Silicon Nanocrystals for Diagnostic Imaging. *Small* **2010**, *6*, 2026–2034.

(15) Erogbogbo, F.; Yong, K.-T.; Roy, I.; Hu, R.; Law, W.-C.; Zhao, W.; Ding, H.; Wu, F.; Kumar, R.; Swihart, M. T.; Prasad, P. N. In Vivo Targeted Cancer Imaging, Sentinel Lymph Node Mapping and Multi-Channel Imaging with Biocompatible Silicon Nanocrystals. *ACS Nano* **2010**, *5*, 413–423.

(16) Al-Jamal, W. T.; Kostarelos, K. Liposomes: From a Clinically Established Drug Delivery System to a Nanoparticle Platform for Theranostic Nanomedicine. *Acc. Chem. Res*. **2011**, *44*, 1094–1104.

(17) Rasch, M. R.; Yu, Y.; Bosoy, C.; Goodfellow, B. W.; Korgel, B. A. Chloroform-Enhanced Incorporation of Hydrophobic Gold Nanocrystals into Dioleoylphosphatidylcholine (DOPC) Vesicle Membranes. *Langmuir* **2012**, *28*, 12971–12981.

(18) Sawant, R. M.; Hurley, J. P.; Salmaso, S.; Kale, A.; Tolcheva, E.; Levchenko, T. S.; Torchilin, V. P. "SMART" Drug Delivery Systems: Double-Targeted PH-Responsive Pharmaceutical Nanocarriers. *Bioconjug. Chem*. **2006**, *17*, 943–949.

(19) European Medicines Agency - Multidisciplinary: nanomedicines http://www.ema.europa.eu/ema/index.jsp?curl=pages/regulation/general/general_content_000564.jsp&mid=WC0b01ac05806403e0 (accessed Oct 24, 2017).

(20) U.S. Department of Health and Human Services, Food and Drug Administration, Center for Drug Evaluation and Research (CDER). *Liposome Drug Products: Guidance for Industry, Rev 1*; 2015; pp. 1–13.

(21) Ferrer-Tasies, L.; Moreno-Calvo, E.; Cano-Sarabia, M.; Aguilella-Arzo, M.; Angelova, A.; Lesieur, S.; Ricart, S.; Faraudo, J.; Ventosa, N.; Veciana, J. Quatsomes: Vesicles Formed by Self-Assembly of Sterols and Quaternary Ammonium Surfactants. *Langmuir* **2013**, *29*, 6519–6528.

(22) Elizondo, E.; Larsen, J.; Hatzakis, N. S.; Cabrera, I.; Bjørnholm, T.; Veciana, J.; Stamou, D.; Ventosa, N. Influence of the Preparation Route on the Supramolecular Organization of Lipids in a Vesicular System. *J. Am. Chem. Soc*. **2012**, *134*, 1918–1921.

(23) Cabrera, I.; Elizondo, E.; Esteban, O.; Corchero, J. L.; Melgarejo, M.; Pulido, D.; Córdoba, A.; Moreno, E.; Unzueta, U.; Vazquez, E.; Abasolo, I.; Schwartz, S.; Villaverde, A.; Albericio, F.; Royo, M.; Garcia-Parajo, M. F.; Ventosa, N.; Veciana, J. Multifunctional Nanovesicle-Bioactive Conjugates Prepared by a One-Step Scalable Method Using CO2-Expanded Solvents. *Nano Lett*. **2013**, *13*, 3766–3774.

(24) Grimaldi, N.; Andrade, F.; Segovia, N.; Ferrer-Tasies, L.; Sala, S.; Veciana, J.; Ventosa, N. Lipid-Based Nanovesicles for Nanomedicine. *Chem. Soc. Rev*. **2016**, *45*, 6520–6545.

(25) Ventosa, N.; Cabrera, I.; Veciana, J.; Santana, H.; Martinez, E.; Berlanga, J. A. Vesicles Comprising Epidermal Growth Factor and Compositions That Contain Them. CU2012-0112, 2012.

(26) Thomas, N.; Dong, D.; Richter, K.; Ramezanpour, M.; Vreugde, S.; Thierry, B.; Wormald, P.-J.; Prestidge, C. A. Quatsomes for the Treatment of Staphylococcus Aureus Biofilm. *J. Mater. Chem. B* **2015**, *3*, 2770–2777.

(27) Liu, X.; Ardizzone, A.; Sui, B.; Anzola, M.; Ventosa, N.; Liu, T.; Veciana, J.; Belfield, K. D. Fluorenyl-Loaded Quatsome Nanostructured Fluorescent Probes. *ACS Omega* **2017**, *2*, 4112–4122.

(28) Casey, K. G.; Quitevis, E. L. Effect of Solvent Polarity on Nonradiative Processes in Xanthene Dyes: Rhodamine B in Normal Alcohols. *J. Phys. Chem*. **1988**, *92*, 6590–6594.

(29) Marques, E. F. Size and Stability of Catanionic Vesicles: Effects of Formation Path, Sonication, and Aging. *Langmuir* **2000**, *16*, 4798–4807.

(30) Alenaizi, R.; Radiman, S.; Abdul Rahman, I.; Mohamed, F. Zwitterionic Betaine-Cholesterol System: Effects of Sonication Duration and Aging on Vesicles Stability. *Colloids Surf. Physicochem. Eng. Asp*. **2015**, *482*, 662–669.

(31) Antonietti, M.; Förster, S. Vesicles and Liposomes: A Self-Assembly Principle Beyond Lipids. *Adv. Mater*. **2003**, *15*, 1323–1333.

(32) Gao, J.; Bender, C. M.; Murphy, C. J. Dependence of the Gold Nanorod Aspect Ratio on the Nature of the Directing Surfactant in Aqueous Solution. *Langmuir* **2003**, *19*, 9065–9070.

(33) Sau, T. K.; Murphy, C. J. Room Temperature, High-Yield Synthesis of Multiple Shapes of Gold Nanoparticles in Aqueous Solution. *J. Am. Chem. Soc*. **2004**, *126*, 8648–8649.

(34) Smith, D. K.; Korgel, B. A. The Importance of the CTAB Surfactant on the Colloidal Seed-Mediated Synthesis of Gold Nanorods. *Langmuir* **2008**, *24*, 644–649.

(35) Sánchez-Iglesias, A.; Grzelczak, M.; Altantzis, T.; Goris, B.; Pérez-Juste, J.; Bals, S.; Van Tendeloo, G.; Donaldson, S. H.; Chmelka, B. F.; Israelachvili, J. N.; Liz-Marzan, L. M. Hydrophobic Interactions Modulate Self-Assembly of Nanoparticles. *ACS Nano* **2012**, *6*, 11059–11065.

(36) Marsh, D. *Handbook of Lipid Bilayers*, Second Edition; CRC Press, 2013.

(37) Szoka, F.; Papahadjopoulos, D. Comparative Properties and Methods of Preparation of Lipid Vesicles (Liposomes). *Annu. Rev. Biophys. Bioeng*. **1980**, *9*, 467–508.

(38) Dohnalová, K.; Gregorkiewicz, T.; Kůsová, K. Silicon Quantum Dots: Surface Matters. *J. Phys. Condens. Matter* **2014**, *26*, 173201.

Chapter 4: Stability of Hydrophilic Ligand Passivated Silicon Nanocrystals in Biological Solutions and Uptake by Cells

4.1 INTRODUCTION

Photoluminescent quantum dots have been investigated for use in medical imaging applications due to their small diameters, photostability, size-tunable emission, and well defined surface chemistries that can allow bioconjugation to various targeting molecules.[1–3] Si based quantum dots have been researched as biocompatible alternatives to heavy metal quantum dots as they offer size-dependent photoluminescence (PL) in the biological optical window.[4–7] While nanocrystals can be dispersed in aqueous solutions using polymers or surfactants, these assemblies are typically much larger than just the nanocrystals, and so there is interest in developing nanocrystals that can be directly dispersed into water.[1,3] Si nanocrystals intended to be used for *in vivo* or *in vitro* applications must, however, also demonstrate photoluminescent stability in aqueous biological solutions, though this can be challenging due to the tendency for Si to oxidize.

Recently, a method to passivate 2.8 nm diameter Si nanocrystals with 10-undecenoic acid was demonstrated.[8] Passivating Si nanocrystals slows surface oxidation, and using ligands with terminal carboxylic acid groups enables the particles to disperse in polar solvents such as ethanol or water. In an aqueous environment, the electric double layer repulsions imparted by a nanoparticle's surface charge must exceed aggregating forces for the particles to remain colloidally dispersed.[9–11] For carboxylic acid terminated nanoparticles the pH must be sufficiently high to deprotonate a large enough fraction of the ligands such that the surface charge can overcome aggregating forces. However, at high pH Si nanocrystal surfaces are subject to increased rates of oxidation from hydroxide ions, which can lead to decrease in Si core size as well as loss of PL.[6,12] Thus, careful control of solvent pH and ionic content is required for Si nanocrystals to remain

photoluminescent and well dispersed in aqueous solutions. Biological solutions encountered in *in vivo* or *in vitro* environments contain a high concentration of biomolecules with a wide variety of ions,[13] and thus it is important to characterize the stability of Si nanocrystal PL in response to biomolecules to understand how many hours, days, or weeks the particles can be used as fluorescent biological probes.

The interactions between nanoparticles and cells have been found to vary significantly based on particle composition, surface curvature, net charge, and ligand density.[13–19] The biomolecules in biological solutions also impact how nanoparticles can interact with cells, since typically a layer of molecules, called a protein corona, is adsorbed to the surfaces of charged particles.[13,17,14]

Here, the photoluminescence stability of 2.8 nm diameter Si nanocrystals capped with 10-undecenoic acid transferred into aqueous solutions was studied and showed that depending on solution pH and content, PL emission was stable for at least one week. Further, we evaluated the uptake of the Si nanocrystals by macrophage cells. The nanocrystals were taken up by endocytosis and did not result in any cell toxicity or immune response, suggesting that the particles can be useful as bioimaging probes.

4.2 EXPERIMENTAL METHODS

4.2.1 Materials

Hydrochloric acid (HCl), hexanes, chloroform, toluene, sodium chloride (NaCl), bovine serum albumin (BSA), acetic acid, amino acids, vitamins, and inorganic salts were purchased from Fisher. 4-(2-hydroxyethyl)-1-piperazineethanesulfonic acid) (HEPES), sodium hydroxide (NaOH), hydrofluoric acid (HF), ethanol (EtOH), Dulbecco's Phosphate Buffered Saline (DPBS), 2-[(2-Hydroxy-1,1-bis(hydroxymethyl)ethyl)amino]

ethanesulfonic acid (TES), 2-Amino-2-(hydroxymethyl)-1,3-propanediol (TRIS), 3-(N-Morpholino)propanesulfonic acid (MOPS), potassium phosphate monobasic, sodium acetate trihydrate, citric acid monohydrate, trisodium citrate dehydrate, Si standard for ICP, amino acids, vitamins, inorganic salts, Cytochalasin D (CytD), and Nocodazole (Noco) were purchased from Sigma. Hydrogen silsesquioxane (HSQ) was purchased from Dow Corning. 4',6-diamidino-2-phenylindole (DAPI)-Fluoromount-G was purchased from SouthernBiotech. Sodium pyruvate (100 mM) and Dulbecco's Modified Eagle Medium (DMEM, containing 4.0 mM l-glutamine and 4500 mg/L glucose, no sodium pyruvate) were purchased from Hyclone. Phosphate buffered saline (PBS) was purchased from Gibco. Lysozyme was purchased from MP Biomedicals. Fetal bovine serum (FBS), penicillin/streptomycin, Modified Eagle Medium (MEM) non-essential amino acids (100x), and MEM vitamin solution (100x) were purchased from Life Technologies. Non-essential amino acids were purchased from Lonza. Deionized water was obtained from a Millipore Synergy Ultrapure water system operating at 18.2 MΩ/cm.

4.2.2 Si Nanocrystal Synthesis

Si nanocrystals were synthesize following a previously reported procedure.[8] Solvent was removed from hydrogen silsesquioxane, and the resulting material was placed in a quartz boat in a tube furnace heat to 1100 °C for 1 hour under forming gas flow. The brown material was then downsized by first grinding with a mortar and pestle and then shaking with borosilicate beads in a wrist action shaker for 9 hours. For a typical reaction, 0.3 g of the Si powder was stirred with 1 ml HCl and 10 ml HF for 4 hours in the dark. The acids were washed away by precipitating the material and redispersing in ethanol, and this rinse was repeated three times. Finally, the nanocrystals were dispersed

in chloroform, once again precipitated, and then redispersed in 15 ml of 10-undecenoic acid. The suspension was transferred to the three neck flask on a Schlenk line and three freeze-pump-thaw cycles were performed to remove oxygen. The dispersion was then stirred overnight at 35 °C. The next day, the dispersion was transferred to a vial and 10 ml of EtOH was added. The vial was capped with a septum, and left to sit on the benchtop for 1 week, during which time the dispersion turned from cloudy to clear as the hydrosilylation reaction yield increased. The dispersion was washed by first precipitating and removing any unpassivated nanocrystals. Then, 5 ml of hexanes was added until the dispersion became turbid, and the sample was centrifuged. The precipitate (containing Si nanocrystals) was redispersed in 5 ml of EtOH, and 3 more hexane washes were performed. The final dispersion of 10-undecenoic acid capped Si nanocrystals was stored in ethanol until use.

4.2.3 Transfer of Si Nanocrystals into Water and Incubation with Biological Solutions

2 ml of Si nanocrystals in ethanol (5 mg/ml) was added to a vial with 8 ml ethanol and 5 ml pH 7.4 water (adjusted with NaOH). After mixing the Si nanocrystals into the ethanol-water mixture, they were transferred into an Amicon 15 30 kDa filter (Millipore) and centrifuged at 1100 g for 7 minutes. At this filter size, Si nanocrystals remain above the filter, and the ethanol-water mixture that passes through can be discarded. 5 more ml of water were then added to the Si nanocrystal solution and the centrifugation process was repeat. This process was repeat a total of 6 times until the Si nanocrystal were in water at a concentration of approximately 2 mg/ml (unless otherwise noted).

For each of the tested biological solution, samples were prepared by adding 0.3 mg of Si nanocrystals in water to 15 ml of the test solution. The samples were incubated

either at room temperature for 7 days or at 37 °C for 1 day. Samples were prepared in triplicate and the results were averaged. The buffers were prepared as follows: DPBS was diluted to a concentration of 10% in water. TES, TRIS, and MOPS buffers were prepared at 0.1 M and adjusted to pH 7 with NaOH or HCl. Phosphate buffer was prepared using 0.1 M potassium phosphate monobasic and adjusted to pH 7 with NaOH. Acetate buffer was prepare with 0.1 M sodium acetate trihydrate, and adjusted to pH 6 with acetic acid. Citrate buffer was prepared at 0.1M with citric acid monohydrate and trisodium citrate dehydrate at pH 6.

All cell culture medium biological solutions were prepared in a biosafety cabinet to reduce the chance of contamination. Cell culture medium was prepared with: 100 ml DMEM, 10 ml FBS, 1 ml penicillin/streptomycin, 1ml sodium pyruvate, and 1 ml non-essential amino acids. For individual testing components: DMEM was not diluted, while FBS, sodium pyruvate, penicillin/streptomycin, and non-essential amino acids were each diluted in water to the appropriate concentration for use in cell culture. Essential amino acids mix was composed of all proteins listed in the DMEM formulation. MEM vitamin mix was dilute to 4% in water to match the DMEM formulation. Inorganic salts mix was prepared by mixing all inorganic salts at the concentrations listed in the DMEM formulation. Each individual component (for example, each amino acid or vitamin) was prepared according to the DMEM formulation concentrations.[20]

4.2.4 Si Nanocrystal Characterization

Photoluminescence spectra were acquired for samples using glass or polymethacrylate cuvettes. Absorbance spectra were captured on a Varian Cary 50 Bio ultraviolet-visible spectrophotometer; a cuvette with water was background subtracted

from each spectrum. Photoluminescence emission (PL) spectra were captured for samples excited at 320 nm on a Varian Cary Eclipse fluorescence spectrometer. PL peak emission was estimated by integrating the PL spectra and calculating the average emission wavelength between 550-800 nm. The Si nanocrystal quantum yields were calculated relative to Rhodamine B (49% quantum yield in ethanol).[23]

Transmission electron microscopy was used for Si nanocrystal samples dropcast on 200 mesh carbon-coated copper grids (Electron Microscopy Sciences). Images were digitally acquired on an FEI Tecnai Biotwin TEM operated at 80 V accelerating voltage. Si nanocrystal size was estimated by measuring 100 particles.

A Mettler Toledo TGA/DSC 1 was used to capture thermal gravimetric analysis (TGA) data. Samples of Si nanocrystals were dried into 70 µl alumina crucibles. Samples were ramped from 25 °C to 800 °C at a rate of 10 °C per minute, and then held at 800 °C for an additional 30 minutes. Experiments were run under 50 ml per minute air flow, such that over time all ligands are removed from the surface and Si is converted to SiO_2.

A Thermo Mattson Infinity Gold Fourier Transform Infrared (FTIR) spectrometer was used to capture attenuated total reflectance (ATR) FTIR spectra. Si nanocrystal samples were drop cast onto a Spectra-Tech Thermal ARK ATR module, then purged with N_2 for 20 minutes to remove residual CO_2. Measurements were taken with 512 scans at a resolution of 4 cm^{-1}, and background (ATR crystal with no sample) was subtracted.

X-ray diffraction data was captured with a Rigaku R-Axis Spider diffractometer using Cu Kα radiation (λ=0.15418 nm) and an image plate detector operated at 40 kV and 40 mA. Si nanocrystals were dried out of solution and then scraped with a needle. The sample was then loaded onto a nylon loop using mineral oil. Two-dimensional diffraction data were collected over 20 minutes while rotating the sample 10° per second. Data was

radially integrated using 2DP Spider software (version 1.0, Rigaku Americas Corp.), and background was removed (background was collected as mineral oil on a nylon loop).

Inductively coupled plasma optical emission spectroscopy (ICP-OES) was conducted on a Varian 710 plasma emission spectrophotometer. Known concentrations of Si nanocrystals in various solutions were dilute 1:1 into 70 wt% nitric acid for digestion for 1 hour. The solutions were then dilute 1:10 into 3% nitric acid for analysis. Si standards were prepared at 6 known concentrations from 0 – 10.0 mg/L for calibration. Three Si analytical lines were measured for each sample and averaged.

X-ray photoelectron spectroscopy (XPS) was performed using a Kratos Axis Ultra X-ray photoelectron spectrometer, utilizing a monochromatic Al Kα X-ray source (hν=1486.5 eV at 150 W, 12 mA and 10 kV), hybrid optics (employing a magnetic and electrostatic lens simultaneously), and a multi-channel plate coupled to a hemispherical photoelectron kinetic analyzer. The instrument work function is calibrated to give a binding energy (BE) of 368.3 eV for the Ag 3d5/2 line for metallic silver. Spectra were charge-corrected by shifting the BE of the carbon 1s (graphite-like carbon) to 284.8 eV. To prepare a sample for XPS, nanocrystals were drop cast onto indium tin oxide coated glass slides, and secured on the experimental tray using double-sided Cu tape. High-resolution spectra were collected with 20 eV pass energy at 0.1 eV intervals and 2000 ms integration time. Casa XPS analysis software (Version 2.3.18 PR 1.0) was used for peak deconvolution.

A Zetasizer Nano ZS (Malvern Instruments) was used to acquire dynamic light scattering (DLS) and zeta potential data. DLS data was acquired for samples in 40 µl disposable cuvettes using an angle of 173°. Sizes were calculated by fitting each measurement to the correlation coefficient data.[24] Zeta potential data was acquired using

folded capillary zeta cells. All measurements were taken in triplicate at 25 °C. Zetasizer software (Malvern Instruments) was used to obtain the correlation data and zeta potential.

4.2.5 Si Nanocrystal Incubation with Cells and Characterization

J774A.1 mouse macrophage cells (ATCC) were grown in DMEM supplemented with 10% fetal bovine serum, 100 U/ml penicillin-streptomycin, and 1 mM sodium pyruvate. CHO-K1 hamster ovary cells (ATCC) were grown in the same medium but without the added sodium pyruvate. Cells were maintained in a humidified 37 °C incubator with an atmosphere of 5% CO_2, unless otherwise indicated.

For confocal microscopy, cells were seeded on glass coverslips in 6-well plates at a density of $2x10^4/cm^2$ three days before the assay. Culture medium was replaced with Si nanocrystals diluted 5-fold in growth medium (0.4 ml of 2 mg/ml Si nanocrystals in water with 1.6 ml of cell culture medium), and incubated for 3 hours at 37 °C, unless otherwise indicated. The coverslips were then washed 4-5 times with PBS to remove Si nanocrystals not taken up by the cells. Next, the cells were fixed with 4% formaldehyde for 10 min at 37 ˚C. The coverslips were washed three times with PBS and mounted on glass slides with DAPI Fluoromount-G. A Zeiss LSM 710 confocal microscope was used to obtain confocal images of cells stained with DAPI (excited at 405 nm, emission filtered to 417-566 nm) and Si nanocrystals (excited at 405 nm, emission filtered to 670-740 nm). Zeiss confocal software was used to overlay the captured images.

For flow cytometry, cells were seeded in 6-well or 24-well plates at a density of $2x10^4/cm^2$ three days before the assay. Culture medium was replaced with 2 ml (for the 6-well plates) or 0.5 ml (for the 24-well plates) containing Si nanocrystals diluted 5-fold in growth medium. Experiments comparing the dilution of Si nanocrystals into cell

culture medium confirmed that the 5-fold dilution did not impact cell viability (data not shown). Cells were removed using ~250 µL 0.25% trypsin-EDTA solution (Sigma T4049) which was quenched with 250 µL of culture media. Cells were washed 3 times by spinning at 250 g for 5 min and resuspended in 1mL ice cold wash buffer (1% FBS in PBS). After the final wash, cells were resuspended in 0.5ml wash buffer and kept on ice. A BD Biosciences LSR Fortessa flow cytometer was used to measure emission from cells incubated with Si nanocrystals. Samples were excited using the violet laser (405 nm) and emission was captured using a 670 nm long pass filter for 10,000 live cells. FlowJo software was used for data analysis.

To test the effect of Si nanocrystals on cell viability, two assays were employed: the lactate dehydrogenase (LDH) assay using CytoTox 96® Non-Radioactive Cytotoxicity Assay kit and MTS assay using CellTiter 96® AQueous Non-Radioactive Cell Proliferation Assay kit (Promega). The LDH assay measures the lactate dehydrogenase enzyme leaked into the culture supernatant upon cell death; while the MTS assay measures the metabolic activity of viable cells to convert MTS into a soluble color product. Both assays were performed according to the manufacturer's instruction. Briefly, cells were seeded and incubated with 5-fold diluted Si nanocrystals or water in a 24-well plate as above for the indicated time. Then, the culture supernatants were transferred to microfuge tubes and centrifuged at 13,000 g for 10 min. 50 µl of each clarified supernatant was transferred to a flat-bottom 96-well plate and mixed with 50 µl of LDH substrate using a multichannel pipette. After 30 min incubation at room temperature in the dark, the absorbance was read at 490 nm with a Spectramax M3 plate reader. The viability % is calculated as follows: [1-(Sample A490- Cells without treatment A490)/(100% lysis A490- Cells without treatment A490)] X 100%. 100% lysis was calculated as the absorbance for cells lysed with 0.9% Triton X-100. The remaining

cells in the plate were immediately washed three times with PBS to remove residual Si nanocrystals, and medium containing 6-fold diluted MTT/PTS solution was added into each well and incubated at 37 ˚C for 1 hour. The supernatants were then transferred to flat-bottom 96-well plate to be read at 490 nm. The viability% is calculated as follows: (Sample A490 – No cell A490)/(Cells without treatment A490– No cell A490) X 100%. Wells without cells were used as the blank to account for automatic coloration.

Silicon nanocrystal uptake was inhibited by administering phagocytic inhibitors. J774 cells were seeded in 6 and 24-well plates as above and incubated with 5-fold diluted silicon nanocrystals with or without cytochalasin D (CytD) or nocodazole (Noco) at the concentrations indicated in the text. Confocal microscopy and flow cytometry were used to assess effects of inhibitors.

Cell inflammatory response to Si nanocrystals was measured. Cells were seeded in 6-well plates as above and incubated with silicon nanocrystals diluted 5-fold in growth media for 3 hours. Control samples were treated with 100 ng/ml lipopolysaccharide (LPS) or water at the same dilution in growth media for 3 hours. Gene expression levels of the proinflammatory markers tumor necrosis factor-α (TNFα) and interleukin-1β (IL-1β) were compared by analyzing total RNA by reverse transcriptase- polymerase chain reaction (RT-PCR).[21,22] β-Actin was used as a reference gene. RNA was extracted using the PureLink ™ RNA mini kit (Ambion #12183020) per the manufacturer's instructions. Isolated RNA was quantified using a NanoDrop 2000 and quality was assessed by the ratio of absorbance at 260 nm / 280 nm. First strand synthesis was carried out using the SuperScript IV first strand synthesis system (Invitrogen) with 1 μg of RNA in a 20 μl reaction using random hexamers per the manufacturer's instructions. Quantitative PCR (qPCR) was performed on the target DNA using Power SYBR® green PCR master mix (Applied Biosystems) in a 20 μl reaction, per manufacturer's instructions, using 1 μl of

the first strand synthesis product and the oligonucleotide primers: TNFα (forward: 5'-GAACTGGCAGAAGAGGCACT-3', reverse: 5'- AGGGTCTGGGCCATAGAACT-3'), IL-1β (forward: 5'- GCCACCTTTTGACAGTGATGAGA-3', reverse: 5'-ATCAGGACAGCCCAGGTCAA-3'), and β-Actin (forward: 5'-CACTGTCGAGTCGCGTCCA-3', reverse: 5'- GCCCACGATGGAGGGGAATA-3'). Amplification was monitored using a Viia-7 Real-Time PCR System and the number of cycles required to reach a threshold level (C_T) was determined using QuantStudio7 software. The differences between C_T values from LPS or Si nanocrystal treated cells and water treated cells for TNF-α and IL-1β ($\Delta C_{T,X}$) were compared using β-Actin as an internal reference ($\Delta C_{T,R}$). The fold expression relative to water was obtained from the software. Amplification was also visualized by separating the gene product on a 1% agarose gel with low molecular weight (NEB) ladder as a marker and observed using ethidium bromide.

4.3 RESULTS AND DISCUSSION

4.3.1 Si Nanocrystals in Biological Solutions

Figure 4.1 shows the characterization of 10-undecenioc acid capped Si nanocrystals. The nanocrystals were prepared according to a previously reported method.[8] The prepared Si nanocrystals were dispersed in ethanol and had a diameter of 2.8 nm ± 0.5 nm. The nanocrystals were then transferred into pH 7.4 water by repeated filtration through a 30 kDa centrifugal filter, which allowed the controlled deprotonation of carboxylic acid groups. Figure 4.1a shows the absorbance and PL spectra for Si nanocrystals in ethanol and after transfer into water. The mean emission wavelength for Si nanocrystals in ethanol was 705 nm, while after transfer to water the emission was at

704 nm, indicating a minimal blue shift. The Si nanocrystal quantum yield was measured relative to a dye standard, and was 10.7% when dispersed in ethanol and 9.1% when dispersed in water. Transmission electron microscopy (TEM) images of the Si nanocrystals before and after transfer into water demonstrate that the particles maintained their integrity (Figure 4.1b and 4.1c). Figure 4.1d shows thermogravimetric analysis (TGA) data for 10-undecenoic acid capped Si nanocrystals, which had a ligand density of 5.2 ligands/nm^2. This corresponds to approximately 126 ligands per Si nanocrystal, suggesting a fairly dense ligand coverage consistent with reports for alkene-capped Si nanocrystals.[4]

Figure 4.1e shows FTIR results for Si nanocrystals before and after transfer into water. While characteristic stretches such as the CH_2 asymmetric and symmetric stretches (2925 and 2850 cm^{-1}), Si-H stretch (2100 cm^{-1}), and Si-O stretch (1096 cm^{-1}) were present in both spectra, only the Si nanocrystals in water showed COO^- asymmetric and symmetric stretches (1600 and 1400 cm^{-1}). This corresponds with the deprotonation of the carboxylic acid groups upon transfer from ethanol to water. The Si-H and Si-O stretches indicate that the surface was not completely passivated by the ligands, which is anticipated due to steric hindrance between the ligands. X-ray diffraction (XRD) patterns collected for Si nanocrystals dried out of ethanol and water indicated that they maintain their diamond cubic lattice structure (Figure 4.1f).

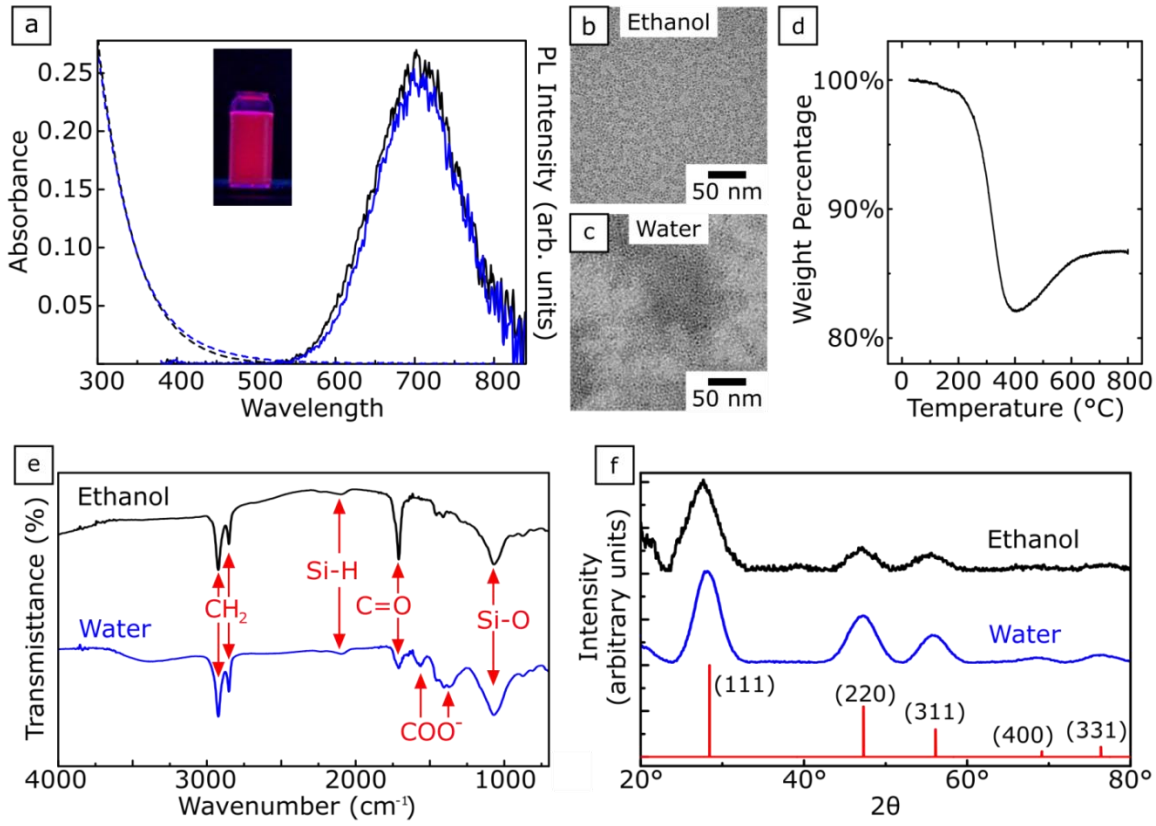

Figure 4.1 Characterization of 10-undecenoic acid passivated Si nanocrystals. (a) Photoluminescence emission (solid lines) and absorbance (dashed lines) spectra captured for samples dispersed in ethanol (black lines) or water (blue lines) indicate minimal shift in photoluminescence properties. Inset is a photo of Si nanocrystals dispersed in water on an ultraviolet lamp (365 nm), demonstrating emission in the visible range. TEM images of Si nanocrystals in (b) ethanol and (c) water. (d) TGA data for the 10-undecenoic acid capped Si nanocrystals. (e) FTIR data for Si nanocrystals dried out of ethanol or water shows the deprotonation of COOH. (f) XRD data for Si nanocrystals dried out of ethanol or water (reference pattern is PDF 027-1402, with a=b=c=0.543088 nm).

The colloidal stability of Si nanocrystals in water depends on the electrostatic repulsive forces between the nanocrystals exceeding the van der Waals attractive forces.[11] Figure 4.2 shows photographs of Si nanocrystals dispersed in water and then placed in water solutions adjusted to pH 2-12 using HCl or NaOH. At neutral pH (pH 7-8) the

nanocrystals appear to stay dispersed over three days. A slight change in color from red to orange suggests some oxidation of the nanocrystal surface, causing Si nanocrystal core size to shrink and therefore an increase in the bandgap. The zeta potential for Si nanocrystals in pH 7.4 water was -47.9 ± 0.6 mV. Zeta potentials with absolute values greater than 30 mV indicate stable dispersions.[25] At low pH, the nanocrystals visibly aggregated. Carboxylic acid has a pKa of 4.8,[26] indicating that as the pH drops below 4.8 a higher proportion of the carboxylic acid groups are protonated. Protonated ligands do not contribute to electrostatic repulsion and thus the nanoparticles aggregate. The aggregates observed at low pH appeared fluorescent even after three days. At the high end of the pH spectrum, at pH 12 the nanocrystal PL degraded immediately, while at pH 10 the PL degraded within one day. The high hydroxide ion content of those solutions can contribute to Si oxidation.[6,12]

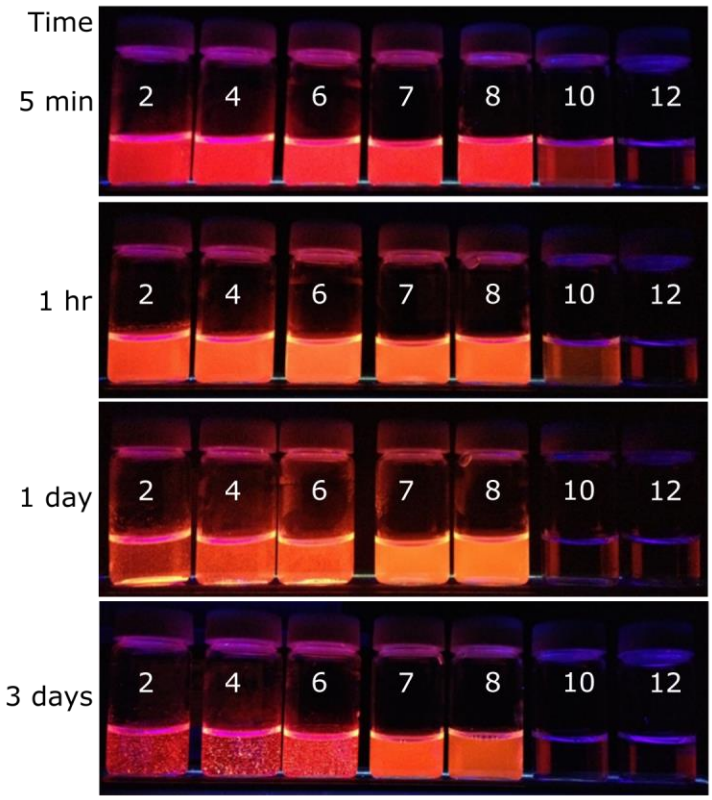

Figure 4.2 Photographs of Si nanocrystals stored in water adjusted to pH 2 – pH 12 (as labeled on vials) over three days.

The PL stability of Si nanocrystals in biological solutions was examined by incubating the nanocrystals in selected solutions for one week. In addition to water and buffer solutions, cell culture medium and all of its individual components were tested to determine if there were specific molecules that contribute to PL degradation.[20] The sample PL emission was monitored on days 0, 1, 2, 4, and 7, and the results for select solutions are shown in Figure 4.3. Figure 4.3a shows that in water the Si nanocrystal PL intensity increased slightly for the first two days, after which it started to decline. The initial increase in intensity may be related to oxidation of the Si nanocrystal surface, which can passivate any remaining dangling Si surface bonds to form an oxide shell that improves quantum confinement and therefore brightness.[6,27] Figures 4.3b and 4.3c shows

that in 0.1 M phosphate buffer and cell culture medium, the PL decreased throughout the seven days. Figure 4.4 shows the Si nanocrystal PL changes for all the biological solutions tested over the seven day period. Decreases in the PL intensity reflect loss of nanocrystal emission, while blue shifts in the peak emission wavelength suggest surface oxidation which results in shrinking of the crystalline core. For most of the solutions higher rates of PL loss corresponded to greater blue shifts in the emission wavelength.

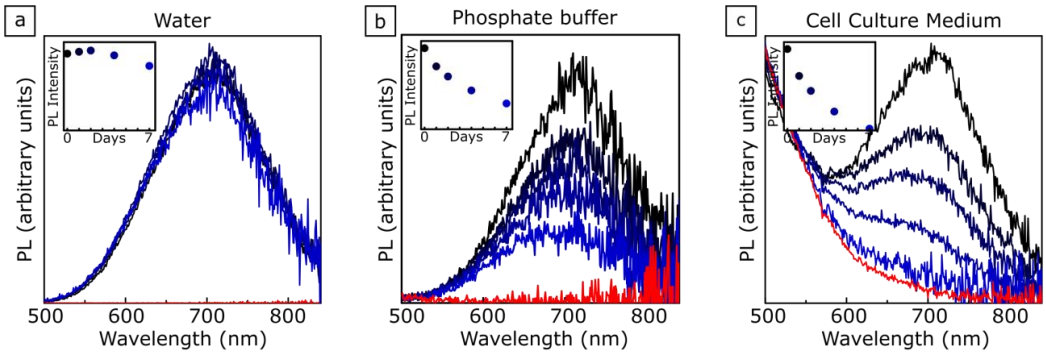

Figure 4.3 PL spectra of Si nanocrystals dispersed in (a) pH 7.4 water, (b) 0.1 M phosphate buffer, and (c) cell culture medium. In each figure, the spectra from days 0, 1, 2, 4, and 7 after adding Si nanocrystals into the solution are shown, with day 0 PL shown in black to day 7 PL shown in blue. Red spectra are PL measured for samples containing no Si nanocrystals and indicate solution fluorescence. Insets show normalized intensity over the same 7 day period (color coded as black for day 0 to blue for day 7).

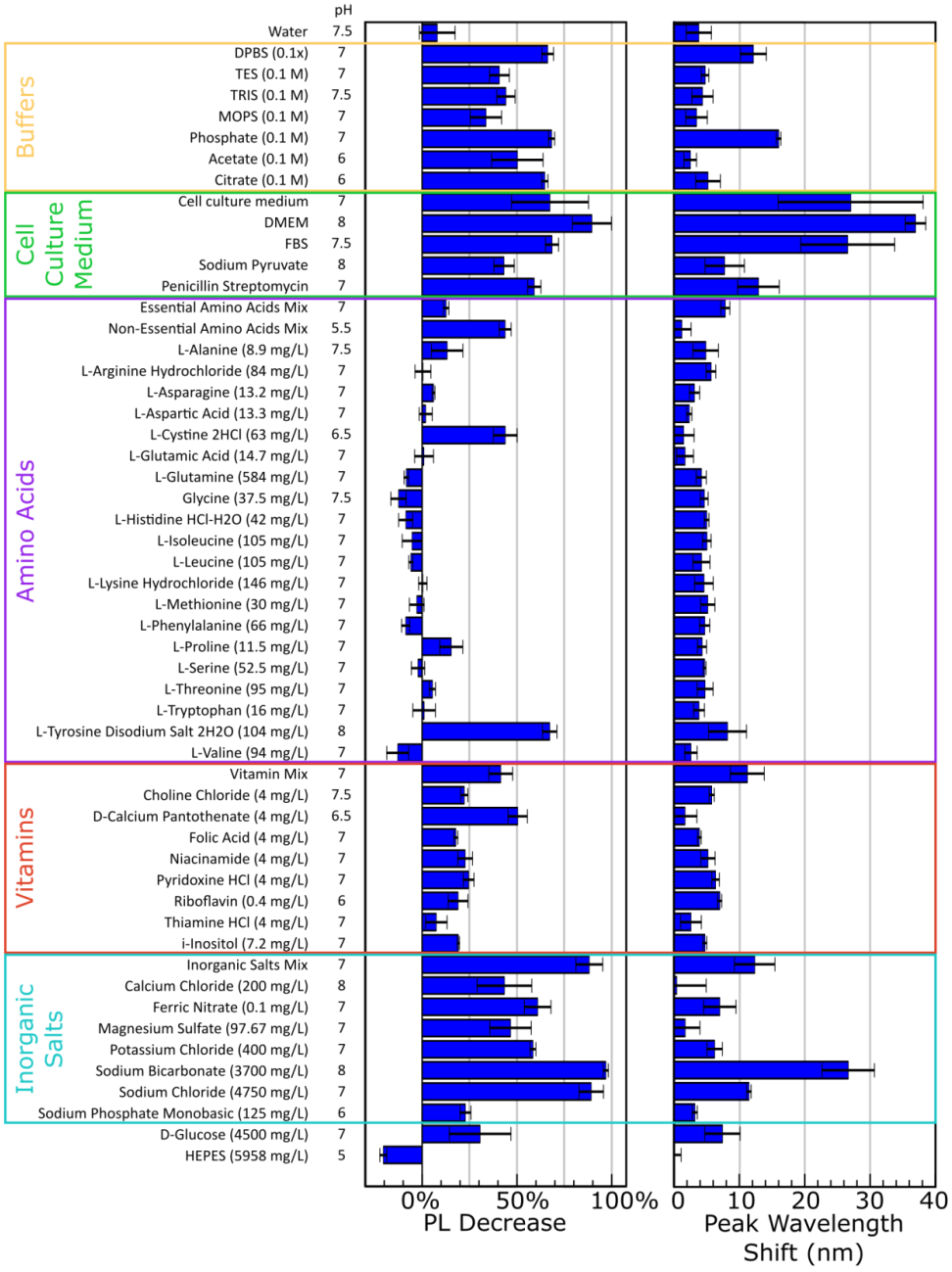

Figure 4.4 Summary of changes in PL for Si nanocrystals dispersed in a variety of buffers and cell culture medium components for 7 days (error bars are standard deviation, n=3). PL decrease was measured by comparing PL intensity on day 7 to day 0. Positive values indicate a decrease in PL intensity. Peak wavelength was calculated as the average emission wavelength. A positive peak wavelength shift indicates a blue shift to lower wavelengths.

Figure 4.5 shows plots of PL decrease and wavelength shift as a function of solution concentration and pH. Trends are visible between the variables: for example, higher pH tends to result in a greater shift in emission wavelength. However, attempts to fit the data to linear or exponential functions resulted in very low fitting. This suggests that other factors such as chemical composition may play a role in PL degradation. Si nanocrystals incubated with L-cystine HCl exhibited a 44% loss in PL intensity, and cysteine has a terminal –SH group which can potentially interact with the silicon surface. Further, phosphate species have been shown to contribute to SiO_2 dissolution,[28] and here phosphate containing solutions resulted in PL degradation.

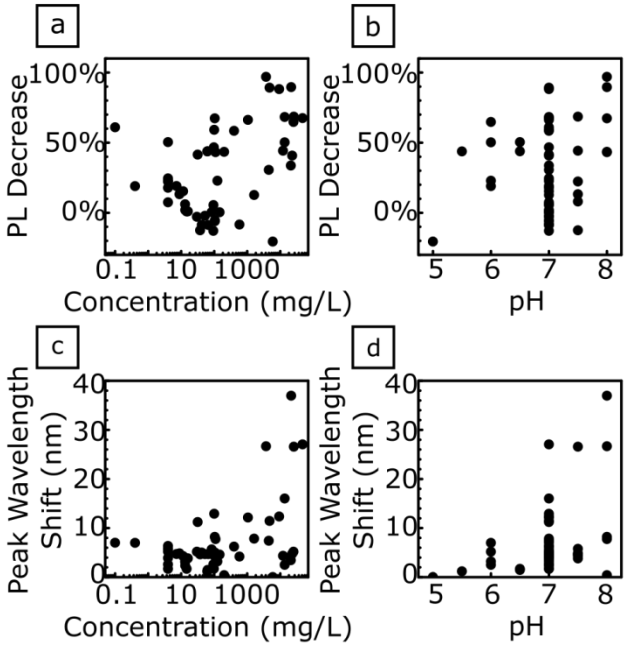

Figure 4.5 Scatter plots showing PL intensity decrease (a-b) and peak emission wavelength (c- d) as a function of concentration or pH.

Figure 4.6 shows XPS results for surface oxidation of Si nanocrystals. For Si nanocrystals dispersed in ethanol, the Si^0 (99.2 eV and 99.7 eV for the 3/2 and 1/2 peaks,

respectively) peak contributions are apparent confirming sample crystallinity, while surface passivation is confirmed by the Si-C (102.0 eV) peak (Figure 6). Peaks corresponding to surface oxidation appear in the ethanol sample as well, including Si^{1+} (100.4 eV), Si^{2+} (100.9 eV), Si^{3+} (102.6 eV), and Si^{4+} (103.7 eV), likely as a result of some surface oxidation that occurs during the synthesis and as the Si nanocrystal sample is dried from solution in air. The oxidation in ethanol is consistent with previous reports.[8] The relative contribution from the oxidized states increased after the Si nanocrystals were transferred to water. For Si nanocrystals in cell culture medium, phosphate buffer, and sodium bicarbonate, XPS shows substantial oxidation of the nanocrystal surface, with almost no Si^0 observed. All three of these solutions resulted in PL intensity decreases >60%, suggesting that surface oxidation contributes to a decrease in PL. However, for Si nanocrystals in the vitamin mix, the XPS measured oxidation levels are similar to those observed for Si nanocrystals in water even though PL intensity decreased by 41% over one week. This suggests that PL loss cannot be attributed to surface oxidation alone.

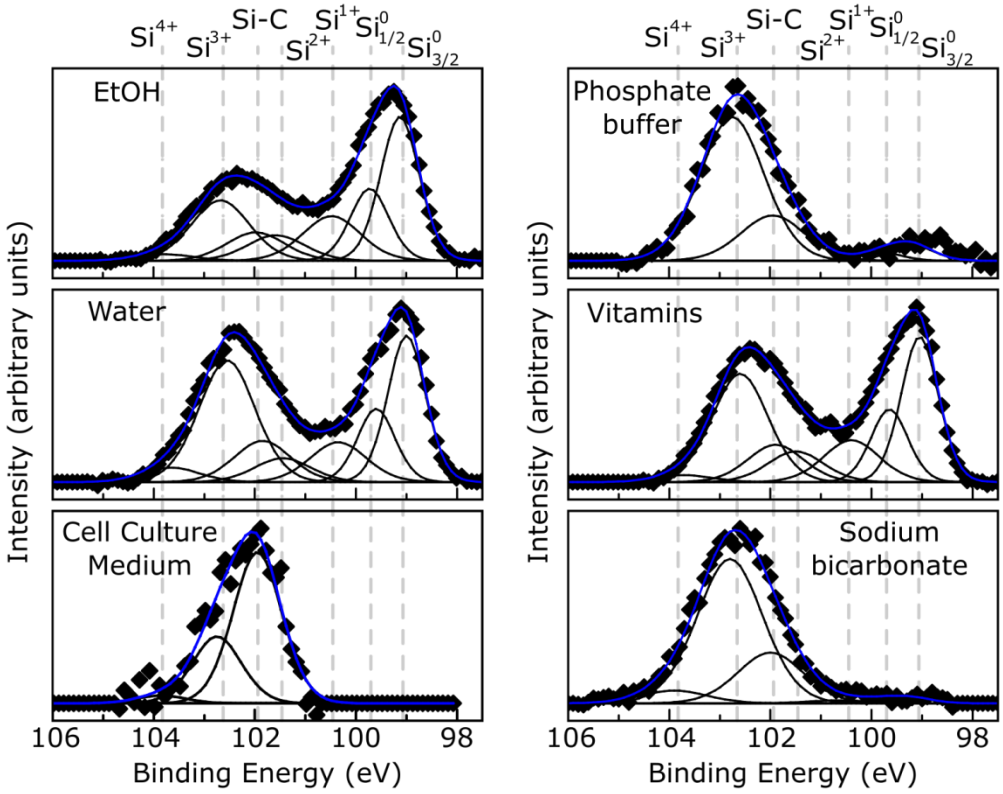

Figure 4.6 XPS Si 2p data for Si nanocrystals dispersed in ethanol, water, cell culture medium, phosphate buffer, vitamin mix, and sodium bicarbonate. Data (black diamonds) was fit (blue line) with the relative contributions (black lines) from oxidized Si states.

Figure 4.7 shows the results of measuring the physical degradation of Si nanocrystals by ICP. Si nanocrystals were incubated with test solutions and on days 1, 4, and 7 the samples were filtered through 30 kDa centrifugal filters. The Si concentration of the filtrate (which excludes whole Si nanocrystals) was then measured to estimate the amount of Si that had been removed from the nanocrystals. As a reference, the maximum Si concentration for the preparation was 1.56 mg/L. The results show an increase of Si present in the filtrate from days 1-7 in all samples (Figure 4.7a). Taking the example of Si nanocrystals in water, which exhibited an 8.0% loss of PL over 7 days (Figure 4.4), the measured mass loss by ICP corresponds to 6.6% of total mass in the preparation. Si

nanocrystals in vitamin solution lost 41% PL intensity over 7 days, and close to 23% Si mass as measured by ICP. Figures 4.7b and 4.7c show plots relating the amount of Si mass loss measured by ICP to the PL degradation, and show positive correlations between the variables (linear fits of the data found R^2 values of 0.68 for PL decrease versus ICP concentration and 0.41 for peak wavelength shift versus ICP concentration). The ICP results provide evidence for PL loss being attributed to physical loss of silicon from the nanocrystals. The results are also consistent with previous reports of fluorescent porous silicon particles, where the particles have been observed to degrade as PL is lost in an aqueous environment.[6]

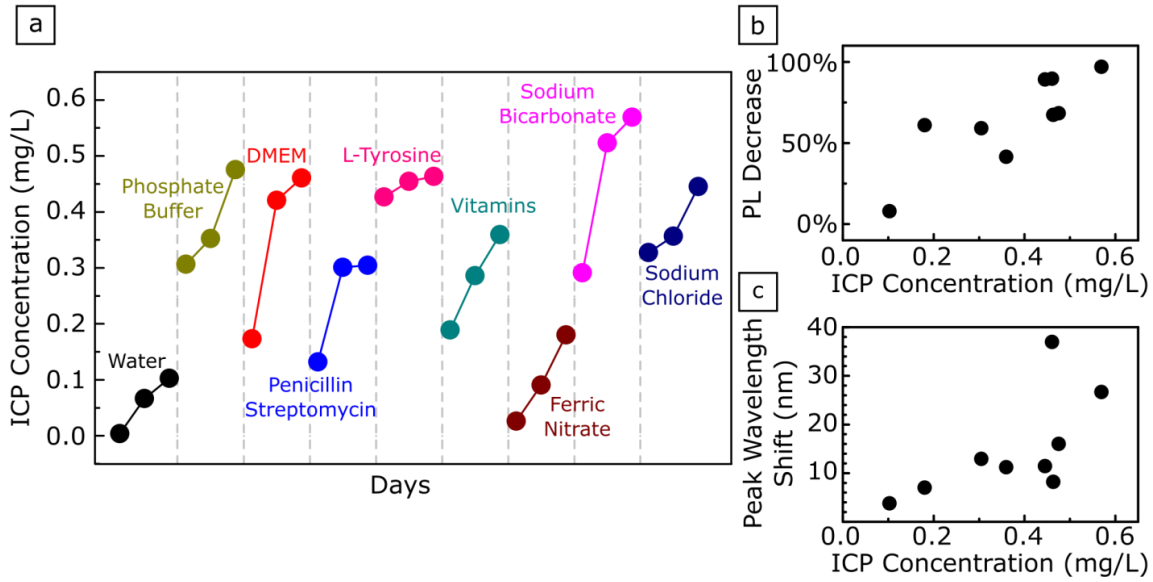

Figure 4.7 (a) Results of ICP analysis of Si concentration in the filtrate from Si nanocrystals dispersed in various solutions. For each solution, the plots represent measurements taken on days 1, 4, and 7 after adding Si nanocrystals. The maximum possible Si concentration for the preparation was 1.56 mg/L. Comparison of the (b) PL intensity decrease and (c) the emission wavelength shift to the filtrate Si concentration on day 7.

While the previous results demonstrate Si nanocrystal PL degradation rate at room temperature, most *in vivo* and *in vitro* studies take place at physiological conditions. Figure 4.8 shows the PL loss at 25 °C and 37 °C over a one day period. The samples incubated at physiological temperature degraded more significantly in all solutions. The increased PL loss at higher temperature can likely be attributed to higher rates of surface oxidation and nanoparticle degradation.

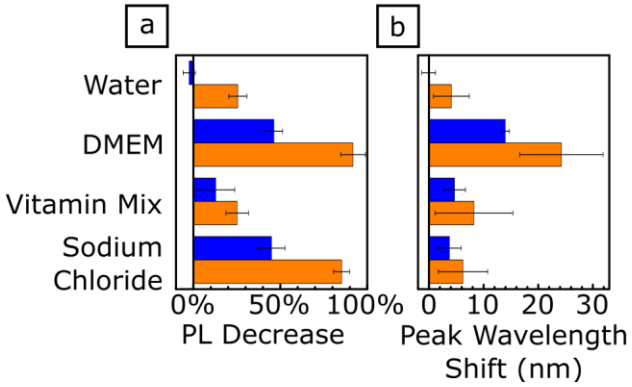

Figure 4.8 Summary of changes in PL for Si nanocrystals dispersed in solutions at either 25 °C (blue bars) or 37 °C (orange bars) over 24 hours.

The interactions of Si nanocrystals and proteins in solution were characterized using DLS (Table 4.1). Particles in biological fluids are known to be coated by a protein corona, which can increase nanoparticle size and how the particles interact with cells.[14,17] Si nanocrystals were incubated for 3 hours at 37 °C either in water or with a molar excess of the proteins bovine serum albumin (BSA) or lysozyme. The colloidal dispersion sizes were measured using dynamic light scattering and the resulting correlation functions were fit to estimate particle sizes.[24] Si nanocrystals in pH 7.4 water were found to have a hydrodynamic diameter of 15.0 nm, which is larger than the expected size of the nanocrystals with ligands attached (around 5 nm), and may be related to the interactions

between the ligands and the surrounding water affecting the hydrodynamic diameter measured by DLS, or may indicate that there is some degree of aggregation between particles in water. Incubation with BSA resulted in an increase in size for the Si nanocrystals to 23.3 nm (a significant population of smaller particles were also present in the dispersion and can be attributed to free BSA molecules). Lysozyme, which was found to have a positive zeta potential, resulted in aggregation with Si nanocrystals and particle sizes around 621.7 nm. In a complex fluid such as cell culture medium where there are a variety of charged species, it is likely that the nanocrystal surface becomes coated with biomolecules and some aggregation at the nanoscale occurs due to electrostatic interactions. Unfortunately, measurement of particle size in a solution containing many different sizes is not possible using DLS, which is a technique best suited for dispersions with no more than two or three discrete particle sizes.[24]

Sample	Particle Diameter	Zeta Potential
Si nanocrystals in water	15.0 ± 1.0 nm	-47.9 ± 0.6 mV
BSA	3.1 ± 0.1 nm	-26.2 ± 1.0 mV
Si nanocrystals + BSA	23.3 ± 1.2 nm *	-43.5 ± 2.7 mV
Lysozyme	1.7 ± 0.2 nm	12.3 ± 0.4 mV
Si nanocrystals + lysozyme	621.7 ± 52.4 nm	19.1 ± 1.0 mV

Table 4.1 Particle sizes as measured by DLS and zeta potentials. Values reported are mean ± standard deviation, for n=3 measurements. * A secondary population of particles with size 2.7 ± 0.1 nm was identified, and corresponds to free BSA molecules.

4.3.2 Si Nanocrystal Uptake, Toxicity, and Inflammatory Response in Macrophage Cells

Figure 4.9 demonstrates the results of 10-undecenoic acid capped Si nanocrystal uptake by J774 macrophage cells or CHO ovary cells. Previous work has identified that

the interactions between nanoparticles and cells are unique to the nanoparticle size and surface composition as well as cell type,[14–16] with non-targeted nanoparticles typically being taken up by processes such as endocytosis.[3,29,30] Si nanocrystals were transferred into water at a concentration of 2 mg/ml and then dilute 5-fold into cell culture medium for incubation with the cells. After incubation for 3 hours at either 4 °C or 37 °C, confocal microscopy confirmed that only J774 cells incubated with Si nanocrystals at physiological temperature showed Si nanocrystal emission in the cell cytoplasm (Figure 4.9a). Emission measured from Si nanocrystals by flow cytometry (using a 670 long pass filter) further confirmed that only the macrophage cells incubated with Si nanocrystals at 37 °C had taken up Si nanocrystals, as the mean fluorescence intensity (MFI) shifted to higher intensities (mean fluorescence intensity (MFI) results for J774 cells were: Si nanocrystals 37 °C = 741.5 ± 3.5; Water 37 °C = 112.5 ± 6.4; Si nanocrystals 4 °C = 131.0 ± 5.6; Water 4 °C = 110.0 ± 6.9 (n=2); and for CHO cells were: Si nanocrystals 37 °C = 62.7 ± 0.2; Water 37 °C = 50.0 ± 1.6; Si nanocrystals 4 °C = 47.1 ± 0.9; Water 4 °C = 46.0 ± 0.8 (n=3)). Taken together, these results suggest that Si nanocrystals are actively endocytosed from the surroundings and do not enter the cell by diffusion across the cell membrane. While CHO cells have been observed to take up silver nanoparticles,[31] the lack of uptake of Si nanocrystals may be related to the particle size and surface characteristics, which may not interact with CHO cells in the same way as silver based particles. Macrophage cells help clear foreign debris from the body as part of the immune system, and thus active uptake of nanoparticles was an expected result consistent with uptake observed in macrophages with other nanoparticles.[14,30,32]

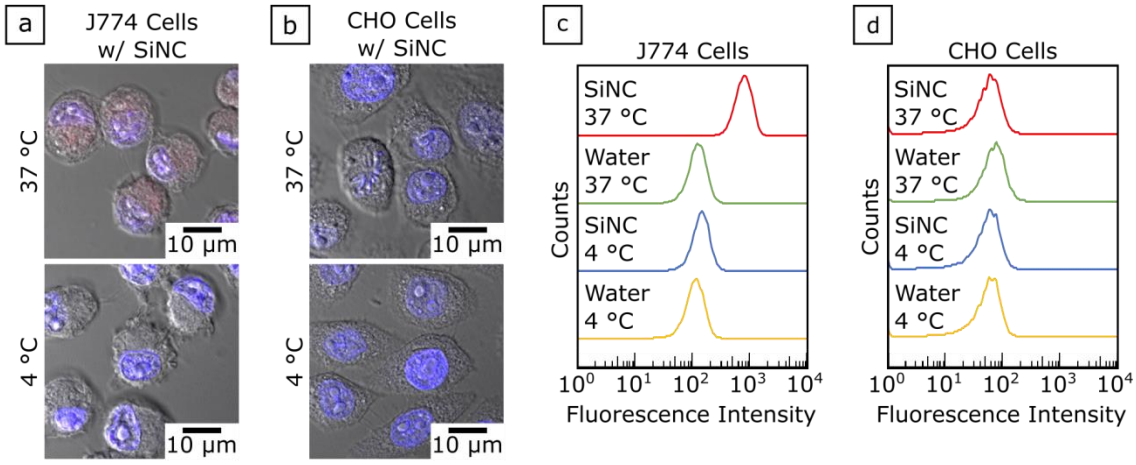

Figure 4.9 Confocal images of (a) J774 and (b) CHO cells incubated with Si nanocrystals (SiNC) for 3 hours at either 4 °C or 37 °C. Excitation wavelength of 405 nm was used, and Si nanocrystal signal (false colored red) was captured at 670-740 nm while DAPI nucleus signal (false colored blue) was captured at 417-566 nm. Flow cytometry fluorescence intensity of (c) J774 and (d) CHO cells incubated with either Si nanocrystals or with just water, at either 4 °C or 37 °C, identified that only J774 cells incubated with Si nanocrystals at physiological temperature showed an increase in emission intensity.

Figure 4.10 shows the time and concentration dependent uptake of Si nanocrystals by macrophage cells. Over a 24 hour period, confocal microscopy (Figure 4.10a) identified that the increase in Si nanocrystal signal spread throughout the cell cytoplasm. The amount of uptake as measured by flow cytometry (Figure 4.10b) gradually increased up to 24 hours for samples incubated at 37 °C, corroborating the results seen in the confocal images. After 24 hours the emission did not increase further, suggesting that Si nanocrystal uptake and degradation had reached steady state. Considering that PL intensity decreased by almost 92% for Si nanocrystals dispersed in DMEM at 37 °C over 24 hours (Figure 4.8a), the identification of Si nanocrystal emission from cells at 24 hours suggests that the Si nanocrystal PL is stabilized inside of the cells. This could occur if the nanocrystals are contained in a low pH environment, where the nanocrystals

aggregate and PL stability is maintained. For example, in Figure 4.2 the low pH vials showed continued fluorescence for three days after the nanocrystals aggregated, and PL intensity was found to increase over one week when Si nanocrystals were dispersed in pH 5 HEPES (Figure 4.4). Thus, the stability of the PL signal over several days may indicate that the Si nanocrystals are being trafficked into low pH regions of the cell, such as lysosomes. This result is also consistent with reports of porous silicon, which lost all photoluminescence within 6 hours after incubation at 37 °C in a buffer solution, however emission was captured for *in vivo* particles 24 hours after injection into a mouse.[6]

Figure 4.10c shows the results of concentration dependent emission measured from J774 macrophages. Si nanocrystals were prepared in water at concentrations from 0.1-5 mg/ml before being added into the cell culture medium. As the loading concentration of Si nanocrystals was increased, the mean fluorescence intensity as measured by flow cytometry also increased in a non-linear manner and appeared to approach a maximum. Previous reports have noted that receptor mediated uptake by cells results in concentration dependent uptake that follow Michaelis-Menten like kinetics.[33–36] Here, the Si nanocrystal uptake could also be fit to a Michaelis-Menten model with relatively good fitting (R^2=0.997, V_{max}=961.01 and K_m=0.941). The concentration dependent uptake indicates that surface receptors are involved in the uptake of Si nanocrystals, though the receptors may be interacting with the protein coronae surrounding the particles rather than the nanocrystals.

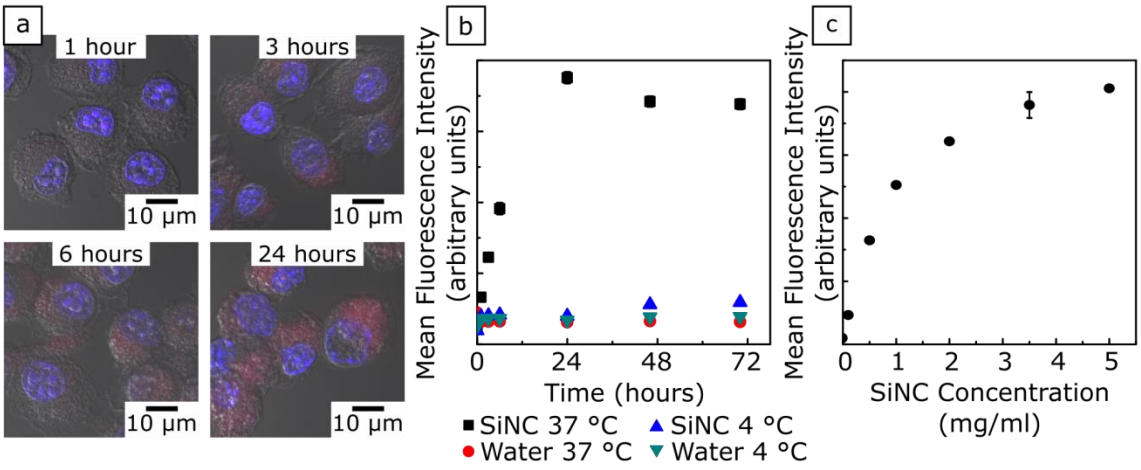

Figure 4.10 (a) Confocal images showing increase in Si nanocrystal (SiNC) signal throughout the cytoplasm of J774 cells after uptake over a 24 hour period. (b) Time dependent uptake of Si nanocrystals as measured by flow cytometry. (c) Concentration dependent uptake of Si nanocrystals as measured by flow cytometry. Error bars are standard deviation (n=3).

Endocytosis of nanoparticles can occur following multiple mechanisms including clathrin-mediated endocytosis, caveolin-mediated endocytosis, macropinocytosis, or an independent endocytosis mechanism.[37,38] To determine the particular uptake pathway(s) for Si nanocrystals, J774 cells were treated with non-toxic levels of two drugs known to inhibit cellular processes necessary for distinct methods of endocytosis. Flow cytometry was used to determine the level of uptake of Si nanocrystals with each drug and was compared to control cells that were not treated with the drug. Incubation with cytochalasin D, a drug that blocks actin polymerization,[29] resulted in a statistically significant reduction in Si nanocrystal uptake, though complete blockage was not observed (Figure 4.11a, $P<0.05$ between samples incubated with 0 mg/ml cytochalasin D and with 2, 4, or 10 mg/ml cytochalasin D). Incubation with nocodazole, which disrupts microtubules,[29] did not reduce Si nanocrystal uptake (Figure 4.11a). Confocal images of cells treated with cytochalasin D (Figure 4.11b) or nocodazole (Figure 4.11c) at 10 µg/ml

identified that Si nanocrystal signal was not observed in the cytochalasin D sample, consistent with the decreased emission intensity measured by flow cytometry. Actin filaments are required for both clathrin-mediated and caveolin-mediated endocytosis, while microtubules are necessary for the transport of caveolin-rafts from the membrane into the cell.[39,40] Disruption of microtubules does not appear to inhibit Si nanocrystal migration to the cell interior suggesting that uptake is primarily dependent on clathrin-mediated endocytosis. Clathrin-mediated endocytosis results in particles being transported into endosomes and then lysosomes inside of cells, which is consistent with our findings that Si nanocrystal PL is visible for a long time (Figure 4.10), suggesting that they are in a low pH environment.

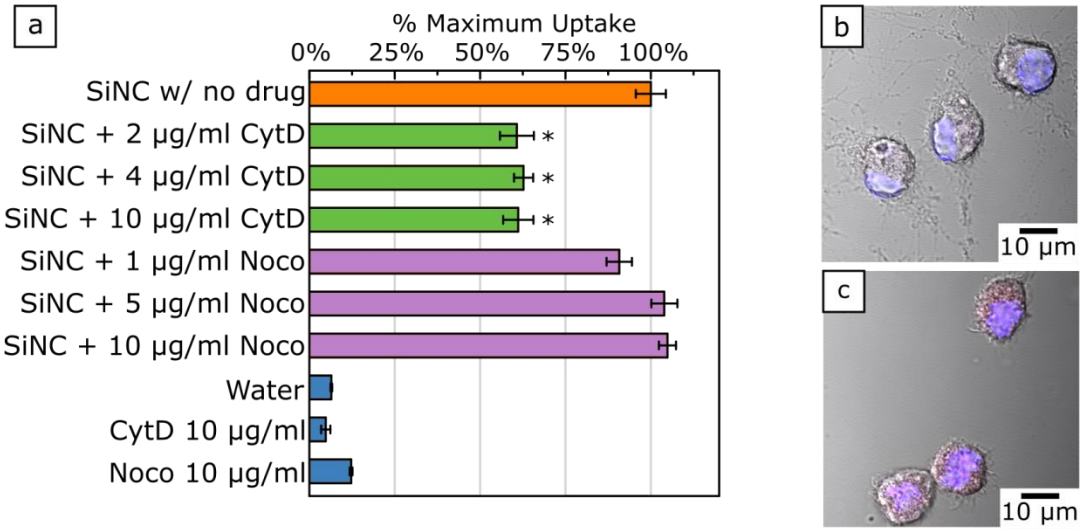

Figure 4.11 (a) Uptake of Si nanocrystals (SiNC) in the presence of cytochalasin D (CytD) and nocodazole (Noco) blockers, as measured by flow cytometry (error bars are standard deviation n=3). * indicate $P<0.05$ between Si nanocrystals with no drug and sample with drug using unpaired Student's t-test. Data normalized to sample with no drug. Confocal images of cells treated with (b) CytD and (c) Noco at 10 µg/ml.

Figure 4.12 shows the results of toxicity testing for the Si nanocrystals in J774 macrophage cells. Two assays were used to assess cell viability over 24 hours. First, a lactate dehydrogenase (LDH) enzyme assay was used, which measures the release of LDH enzyme upon damage to the plasma membrane. Second, a 3-(4,5-dimethylthiazol-2-yl)-5-(3-carboxymethoxyphenyl)-2-(4-sulfophenyl)-2H-tetrazolium (MTS) assay was used to measure the metabolic activity of living cells. Si nanocrystal treated samples were compared to a no treatment and a Triton-X100 treated control. Both assays showed minimal cell toxicity as a result of Si nanocrystal uptake, with no discernible impact of Si nanocrystals compared to cells that were not exposed to the Si nanocrystals.

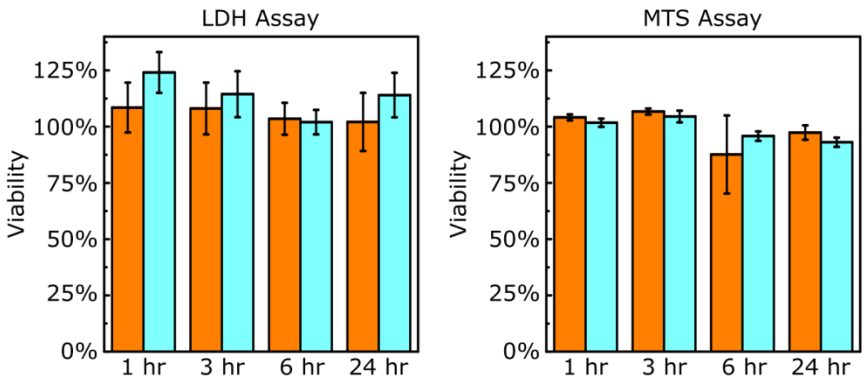

Figure 4.12 Viability assays using LDH and MTS for cells incubated (orange bars) with Si nanocrystals or (blue bars) without Si nanocrystals.

Figure 4.13 shows the results of testing to characterize the inflammatory response of Si nanocrystals in the macrophage cells. An inflammatory response can affect metabolic functions and increases gene expression of certain cytokines including tumor necrosis factor-α (TNF-α) and interleukin 1-β.[22,30] To determine if an inflammatory response was taking place, the mRNA expression of TNF-α and IL-1β was measured using quantitative real time polymerase chain reaction (qPCR) for cells incubated with Si

nanocrystals, water, or lipopolysaccharide (LPS), a known stimulator of cytokine expression which acts as a positive control.[22] As shown in Figure 4.13, the relative expression level of TNF-α or IL-1β is much greater in cells treated with LPS compared to water suggesting that an inflammatory response was triggered in the LPS treated cells. In contrast, J774 cells treated with Si nanocrystals have a nearly identical expression level of TNF-α and IL-1β to water treated cells. These results show that uptake of Si nanocrystals did not induce an inflammatory response in the macrophages.

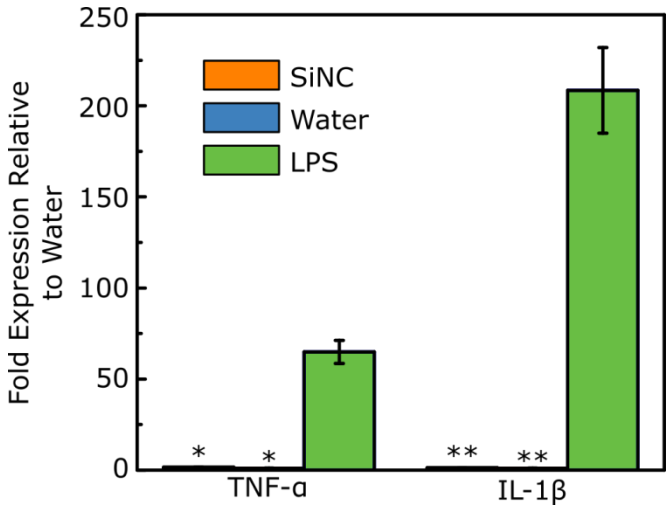

Figure 4.13 mRNA expression levels of inflammation markers TNF-α and IL-1β as measured by qPCR. Expression levels are reported as fold expression relative to cells treated with media containing only water. LPS was a positive control. Error bars are standard deviation (n=2). * indicate P<0.1 and ** indicate P<0.05 between LPS control and samples using unpaired Student's t-test.

4.4 CONCLUSION

Here, we have studied the feasibility of dispersing 10-undecenoic acid 2.8 nm Si nanocrystals in biological solutions and for imaging with live cells. We have

demonstrated that the nanocrystals lose PL intensity and exhibit a blue shift over time due to silicon oxidation and degradation. However PL emission was still detectable from macrophage cells by confocal microscopy after 24 hours, which may be related to the localization of the particles in low pH vesicles. Considering that many biomedical applications require several hours or even days for photoluminescent particles to accumulate in target tissue, the stability of Si nanocrystals compared to other quantum dots is promising for *in vivo* applications.[3] We have also demonstrated that Si nanocrystals are taken up by macrophage cells through clathrin-mediated endocytosis even in the absence of surface conjugated targeting molecules. Future work can be done to explore how attaching biomolecules to the nanocrystal surfaces may change interactions with specific cell types. Further, since the Si nanocrystals can be prepared at larger sizes that emit at infrared wavelengths, which are ideal for deep tissue penetration applications, future work can investigate the use of larger nanocrystals in cell imaging applications.

4.5 REFERENCES

(1) Dubertret, B.; Skourides, P.; Norris, D. J.; Noireaux, V.; Brivanlou, A. H.; Libchaber, A. In Vivo Imaging of Quantum Dots Encapsulated in Phospholipid Micelles. *Science* **2002**, *298*, 1759–1762.

(2) Michalet, X.; Pinaud, F. F.; Bentolila, L. A.; Tsay, J. M.; Doose, S.; Li, J. J.; Sundaresan, G.; Wu, A. M.; Gambhir, S. S.; Weiss, S. Quantum Dots for Live Cells, in Vivo Imaging, and Diagnostics. *Science* **2005**, *307*, 538–544.

(3) Wegner, K. D.; Hildebrandt, N. Quantum Dots: Bright and Versatile in Vitro and in Vivo Fluorescence Imaging Biosensors. *Chem. Soc. Rev.* **2015**, *44*, 4792–4834.

(4) Hessel, C. M.; Reid, D.; Panthani, M. G.; Rasch, M. R.; Goodfellow, B. W.; Wei, J.; Fujii, H.; Akhavan, V.; Korgel, B. A. Synthesis of Ligand-Stabilized Silicon Nanocrystals with Size-Dependent Photoluminescence Spanning Visible to Near-Infrared Wavelengths. *Chem. Mater.* **2012**, *24*, 393–401.

(5) O'Farrell, N.; Houlton, A.; Horrocks, B. R. Silicon Nanoparticles: Applications in Cell Biology and Medicine. *Int. J. Nanomedicine* **2006**, *1*, 451–472.

(6) Park, J.-H.; Gu, L.; Maltzahn, G. von; Ruoslahti, E.; Bhatia, S. N.; Sailor, M. J. Biodegradable Luminescent Porous Silicon Nanoparticles for in Vivo Applications. *Nat. Mater.* **2009**, *8*, 331–336.

(7) Bhattacharjee, S.; Rietjens, I. M. C. M.; Singh, M. P.; Atkins, T. M.; Purkait, T. K.; Xu, Z.; Regli, S.; Shukaliak, A.; Clark, R. J.; Mitchell, B. S.; Alink, G. M.; Marcelis, A. T. M.; Fink, M. J.; Veinot, J. G. C.; Kauzlarich, S. M.; Zuilhof, H. Cytotoxicity of Surface-Functionalized Silicon and Germanium Nanoparticles: The Dominant Role of Surface Charges. *Nanoscale* **2013**, *5*, 4870–4883.

(8) Yu, Y.; Hessel, C. M.; Bogart, T. D.; Panthani, M. G.; Rasch, M. R.; Korgel, B. A. Room Temperature Hydrosilylation of Silicon Nanocrystals with Bifunctional Terminal Alkenes. *Langmuir* **2013**, *29*, 1533–1540.

(9) Glendinning, A. B.; Russel, W. B. The Electrostatic Repulsion between Charged Spheres from Exact Solutions to the Linearized Poisson-Boltzmann Equation. *J. Colloid Interface Sci.* **1983**, *93*, 95–104.

(10) Laaksonen, T.; Ahonen, P.; Johans, C.; Kontturi, K. Stability and Electrostatics of Mercaptoundecanoic Acid-Capped Gold Nanoparticles with Varying Counterion Size. *ChemPhysChem* **2006**, *7*, 2143–2149.

(11) *Colloid Science: Principles, Methods and Applications*; Cosgrove, T., Ed.; 2nd ed.; John Wiley & Sons, Inc., 2010.

(12) *Colloidal Silica: Fundamentals and Applications*; Bergna, H. E.; Roberts, W. O., Eds.; CRC Press, 2005.

(13) Rahman, M.; Laurent, S.; Tawil, N.; Yahia, L.; Mahmoudi, M. *Protein-Nanoparticle Interactions : The Bio-Nano Interface*; 1st ed.; Springer: Dordrecht, 2013.

(14) Oh, N.; Park, J.-H. Endocytosis and Exocytosis of Nanoparticles in Mammalian Cells. *Int. J. Nanomedicine* **2014**, *9*, 51–63.

(15) Albanese, A.; Tang, P. S.; Chan, W. C. W. The Effect of Nanoparticle Size, Shape, and Surface Chemistry on Biological Systems. *Annu. Rev. Biomed. Eng.* **2012**, *14*, 1–16.

(16) Barua, S.; Mitragotri, S. Challenges Associated with Penetration of Nanoparticles across Cell and Tissue Barriers: A Review of Current Status and Future Prospects. *Nano Today* **2014**, *9*, 223–243.

(17) Monopoli, M. P.; Walczyk, D.; Campbell, A.; Elia, G.; Lynch, I.; Baldelli Bombelli, F.; Dawson, K. A. Physical−Chemical Aspects of Protein Corona: Relevance to in Vitro and in Vivo Biological Impacts of Nanoparticles. *J. Am. Chem. Soc.* **2011**, *133*, 2525–2534.

(18) Walkey, C. D.; Olsen, J. B.; Guo, H.; Emili, A.; Chan, W. C. W. Nanoparticle Size and Surface Chemistry Determine Serum Protein Adsorption and Macrophage Uptake. *J. Am. Chem. Soc.* **2012**, *134*, 2139–2147.

(19) Elias, D. R.; Poloukhtine, A.; Popik, V.; Tsourkas, A. Effect of Ligand Density, Receptor Density, and Nanoparticle Size on Cell Targeting. *Nanomedicine Nanotechnol. Biol. Med.* **2013**, *9*, 194–201.

(20) Documents & Support and Media Formulations | Thermo Fisher Scientific https://www.thermofisher.com/search/supportSearch?query=&type=Media+Formulations (accessed Oct 3, 2017).

(21) Prabhu, A.; Shelburne, C. E.; Gibbons, D. F. Cellular Proliferation and Cytokine Responses of Murine Macrophage Cell Line J774A.1 to Polymethylmethacrylate and Cobalt-Chrome Alloy Particles. *J. Biomed. Mater. Res.* **1998**, *42*, 655–663.

(22) Wang, G.; Petzke, M. M.; Iyer, R.; Wu, H.; Schwartz, I. Pattern of Proinflammatory Cytokine Induction in RAW264.7 Mouse Macrophages Is Identical for Virulent and Attenuated Borrelia Burgdorferi. *J. Immunol.* **2008**, *180*, 8306–8315.

(23) Casey, K. G.; Quitevis, E. L. Effect of Solvent Polarity on Nonradiative Processes in Xanthene Dyes: Rhodamine B in Normal Alcohols. *J. Phys. Chem.* **1988**, *92*, 6590–6594.

(24) Berne, B. J.; Pecora, R. *Dynamic Light Scattering: With Applications to Chemistry, Biology, and Physics*; Courier Corporation, 2000.

(25) International Organization for Standardization. *ISO 14887:2000. Sample Preparation -- Dispersing Procedures for Powders in Liquids*; 2000.

(26) Klein, D. *Organic Chemistry*; John Wiley & Sons, Inc., 2012.

(27) Zhelev, Z.; Jose, R.; Nagase, T.; Ohba, H.; Bakalova, R.; Ishikawa, M.; Baba, Y. Enhancement of the Photoluminescence of CdSe Quantum Dots during Long-Term UV-Irradiation: Privilege or Fault in Life Science Research? *J. Photochem. Photobiol. B* **2004**, *75*, 99–105.

(28) Dekeyser, C. M.; Buron, C. C.; Derclaye, S. R.; Jonas, A. M.; Marchand-Brynaert, J.; Rouxhet, P. G. Degradation of Bare and Silanized Silicon Wafer Surfaces by Constituents of Biological Fluids. *J. Colloid Interface Sci.* **2012**, *378*, 77–82.

(29) Zhang, L. W.; Monteiro-Riviere, N. A. Mechanisms of Quantum Dot Nanoparticle Cellular Uptake. *Toxicol. Sci.* **2009**, *110*, 138–155.

(30) Fernando, L. P.; Kandel, P. K.; Yu, J.; McNeill, J.; Ackroyd, P. C.; Christensen, K. A. Mechanism of Cellular Uptake of Highly Fluorescent Conjugated Polymer Nanoparticles. *Biomacromolecules* **2010**, *11*, 2675–2682.

(31) Jiang, X.; Miclăuş, T.; Wang, L.; Foldbjerg, R.; Sutherland, D. S.; Autrup, H.; Chen, C.; Beer, C. Fast Intracellular Dissolution and Persistent Cellular Uptake of Silver Nanoparticles in CHO-K1 Cells: Implication for Cytotoxicity. *Nanotoxicology* **2015**, *9*, 181–189.

(32) *Macrophages*; Kloc, M., Ed.; Springer International Publishing: Cham, 2017; Vol. 62.

(33) Medina, S. H.; Tekumalla, V.; Chevliakov, M. V.; Shewach, D. S.; Ensminger, W. D.; El-Sayed, M. E. H. N-Acetylgalactosamine-Functionalized Dendrimers as Hepatic Cancer Cell-Targeted Carriers. *Biomaterials* **2011**, *32*, 4118–4129.

(34) Zeng, X.; Zhang, Y.; Nyström, A. M. Endocytic Uptake and Intracellular Trafficking of Bis-MPA-Based Hyperbranched Copolymer Micelles in Breast Cancer Cells. *Biomacromolecules* **2012**, *13*, 3814–3822.

(35) Schwartz, A. L.; Fridovich, S. E.; Lodish, H. F. Kinetics of Internalization and Recycling of the Asialoglycoprotein Receptor in a Hepatoma Cell Line. *J. Biol. Chem.* **1982**, *257*, 4230–4237.

(36) Zaki, N. M.; Nasti, A.; Tirelli, N. Nanocarriers for Cytoplasmic Delivery: Cellular Uptake and Intracellular Fate of Chitosan and Hyaluronic Acid-Coated Chitosan Nanoparticles in a Phagocytic Cell Model. *Macromol. Biosci.* **2011**, *11*, 1747–1760.

(37) Zhao, F.; Zhao, Y.; Liu, Y.; Chang, X.; Chen, C.; Zhao, Y. Cellular Uptake, Intracellular Trafficking, and Cytotoxicity of Nanomaterials. *Small* **2011**, *7*, 1322–1337.

(38) Salatin, S.; Yari Khosroushahi, A. Overviews on the Cellular Uptake Mechanism of Polysaccharide Colloidal Nanoparticles. *J. Cell. Mol. Med.* **2017**, *21*, 1668–1686.

(39) Lamaze, C.; Fujimoto, L. M.; Yin, H. L.; Schmid, S. L. The Actin Cytoskeleton Is Required for Receptor-Mediated Endocytosis in Mammalian Cells. *J. Biol. Chem.* **1997**, *272*, 20332–20335.

(40) Mundy, D. I.; Machleidt, T.; Ying, Y.; Anderson, R. G. W.; Bloom, G. S. Dual Control of Caveolar Membrane Traffic by Microtubules and the Actin Cytoskeleton. *J. Cell Sci.* **2002**, *115*, 4327–4339.

Chapter 5: Aqueous Dispersibility and Photoluminescence of Near-Infrared Emitting Si Nanocrystals

5.1 INTRODUCTION

Fluorescence imaging has become a common tool used to resolve biological structures and processes in real-time, non-invasively, and at a low cost, and as a result has found clinical application in a number of medical fields.[1–3] Near infrared (NIR) emitting probes have drawn considerable interest for *in vivo* imaging because NIR wavelengths penetrate tissues at depths of a cm or more due to a minimum of photon absorption by biomolecules and cells.[1,2,4–8] Additionally, photoluminescence (PL) in the NIR is well-suited for imaging biological samples since it is possible to filter out cell autofluorescence which is present in blue-green wavelengths.[5] Probes developed for NIR imaging include small molecules[5,7] and a variety of nanoparticles such as semiconductor quantum dots,[9–15] carbon nanotubes,[16,17] upconverting nanoparticles,[18,19] and porous silicon particles.[20,21] Silicon (Si) based quantum dot fluorescence can be tuned by size across most of the visible range into NIR.[22] Si quantum dots are biocompatible and can be used for *in vitro* and *in vivo* imaging.[22–25] However, challenges remain for the use of Si nanocrystals in biological environments, such as the photoluminescence stability of the particles in aqueous solvents and surface oxidation.

Previous reports have utilized surfactants or bulky polymers to disperse NIR emitting Si nanocrystals into aqueous environments,[23,25–27] though these assemblies are an order of magnitude larger (50-150 nm) than the as-prepared Si nanocrystals, which can range in size from 2-15 nm. Because particle size and surface chemistry play crucial roles in cell uptake,[28] it is of great interest to examine the use of particles < 50 nm for cell imaging work. Si nanocrystals can be directly capped with ligands containing terminal carboxylic acid or amine functional groups, allowing direct dispersion of the particles

into aqueous solvents, though previous reports did not result in stable, photoluminescent colloidal dispersions with size-dependent PL in red to NIR wavelengths.[29–32] It was recently shown that NIR-emitting Si nanocrystals can be passivated using bifunctional alkenes with distal polar groups.[33] While the smallest Si nanocrystals (around 3 nm) could be directly passivated with carboxylic acid terminated ligands, the larger Si nanocrystals ranging in size from 5.5 – 8.0 nm could be passivated with ethyl ester groups and were dispersible in a mixture of toluene and ethanol. Ester groups can be hydrolyzed into caryboxylic acids using an aqueous base, such as sodium hydroxide,[34] and these carboxylic acid groups can then enable the particles to be directly dispersed into water. While the Si nanocrystal surfaces are passivated to prevent surface oxidation, the presence of hydroxide ions can contribute to oxidation and degradation of the nanoparticle photoluminescence. Here, we characterize the hydrolysis of ethyl ester terminated Si nanocrystals with diameters of 4.7 nm and 6.3 nm. We also study the stability of the particles in water. Both the Si nanocrystal surface properties and photoluminescence characteristics were examined and revealed substantial surface oxidation as well as very low PL quantum yields after hydrolysis and then transfer into water.

5.2 EXPERIMENTAL METHODS

5.2.1 Materials

Hydrogen silsesquoixane (HSQ, Fox®-16) was purchased from Dow Corning. Ethyl 10-undecenoate, sodium hydroxide (NaOH), and hydrofluoric acid (HF) were purchased from Sigma. Ethanol, hexanes, toluene, hydrochloric acid (HCl), and sodium chloride (NaCl) were purchased from Fisher. Rhodamine B was obtained from Acros.

Deionized water was obtained from a Millipore Synergy Ultrapure water system (18.2 MΩ/cm).

5.2.2 Si Nanocrystal Synthesis

Si nanocrystals were synthesized according to a previously reported procedure.[33] HSQ was dried under vacuum and transferred to a quartz boat. The material was placed in a furnace and heat to either 1200 °C or 1250 °C for 1 hour under forming gas flow. After annealing the material, which resulted in Si nanocrystals embedded in an SiO_2 matrix, the product was downsized first by mortar and pestle and then by shaking for 9 hours with borosilicate beads in a wrist-action shaker. The Si nanocrystals were liberated from the SiO_2 matrix by stirring for 6 hours in the dark in a solution of 10 ml HF and 1 ml HCl. The HF solution was washed away by precipitating the nanocrystals by centrifugation (8000 rpm for 5 min), resuspending the material in 10 ml ethanol, and repeating the wash 3 times in ethanol and then once more in chloroform. The hydrogen terminated Si nanocrystals were then dispersed in 10 ml of ethyl 10-undecenoate and transferred into a three neck flask on a Schlenk line. Three freeze-pump-thaw cycles were used to degas the sample. The nanocrystal dispersion was then left stirring overnight under N_2 gas at room temperature (30 °C). The resulting solution, which contained partially passivated Si nanocrystals, was then transferred to a 20 ml vial with an additional 5 ml of ethanol and 5 ml of toluene. The vial was sealed with a septum and left on the bench top for at least one month, during which time the dispersion went from cloudy to transparent as the nanocrystals were passivated.

The ethyl 10-undecenocate coated Si nanocrystals were then washed to remove unpassivated particles and excess capping ligands. The nanocrystal dispersion was

centrifuged at 8000 rpm for 5 min to precipitate out poorly passivated nanocrystals. The supernatant was transferred to a new centrifuge tube and hexane was added until the solution became turbid. The sample was then centrifuged, and the precipitated Si nanocrystals were collected and redispersed in a 1:1 v/v mix of ethanol:toluene. Washing was repeat 3 more times using hexane as the antisolvent and a mixture of toluene and ethanol as the solvent. The final washed Si nanocrystals were dispersed in 1:1 v/v ethanol:toluene solution.

Si nanocrystals were hydrolyzed using sodium hydroxide. 1 ml of ethyl 10-undecenoate Si nanocrystals in 1:1 v/v ethanol:toluene at a concentration of 10 mg/ml was mixed with 2 ml of deionized water adjusted to pH 8.5 using NaOH. The solution became turbid and phase separated. While stirring, ethanol was added drop-wise until the nanocrystal dispersion was no longer turbid. The solution was then transferred to a 100 kDa centrifugal filter (Millipore) and centrifuged for 5 min at 1100 g to remove excess solvent, while Si nanocrystals remained above the filter. Ethanol was then added to the nanocrystal dispersion and the solution was centrifuged again. The ethanol wash was repeat 5 times to remove excess toluene and water, resulting in a clear dispersion of hydrolyzed Si nanocrystals in ethanol.

The Si nanocrystals were transferred from ethanol to water (pH 8.5) using 100 kDa centrifugal filters. 1 ml of the hydrolyzed Si nanocrystals in ethanol were dilute into 5 ml of ethanol, and 5 ml of water was added. The solution was mixed with a pipette and then transferred to the centrifugal filter. After centrifugation (1000 g for 7 min), 5 more ml of water was added to the nanocrystals. This process was repeat 5 times to transfer the Si nanocrystals from ethanol to water.

5.2.3 Characterization

Transmission electron microscopy (TEM) was conducted on an FEI Tecnai Biotwin operated at 80 kV and images were collected digitally. The Si nanocrystals were drop cast onto 200 mesh carbon-coated copper grids (Electron Microscopy Sciences) and dried overnight. Si nanocrystal sizes were estimated from TEM images (n=100).

Thermal gravimetric analysis (TGA) was conducted on a Mettler Toledo TGA/DSC 1. Samples were dried into 70 µl alumina crucibles. The samples were heat under air flow from 25 °C to 800 °C at a rate of 10 °C per minute, and then held at 800 °C for an additional 120 minutes.

Fourier transform infrared spectroscopy (FTIR) was conducted on a Thermo Mattson Infinity Gold FTIR. Samples were drop cast onto undoped silicon wafers (Virginia Semiconductor) and dried overnight. The chamber was purged with N2 for 20 minutes to remove residual CO_2. Measurements were taken in transmission mode with 1024 scans at a resolution of 4 cm^{-1}. Background was calculated as the transmission through a bare Si wafer and subtracted from the samples.

X-ray diffraction (XRD) was conducted on a Rigaku R-Axis Spider diffractometer. Cu Kα radiation (λ=0.15418 nm) was used, operated at 40 kV and 40 mA. Si nanocrystals were dried out of solution overnight and then loaded onto a nylon loop using mineral oil. The sample was scanned for 20 minutes while rotating at 10° per second. The two-dimensional diffraction data was integrated radially with 2DP Spider software (version 1.0, Rigaku Americas Corp.). Background was collected for the nylon loop with mineral oil and subtracted from the samples.

X-ray photoelectron spectroscopy (XPS) was conducted on a Kratos Axis Ultra X-ray photoelectron spectrometer. A monochromatic Al Kα x-ray source was used operating at hν=1486.5, 150 W, 12 mA and 10 kV. Hybrid optics employing a

simultaneous magnetic and electrostatic lens was used with a multi-channel plate coupled to a hemispherical photoelectron kinetic analyzer. The instrument was calibrated such that the instrument work function had a binding energy of 368.3 eV for the Ag 3d5/2 line for metallic silver. Spectra were charge-corrected by shifting the binding energy of carbon 1s to 284.8 eV. Si nanocrystals were drop cast onto indium tin oxide glass slides and secured to the experimental try with double sided copper tape and allowed to dry overnight. High resolution spectra were collected with 20 eV pass energy at 0.1 eV intervals, with 2000 ms integration time. Casa XPS software (version 2.3.18 PR 1.0) was used for peak deconvolution.

Zeta potential was acquired with a Zetasizer Nano ZS (Malvern Instruments) at an angle of 173° and temperature of 25 °C. Sample sizes were measured in triplicate in disposable folded capillary zeta cells.

Photoluminescence spectra were acquired for samples in glass cuvettes with 1 cm pathlength. Absorbance was captured on a Varian Cary 50 Bio ultraviolet-visible spectrophotometer. Background (cuvettes containing only solvent) was subtracted from all absorbance plots. Photoluminescence emission (PL) and photoluminescence excitation (PLE) spectra were captured on either a Varian Cary Eclipse fluorescence spectrometer (for wavelengths below 850 nm) or on a Fluorolog3 Fluorimeter (for wavelengths above 800 nm). PL spectra were captured upon excitation at 400 nm. For quantum yield measurements PL was excited at 350 nm and Rhodamine B was used as a standard (quantum yield of 0.49 in ethanol).[35] Quantum yield was calculated according to the relation: $QY_{Si}=(QY_{ref})(A_{ref}/A_{Si})(I_{si}/I_{ref})(\eta_{Si}/\eta_{ref})^2$, where QY is the quantum yield, A is the absorbance at 350 nm, I is the PL intensity, η is the solvent refractive index, and the subscripts *Si* and *ref* refer to the Si nanocrystal samples and Rhodamine B reference, respectively.

5.3 Results and Discussion

5.3.1 Si Nanocrystal Hydrolysis and Transfer into Water

Ethyl ester capped Si nanocrystals were prepared by thermal annealing of HSQ at either 1200 °C or 1250 °C and passivating with ethyl 10-undecenoate. Nanocrystals prepared at 1200 °C were 4.7 ± 0.9 nm in diameter and had a peak emission wavelength of 952 nm, while nanocrystals prepared at 1250 °C were 6.3 ± 1.1 nm in diameter and had a peak emission wavelength of 985 nm. The ester capped Si nanocrystals could be directly dispersed in a 1:1 v/v mixture of ethanol and toluene. After hydrolysis of the ester group on the capping ligands, the nanocrystals could be dispersed in ethanol. The nanocrystals were transferred to pH 8.5 water which deprotonates some of the carboxylic acid groups and results in electrostatic colloidal stability between the anionic nanocrystals (Figure 5.1).

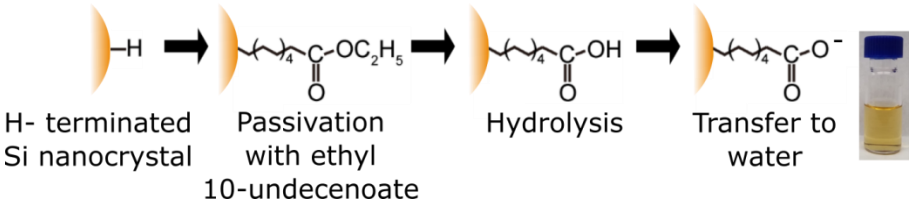

Figure 5.1 Illustration of Si nanocrystal passivation, hydrolysis, and transfer to water. The photograph shows a vial containing 6.3 nm Si nanocrystals dispersed in water.

After transfer into water, the Si nanocrystal dispersions appeared optically clear, suggesting that the nanocrystals were well dispersed. The zeta potential of the 6.3 nm Si nanocrystals in pH 8.5 water was -37.7 mV. Colloidal dispersions with zeta potential absolute values greater than 30 mV are considered stable and unlikely to aggregate. Thus, the pH 8.5 water was high enough to deprotonate a sufficient percentage of ligand carboxylic acid groups to confer electrostatic repulsion between the nanoparticles.

Figure 5.2 shows TEM images of the nanocrystals at each stage in the process, and after one week in water. The images show that the nanocrystals maintain their integrity after hydrolysis of the ester group on the capping ligands as well as after dispersion in water. However, after one week in water the 4.7 nm nanocrystals were no longer visible under TEM, and only amorphous material was observed on the TEM grid. For the 6.3 nm nanocrystals, after one week in water nanocrystals were observed embedded in large, irregularly shaped material.

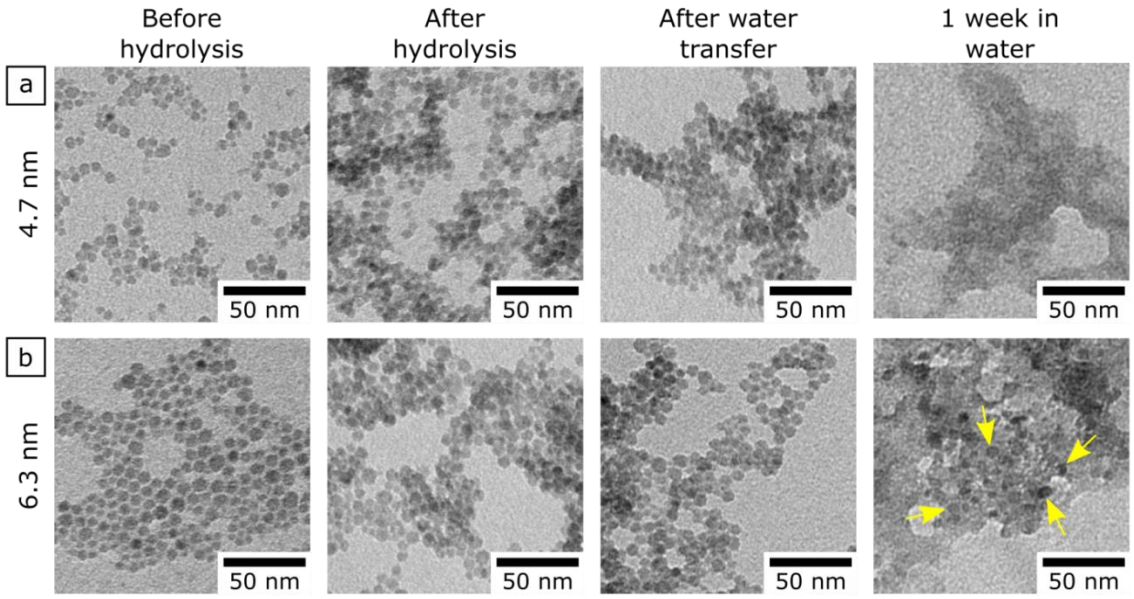

Figure 5.2 Transmission electron microscopy images of Si nanocrystals capped with ethyl 10-undecnocate with diameters of (a) 4.7 nm or (b) 6.3 nm. After one week in water the 6.3 nm nanocrystals (yellow arrows) appeared embedded in larger, amorphous material.

Si is prone to oxidation, however, alkene ligand passivation is an effective way to prevent oxidative degradation of Si nanocrystals. The ligand coverage on the Si nanocrystals was determined by thermal gravimetric analysis (TGA) performed under air flow. The TGA data in Figure 5.3 show a mass loss event between 250-400 °C, which

can be attributed to removal of the ligands. At higher temperatures, the mass of the sample begins to increase again as Si transforms into SiO_2 in the air atmosphere. The TGA results indicate that the 4.7 nm Si nanocrystals are 51% by mass Si (the remaining mass is ligand), which corresponds to a ligand density of 4.9 ligands/nm^2. In comparison, the 6.3 nm Si nanocrystals are 62% by mass Si, which corresponds to a ligand density of 4.3 ligands/nm^2. These results are comparable to surface coverage reported with alkene ligands (3-6 ligands/nm^2 for particles in the same size range).[22]

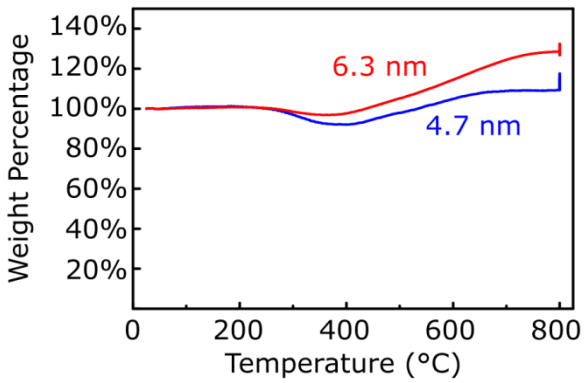

Figure 5.3 TGA results for ethyl 10-undecenoic acid Si nanocrystals performed in air atmosphere.

FTIR spectra, XPS and XRD characterization of 6.3 nm Si nanocrystals after hydrolysis and transfer into water is presented in Figure 5.4. FTIR spectra (Figure 5.4a) show that while CH_3 stretching is present before hydrolysis, after hydrolysis and transfer to water this stretch disappears. This indicates that the ester groups are hydrolyzed into carboxylic acids. In all spectra Si-H stretching is observed, indicating incomplete passivation of the Si nanocrystal surface. The Si-O stretching at 1100 cm^{-1} is also present in all three spectra, and indicates surface oxidation. Since all samples were dried out of solution overnight, it is possible that some of the oxidation observed was the result of

sample preparation. XRD spectra (Figure 5.4b) demonstrate that the Si nanocrystals maintain their diamond cubic lattice. The crystal size can be estimated from the XRD peak widths using the Scherrer equation.[36] The calculated sizes were: 5.8 ± 0.4 nm before hydrolysis, 5.1 ± 0.6 nm after hydrolysis, and 5.6 ± 0.2 nm after transfer into water (n=3 for 3 peaks used in analysis of each XRD pattern). These sizes indicate the crystalline cores remain at nearly constant size through hydrolysis and water transfer. Surface oxidation was characterized using XPS (Figure 5.4c). Before hydrolysis, the crystalline Si^0 peaks are observed. There is also contribution from Si-C (indicating surface passivation) as well as from peaks corresponding to surface oxidation (Si^{1+}, Si^{2+}, Si^{3+}, and Si^{4+}). After hydrolysis and transfer into water, the surface becomes more oxidized. After one week in water, there was no Si^0 identified and the sample appeared to be completely oxidized. Though there may be some crystalline material remaining (see TEM of 6.3 nm Si nanocrystals after one week in water, Figure 5.2b), oxidation of the outer Si nanocrystal surface may obscure the interior crystalline material. The substantial Si oxidation was anticipated for these samples, since pH 8.5 water (adjusted with NaOH) was used for hydrolysis and to store the Si nanocrystal dispersion, and hydroxide ions contribute to Si oxidation.[37]

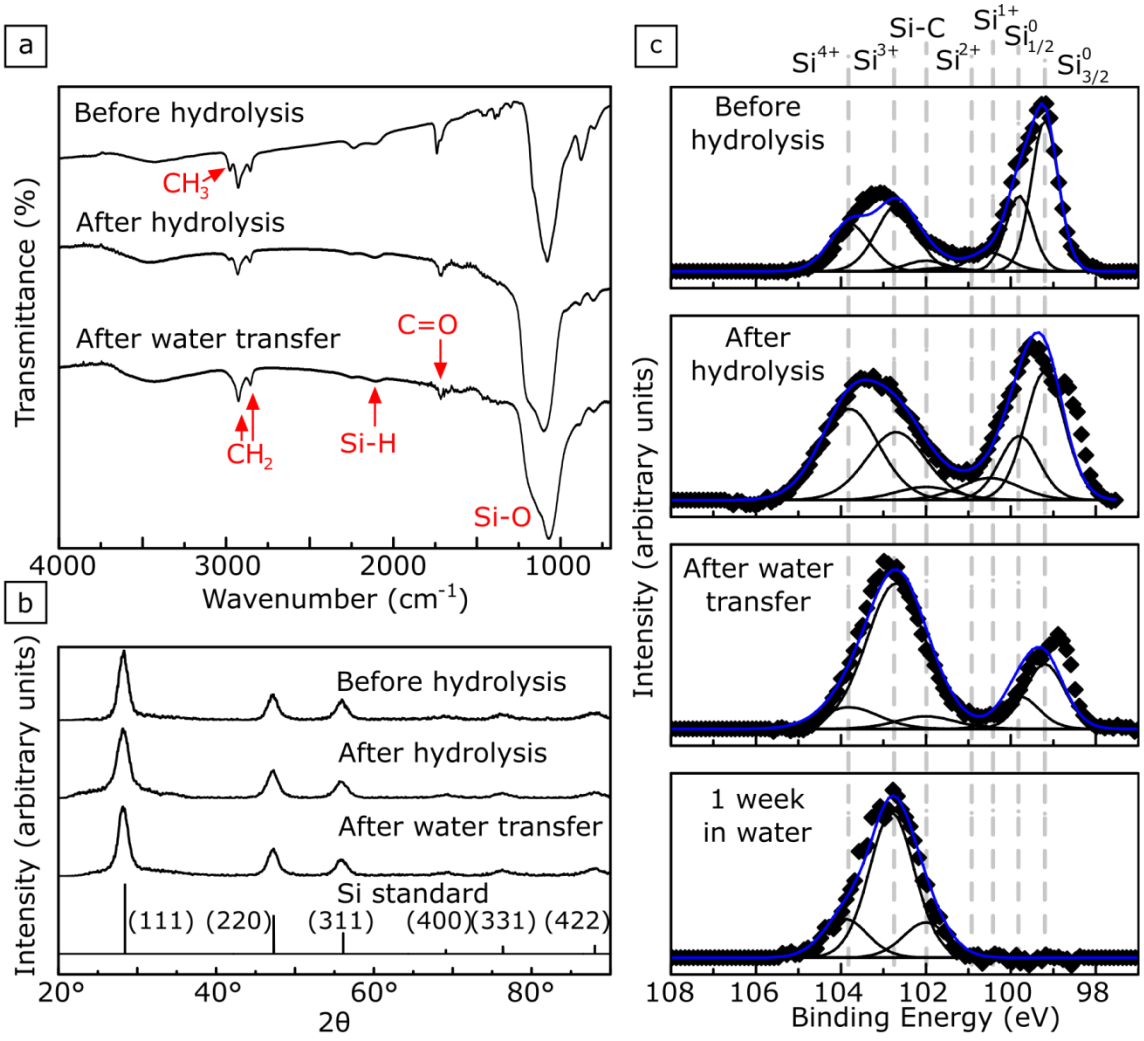

Figure 5.4 Characterization results of 6.3 nm Si nanocrystal hydrolysis and transfer into water. (a) FTIR spectra show the hydrolysis of ethyl 10-undecenoate ligands into carboxylic acids. (b) XRD patterns for Si nanocrystals throughout the process show no change to the crystal structure. The reference pattern is for diamond cubic silicon (PDF 027-1402, with a=b=c=0.543088 nm). (c) XPS spectra for Si nanocrystals. Raw data (black diamonds) was fit (blue line) by summing Si peak contributions (black lines).

5.3.2 Photoluminescence of NIR Emitting Si Nanocrystals

The photoluminescence stability of the NIR emitting Si nanocrystals was measured. Figure 5.5 shows the normalized PL and absorbance spectra for the Si nanocrystals. The peak emission wavelength before hydrolysis was 952 nm for the 4.7 nm Si nanocrystals and 985 nm for the 6.3 nm Si nanocrystals dispersed in 1:1 v/v ethanol:toluene, which is consistent with the PL emission observed for alkene coated Si nanocrystals synthesized from HSQ at the same temperatures.[22] The PL emission peak wavelength did not change after hydrolyzing the ester and dispersing the nanocrystals in ethanol; however, it did shift 20 nm towards the blue after dispersing in pH 8.5 water (to 934 nm and 967 nm for the 4.7 nm and 6.3 nm Si nanocrystals, respectively). The PL blue-shift suggests that as the nanocrystal surfaces oxidize, the crystalline Si core shrinks or trap states are introduced.[38]

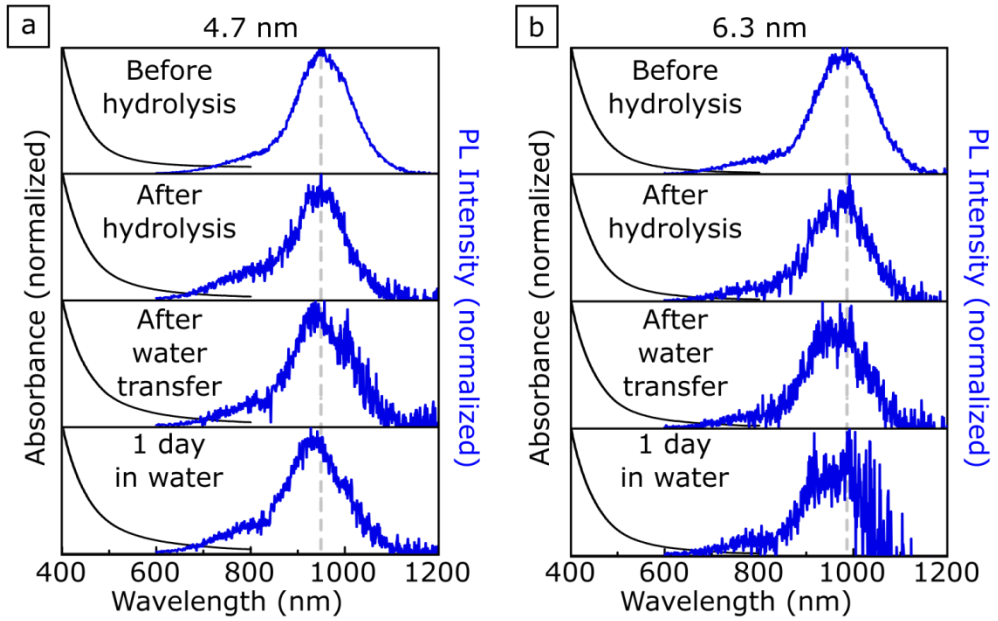

Figure 5.5 Normalized absorbance and PL emission spectra for (a) 4.7 nm and (b) 6.3 nm Si nanocrystals, showing changes in spectra after hydrolysis of ethyl 10-undecenoate and then transfer into water. Si nanocrystals were dispersed in 1:1 v/v ethanol:toluene before hydrolysis, in ethanol after hydrolysis, and in pH 8.5 water after water transfer. Grey dashed lines indicate peak PL wavelength before hydrolysis (952 nm for the 4.7 nm Si nanocrystals and 985 nm for the 6.3 nm Si nanocrystals).

Si nanocrystal PL was further characterized by estimating the quantum yield. Quantum yield (QY) measurements of NIR emitters are challenging because of a lack of adequate infrared reference standards.[39] Here, Rhodamine B was used as a standard, although the dye does not have significant spectral overlap with the NIR Si nanocrystals, and thus the values calculated are an estimate of quantum yield magnitude. Figure 5.6 shows the PL quantum yields for 4.7 nm and 6.3 nm Si nanocrystals measured before hydrolysis, after hydrolysis, and after transfer into water. The QY for both samples were very low (< 1.0%) in comparison to alkene capped Si nanocrystals in the same size range which exhibit quantum yields of 30-45%.[40] In this case, the ethyl 10-undecenoate capped nanocrystals were considerably more oxidized than nanocrystals of the same size

passivated with alkenes, which may contribute to the low QY.[40] Lower PL QY has previously been observed for carboxylic acid terminated Si nanocrystals in comparison to alkene capped nanocrystals,[33] and thus the low QY may be attributed to the ligands used and surface oxidation. The QY was further reduced for both samples after hydrolyzing the ester and transferring into water.[29] Almost no emission was captured from the NIR emitting Si nanocrystals after one day in water.

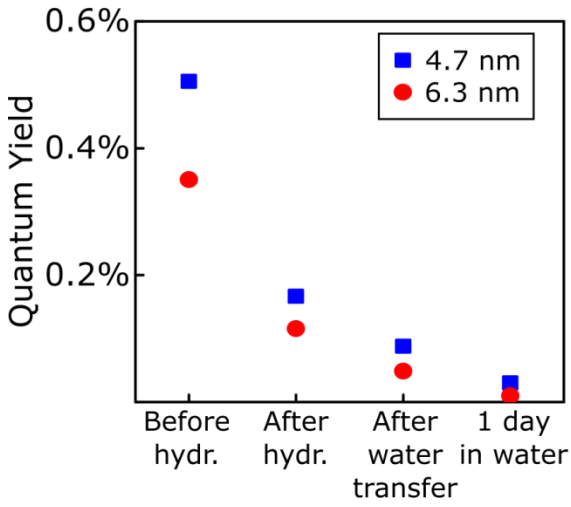

Figure 5.6 PL emission quantum yields of 4.7 nm and 6.3 nm Si nanocrystal samples. Si nanocrystals were dispersed in 1:1 v/v ethanol:toluene before hydrolysis, in ethanol after hydrolysis, and in pH 8.5 water after water transfer.

5.4 Conclusion

The aqueous dispersibility of NIR emitting Si nanocrystals has been demonstrated. However, the photoluminescence quantum yields for the Si nanocrystals, particularly after transfer into water, were extremely low and thus these particles would likely not be useful for bioimaging. For these Si nanocrystals to be sufficiently bright for

bioimaging applications, improvements to the quantum yield through the use of different ligands, polymer shells, or surfactants will be required.[29] Adding polymer shells onto the Si nanocrystals would not only deter surface oxidation, but can also support colloidal stability.[41] Additionally, while the Si nanocrystals emit in the NIR, here we used excitation in the visible range (400 nm). In order to take full advantage of NIR wavelengths for *in vivo* imaging it would be ideal for NIR excitation to be used as well. NIR excitation has been explored using up-converting nanoparticles, as well as through the use of multi-photon excitation of semiconductor quantum dots.[11,21,42] Si nanocrystals have already been demonstrated to have two photon absorption,[43] and thus two photon excitation can enable the use of NIR excitation and emission. There is opportunity to continue developing NIR emitting Si nanocrystals for bioimaging applications, however improvements to the photoluminescence stability must be accomplished for these particles to be bright enough for *in vivo* imaging.

5.5 REFERENCES

(1) Weissleder, R. A Clearer Vision for in Vivo Imaging. *Nat. Biotechnol.* **2001**, *19*, 316–317.

(2) Ntziachristos, V.; Bremer, C.; Weissleder, R. Fluorescence Imaging with Near-Infrared Light: New Technological Advances That Enable in Vivo Molecular Imaging. *Eur. Radiol.* **2003**, *13*, 195–208.

(3) Yao, J.; Yang, M.; Duan, Y. Chemistry, Biology, and Medicine of Fluorescent Nanomaterials and Related Systems: New Insights into Biosensing, Bioimaging, Genomics, Diagnostics, and Therapy. *Chem. Rev.* **2014**, *114*, 6130–6178.

(4) Stolik, S.; Delgado, J. A.; Pérez, A.; Anasagasti, L. Measurement of the Penetration Depths of Red and near Infrared Light in Human "Ex Vivo" Tissues. *J. Photochem. Photobiol. B* **2000**, *57*, 90–93.

(5) Frangioni, J. V. In Vivo Near-Infrared Fluorescence Imaging. *Curr. Opin. Chem. Biol.* **2003**, *7*, 626–634.

(6) Bashkatov, A. N.; Genina, E. A.; Kochubey, V. I.; Tuchin, V. V. Optical Properties of Human Skin, Subcutaneous and Mucous Tissues in the Wavelength Range from 400 to 2000 Nm. *J. Phys. Appl. Phys.* **2005**, *38*, 2543.

(7) Kosaka, N.; Ogawa, M.; Choyke, P. L.; Kobayashi, H. Clinical Implications of Near-Infrared Fluorescence Imaging in Cancer. *Future Oncol. Lond. Engl.* **2009**, *5*, 1501–1511.

(8) Hilderbrand, S. A.; Weissleder, R. Near-Infrared Fluorescence: Application to in Vivo Molecular Imaging. *Curr. Opin. Chem. Biol.* **2010**, *14*, 71–79.

(9) Kim, S.; Lim, Y. T.; Soltesz, E. G.; De Grand, A. M.; Lee, J.; Nakayama, A.; Parker, J. A.; Mihaljevic, T.; Laurence, R. G.; Dor, D. M.; Cohn, L. H.; Bawendi, M. G.; Frangioni, J. V. Near-Infrared Fluorescent Type II Quantum Dots for Sentinel Lymph Node Mapping. *Nat. Biotechnol.* **2004**, *22*, 93–97.

(10) Cai, W.; Shin, D.-W.; Chen, K.; Gheysens, O.; Cao, Q.; Wang, S. X.; Gambhir, S. S.; Chen, X. Peptide-Labeled Near-Infrared Quantum Dots for Imaging Tumor Vasculature in Living Subjects. *Nano Lett.* **2006**, *6*, 669–676.

(11) Xu, C. T.; Svensson, N.; Axelsson, J.; Svenmarker, P.; Somesfalean, G.; Chen, G.; Liang, H.; Liu, H.; Zhang, Z.; Andersson-Engels, S. Autofluorescence Insensitive Imaging Using Upconverting Nanocrystals in Scattering Media. *Appl. Phys. Lett.* **2008**, *93*, 171103.

(12) Li, L.; Daou, T. J.; Texier, I.; Kim Chi, T. T.; Liem, N. Q.; Reiss, P. Highly Luminescent CuInS2/ZnS Core/Shell Nanocrystals: Cadmium-Free Quantum Dots for In Vivo Imaging. *Chem. Mater.* **2009**, *21*, 2422–2429.

(13) Choi, H. S.; Ipe, B. I.; Misra, P.; Lee, J. H.; Bawendi, M. G.; Frangioni, J. V. Tissue- and Organ-Selective Biodistribution of NIR Fluorescent Quantum Dots. *Nano Lett.* **2009**, *9*, 2354–2359.

(14) Allen, P. M.; Liu, W.; Chauhan, V. P.; Lee, J.; Ting, A. Y.; Fukumura, D.; Jain, R. K.; Bawendi, M. G. InAs(ZnCdS) Quantum Dots Optimized for Biological Imaging in the Near-Infrared. *J. Am. Chem. Soc.* **2010**, *132*, 470–471.

(15) Panthani, M. G.; Khan, T. A.; Reid, D. K.; Hellebusch, D. J.; Rasch, M. R.; Maynard, J. A.; Korgel, B. A. In Vivo Whole Animal Fluorescence Imaging of a Microparticle-Based Oral Vaccine Containing (CuInSexS2–x)/ZnS Core/Shell Quantum Dots. *Nano Lett.* **2013**, *13*, 4294–4298.

(16) Welsher, K.; Liu, Z.; Sherlock, S. P.; Robinson, J. T.; Chen, Z.; Daranciang, D.; Dai, H. A Route to Brightly Fluorescent Carbon Nanotubes for Near-Infrared Imaging in Mice. *Nat. Nanotechnol.* **2009**, *4*, 773-780.

(17) Robinson, J. T.; Hong, G.; Liang, Y.; Zhang, B.; Yaghi, O. K.; Dai, H. In-Vivo Fluorescence Imaging in the NIR-II with Long Circulating Carbon Nanotubes

Capable of Ultra-High Tumor Uptake. *J. Am. Chem. Soc.* **2012**, *134*, 10664–10669.

(18) Nyk, M.; Kumar, R.; Ohulchanskyy, T. Y.; Bergey, E. J.; Prasad, P. N. High Contrast In Vitro and In Vivo Photoluminescence Bioimaging Using Near Infrared to Near Infrared Up-Conversion in Tm3+ and Yb3+ Doped Fluoride Nanophosphors. *Nano Lett.* **2008**, *8*, 3834–3838.

(19) Chen, G.; Shen, J.; Ohulchanskyy, T. Y.; Patel, N. J.; Kutikov, A.; Li, Z.; Song, J.; Pandey, R. K.; Ågren, H.; Prasad, P. N.; Han, G. (α-NaYbF4:Tm3+)/CaF2 Core/Shell Nanoparticles with Efficient Near-Infrared to Near-Infrared Upconversion for High-Contrast Deep Tissue Bioimaging. *ACS Nano* **2012**, *6*, 8280–8287.

(20) Park, J.-H.; Gu, L.; Maltzahn, G. von; Ruoslahti, E.; Bhatia, S. N.; Sailor, M. J. Biodegradable Luminescent Porous Silicon Nanoparticles for in Vivo Applications. *Nat. Mater.* **2009**, *8*, 331–336.

(21) Kim, D.; Kang, J.; Wang, T.; Ryu, H. G.; Zuidema, J. M.; Joo, J.; Kim, M.; Huh, Y.; Jung, J.; Ahn, K. H.; Kim, K. H.; Sailor, M. J. Two-Photon In Vivo Imaging with Porous Silicon Nanoparticles. *Adv. Mater.* **2017**, 1703309.

(22) Hessel, C. M.; Reid, D.; Panthani, M. G.; Rasch, M. R.; Goodfellow, B. W.; Wei, J.; Fujii, H.; Akhavan, V.; Korgel, B. A. Synthesis of Ligand-Stabilized Silicon Nanocrystals with Size-Dependent Photoluminescence Spanning Visible to Near-Infrared Wavelengths. *Chem. Mater.* **2012**, *24*, 393–401.

(23) Henderson, E. J.; Shuhendler, A. J.; Prasad, P.; Baumann, V.; Maier-Flaig, F.; Faulkner, D. O.; Lemmer, U.; Wu, X. Y.; Ozin, G. A. Colloidally Stable Silicon Nanocrystals with Near-Infrared Photoluminescence for Biological Fluorescence Imaging. *Small* **2011**, *7*, 2507–2516.

(24) O'Farrell, N.; Houlton, A.; Horrocks, B. R. Silicon Nanoparticles: Applications in Cell Biology and Medicine. *Int. J. Nanomedicine* **2006**, *1*, 451–472.

(25) Erogbogbo, F.; Yong, K.-T.; Roy, I.; Xu, G.; Prasad, P. N.; Swihart, M. T. Biocompatible Luminescent Silicon Quantum Dots for Imaging of Cancer Cells. *ACS Nano* **2008**, *2*, 873–878.

(26) Hessel, C. M.; Rasch, M. R.; Hueso, J. L.; Goodfellow, B. W.; Akhavan, V. A.; Puvanakrishnan, P.; Tunnel, J. W.; Korgel, B. A. Alkyl Passivation and Amphiphilic Polymer Coating of Silicon Nanocrystals for Diagnostic Imaging. *Small* **2010**, *6*, 2026–2034.

(27) Erogbogbo, F.; Yong, K.-T.; Roy, I.; Hu, R.; Law, W.-C.; Zhao, W.; Ding, H.; Wu, F.; Kumar, R.; Swihart, M. T.; Prasad, P. N. In Vivo Targeted Cancer Imaging, Sentinel Lymph Node Mapping and Multi-Channel Imaging with Biocompatible Silicon Nanocrystals. *ACS Nano* **2010**, *5*, 413–423.

(28) Zhao, F.; Zhao, Y.; Liu, Y.; Chang, X.; Chen, C.; Zhao, Y. Cellular Uptake, Intracellular Trafficking, and Cytotoxicity of Nanomaterials. *Small* **2011**, *7*, 1322–1337.

(29) Li, Z. F.; Ruckenstein, E. Water-Soluble Poly(Acrylic Acid) Grafted Luminescent Silicon Nanoparticles and Their Use as Fluorescent Biological Staining Labels. *Nano Lett.* **2004**, *4*, 1463–1467.

(30) Warner, J. H.; Hoshino, A.; Yamamoto, K.; Tilley, R. D. Water-Soluble Photoluminescent Silicon Quantum Dots. *Angew. Chem.* **2005**, *117*, 4626–4630.

(31) Sato, S.; Swihart, M. T. Propionic-Acid-Terminated Silicon Nanoparticles: Synthesis and Optical Characterization. *Chem. Mater.* **2006**, *18*, 4083–4088.

(32) Clark, R. J.; Dang, M. K. M.; Veinot, J. G. C. Exploration of Organic Acid Chain Length on Water-Soluble Silicon Quantum Dot Surfaces. *Langmuir* **2010**, *26*, 15657–15664.

(33) Yu, Y.; Hessel, C. M.; Bogart, T. D.; Panthani, M. G.; Rasch, M. R.; Korgel, B. A. Room Temperature Hydrosilylation of Silicon Nanocrystals with Bifunctional Terminal Alkenes. *Langmuir* **2013**, *29*, 1533–1540.

(34) Klein, D. *Organic Chemistry*; John Wiley & Sons, Inc., 2012.

(35) Casey, K. G.; Quitevis, E. L. Effect of Solvent Polarity on Nonradiative Processes in Xanthene Dyes: Rhodamine B in Normal Alcohols. *J. Phys. Chem.* **1988**, *92*, 6590–6594.

(36) Patterson, A. L. The Scherrer Formula for X-Ray Particle Size Determination. *Phys. Rev.* **1939**, *56*, 978–982.

(37) *Colloidal Silica: Fundamentals and Applications*; Bergna, H. E.; Roberts, W. O., Eds.; CRC Press, 2005.

(38) Sinelnikov, R.; Dasog, M.; Beamish, J.; Meldrum, A.; Veinot, J. G. C. Revisiting an Ongoing Debate: What Role Do Surface Groups Play in Silicon Nanocrystal Photoluminescence? *ACS Photonics* **2017**, *4*, 1920–1929.

(39) van Veggel, F. C. J. M. Near-Infrared Quantum Dots and Their Delicate Synthesis, Challenging Characterization, and Exciting Potential Applications. *Chem. Mater.* **2014**, *26*, 111–122.

(40) Yu, Y.; Fan, G.; Fermi, A.; Mazzaro, R.; Morandi, V.; Ceroni, P.; Smilgies, D.-M.; Korgel, B. A. Size-Dependent Photoluminescence Efficiency of Silicon Nanocrystal Quantum Dots. *J. Phys. Chem. C* **2017**, *121*, 23240–23248.

(41) Pinaud, F.; Michalet, X.; Bentolila, L. A.; Tsay, J. M.; Doose, S.; Li, J. J.; Iyer, G.; Weiss, S. Advances in Fluorescence Imaging with Quantum Dot Bio-Probes. *Biomaterials* **2006**, *27*, 1679–1687.

(42) Denk, W.; Strickler, J. H.; Webb, W. W. Two-Photon Laser Scanning Fluorescence Microscopy. *Science* **1990**, *248*, 73–76.

(43) He, G. S.; Zheng, Q.; Yong, K.-T.; Erogbogbo, F.; Swihart, M. T.; Prasad, P. N. Two- and Three-Photon Absorption and Frequency Upconverted Emission of Silicon Quantum Dots. *Nano Lett.* **2008**, *8*, 2688–2692.

Chapter 6: Spectral and Temporal Multiplexing for Colocalization of Silicon Nanocrystals in Mouse Macrophage Cells

6.1 INTRODUCTION

The field of bioimaging with fluorescent probes has grown tremendously for applications in research and medicine due to the ability to quickly examine biomolecules and tissue with minimal equipment.[1–5] Silicon (Si) based nanoparticles are biocompatible and exhibit bright, size-tunable photoluminescence (PL) in the visible to infrared wavelengths and have been demonstrated for *in vitro* and *in vivo* bioimaging applications.[6–16] However, challenges remain with using Si nanocrystals for bioimaging. First, while the Si nanocrystals exhibit size dependent emission, the emission spectrum is broad, often with full width at half maximum (FWHM) on the order of 150-200 nm.[14,17] Compared to other semiconductor quantum dots which have narrow emission spectra,[18] the broad emission spectrum of Si nanocrystals makes it difficult to spectrally multiplex simultaneously with multiple fluorescent probes without conducting multiple scans of the sample, which can result in fluorophore photobleaching.[1] The development of temporal multiplexing has offered new opportunities for simultaneously imaging multiple probes with spectral overlap.[1,19] In fluorescence lifetime imaging microscopy (FLIM), the fluorescence decay is monitored at each pixel using time-correlated single photon counting (TCSPC), enabling fluorophores with similar emission color to be distinguished and mapped independently according to their PL lifetime.[19] FLIM has been used to simultaneously image several fluorophores using both spectral and temporal separation.[20] For quantum dots, which typically have longer PL lifetimes (10's-100's of ns) than fluorescent dyes (< 10 ns),[18] TCSPC has been used either as a mechanism for gating PL between short lived and long lived emission (for example, to remove short-lived cell autofluorescence),[21–24] or as a direct measure of PL lifetime, which can be useful for

sensing applications.[22,25–34] Si based nanoparticles have significantly longer decay times on the order of 10's of microseconds[13,17,35] and can be used as probes for lifetime gating since any remaining fluorescence after several nanoseconds can be attributed to the Si nanocrystals.[16,36,37]

The other remaining challenge for bioimaging with Si nanocrystals is that since Si is an indirect bandgap semiconductor with a wide apparent Stokes shift, excitation is typically accomplished with blue wavelengths. However, red to infrared wavelengths are optimal for bioimaging applications because light at these wavelengths can penetrate deep into tissue and biomolecule autofluorescence is minimized.[38,39] Multiphoton microscopy can allow for imaging using longer wavelengths. Instead of a single photon exciting a molecule or quantum dot from the ground state to the excited state, in multi-photon microscopy two or more photons are absorbed at once.[40,41] Since the photons must be absorbed near-simultaneously the probability of two-photon absorption depends quadratically on the incident light intensity and requires a high flux of excitation photons from a pulsed laser source.[1,41] The requirement for high power density provides the added benefit of confining excitation to a small focal volume, which allows for three dimensional spatial resolution not possible with single photon excitation. Additionally, because selection rules for two-photon absorption processes in molecular dyes are different than single-photon selection rules, dyes that require separate one-photon excitation wavelengths may be excited with the same two-photon excitation wavelengths.[41] Si nanoparticles have two-photon absorption cross-sections comparable to fluorescent dyes and quantum dots, and two-photon microscopy has been demonstrated with Si nanoparticles.[12,42,43]

Here, we demonstrate the use of FLIM with two-photon excitation of Si nanocrystal quantum dots and fluorescent dyes to image fixed cells with a single scan.

Spectral separation is used to resolve the locations of blue vs red emitters and temporal separation to resolve the locations of fast vs slow emitters. The spectral and temporal multiplexing was applied to study the uptake mechanism of 10-undecenoic acid coated Si nanocrystals in mouse macrophage cells.

6.2 EXPERIMENTAL METHODS

6.2.1 Materials

Hydrogen silsesquoixane (HSQ, Fox®-16) was purchased from Dow Corning. 10-Undecenoic acid, sodium hydroxide (NaOH), hydrofluoric acid (HF), and Dulbecco's Modified Eagle Medium (DMEM) were purchased from Sigma. Ethanol, hexanes, toluene, and hydrochloric acid (HCl) were purchased from Fisher. Rhodamine B was purchased from Acros. Fetal bovine serum (FBS), penicillin-streptomycin, and sodium pyruvate were purchased from Life Technologies. Dextran (10k)-Cascade Blue was purchased from Invitrogen. CellMask Deep Red was purchased from Thermo Fisher Scientific. eFluor 660 conjugated to CD107a (LAMP-1) was purchased from eBioscience. Fluoromount-G and DAPI-Fluoromount-G were purchased from SouthernBiotech. A Millipore Synergy Ultrapure water system operated at 18.2 MΩ/cm was used for deionized water.

6.2.2 Si Nanocrystal Synthesis and Transfer into Water

Silicon (Si) nanocrystals passivated with 10-undecenoic acid were prepared per a previous protocol.[44] Solvent was removed from HSQ and the resulting material was annealed in a tube furnace set to 1100 °C for one hour under forming gas flow. The annealed material (Si nanocrystals embedded in an SiO_2 matrix) was ground by mortar

and pestle and downsized by 9 hours of shaking with borosilicate beads in a wrist action shaker, and then etched while stirring in a solution of 10 ml hydrofluoric acid and 1 ml HCl in the dark for 3 hours. The acids were removed by centrifuging the nanoparticle dispersion (8000 rpm, 5 min) and removing the supernatant. The precipitate was then redispersed in ethanol and centrifuged again. The washing process was repeat for a total of three washes in ethanol and one wash in chloroform. Finally, the nanocrystals were dispersed in 15 ml of 10-undecenoic acid. The dispersion was degassed using three freeze-pump-thaw cycles with liquid nitrogen, and finally left to stir overnight at 35 °C under nitrogen gas flow. The Si nanocrystals were then transferred to a vial with 5 ml of ethanol and the vial was sealed with a septum. The vial was allowed to sit on the benchtop for one month as the dispersion turned from cloudy to clear as the passivation yield increased. The resulting passivated Si nanocrystals were washed with centrifugation using ethanol as the solvent and hexane as the antisolvent. The prepared Si nanocrystals were stored in ethanol until use.

Si nanocrystals were transferred from ethanol to water for cell uptake experiments. The transfer process requires gradual dilution of Si nanocrystals into pH 7.4 water (pH adjusted with NaOH) to deprotonate the distal carboxylic acid groups. The deprotonated carboxyl groups can then electrostatically stabilize the colloidal dispersion. The water transfer was accomplished by adding 5 ml of 5 mg/ml 10-undecenoic acid coated Si nanocrystals in ethanol to a 30 kDa centrifugal filter (EMD Millipore). 2 ml of pH 7.4 water was added and a pipette was used to mix the dispersion. The filter was then centrifuged at 1000 g for 5 min, and the solution that passed through the filter was discarded. An additional 5 ml of water was again added to the dispersion and the filtration process was repeated. A total of five rinses into water were used to completely transfer the nanocrystals into water.

6.2.3 Cell Culture and Incubation with Si Nanocrystals

J774A.1 cells (ATCC) were grown in a humidified 37 ˚C incubator with an atmosphere of 5% CO_2 in cell culture medium containing DMEM supplemented with 10% fetal bovine serum, 100 U/mL penicillin-streptomycin, and 1 mM sodium pyruvate. Cells were seeded on glass coverslips in 6-well plates at a density of 2 X $10^4/cm^2$ three days before the assay. Culture medium was replaced with SiNC and/or 1mg/ml Dextran 10K Cascade Blue and incubated for 30 minutes or 3 hours. The coverslips were then washed 4-5 times with PBS to remove extracellular SiNC. For membrane staining, coverslips were washed three times with PBS and stained with CellMask Deep Red at 0.1X by inverting onto a 95ul droplet on parafilm for 10 min at 37 ˚C. Coverslips were washed three times with PBS before fixation with 4% formaldehyde for 10 min at 37 ˚C followed by three more washes with PBS. For intracellular staining, coverslips were permeabilized with 1% TritonX100 for 10min at 37 ˚C, washed three times with PBS, and blocked with 1%FBS in PBS before 1˚ antibody staining with 1:100 dilution of monoclonal CD107a (LAMP-1) antibody conjugated to eFluor 660 by inverting onto a 95ul droplet on parafilm for 30 minutes at room temp. The coverslips were finally washed three times with 1% FBS in PBS and mounted on glass slides with Fluoromount-G or DAPI Fluoromount-G. Slides were imaged within 1 hour after preparation.

6.2.4 Characterization and Imaging

Transmission electron microscopy (TEM) was conducted on an FEI Tecnai Biotwin TEM operated at 80 kV. Si nanocrystal samples were dropcast on 200 mesh carbon-coated copper grids (Electron Microscopy Science). Si nanocrystal size was estimated from the TEM images by measuring 100 particles.

Photoluminescence (PL) emission spectra were collected on a Varian Cary Eclipse fluorescence spectrometer.

Confocal images using one-photon excitation were captured on a Zeiss LSM 710 Confocal. DAPI was excited at 405 nm and emission was captured from 417-566 nm. Si nanocrystals were excited at 405 nm and emission was captured from 660-740 nm.

The two photon response of Si nanocrystals was characterized by varying the input Ti:sapphire laser power and measuring the emission intensity. 40 µl of Si nanocrystals (1 mg/ml) were dispersed in water. Emitted photons were filtered with a 609/181 nm bandpass filter and recorded by a photomultiplier tube (PMT). Photon counts were monitored by a digital photon counting board (DPC-230 Becker & Hickl GmbH) at increasing laser powers; each measurement was taken in triplicate (error bars represent standard deviation). Background emission was measured using 40 µl of water and the logarithm of the background-subtracted signal values is plotted as a function of logarithmic excitation power.

The PL decay of Si nanocrystals upon two photon excitation was measured with TCSPC using a temporally-gated Ti:sapphire oscillator as the excitation laser. Due to the long fluorescence lifetime of SiNCs (10s of µs), the temporal separation between laser pulses in a Ti:sapphire oscillator (76 MHz, 13 ns) is not sufficient to sample the full decay. To overcome this challenge, an electro-optic modulator was used to generate a short gate of pulsed excitation light with user-controlled inter-gate intervals as previously described.[45] Briefly, a 20-µs gate of excitation pulses was used at a modulation rate of 5 kHz, which resulted in a 200-µs window of measurable fluorescence decay. This window is approximately 2-3 times longer than the SiNC lifetime and is sufficient for sampling the full decay. Emission was filtered with a 609/181 nm bandpass filter.

TCSPC data was processed using Matlab R2017a and ImageJ 1.48v. The JaCOP plugin for ImageJ was used to compute colocalization statistics.[46]

6.3 Results and Discussion

6.3.1 Time Gated Imaging Setup

Figure 6.1a shows an illustration of the microscope used to acquire TCSPC data. A femtosecond titanium: sapphire laser tuned to 800 nm (Mira 900, Coherent) was scanned across the sample to excite the fluorescent samples, and the emission was captured simultaneously by two GaAsP photomultiplier tubes (PMT) (H7422PA-40, Hamamatsu) with 457/50 nm ("blue PMT") and 675/67 nm ("red PMT") bandpass filters in a non-descanned detection scheme. The output current from each PMT was amplified using a preamplifier (HFAC-26, Becker & Hickl GmnH) and routed to the photon counting board (SPC-150, Becker & Hickl GmbH) by a four-channel router (HRT-41, Becker & Hickl GmbH). Fluorescence lifetimes were recorded for an array of 250 x 250 pixels (square area of 58 μm x 58 μm) with 20 ps time resolution and a pixel dwell time of 5 ms. The point spread function of the microscope was characterized by imaging 100-nm fluorescent beads, and the image resolution was 0.35 μm in the plane of the substrate and 1.37 μm perpendicular to the substrate. A timing delay between the laser trigger pulse and fluorescent emission resulted in a shifted lifetime curve with electrical noise at the late time points. The curve was processed and shifted, and the electrical noise was excluded.

Lifetime gating within the red PMT was performed as depicted in Figure 6.1b: at each pixel, 13 ns of PL data were captured and separated into two temporal regions, "R1" and "R2." R1 started at the apex of the photoluminescence (PL) decay curve, and R2

started 9.5 ns seconds later, with each region lasting for 2 ns. Both short-lived dye emission and long-lived Si nanocrystal emission contribute to R1, whereas only the long-lived Si nanocrystal emission is observed in R2. The PL intensity within each time period was summed to give the intensity in the region. Thus, the intensity measured in R2 can be attributed to Si nanocrystals, while a subtraction of intensity at R1 minus intensity at R2 results in the intensity attributed to the short lived red emitting fluorescent dye (R1-R2).

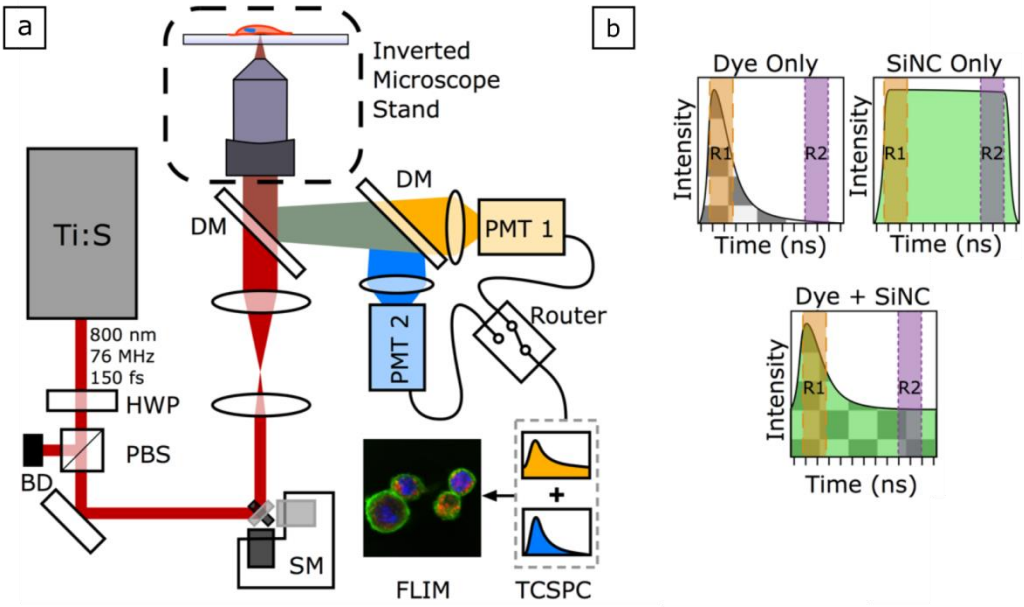

Figure 6.1 (a) Schematic depiction of TCSPC microscope setup, showing data capture from two PMTs to enable simultaneous capture of emission from spectrally distinct probes. HWP: half-wave plate, BD: beam dump, PBS: polarizing beam splitter, SM: scanning mirrors, DM: dichroic mirror. (b) Depiction of lifetime gating, showing the regions "R1" (0-2 ns after the PL peak) and "R2" (9.5-11.5 ns after the peak). The difference between the two sums (R1-R2) corresponds to the contribution from the short-lived emitting dye, while R2 corresponds to the contribution from the long-lived Si nanocrystals.

Si nanocrystals with diameter 2.7 ± 0.6 nm (n=100, as measured by TEM) were prepared and passivated with 10-undecenoic acid as the capping ligand.[44] The resulting

nanocrystals could be dispersed in ethanol or transferred into pH 7.4 water. In water, the distal carboxylic acid group on the ligands deprotonates and imparts electrostatic stability on the colloidal dispersion. Figure 6.2a shows the emission from 10-undecenoic acid Si nanocrystals. The peak emission wavelength was 698 nm, and the measured full width at half maximum of the emission curve was 159 nm.

Figure 6.2b shows the time-dependent PL of the Si nanocrystals as measured with TCSPC using a temporally-gated Ti:sapphire oscillator as the excitation laser. The data fit a triple exponential decay (Equation 6.1),

$$Y = Y_0 + A_1 e^{-(t-t_0)/\tau_1} + A_2 e^{-(t-t_0)/\tau_2} + A_3 e^{-(t-t_0)/\tau_3} \qquad \text{Equation 6.1}$$

with values of A_1=0.40, τ_1=60.54 μs, A_2=0.34, τ_2=16.30 μs, A_3=0.32, τ_3=2.87 μs (R^2=0.991). The PL decays over hundreds of microseconds, typical of Si nanocrystals.[13,17]

Figure 6.2c shows the PL emission intensity as a function of excitation laser power for 10-undecenoic acid capped 2.7 nm Si nanocrystals dispersed in water. Two photon absorption is expected to show a quadratic dependence between the excitation power and emission intensity (I_{PL} α P^2).[40,41] A linear fit of the log-log data confirmed a slope of 1.95 (R^2=0.994), indicating two-photon absorption for Si nanocrystals dispersed in water. Two-photon absorption by Si nanocrystals has been reported in a number of previous studies, with two-photon absorption cross-sections ranging from 1-6 GM.[42,43]

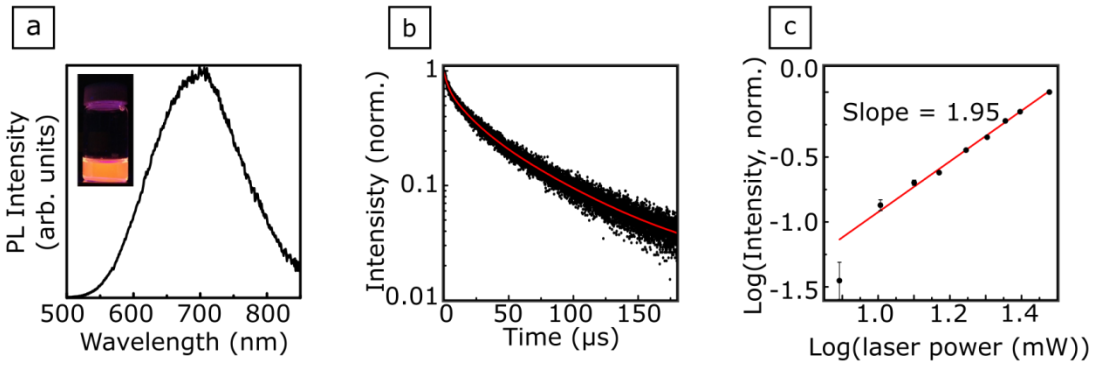

Figure 6.2 (a) PL spectrum for 10-undecenoic acid capped Si nanocrystals excited at 320 nm. Inset shows a vial of 10-undecenoic acid capped Si nanocrystals dispersed in water on a 365 nm ultraviolet lamp. (b) Time-resolved PL emission of Si nanocrystals dispersed in water exhibiting microsecond fluorescence decay lifetime; the data are fit to Equation 6.1 (red line). (c) Si nanocrystal PL intensity measured at increasing excitation laser powers. A linear fit (red line) to the log-log plot had a slope close to 2, confirming two-photon absorption.

6.3.2 Cell Imaging with Si Nanocrystals, CellMask Deep Red, and DAPI

For cell uptake testing, 0.4 ml of Si nanocrystals (2 mg/ml dispersed in water) was added to 1.6 ml of cell culture medium and incubated with J774 mouse macrophage cells at 37 °C for 30 min or 3 hr. Prior to fixing the cells for imaging, a buffer was used to rinse the cells in order to remove non-internalized materials. Macrophage cells, which are part of the body's immune response, employ endocytosis (primarily phagocytosis) to actively internalize nanomaterials.[47–51] Figure 6.3 shows confocal microscopy images using one photon excitation at 405 nm demonstrating that after the 3 hr incubation Si nanocrystals were located throughout the cell interior, but not in the nucleus. In contrast, incubation at 4 °C did not result in Si nanocrystal uptake. These results suggest that the Si nanocrystals are taken up by an active endocytosis pathway and are transported to organelles in the cell interior.[47,51]

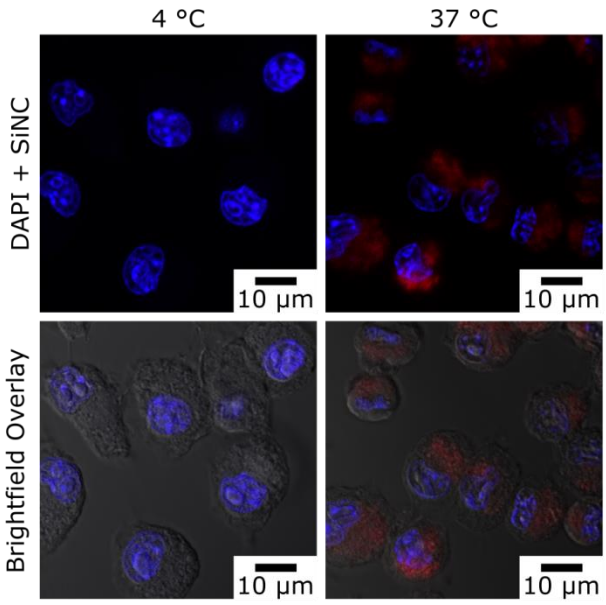

Figure 6.3 One-photon confocal microscopy images of J774 cells after 3 hours of incubation with 10-undecenoic acid capped Si nanocrystals. DAPI emission is false colored blue and Si nanocrystal emission is false colored red.

For two-photon multiplexed cell imaging, macrophage cells were incubated with Si nanocrystals and stained with dyes that selectively locate in the cell membrane and cell nucleus: CellMask Deep Red (a membrane stain) and 4',6-diamidino-2-phenylindole (DAPI, a nucleus stain). Figure 6.4a illustrates the emission wavelengths of the dyes and Si nanocrystals. Si nanocrystal emission overlaps with CellMask Deep Red (emission maximum 666 nm), but the PL lifetimes of the two probes are significantly different, which enables the use of lifetime gating to separate the signals. DAPI emits in blue wavelengths (emission maximum 461 nm), and thus can be separated from the Si nanocrystal and CellMask Deep Red emission using the blue optical filter. The gating parameters for the probes were as follows: (i) CellMask Deep Red emission was defined as the difference between the short lived emission (R1) and long lived emission (R2) in the red PMT, (ii) Si nanocrystal emission was defined as the long-lived emission (R2) in

the red PMT, and (iii) DAPI emission was defined as the short lived emission (R1) in the blue PMT.

Control experiments were conducted by imaging cells stained with no dye, or with only CellMask Deep Red, DAPI, or Si nanocrystals. Figures 6.4b-6.4c demonstrate the relative contribution from each of the control samples to time correlated PL. Figure 6.4c shows that the Si nanocrystal signal is nearly constant on the 13 ns timescale, while cell autofluorescence and the fluorescent dyes exhibit PL decay within the first few nanoseconds. The PL lifetimes for CellMask Deep Red and DAPI were calculated by fitting the PL decays to single exponential functions, and were found to be 1.83 ns and 1.41 ns, respectively. Figure 6.4d shows the relative peak intensities obtained for each control sample when analyzed using the gating parameters. For example, the intensity of (R1-R2) in the red PMT was highest for CellMask Deep Red by at least an order of magnitude compared to the other control samples. Similarly, within the red PMT region R2, the Si nanocrystals exhibited the highest intensities, while in the blue PMT the DAPI signal was most intense. In each case, the photoluminescent probe with the highest intensity was at least one order of magnitude more intense than all the other emitters. These results indicate that there is minimal contribution from other dyes or cell autofluorescence using the gating parameters defined above.

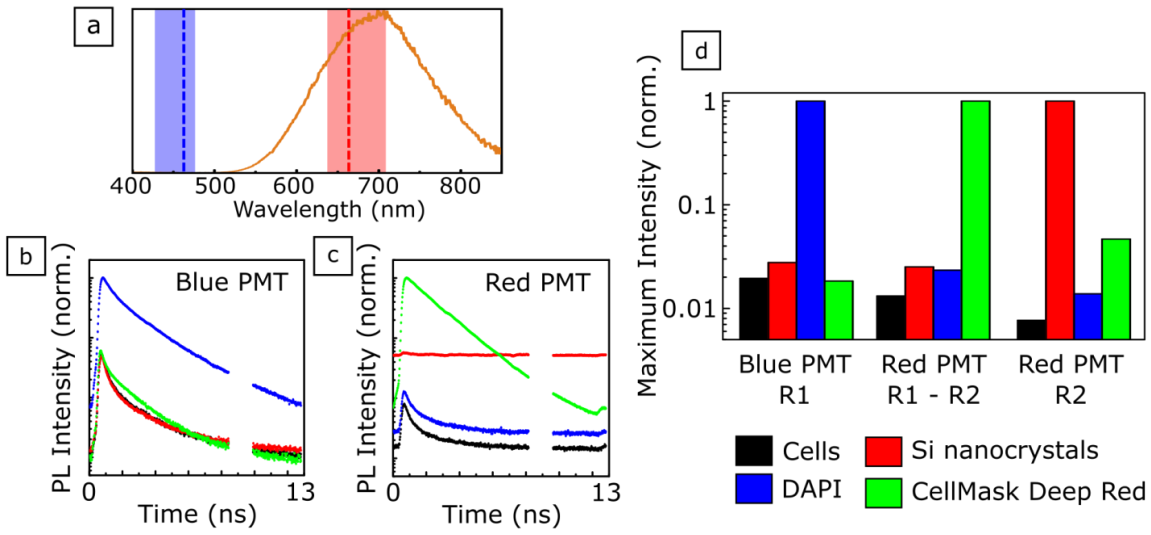

Figure 6.4 (a) Si nanocrystal emission (orange line) shown in relation to peak DAPI emission (blue dotted line) and CellMask Deep Red (red dotted line), with shaded regions showing positions of the blue and red PMT emission filters. For control experiments containing either no probes or just one of the probes, the PL intensity over time for each image was summed in (b) the blue PMT and (c) the red PMT. Samples contained either no probes (cells only, black dots), Si nanocrystals only (red dots), DAPI only (blue dots), or CellMask Deep Red only (green dots). (c) The gating parameters selected were used to analyze images taken of the control samples, and the maximum intensity within each of the defined gating regions was normalized to the highest intensity probe.

Figure 6.5 shows the results of time gated two photon imaging of for cells incubated with Si nanocrystals, DAPI, and CellMask Deep Red simultaneously. Data were captured for three optical sections that were 4 µm apart, providing images at the top, middle, and bottom of the cells. Figure 6.5a shows the time correlated PL curves for the red and blue PMTs as sums across all pixels. The PL intensity in the region R2 (9.5-11.5 ns) in the red PMT corresponds to the long-lived Si nanocrystal emission, and demonstrates that PL emission from the nanocrystals is distinct from the dye PL.

Figure 6.5b shows the intensity maps of the time gated data for each probe. The images are displayed with a 99.99% maximum pixel intensity threshold, and images for

each probe were individually scaled to display the full range of pixel intensities. Overlaid images of the signals from Si nanocrystals, CellMask Deep Red, and DAPI demonstrate the spatial separation of the signals throughout the cells (Figure 6.5c). CellMask Deep Red dye is concentrated at the outer edges of the cells, DAPI is located in the nucleus, and the Si nanocrystals are spread throughout the cell interior. There are regions in the cell where Si nanocrystals appear to have accumulated, most likely in vesicles such as endosomes or lysosomes.[47,48,50–52] The optical sections showing the top, middle, and bottom of the cells confirm that the nanocrystals are dispersed in all three dimensions within the cell interior. By comparing the ratio of Si nanocrystal intensity to DAPI intensity at 30 min and 3 hr in the middle plane, it was estimated that the Si nanocrystal signal doubled, suggesting that Si nanocrystal uptake increased during that time period. The observation of Si nanocrystal emission spread throughout the cell interiors at both the 30 min and 3 hr time points are consistent with the expected kinetics of macrophage endocytosis, which take place on the timescale of minutes to hours.[51,53]

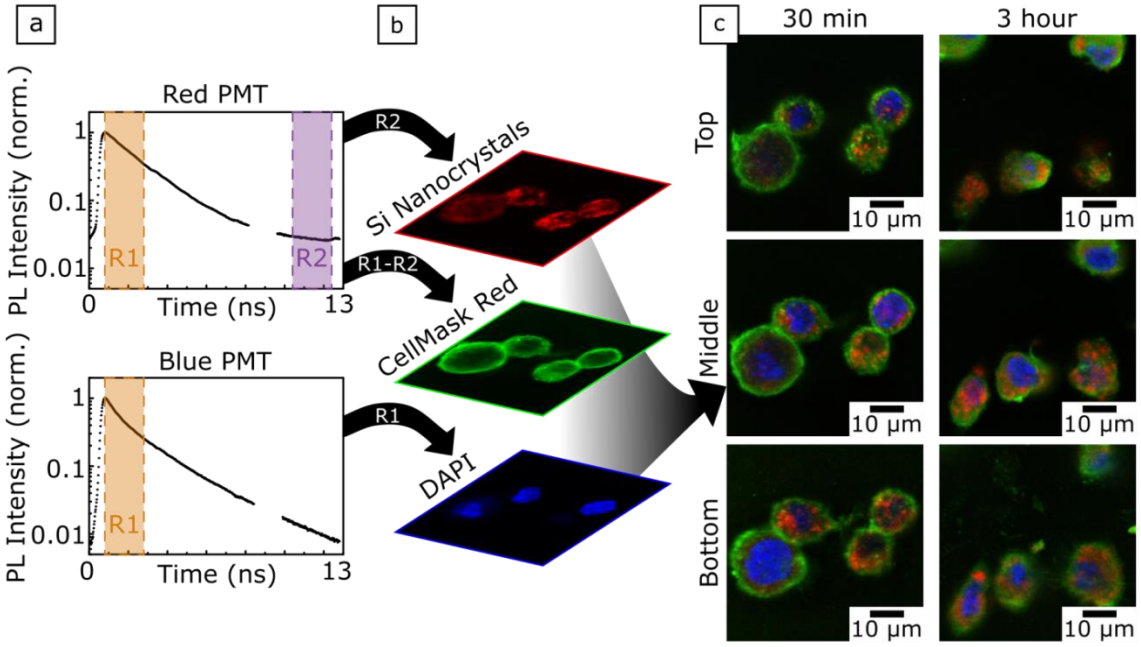

Figure 6.5 (a) PL decay curves captured by the red and blue PMTs and integrated over all pixels show the fast and slow lifetime components of the fluorescent dyes and the Si nanocrystals. A brief gap in the lifetime data was an artifact of the collection system. (b) Intensity maps for each probe were constructed using the summed PL intensity in regions R1 and R2 at each pixel. (c) Overlaid images of the cells with emission from Si nanocrystals (false colored red), CellMask Deep Red dye (false colored green), and DAPI dye (false colored blue), show that the nanocrystals appear throughout the interior of the cell cytoplasm. The optical sections showing the top, middle, and bottom of the cells were taken 4 µm apart.

6.3.3 Localization of Si Nanocrystals in Macrophage Cells

To further demonstrate the utility of lifetime gated imaging with dyes and nanocrystals, we investigated the colocalization of Si nanocrystals with other fluorophores. Dextran (10,000 MW)-Cascade Blue was co-incubated with the Si nanocrystals. Dextran molecules are expected to follow an endocytosis pathway in macrophage cells and thus can be used as a marker for the movement of nanomaterials

into cells.[52] Since lysosomes are often the ultimate destination for materials carried into cells via endocytosis,[47,53] lysosome tagging anti-CD107a (lysosomal-associated-membrane protein 1, LAMP-1) conjugated with EFluor 660 fluorescent dye was used. In these experiments, data processing was performed using the same time gating windows as with the DAPI and CellMask Deep Red experiments, with Cascade Blue emitting in the blue PMT range (emission maximum 420 nm) and EFluor 660 emitting in the red PMT range (emission maximum 668 nm). Figure 6.6 shows the overlaid images taken of the cells at 30 min and 3 hr at three planes 4 μm apart. Compared to the samples stained with DAPI and CellMask Deep Red (Figure 6.5), the images with the dextran and lysosome dyes exhibit significant overlap between the probes: for example, yellow color where the red and green false colored images overlap, indicating colocalization of Si nanocrystals with lysosomes.

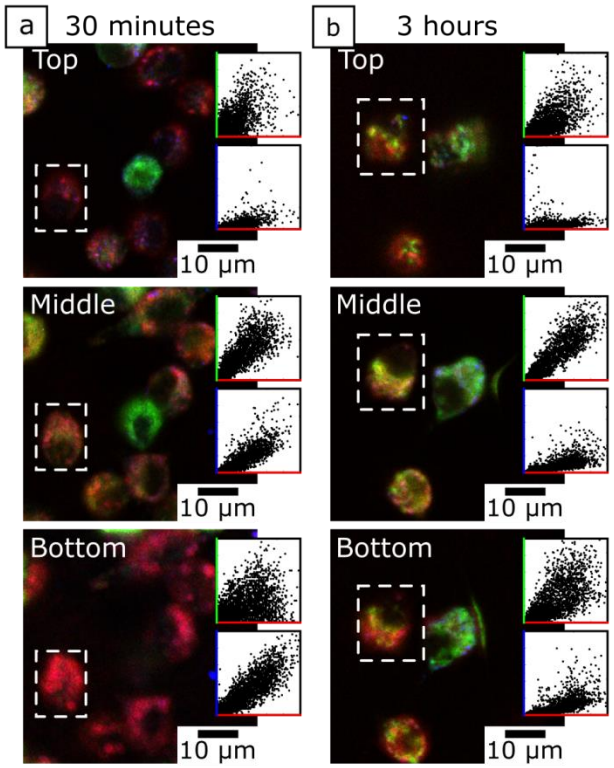

Figure 6.6 Lifetime-gated images showing overlaid Si nanocrystals (false colored red), lysosomes (false colored green), and dextran (false colored blue). The cells were incubated with the Si nanocrystals for either (a) 30 minutes or (b) 3 hours, and the optical sections were taken 4 μm apart to show the top, middle, and bottom of the cells. Cells selected for colocalization analysis are outlined with white dashed boxes. Insets show intensity scatter plots of the selected cells comparing the (top) green-lysosome and red-Si nanocrystal pixel intensities, and the (bottom) blue-dextran and red-Si nanocrystal pixel intensities, with linear data indicating colocalization.

To assess the correlation between overlapping probe emission, pixel intensity scatter plots were constructed to show the relative photoluminescence of each emitter at each pixel. A linear relationship between pixel intensities is expected if there is colocalization between probes.[46] Scatter plots shown in Figure 6.6 provide evidence for partial colocalization of Si nanocrystals with the dextran and lysosomes.

Table 6.1 shows the Pearson's coefficients calculated for single cells in each of the images to quantify the colocalization of Si nanocrystals with either dextran or lysosomes.[46] For Pearson's coefficients, -1 indicates inverse correlation, 0 indicates no correlation, and 1 indicates perfect correlation. For dextran and Si nanocrystals the colocalization was most evident at the top and middle of the cells, with a slight decrease in colocalization at 3 hr compared to at 30 min. These results suggest that while Si nanocrystals and dextran may be initially internalized using similar endocytotic pathways, over time the particles may be processed differently inside the cells. This may be due to factors such as differences in size or surface charge between the dextran and Si nanocrystals, and the specific type of endocytosis (for example, clathrin-dependent or caveolin-dependent endocytosis).[47,54] In contrast, the Si nanocrystals show increased colocalization with lysosomes at the 3 hr time point compared to at 30 min. In endocytosis nanomaterials are internalized through an energy dependent process and transferred through vesicles (such as endosomes) to lysosomes,[47] and thus the colocalization statistics combined with the temperature dependent Si nanocrystal uptake (Figure 6.3) suggest the 2.7 nm Si nanocrystals are taken up by endocytosis. Additional analysis of the images using a method proposed by Van Steensel et al.[55] confirmed partial colocalization between the dyes and the Si nanocrystals (data not shown).

Sample	30 minutes Pearson Coefficient	3 hours Pearson Coefficient
Dextran : Si Nanocrystals		
Top	0.871	0.759
Middle	0.869	0.797
Bottom	0.664	0.317
Lysosome : Si Nanocrystals		
Top	0.39	0.796
Middle	0.853	0.927
Bottom	0.653	0.766

Table 6.1 Pearson's coefficients for PL colocalization calculated between Si nanocrystals and dextran or lysosomes.

As a comparison, the colocalization of Si nanocrystals with DAPI and CellMask Deep Red was also assessed. Table 6.2 shows that there was considerably less colocalization between these dyes and the Si nanocrystals.

Sample	30 minutes Pearson Coefficient	3 hours Pearson Coefficient
DAPI : Si Nanocrystal		
Top	-0.072	0.1
Middle	0.084	0.133
Bottom	0.106	0.36
Cell Mask Deep Red: Si Nanocrystal		
Top	0.166	0.713
Middle	0.4	0.672
Bottom	0.62	0.773

Table 6.2 Pearson's coefficients for PL colocalization calculated between Si nanocrystals and DAPI or CellMask Deep Red.

The colocalization results shown here demonstrate that J774 macrophage cells take up Si nanocrystals by endocytosis. Within endocytosis, processes such as phagocytosis, pinocytosis, caveolae-dependent endocytosis, or clathrin-mediated

endocytosis may be contributing to the uptake of Si nanocrystals, depending on factors such as particle size, charge, and how proteins in the cell culture medium adhere to the nanoparticle surfaces and communicate with cell surface receptors.[47,56] The movement of Si nanocrystals into lysosomes not only confirms their intracellular fate, but can also guide future nanocrystal design. Since lysosomes have a low pH that can degrade nanocrystals and lead to PL loss, it may be desirous to avoid accumulation of Si nanocrystals in lysosomes. Methods to avoid lysosomes include, for example, designing the fluorescent probes to be preferentially taken up by a caveolae-dependent pathway, which can allow particles to avoid lysosomes.[57]

6.4 CONCLUSION

We have demonstrated the use of two-photon time gated confocal imaging with Si nanocrystals to study nanoparticle uptake in cells. Not only was it possible to image multiple fluorophores with Si nanocrystals using a single 800 nm excitation source, but the resulting emission could be captured simultaneously by multiple PMTs, enabling a single scan of the sample without risk of photobleaching effects. The resulting images could be analyzed using colocalization statistics to determine that the Si nanocrystals move into macrophage cell lysosomes.

6.5 REFERENCES

(1) *Handbook of Biological Confocal Microscopy*; Pawley, J. B., Ed.; 3rd ed.; Springer US: Boston, MA, 2006.

(2) Terai, T.; Nagano, T. Fluorescent Probes for Bioimaging Applications. *Curr. Opin. Chem. Biol.* **2008**, *12*, 515–521.

(3) Hilderbrand, S. A.; Weissleder, R. Near-Infrared Fluorescence: Application to in Vivo Molecular Imaging. *Curr. Opin. Chem. Biol.* **2010**, *14*, 71–79.

(4) Chan, J.; Dodani, S. C.; Chang, C. J. Reaction-Based Small-Molecule Fluorescent Probes for Chemoselective Bioimaging. *Nat. Chem.* **2012**, *4*, 973–984.

(5) Yao, J.; Yang, M.; Duan, Y. Chemistry, Biology, and Medicine of Fluorescent Nanomaterials and Related Systems: New Insights into Biosensing, Bioimaging, Genomics, Diagnostics, and Therapy. *Chem. Rev.* **2014**, *114*, 6130–6178.

(6) Li, Z. F.; Ruckenstein, E. Water-Soluble Poly(Acrylic Acid) Grafted Luminescent Silicon Nanoparticles and Their Use as Fluorescent Biological Staining Labels. *Nano Lett.* **2004**, *4*, 1463–1467.

(7) Warner, J. H.; Hoshino, A.; Yamamoto, K.; Tilley, R. D. Water-Soluble Photoluminescent Silicon Quantum Dots. *Angew. Chem.* **2005**, *117*, 4626–4630.

(8) O'Farrell, N.; Houlton, A.; Horrocks, B. R. Silicon Nanoparticles: Applications in Cell Biology and Medicine. *Int. J. Nanomedicine* **2006**, *1*, 451–472.

(9) Erogbogbo, F.; Yong, K.-T.; Roy, I.; Xu, G.; Prasad, P. N.; Swihart, M. T. Biocompatible Luminescent Silicon Quantum Dots for Imaging of Cancer Cells. *ACS Nano* **2008**, *2*, 873–878.

(10) Park, J.-H.; Gu, L.; Maltzahn, G. von; Ruoslahti, E.; Bhatia, S. N.; Sailor, M. J. Biodegradable Luminescent Porous Silicon Nanoparticles for in Vivo Applications. *Nat. Mater.* **2009**, *8*, 331–336.

(11) Erogbogbo, F.; Yong, K.-T.; Roy, I.; Hu, R.; Law, W.-C.; Zhao, W.; Ding, H.; Wu, F.; Kumar, R.; Swihart, M. T.; Prasad, P. N. In Vivo Targeted Cancer Imaging, Sentinel Lymph Node Mapping and Multi-Channel Imaging with Biocompatible Silicon Nanocrystals. *ACS Nano* **2010**, *5*, 413–423.

(12) Tu, C.; Ma, X.; Pantazis, P.; Kauzlarich, S. M.; Louie, A. Y. Paramagnetic, Silicon Quantum Dots for Magnetic Resonance and Two-Photon Imaging of Macrophages. *J. Am. Chem. Soc.* **2010**, *132*, 2016–2023.

(13) Henderson, E. J.; Shuhendler, A. J.; Prasad, P.; Baumann, V.; Maier-Flaig, F.; Faulkner, D. O.; Lemmer, U.; Wu, X. Y.; Ozin, G. A. Colloidally Stable Silicon Nanocrystals with Near-Infrared Photoluminescence for Biological Fluorescence Imaging. *Small* **2011**, *7*, 2507–2516.

(14) Hessel, C. M.; Reid, D.; Panthani, M. G.; Rasch, M. R.; Goodfellow, B. W.; Wei, J.; Fujii, H.; Akhavan, V.; Korgel, B. A. Synthesis of Ligand-Stabilized Silicon Nanocrystals with Size-Dependent Photoluminescence Spanning Visible to Near-Infrared Wavelengths. *Chem. Mater.* **2012**, *24*, 393–401.

(15) Bhattacharjee, S.; Rietjens, I. M. C. M.; Singh, M. P.; Atkins, T. M.; Purkait, T. K.; Xu, Z.; Regli, S.; Shukaliak, A.; Clark, R. J.; Mitchell, B. S.; Alink, G. M.; Marcelis, A. T. M.; Fink, M. J.; Veinot, J. G. C.; Kauzlarich, S. M.; Zuilhof, H. Cytotoxicity of Surface-Functionalized Silicon and Germanium Nanoparticles: The Dominant Role of Surface Charges. *Nanoscale* **2013**, *5*, 4870–4883.

(16) Gu, L.; Hall, D. J.; Qin, Z.; Anglin, E.; Joo, J.; Mooney, D. J.; Howell, S. B.; Sailor, M. J. In Vivo Time-Gated Fluorescence Imaging with Biodegradable Luminescent Porous Silicon Nanoparticles. *Nat. Commun.* **2013**, *4*.

(17) Yu, Y.; Fan, G.; Fermi, A.; Mazzaro, R.; Morandi, V.; Ceroni, P.; Smilgies, D.-M.; Korgel, B. A. Size-Dependent Photoluminescence Efficiency of Silicon Nanocrystal Quantum Dots. *J. Phys. Chem. C* **2017**, *121*, 23240–23248.

(18) Resch-Genger, U.; Grabolle, M.; Cavaliere-Jaricot, S.; Nitschke, R.; Nann, T. Quantum Dots versus Organic Dyes as Fluorescent Labels. *Nat. Methods* **2008**, *5*, 763–775.

(19) Berezin, M. Y.; Achilefu, S. Fluorescence Lifetime Measurements and Biological Imaging. *Chem. Rev.* **2010**, *110*, 2641–2684.

(20) Niehörster, T.; Löschberger, A.; Gregor, I.; Krämer, B.; Rahn, H.; Patting, M.; Koberling, F.; Enderlein, J.; Sauer, M. Multi-Target Spectrally Resolved Fluorescence Lifetime Imaging Microscopy. *Nat. Methods* **2016**, *13*, 257–262.

(21) Dahan, M.; Laurence, T.; Pinaud, F.; Chemla, D. S.; Alivisatos, A. P.; Sauer, M.; Weiss, S. Time-Gated Biological Imaging by Use of Colloidal Quantum Dots. *Opt. Lett.* **2001**, *26*, 825–827.

(22) Giraud, G.; Schulze, H.; Bachmann, T. T.; Campbell, C. J.; Mount, A. R.; Ghazal, P.; Khondoker, M. R.; Ross, A. J.; Ember, S. W. J.; Ciani, I.; Tlili, C.; Walton, A. J.; Terry, J. G.; Crain, J. Fluorescence Lifetime Imaging of Quantum Dot Labeled DNA Microarrays. *Int. J. Mol. Sci.* **2009**, *10*, 1930–1941.

(23) Mandal, G.; Darragh, M.; Andrew Wang, Y.; D. Heyes, C. Cadmium-Free Quantum Dots as Time-Gated Bioimaging Probes in Highly-Autofluorescent Human Breast Cancer Cells. *Chem. Commun.* **2013**, *49*, 624–626.

(24) Bouccara, S.; Fragola, A.; Giovanelli, E.; Sitbon, G.; Lequeux, N.; Pons, T.; Loriette, V. Time-Gated Cell Imaging Using Long Lifetime near-Infrared-Emitting Quantum Dots for Autofluorescence Rejection. *J. Biomed. Opt.* **2014**, *19*, 051208.

(25) Grecco, H. e.; Lidke, K. a.; Heintzmann, R.; Lidke, D. s.; Spagnuolo, C.; Martinez, O. e.; Jares-Erijman, E. a.; Jovin, T. m. Ensemble and Single Particle Photophysical Properties (Two-Photon Excitation, Anisotropy, FRET, Lifetime, Spectral Conversion) of Commercial Quantum Dots in Solution and in Live Cells. *Microsc. Res. Tech.* **2004**, *65*, 169–179.

(26) Conroy, J.; Byrne, S. J.; Gun'ko, Y. K.; Rakovich, Y. P.; Donegan, J. F.; Davies, A.; Kelleher, D.; Volkov, Y. CdTe Nanoparticles Display Tropism to Core Histones and Histone-Rich Cell Organelles. *Small* **2008**, *4*, 2006–2015.

(27) Ruedas-Rama, M. J.; Orte, A.; Hall, E. A. H.; Alvarez-Pez, J. M.; Talavera, E. M. Quantum Dot Photoluminescence Lifetime-Based PH Nanosensor. *Chem. Commun.* **2011**, *47*, 2898–2900.

(28) Tang, R.; Lee, H.; Achilefu, S. Induction of PH Sensitivity on the Fluorescence Lifetime of Quantum Dots by NIR Fluorescent Dyes. *J. Am. Chem. Soc.* **2012**, *134*, 4545–4548.

(29) Sutter, J. U.; Birch, D. J. S.; Rolinski, O. J. CdSe/ZnS Core/Shell Quantum Dots as Luminescence Lifetime Sensors for Cu 2+. *Meas. Sci. Technol.* **2012**, *23*, 055103.

(30) Orte, A.; Alvarez-Pez, J. M.; Ruedas-Rama, M. J. Fluorescence Lifetime Imaging Microscopy for the Detection of Intracellular PH with Quantum Dot Nanosensors. *ACS Nano* **2013**, *7*, 6387–6395.

(31) Carlini, L.; Nadeau, J. L. Uptake and Processing of Semiconductor Quantum Dots in Living Cells Studied by Fluorescence Lifetime Imaging Microscopy (FLIM). *Chem. Commun.* **2013**, *49*, 1714–1716.

(32) Lu, Y.; Zhao, J.; Zhang, R.; Liu, Y.; Liu, D.; Goldys, E. M.; Yang, X.; Xi, P.; Sunna, A.; Lu, J.; Shi, Y.; Leif, R. C.; Huo, Y.; Shen, J.; Piper, J. A.; Robinson, J. P.; Jin, D. Tunable Lifetime Multiplexing Using Luminescent Nanocrystals. *Nat. Photonics* **2014**, *8*, 32–36.

(33) Damalakiene, L.; Karabanovas, V.; Bagdonas, S.; Rotomskis, R. Fluorescence-Lifetime Imaging Microscopy for Visualization of Quantum Dots' Endocytic Pathway. *Int. J. Mol. Sci.* **2016**, *17*, 473.

(34) Bangalore Rajeeva, B.; Lin, L.; Perillo, E. P.; Peng, X.; Yu, W. W.; Dunn, A. K.; Zheng, Y. High-Resolution Bubble Printing of Quantum Dots. *ACS Appl. Mater. Interfaces* **2017**, *9*, 16725–16733.

(35) Sinelnikov, R.; Dasog, M.; Beamish, J.; Meldrum, A.; Veinot, J. G. C. Revisiting an Ongoing Debate: What Role Do Surface Groups Play in Silicon Nanocrystal Photoluminescence? *ACS Photonics* **2017**, *4*, 1920–1929.

(36) Joo, J.; Liu, X.; Kotamraju, V. R.; Ruoslahti, E.; Nam, Y.; Sailor, M. J. Gated Luminescence Imaging of Silicon Nanoparticles. *ACS Nano* **2015**, *9*, 6233–6241.

(37) Tu, C.-C.; Awasthi, K.; Chen, K.-P.; Lin, C.-H.; Hamada, M.; Ohta, N.; Li, Y.-K. Time-Gated Imaging on Live Cancer Cells Using Silicon Quantum Dot Nanoparticles with Long-Lived Fluorescence. *ACS Photonics* **2017**, *4*, 1306–1315.

(38) Bashkatov, A. N.; Genina, E. A.; Kochubey, V. I.; Tuchin, V. V. Optical Properties of Human Skin, Subcutaneous and Mucous Tissues in the Wavelength Range from 400 to 2000 Nm. *J. Phys. Appl. Phys.* **2005**, *38*, 2543.

(39) Kobayashi, H.; Ogawa, M.; Alford, R.; Choyke, P. L.; Urano, Y. New Strategies for Fluorescent Probe Design in Medical Diagnostic Imaging. *Chem. Rev.* **2010**, *110*, 2620–2640.

(40) Denk, W.; Strickler, J. H.; Webb, W. W. Two-Photon Laser Scanning Fluorescence Microscopy. *Science* **1990**, *248*, 73–76.

(41) Zipfel, W. R.; Williams, R. M.; Webb, W. W. Nonlinear Magic: Multiphoton Microscopy in the Biosciences. *Nat. Biotechnol.* **2003**, *21*, 1369–1377.

(42) He, G. S.; Zheng, Q.; Yong, K.-T.; Erogbogbo, F.; Swihart, M. T.; Prasad, P. N. Two- and Three-Photon Absorption and Frequency Upconverted Emission of Silicon Quantum Dots. *Nano Lett.* **2008**, *8*, 2688–2692.

(43) Kim, D.; Kang, J.; Wang, T.; Ryu, H. G.; Zuidema, J. M.; Joo, J.; Kim, M.; Huh, Y.; Jung, J.; Ahn, K. H.; Kim, K. H., Sailor, M. J. Two-Photon In Vivo Imaging with Porous Silicon Nanoparticles. *Adv. Mater.* **2017**, 1703309.

(44) Yu, Y.; Hessel, C. M.; Bogart, T. D.; Panthani, M. G.; Rasch, M. R.; Korgel, B. A. Room Temperature Hydrosilylation of Silicon Nanocrystals with Bifunctional Terminal Alkenes. *Langmuir* **2013**, *29*, 1533–1540.

(45) Kazmi, S. M. S.; Salvaggio, A. J.; Estrada, A. D.; Hemati, M. A.; Shaydyuk, N. K.; Roussakis, E.; Jones, T. A.; Vinogradov, S. A.; Dunn, A. K. Three-Dimensional Mapping of Oxygen Tension in Cortical Arterioles before and after Occlusion. *Biomed. Opt. Express* **2013**, *4*, 1061–1073.

(46) Bolte, S.; Cordelières, F. P. A Guided Tour into Subcellular Colocalization Analysis in Light Microscopy. *J. Microsc.* **2006**, *224*, 213–232.

(47) Zhao, F.; Zhao, Y.; Liu, Y.; Chang, X.; Chen, C.; Zhao, Y. Cellular Uptake, Intracellular Trafficking, and Cytotoxicity of Nanomaterials. *Small* **2011**, *7*, 1322–1337.

(48) Kim, S.; Choi, I.-H. Phagocytosis and Endocytosis of Silver Nanoparticles Induce Interleukin-8 Production in Human Macrophages. *Yonsei Med. J.* **2012**, *53*, 654–657.

(49) Fernando, L. P.; Kandel, P. K.; Yu, J.; McNeill, J.; Ackroyd, P. C.; Christensen, K. A. Mechanism of Cellular Uptake of Highly Fluorescent Conjugated Polymer Nanoparticles. *Biomacromolecules* **2010**, *11*, 2675–2682.

(50) *Macrophages*; Kloc, M., Ed.; Springer International Publishing: Cham, 2017; Vol. 62.

(51) Lee, K. D.; Nir, S.; Papahadjopoulos, D. Quantitative Analysis of Liposome-Cell Interactions in Vitro: Rate Constants of Binding and Endocytosis with Suspension and Adherent J774 Cells and Human Monocytes. *Biochemistry (Mosc.)* **1993**, *32*, 889–899.

(52) *Fluorescence Microscopy of Living Cells in Culture, Part A: Fluorescent Analogs, Labeling Cells and Basic Microscopy*; Wang, Y. L.; Taylor, D. L., Eds.; Academic Press, 1989; Vol. 29.

(53) Schmid, S. L.; Fuchs, R.; Male, P.; Mellman, I. Two Distinct Subpopulations of Endosomes Involved in Membrane Recycling and Transport to Lysosomes. *Cell* **1988**, *52*, 73–83.

(54) dos Santos, T.; Varela, J.; Lynch, I.; Salvati, A.; Dawson, K. A. Effects of Transport Inhibitors on the Cellular Uptake of Carboxylated Polystyrene Nanoparticles in Different Cell Lines. *PLoS ONE* **2011**, *6*.

(55) van Steensel, B.; van Binnendijk, E. P.; Hornsby, C. D.; van der Voort, H. T.; Krozowski, Z. S.; de Kloet, E. R.; van Driel, R. Partial Colocalization of Glucocorticoid and Mineralocorticoid Receptors in Discrete Compartments in Nuclei of Rat Hippocampus Neurons. *J. Cell Sci.* **1996**, *109*, 787–792.

(56) Monopoli, M. P.; Walczyk, D.; Campbell, A.; Elia, G.; Lynch, I.; Baldelli Bombelli, F.; Dawson, K. A. Physical−Chemical Aspects of Protein Corona: Relevance to in Vitro and in Vivo Biological Impacts of Nanoparticles. *J. Am. Chem. Soc.* **2011**, *133*, 2525–2534.

(57) Shin, J.-S.; Abraham, S. N. Caveolae--Not Just Craters in the Cellular Landscape. *Science* **2001**, *293*, 1447–1448.

Chapter 7: Bioconjugation of Si Nanocrystals

7.1 INTRODUCTION

Si nanocrystals are fluorescent probes that may be useful for *in vivo* and *in vitro* bioimaging applications.[1] Fluorescent probes used in imaging applications can be used to tag specific types of cells or biomolecules by accumulating at the target site.[2,3] Attaching biomolecules, such as proteins, antibodies, or antibody fragments, to the surface of nanoparticles is one way to achieve active targeting. Quantum dots can be engineered to have surfaces that act as platforms for bioconjugation, and have been used to demonstrate targeted bioimaging in various cell types.[2,4–7] Si nanocrystals (2.8 nm diameter, 700 nm emission wavelength) can be synthesized with hydrophilic ligands that have a distal carboxylic acid group,[8] which can allow for bioconjugation to biomolecules with primary amines using carbodiimide crosslinker chemistry.[9]

However, challenges exist with the bioconjugation of Si nanocrystals to biomolecules. First, Si surfaces are prone to surface oxidation which can affect fluorescence stability of samples. Previous reports of bioconjugation using Si nanocrystals have reported that the fluorescence after conjugation to streptavidin and DNA appears at blue wavelengths,[10,11] which are not ideal for bioimaging applications and likely indicate degradation of the Si nanocrystal surface.[12] The second challenge is around confirmation of the successful conjugation to the surface. While Si nanocrystals have been reportedly conjugated to molecules such as lysine or folate,[13] clear evidence of the conjugation is difficult to obtain, and most reports rely on successful uptake by cells as indication of conjugation. For example while Fourier transform infrared spectroscopy (FTIR) may be useful for observing the formation of amide bonds, if a biomolecule also contains amide bonds (and many do) then FTIR results would be inconclusive. Here, we present the results of bioconjugating 2.8 nm, highly fluorescent Si nanocrystals to an

amine-PEGn-biotin molecule. Biotin is a commonly used biomolecule in chemistry for tagging proteins as well as for amplification assays and there are numerous probes for its detection.[14–16] The results indicate a low conjugation efficiency, though the Si nanocrystals maintain their bright fluorescence.

7.2 EXPERIMENTAL METHODS

7.2.1 Materials

Hydrogen silsesquoixane (HSQ, Fox®-16) was purchased from Dow Corning. 10-Undecenoic acid, sodium hydroxide (NaOH), and hydrofluoric acid (HF) were purchased from Sigma. Ethanol, hexanes, toluene, hydrochloric acid (HCl), 2-(N-morpholino)ethanesulfonic acid (MES), 1-ethyl-3-(3-dimethylaminopropyl)carbodiimide hydrochloride (EDC), N-hydroxysulfosuccinimide (sulfo-NHS), 2-mercaptoethanol, amine-PEG_n-biotin, biotin quantitation kit, and streptavidin magnetic beads were purchased from Fisher. Rhodamine B was purchased from Acros. A Millipore Synergy Ultrapure water system operated at 18.2 MΩ/cm was used for deionized water.

7.2.2 Silicon Nanocrystal Synthesis

Silicon (Si) nanocrystals passivated with 10-undecenoic acid were prepared per a previous protocol.[8] Solvent was removed from HSQ and the material was annealed under forming gas flow in a tube furnace for one hour at 1100 °C. The material was then ground by mortar and pestle and downsized by shaking with borosilicate beads for 9 hours. The powder was then etched in 10 ml HF and 1 ml HCl in the dark for one hour. The hydrogen terminated nanocrystals were removed from the acids by centrifugation, and then washed twice in ethanol and once in chloroform. The particles were resuspended

in 10 ml 10-undecenoic acid and transferred to a Schleck line. The dispersion was put through three freeze-pump-thaw cycles to remove oxygen, and then left stirring overnight under nitrogen flow. The Si nanocrystals were then transferred to a septum-sealed vial with 5 ml of ethanol to ensure complete passivation of the nanocrystal surface. The resulting passivated Si nanocrystals were washed with centrifugation using ethanol as the solvent and hexane as the antisolvent, and then stored in ethanol until use. Nanocrystals were transferred into pH 7.4 water (pH adjusted with NaOH) by repeated dilution through a 30 kDa centrifugal filter (Millipore).

7.2.3 Bioconjugation

Si nanocrystals were conjugated with amine-PEG_n-biotin (n= 2 or 11) using carbodiimide chemistry with EDC and sulfo-NHS.[9] The Si nanocrystals (0.5 mg/ml) were stirred at 400 rpm as freshly prepared EDC (5 mg/ml) and sulfo-NHS (5 mg/ml) in water were added drop-wise. The solution was allowed to stir for 10 minutes at room temperature. In some preparations, an inactivation step was used. The inactivation step included adding either 9.3 µl of 2-mercaptoethanol or washing the Si nanocrystals with a centrifugal filter. Then, the amine-PEGn-biotin molecule (10 mg/ml in water) was added to the stirring solution with 2 ml of 0.01 M MES buffer at pH 7, and the solution was stirred for another 1 hour. The final product was washed 5 times through a 30 kDa centrifuge column into 0.01 M MES buffer at pH 7. Five washes was selected since measurements of free biotin in solution dropped over the first three washes, and so two additional washes were performed to ensure no unbound biotin molecules were present in the solution.

7.2.4 Characterization

An FEI Tecnai Biotwin operated at 80 kV was used to collect transmission electron microscopy (TEM) images. The Si nanocrystals were drop cast onto 200 mesh carbon-coated copper grids (Electron Microscopy Sciences).

A Zetasizer Nano ZS (Malvern Instruments) was used to acquire dynamic light scattering (DLS). DLS data was acquired for samples in 40 µl disposable cuvettes using an angle of 173°. Sizes were calculated by fitting each measurement to the correlation coefficient data from the Zetasizer software (Malvern Instruments).[17] All measurements were taken in triplicate at 25 °C.

Photoluminescence spectra were acquired for samples in 1 cm pathlength glass cuvettes. Absorbance was measured on a Varian Cary 50 Bio ultraviolet-visible spectrophotometer. Photoluminescence emission (PL) spectra were captured on either a Varian Cary Eclipse fluorescence spectrometer. PL spectra were captured upon excitation at 320 nm. For quantum yield measurements PL was excited at 350 nm and Rhodamine B was used as a standard (quantum yield of 0.49 in ethanol).[18] Quantum yield was calculated according to the relation: $QY_{Si}=(QY_{ref})\ (A_{ref}/A_{Si})(I_{si}/I_{ref})(\eta_{Si}/\eta_{ref})^2$, where QY is the quantum yield, A is the absorbance at 350 nm, I is the PL intensity, η is the solvent refractive index, and the subscripts *Si* and *ref* refer to the Si nanocrystal samples and Rhodamine B reference, respectively.

Biotin quantification was conducted by measuring absorbance at 500 nm in a solution containing 4'-hydroxyazobenzene-2-carboxylic acid (HABA) with avidin. In the presence of biotin, HABA dissociates from avidin due to the high affinity between biotin and avidin. The extinction coefficient of HABA bound to avidin (34,000/Mcm) can be used to calculate the amount of biotin in solution by measuring the absorbance before and after adding a biotin containing sample to the HABA-avidin mix. The HABA-avidin

concentration can be calculated according to $C=A/(\varepsilon l)$, where A is the absorbance at 500 nm, ε is the molar extinction coefficient, and l is the pathlength.

Magnetic beads coated with streptavidin were used to separate the biotin-capped Si nanocrystals according to the manufacturer's instructions. The beads were washed by collection with a magnet and removing supernatant twice before resuspending them in 0.01 M MES pH 7 buffer. The beads were added to Si nanocrystals prepared with biotin and mixed by inverting the vial, and was then allowed to sit on the benchtop for 2 hours. A magnet was used to separate the beads from the solution.

7.3 Results and Discussion

7.3.1 Bioconjugation

Figure 7.1 illustrates the steps used in bioconjugation of amine-PEGn-biotin to Si nanocrystals. Si nanocrystals capped with 10-undecenoic acid were prepared according to a previously reported method.[8] The first step of bioconjugation is the activation of the carboxylic acid group. EDC and sulfo-NHS can react with the carboxylic acid groups to form semi-stable amine-reactive sulfo-NHS esters. During the activation step, low pH (around 5) is typically used, as lower pH results in more efficient formation of the semi-stable esters.[9,19] Since Si nanocrystals can aggregate in low pH conditions, here we limit the time for the activation step to 10 minutes and keep the solution spinning rapidly. It is necessary to add the EDC and sulfo-NHS slowly (drop-wise) to the solution to prevent aggregation of the nanoparticles. After activation, the reaction can proceed to the conjugation step. However, in cases where the target biomolecule contains both carboxyl and amine groups (for example, in antibodies), it is necessary to first inactivate any excess EDC or sulfo-NHS. This can be done by either (i) physically washing away the

EDC and sulfo-NHS, for example by centrifugal filtration, or (ii) inactivating the EDC reaction by quenching with 2-mercaptoethanol. Finally, the conjugation step is typically performed at a pH where the biomolecule is stable (commonly around 7) by adding the amine-terminated biomolecule of interest. Two different polyethylene glycol lengths linkers were used to assess how the biomolecule length could affect conjugation efficiency.

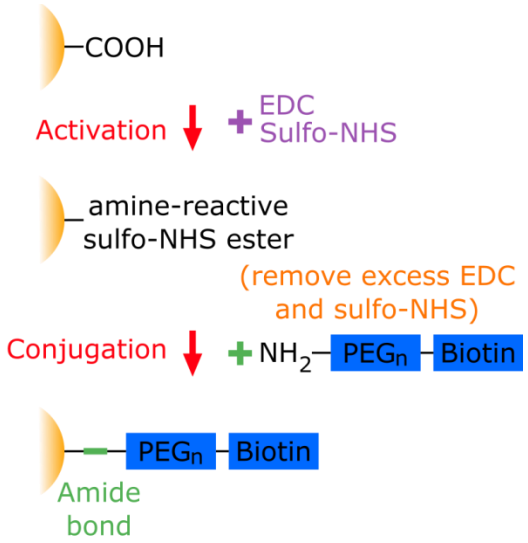

Figure 7.1 Illustration of the bioconjugation of biotin to Si nanocrystals.

Table 7.1 outlines the conditions used for the samples presented here. In all cases, EDC and sulfo-NHS were used, however different inactivation conditions were attempted. The molar ratio of Si nanocrystal carboxyl groups to EDC, sulfo-NHS, and biotin, was selected to optimize the bioconjugation while avoiding aggregation of the nanocrystals. The calculations were based on an estimate that there are approximately 200 carboxylic acid groups per 2.8 nm Si nanocrystal, which was based on previous thermal gravimetric analysis data for 10-undecenoic acid capped Si nanocrystals.[8] In all

preparations the samples were washed by centrifugal filtration five times after the conjugation reaction to remove free biotin and crosslinking agents.

Sample	Activation	Inactivation	Conjugation
A	Si nanocrystals (14 µmol carboxylic acid groups) + EDC (14 µmol) + sulfo-NHS (14 µmol) in water	None	amine-PEGn-biotin (21 µmol) in 0.01 M MES buffer, pH 7
B	Si nanocrystals (14 µmol carboxylic acid groups) + EDC (14 µmol) + sulfo-NHS (14 µmol) in water	2-mercaptoethanol	amine-PEGn-biotin (21 µmol) in 0.01 M MES buffer, pH 7
C	Si nanocrystals (14 µmol carboxylic acid groups) + EDC (14 µmol) + sulfo-NHS (14 µmol) in water	Wash three times through a 30 kDa filter into 0.01 M MES buffer, pH 7	amine-PEGn-biotin (21 µmol) in 0.01 M MES buffer, pH 7
D	Si nanocrystals (14 µmol carboxylic acid groups) + EDC (14 µmol) + sulfo-NHS (14 µmol) in ethanol	Wash three times through a 30 kDa filter into 0.01 M MES buffer, pH 7	amine-PEGn-biotin (21 µmol) in 0.01 M MES buffer, pH 7

Table 7.1 Summary of conditions tested for bioconjugation of Si nanocrystals to amine-PEG11-Biotin.

Figure 7.2 shows TEM images of the samples A-D after preparation, indicating that the Si nanocrystal integrity was maintained. Insets show that the dispersions remain brightly fluorescent after bioconjugation. The quantum yields of the dispersions were measured relative to Rhodamine B to verify that the nanocrystals maintained brightness. The results, presented in Figure 7.2, indicate that there was a drop in the quantum yield

after bioconjugation (before conjugation, Si nanocrystals dispersed in water had a quantum yield of 10.7%), however the quantum yields still remained bright (4.6%-5.2%).

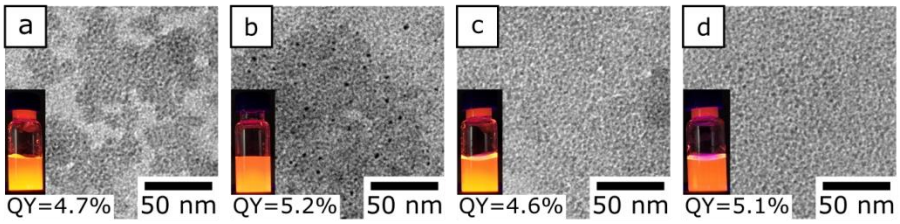

Figure 7.2 TEM images of Si nanocrystals after conjugation to amine-PEG11-biotin, and pictures of the vials on 365 nm ultraviolet lamp. (a-d) correspond to samples A-D as outlined in Table 7.1.

7.3.2 Measurement of Bioconjugation Efficiency

Table 7.2 shows the results of using the HABA-avidin assay to determine the amount of biotin in the solution after five washes. The HABA-avidin assay measures the change in absorbance as a result of biotin binding to avidin and displacing the HABA molecules. The results show that there was some Si nanocrystal conjugated biotin measured, though it was significantly less than the amount of biotin added (biotin was added at a ratio of 300 biotin molecules per Si nanocrystal at the start of the reaction). These very low results suggest that conjugation was not efficient for the nanocrystals. Also, the results indicate that the error in the assay is on the same order of magnitude as the measured biotin concentrations (-0.29 biotin/Si nanocrystal measured for sample without any biotin present). Thus, the assay results suggest some bioconjugation, however do not provide sufficient confidence on the number of molecules per Si nanocrystal. The assay did indicate that there was more bioconjugation for the biotin molecules with longer polyethylene glycol (PEG) chains. This can suggest that steric

hinderance at the nanocrystal surface may prevent the formation of amid bonds for short chain molecules. The results also show that using preparation conditions D, which include washing away excess EDC and sulfo-NHS, did not have an adverse effect on the bioconjugation efficiency. This indicates that for future experiments using molecules such as antibodies, EDC and sulfo-NHS can be removed by washing through centrifugal filters to prevent crosslinking of the antibodies.

Sample	Amine-PEG_2-Biotin per Si nanocrystal	Amine-PEG_{11}-Biotin per Si nanocrystal
A	0.07	0.36
B	0.10	0.18
C	-0.19	0.21
D	0.17	0.54
Si nanocrystals in water (no bioconjugation)	-0.29	

Table 7.2 Results of the HABA-avidin assay to measure biotin on Si nanocrystals.

Figure 7.3 shows particle diameters as measured by DLS after biotin conjugation. The results show that compared to Si nanocrystals that were not conjugated, there was a slight increase in size for the bioconjugated samples A and C (from around 17 nm in water to 25-28 nm after conjugation). For sample B, the DLS sizes measured were very large (160-180 nm), and suggest that there was significant aggregation in those preparations. Since sample B contained the 2-mercaptoethanol, it is possible that the inactivation agent interacted with the charged nanoparticles to induce aggregation. Sample D also showed larger than expected sizes (40-45 nm) and may indicate limited crosslinking or aggregation between the particles.

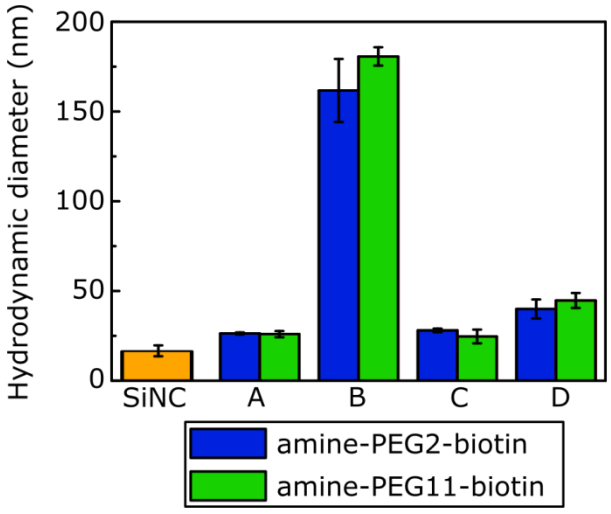

Figure 7.3 Dynamic light scattering data for bioconjugated samples. Measurements were taken in triplicate (error bars are standard deviation, n=3) at 25 °C.

Biotinylation is frequently used in biology experiments as a way to tag and separate biomolecules, and thus there are a number of methods available to physically separate biotinylated materials from non-conjugated particles. Attempts to use avidin columns, which retain biotin conjugated products, did not work for the Si nanocrystal dispersions, as non-conjugated Si nanocrystals could not pass through the column (likely due to aggregation of the nanocrystals with the agarose beads). Figure 7.4a shows the results of using magnetic beads coated with streptavidin to separate conjugated Si nanocrystals from non-conjugated Si nanocrystals. The magnetic beads were added to Si nanocrystals that either had not been conjugated or that had been conjugated according to the process for sample D with amine-PEG_{11}-biotin. The results showed that while the magnetic beads were able to separate out of solution, there was very little change in fluorescence in the nanocrystal dispersions. Measurements of the photoluminescence (PL) intensity for samples that had been separated with the magnetic beads were used to estimate amount of bioconjugated nanocrystals (Figures 7.4b and 7.4c). For Si

nanocrystals without biotin, there was a 6% decrease in PL intensity after using the magnetic separation beads. This slight drop may be a result of some Si nanocrystals becoming aggregated with the magnetic beads even without biotin attached. In comparison, for biotin conjugated Si nanocrystals there was a 16% drop in PL intensity (the absorbance of the samples dropped by 4% for Si nanocrystals alone and 14% for bioconjugated Si nanocrystals, suggesting that the PL emission intensity changes are valid estimates for Si nanocrystal concentration changes). This suggests that up to 16% of the Si nanocrystals may have been conjugated to the biotin molecules. Comparing this value to the 0.54 biotin molecules per Si nanocrystal compared above, this indicates that those Si nanocrystals may have actually had a coverage density of 3.3 biotin molecules per Si nanocrystal.

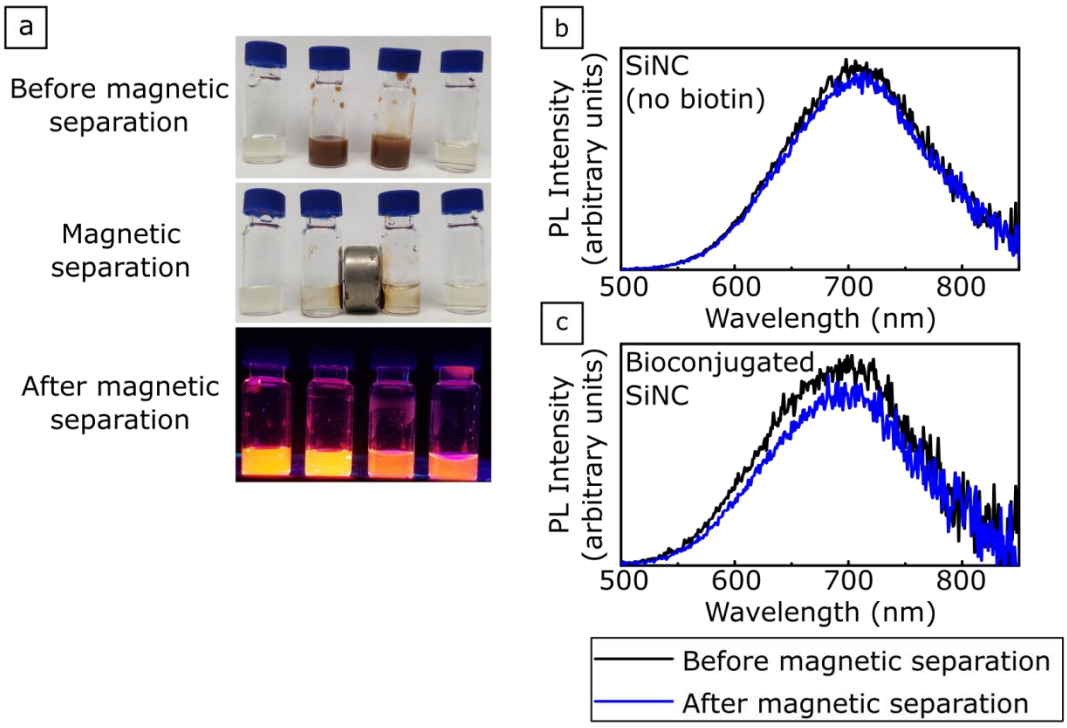

Figure 7.4 (a) Photographs of nanocrystal dispersions before and after magnetic bead separation. Left two vials contain Si nanocrystals not conjugated to biotin. Right two vials contain Si nanocrystals conjugated to biotin. Middle two vials have streptavidin magnetic beads added. PL intensity of samples containing Si nanocrystals (SiNC) (b) or Si nanocrystals conjugated to biotin (c), measured before and after separation with magnetic beads.

7.4 CONCLUSION

The conjugation of an amine-terminated biotin molecule to Si nanocrystals was demonstrated. We found that the conjugation rates are low, however, and indicate very low reaction efficiency. For practical application of bioconjugated probes, it would be ideal to have at least one, if not more, conjugated molecules per particle,[3,7] and thus the results presented here would need to be improved before attempting to use these targeted probes for imaging applications. The fact that all of the conjugated Si nanocrystal

samples retained their bright fluorescence, however, indicates that EDC and sulfo-NHS assisted conjugation can be compatible with Si nanocrystals passivated with 10-undecenoic acid. Thus, further development is needed to optimize the conjugation conditions.

7.5 REFERENCES

(1) O'Farrell, N.; Houlton, A.; Horrocks, B. R. Silicon Nanoparticles: Applications in Cell Biology and Medicine. *Int. J. Nanomedicine* **2006**, *1*, 451–472.

(2) Jaiswal, J. K.; Mattoussi, H.; Mauro, J. M.; Simon, S. M. Long-Term Multiple Color Imaging of Live Cells Using Quantum Dot Bioconjugates. *Nat. Biotechnol*. **2003**, *21*, 47–51.

(3) Medintz, I. L.; Uyeda, H. T.; Goldman, E. R.; Mattoussi, H. Quantum Dot Bioconjugates for Imaging, Labelling and Sensing. *Nat. Mater*. **2005**, *4*, 435–446.

(4) Wu, X.; Liu, H.; Liu, J.; Haley, K. N.; Treadway, J. A.; Larson, J. P.; Ge, N.; Peale, F.; Bruchez, M. P. Immunofluorescent Labeling of Cancer Marker Her2 and Other Cellular Targets with Semiconductor Quantum Dots. *Nat. Biotechnol*. **2003**, *21*, 41–46.

(5) Resch-Genger, U.; Grabolle, M.; Cavaliere-Jaricot, S.; Nitschke, R.; Nann, T. Quantum Dots versus Organic Dyes as Fluorescent Labels. *Nat. Methods* **2008**, *5*, 763–775.

(6) Kang, W. J.; Chae, J. R.; Cho, Y. L.; Lee, J. D.; Kim, S. Multiplex Imaging of Single Tumor Cells Using Quantum-Dot-Conjugated Aptamers. *Small* **2009**, *5*, 2519–2522.

(7) Wegner, K. D.; Hildebrandt, N. Quantum Dots: Bright and Versatile in Vitro and in Vivo Fluorescence Imaging Biosensors. *Chem. Soc. Rev*. **2015**, *44*, 4792–4834.

(8) Yu, Y.; Hessel, C. M.; Bogart, T. D.; Panthani, M. G.; Rasch, M. R.; Korgel, B. A. Room Temperature Hydrosilylation of Silicon Nanocrystals with Bifunctional Terminal Alkenes. *Langmuir* **2013**, *29*, 1533–1540.

(9) Hermanson, G. T. *Bioconjugate Techniques*; 2nd ed.; Elsevier Science: Burlington, 2010.

(10) Choi, J.; Wang, N. S.; Reipa, V. Conjugation of the Photoluminescent Silicon Nanoparticles to Streptavidin. *Bioconjug. Chem*. **2008**, *19*, 680–685.

(11) Wang, L.; Reipa, V.; Blasic, J. Silicon Nanoparticles as a Luminescent Label to DNA. *Bioconjug. Chem*. **2004**, *15*, 409–412.

(12) Clark, R. J.; Aghajamali, M.; Gonzalez, C. M.; Hadidi, L.; Islam, M. A.; Javadi, M.; Mobarok, M. H.; Purkait, T. K.; Robidillo, C. J. T.; Sinelnikov, R.; Thiessen, A. N.; Washington, J.; Yu, H.; Veinot, J. G. C. From Hydrogen Silsesquioxane to Functionalized Silicon Nanocrystals. *Chem. Mater*. **2017**, *29*, 80–89.

(13) Erogbogbo, F.; Tien, C.-A.; Chang, C.-W.; Yong, K.-T.; Law, W.-C.; Ding, H.; Roy, I.; Swihart, M. T.; Prasad, P. N. Bioconjugation of Luminescent Silicon Quantum Dots for Selective Uptake by Cancer Cells. *Bioconjug. Chem*. **2011**, *22*, 1081–1088.

(14) Lingerfelt, B. M.; Mattoussi, H.; Goldman, E. R.; Mauro, J. M.; Anderson, G. P. Preparation of Quantum Dot−Biotin Conjugates and Their Use in Immunochromatography Assays. *Anal. Chem*. **2003**, *75*, 4043–4049.

(15) Aslan, K.; Luhrs, C. C.; Pérez-Luna, V. H. Controlled and Reversible Aggregation of Biotinylated Gold Nanoparticles with Streptavidin. *J. Phys. Chem. B* **2004**, *108*, 15631–15639.

(16) Pulkkinen, M.; Pikkarainen, J.; Wirth, T.; Tarvainen, T.; Haapa-aho, V.; Korhonen, H.; Seppälä, J.; Järvinen, K. Three-Step Tumor Targeting of Paclitaxel Using Biotinylated PLA-PEG Nanoparticles and Avidin–biotin Technology: Formulation Development and in Vitro Anticancer Activity. *Eur. J. Pharm. Biopharm*. **2008**, *70*, 66–74.

(17) Berne, B. J.; Pecora, R. *Dynamic Light Scattering: With Applications to Chemistry, Biology, and Physics*; Courier Corporation, 2000.

(18) Casey, K. G.; Quitevis, E. L. Effect of Solvent Polarity on Nonradiative Processes in Xanthene Dyes: Rhodamine B in Normal Alcohols. *J. Phys. Chem*. **1988**, *92*, 6590–6594.

(19) Nakajima, N.; Ikada, Y. Mechanism of Amide Formation by Carbodiimide for Bioconjugation in Aqueous Media. *Bioconjug. Chem*. **1995**, *6*, 123–130.

Chapter 8: Conclusions and Future Directions

8.1 CONCLUSIONS

Si nanocrystals offer the possibility to conduct fluorescence imaging with biocompatible particles that have size-dependent, bright emission. Methods to produce Si nanocrystals have improved such that pure nanocrystals can be reproducibly synthesized at controlled sizes by the thermal annealing of hydrogen silsesquioxane.[1,2] However, the ability to use Si nanocrystals for practical applications requires that the particles can be dispersed into biological environments while maintaining their photoluminescence, and that the particles be bright and stable enough for imaging over several hours or days. The aqueous dispersibility and photoluminescence stability of Si nanocrystals has been explored. The results indicate that Si nanocrystals which emit in visible to near infrared wavelengths are non-toxic and are bright and stable for *in vitro* imaging.

8.1.1 Si Nanocrystal-Surfactant Assemblies

Si nanocrystals were incorporated into assemblies composed of lipids and quatsomes, resulting in stable dispersion in aqueous solvents. When assembled with liposomes, it was estimated that up to half of the Si nanocrystals available for assembly could be dispersed with the lipids. The quantum yields for the liposome-Si nanocrystal assemblies were 3.2%, and up to 60% of the sample photoluminescence remained after three weeks. The quatsome assemblies resulted in even higher photoluminescence stability: the quantum yield for these assemblies was 6.6%, and bright dispersions were visible for twelve weeks after preparation. Furthermore, the quatsomes maintained stable dispersions after repeated dilution. In both the liposome and quatsome assemblies, the Si nanocrystals incorporated into the dispersions as aggregates coated with a monolayer of

surfactant molecules. The surfactant dispersed Si nanocrystal assemblies thus provide a platform for delivering hydrophobic Si nanocrystals into biological environments.

8.1.2 Hydrophilic Ligand Passivated Si Nanocrystals

Si nanocrystals passivated with hydrophilic ligands could be dispersed directly into water. Small nanocrystals of approximately 3 nm capped with 10-undecenoic acid which emit at 700 nm could be transferred into water and photoluminescence was stable for at least one week, with a quantum yield of 9.1% in water. Larger nanocrystals capped with ethyl 10-undecenoate that emit at 900-1000 nm could be transferred into water by first hydrolyzing the ligand ester groups and then transferring the particles into water. However, these larger nanocrystals exhibited very low quantum yield (<0.1% in water). All of the Si nanocrystals dispersed in water or biological solutions exhibited surface oxidation.

8.1.3 Cell Uptake of Si Nanocrystals and Toxicity

Si nanocrystals dispersed in liposome assemblies or directly dispersed into water were taken up by mouse macrophage cells at biological temperatures by endocytosis. For the 10-undecenoic acid capped Si nanocrystals, uptake was found to be by clathrin-mediated endocytosis and the nanocrystals were trafficked into cell lysosomes. The clathrin-mediated uptake into lysosomes resulted in photoluminescence emission from the Si nanocrystals for up to three days, suggesting that the low pH environment contributes to stabilizing the Si nanocrystals against degradation. Experiments with other cell lines did not show significant uptake of the nanocrystals, which was expected since the liposomes and 10-undecenoic acid capped Si nanocrystals were not conjugated to any

targeting molecules. Toxicity assays performed on the cells showed that the Si nanocrystals did not result in any toxicity, and the hydrophilic nanocrystals did not induce an inflammatory response in macrophage cells.

8.1.4 Imaging

Si nanocrystals that emit at 700 nm could be imaged using one-photon confocal or two-photon microscopy following incubation with mouse macrophage cells, indicating that the nanocrystal emission was sufficiently bright enough for commercially available imaging equipment to detect. The Si nanocrystal emission could be observed for up to 24 hours using confocal microscopy. Lifetime gated imaging was also possible using the Si nanocrystals, and demonstrated that temporal multiplexing can help solve the challenges associated with the broad emission spectra characteristic of Si nanocrystals.

8.1.5 Bioconjugation

The bioconjugation of an amine-PEGn-biotin molecule to 10-undecenoic acid capped Si nanocrystals was performed by carbodiimide chemistry without any adverse effects to the nanocrystal photoluminescence. However, the conjugation efficiency was low, with <1 biotin molecule per Si nanocrystal, indicating that the methods used require further development for successful bioconjugation of molecules to Si nanocrystal surfaces.

8.2 FUTURE DIRECTIONS

8.2.1 Active Targeting through Bioconjugated Molecules

Nanoparticles make excellent platforms for bioimaging because their surface chemistries can be engineered with various shells, ligands, and adsorbed molecules. The coating of nanoparticle surfaces with biomolecules is an important technique that allows for the targeted accumulation of fluorescent probes or control of the particle fate inside of cells. Liposomes have been studied with various targeting ligands,[3] and thus using tagged liposomes loaded with Si nanocrystals can provide a straightforward approach to enable targeted delivery of Si nanocrystal probes. For hydrophilic Si nanocrystals, while bioconjugation to Si nanocrystals has previously been demonstrated with streptavidin[4] and DNA,[5] most attempts have resulted in blue emitting Si nanocrystals, where emission is not as useful for bioimaging applications. The carboxylic acid terminal groups on 10-undecenoic acid capped Si nanocrystals provide a convenient platform for direct conjugation to molecules with primary amines through carbodiimide chemistry,[6] and a previous work has demonstrated that Si nanocrystals can be conjugated with lysine or folate.[7] Here, we found very low conjugation efficiency for Si nanocrystals with amine-PEGn-biotin molecules, and thus further work will be needed to improve those results. The bioconjugation of Si nanocrystals to antibodies or antibody fragments would be an interesting system to explore, since these molecules can be used to tag cells directly or through the use of primary and secondary antibodies. The conjugation with antibodies must be carefully controlled, however, since the conjugation reaction can result in crosslinking between antibodies and thus inefficient conjugation to nanocrystals.[6]

8.2.2 Near Infrared Imaging

The biological imaging window in the near infrared (NIR) continues to drive the development of new fluorescent probes.[8] Si nanocrystals capped with distal ester groups resulted in very weak fluorescence which was almost negligible after transfer into an aqueous environment. Thus, in order for Si nanocrystals produced by annealing hydrogen silsesquioxane to be useful for NIR imaging applications, the quantum yield of these probes must be improved. This can be accomplished either by (i) encapsulating hydrophobic, alkene terminated Si nanocrystals which already display bright photoluminescence[9] into surfactant assemblies, or (ii) applying surface coatings such as polymers which can coat the surfaces of Si nanocrystals.

Multi-photon excitation is also important for NIR imaging applications, since excitation sources in the infrared can be used. Here, Si nanocrystal emission was able to be captured after two-photon excitation at 800 nm. Further work can also be conducted to look at the possibility of using three-photon excitation with Si nanocrystals, which can use even longer wavelength lasers and allow multiplexing with different organic dyes.

8.2.3 *In Vivo* Imaging

The work in this dissertation has demonstrated *in vitro* imaging using Si nanocrystals, however there are many *in vivo* fluorescence imaging applications that can benefit from the use of biocompatible particles. Full scale animal imaging has been conducted using porous silicon particles and nanocrystals.[10,11] Based on the *in vitro* results obtained with Si nanocrystals, it is likely that by first ensuring that the nanocrystals can accumulate in the target region, for example by using bioconjugated targeting molecules, the nanocrystal emission could be bright enough to image through tissue. The ability for nanoparticles to reach target tissue depends not only on tissue

characteristics, but also on nanoparticle size, shape, and surface chemistry.[12] Porous silicon nanoparticles have been found to biodegrade *in vivo*,[10] and here the 10-undecenoic acid capped Si nanocrystals degraded in aqueous solvents. However, studies on Si nanocrystals in mice found that the particles did not degrade as expected within three months,[13] suggesting that the crystalline material takes far longer to degrade than porous silicon. Thus, studies on the fate of Si nanocrystals as they degrade and are cleared from living specimens would be necessary before these particles can be used for *in vivo* applications.

8.2.4 Therapy with Si Nanocrystals

In addition to uses in bioimaging, Si nanocrystals can also find therapeutic applications. For example, photodynamic therapy (PDT) makes uses of singlet oxygen generated upon excitation of fluorescent probes to cause photodamage to local cells.[14] PDT is most efficient when fluorescent probes have long lifetimes, and thus Si nanoparticles have been investigated as PDT photosensitizers.[15] However, challenges remain with the use of Si nanocrystals for PDT since the ligand shell which protects the nanocrystals from oxidation can prevent the efficient formation and transfer of singlet oxygen from the nanocrystal to the target cells. By engineering the nanocrystals to allow for more efficient transfer of the singlet oxygen, Si nanocrystals can become useful PDT photosensitizers.

8.3 REFERENCES

(1) Hessel, C. M.; Reid, D.; Panthani, M. G.; Rasch, M. R.; Goodfellow, B. W.; Wei, J.; Fujii, H.; Akhavan, V.; Korgel, B. A. Synthesis of Ligand-Stabilized Silicon Nanocrystals with Size-Dependent Photoluminescence Spanning Visible to Near-Infrared Wavelengths. *Chem. Mater.* **2012**, *24*, 393–401.

(2) Yu, Y.; Hessel, C. M.; Bogart, T. D.; Panthani, M. G.; Rasch, M. R.; Korgel, B. A. Room Temperature Hydrosilylation of Silicon Nanocrystals with Bifunctional Terminal Alkenes. *Langmuir* **2013**, *29*, 1533–1540.

(3) Allen, T. M.; Cullis, P. R. Liposomal Drug Delivery Systems: From Concept to Clinical Applications. *Adv. Drug Deliv. Rev.* **2013**, *65*, 36–48.

(4) Choi, J.; Wang, N. S.; Reipa, V. Conjugation of the Photoluminescent Silicon Nanoparticles to Streptavidin. *Bioconjug. Chem.* **2008**, *19*, 680–685.

(5) Wang, L.; Reipa, V.; Blasic, J. Silicon Nanoparticles as a Luminescent Label to DNA. *Bioconjug. Chem.* **2004**, *15*, 409–412.

(6) Hermanson, G. T. *Bioconjugate Techniques*; 2nd ed.; Elsevier Science: Burlington, 2010.

(7) Erogbogbo, F.; Tien, C.-A.; Chang, C.-W.; Yong, K.-T.; Law, W.-C.; Ding, H.; Roy, I.; Swihart, M. T.; Prasad, P. N. Bioconjugation of Luminescent Silicon Quantum Dots for Selective Uptake by Cancer Cells. *Bioconjug. Chem.* **2011**, *22*, 1081–1088.

(8) Frangioni, J. V. In Vivo Near-Infrared Fluorescence Imaging. *Curr. Opin. Chem. Biol.* **2003**, *7*, 626–634.

(9) Yu, Y.; Fan, G.; Fermi, A.; Mazzaro, R.; Morandi, V.; Ceroni, P.; Smilgies, D.-M.; Korgel, B. A. Size-Dependent Photoluminescence Efficiency of Silicon Nanocrystal Quantum Dots. *J. Phys. Chem. C* **2017**, *121*, 23240–23248.

(10) Park, J.-H.; Gu, L.; Maltzahn, G. von; Ruoslahti, E.; Bhatia, S. N.; Sailor, M. J. Biodegradable Luminescent Porous Silicon Nanoparticles for in Vivo Applications. *Nat. Mater.* **2009**, *8*, 331–336.

(11) Erogbogbo, F.; Yong, K.-T.; Roy, I.; Hu, R.; Law, W.-C.; Zhao, W.; Ding, H.; Wu, F.; Kumar, R.; Swihart, M. T.; Prasad, P. N. In Vivo Targeted Cancer Imaging, Sentinel Lymph Node Mapping and Multi-Channel Imaging with Biocompatible Silicon Nanocrystals. *ACS Nano* **2010**, *5*, 413–423.

(12) Barua, S.; Mitragotri, S. Challenges Associated with Penetration of Nanoparticles across Cell and Tissue Barriers: A Review of Current Status and Future Prospects. *Nano Today* **2014**, *9*, 223–243.

(13) Liu, J.; Erogbogbo, F.; Yong, K.-T.; Ye, L.; Liu, J.; Hu, R.; Chen, H.; Hu, Y.; Yang, Y.; Yang, J.; Roy, I.; Karker, N. A.; Swihart, M. T.; Prasad, P. N. Assessing Clinical Prospects of Silicon Quantum Dots: Studies in Mice and Monkeys. ACS Nano 2013, 7, 7303–7310.

(14) Dougherty, T. J.; Gomer, C. J.; Henderson, B. W.; Jori, G.; Kessel, D.; Korbelik, M.; Moan, J.; Peng, Q. Photodynamic Therapy. *J. Natl. Cancer Inst.* **1998**, *90*, 889–905.

(15) Xiao, L.; Gu, L.; Howell, S. B.; Sailor, M. J. Porous Silicon Nanoparticle Photosensitizers for Singlet Oxygen and Their Phototoxicity against Cancer Cells. *ACS Nano* **2011**, *5*, 3651–3659.

References

Al-Jamal, W. T.; Al-Jamal, K. T.; Tian, B.; Lacerda, L.; Bomans, P. H.; Frederik, P. M.; Kostarelos, K. Lipid−Quantum Dot Bilayer Vesicles Enhance Tumor Cell Uptake and Retention in Vitro and in Vivo. *ACS Nano* **2008**, *2*, 408–418.

Al-Jamal, W. T.; Kostarelos, K. Liposomes: From a Clinically Established Drug Delivery System to a Nanoparticle Platform for Theranostic Nanomedicine. *Acc. Chem. Res*. **2011**, *44*, 1094–1104.

Albanese, A.; Tang, P. S.; Chan, W. C. W. The Effect of Nanoparticle Size, Shape, and Surface Chemistry on Biological Systems. *Annu. Rev. Biomed. Eng*. **2012**, *14*, 1–16.

Alenaizi, R.; Radiman, S.; Abdul Rahman, I.; Mohamed, F. Zwitterionic Betaine-Cholesterol System: Effects of Sonication Duration and Aging on Vesicles Stability. *Colloids Surf. Physicochem. Eng. Asp*. **2015**, *482*, 662–669.

Alivisatos, A. P. Perspectives on the Physical Chemistry of Semiconductor Nanocrystals. *J. Phys. Chem*. **1996**, *100*, 13226–13239.

Allen, P. M.; Liu, W.; Chauhan, V. P.; Lee, J.; Ting, A. Y.; Fukumura, D.; Jain, R. K.; Bawendi, M. G. InAs(ZnCdS) Quantum Dots Optimized for Biological Imaging in the Near-Infrared. *J. Am. Chem. Soc.* **2010**, *132*, 470–471.

Allen, T. M.; Cullis, P. R. Liposomal Drug Delivery Systems: From Concept to Clinical Applications. *Adv. Drug Deliv. Rev*. **2013**, *65*, 36–48.

Antonietti, M.; Förster, S. Vesicles and Liposomes: A Self-Assembly Principle Beyond Lipids. *Adv. Mater*. **2003**, *15*, 1323–1333.

Aslan, K.; Luhrs, C. C.; Pérez-Luna, V. H. Controlled and Reversible Aggregation of Biotinylated Gold Nanoparticles with Streptavidin. *J. Phys. Chem*. *B* **2004**, *108*, 15631–15639.

Balazs, D. A.; Godbey, W. T. Liposomes for Use in Gene Delivery. *J. Drug Deliv*. **2010**, *2011*, e326497.

Bangalore Rajeeva, B.; Lin, L.; Perillo, E. P.; Peng, X.; Yu, W. W.; Dunn, A. K.; Zheng, Y. High-Resolution Bubble Printing of Quantum Dots. *ACS Appl. Mater. Interfaces* **2017**, *9*, 16725–16733.

Barua, S.; Mitragotri, S. Challenges Associated with Penetration of Nanoparticles across Cell and Tissue Barriers: A Review of Current Status and Future Prospects. *Nano Today* **2014**, *9*, 223–243.

Bashkatov, A. N.; Genina, E. A.; Kochubey, V. I.; Tuchin, V. V. Optical Properties of Human Skin, Subcutaneous and Mucous Tissues in the Wavelength Range from 400 to 2000 nm. *J. Phys. Appl. Phys*. **2005**, *38*, 2543.

Berezin, M. Y.; Achilefu, S. Fluorescence Lifetime Measurements and Biological Imaging. *Chem. Rev*. **2010**, *110*, 2641–2684.

Berne, B. J.; Pecora, R. *Dynamic Light Scattering: With Applications to Chemistry, Biology, and Physics*; Courier Corporation, 2000.

Bhattacharjee, S.; Rietjens, I. M. C. M.; Singh, M. P.; Atkins, T. M.; Purkait, T. K.; Xu, Z.; Regli, S.; Shukaliak, A.; Clark, R. J.; Mitchell, B. S.; Alink, G. M.; Marcelis, A. T. M.; Fink, M. J.; Veinot, J. G. C.; Kauzlarich, S. M.; Zuilhof, H. Cytotoxicity of Surface-Functionalized Silicon and Germanium Nanoparticles: The Dominant Role of Surface Charges. *Nanoscale* **2013**, *5*, 4870–4883.

Biomedical Optical Imaging; Fujimoto, J. G.; Farkas, D., Eds.; Oxford University Press, 2009.

Bley, R. A.; Kauzlarich, S. M. A Low-Temperature Solution Phase Route for the Synthesis of Silicon Nanoclusters. *J. Am. Chem. Soc*. **1996**, *118*, 12461–12462.

Bolte, S.; Cordelières, F. P. A Guided Tour into Subcellular Colocalization Analysis in Light Microscopy. *J. Microsc.* **2006**, *224*, 213–232.

Bouccara, S.; Fragola, A.; Giovanelli, E.; Sitbon, G.; Lequeux, N.; Pons, T.; Loriette, V. Time-Gated Cell Imaging Using Long Lifetime near-Infrared-Emitting Quantum Dots for Autofluorescence Rejection. *J. Biomed. Opt*. **2014**, *19*, 051208.

Brannon-Peppas, L.; Blanchette, J. O. Nanoparticle and Targeted Systems for Cancer Therapy. *Adv. Drug Deliv. Rev*. **2004**, *56*, 1649–1659.

Briuglia, M.-L.; Rotella, C.; McFarlane, A.; Lamprou, D. A. Influence of Cholesterol on Liposome Stability and on in Vitro Drug Release. *Drug Deliv. Transl. Res*. **2015**, *5*, 231–242.

Bruchez, M.; Moronne, M.; Gin, P.; Weiss, S.; Alivisatos, A. P. Semiconductor Nanocrystals as Fluorescent Biological Labels. *Science* **1998**, *281*, 2013–2016.

Brus, L. E. Electron–electron and Electron-hole Interactions in Small Semiconductor Crystallites: The Size Dependence of the Lowest Excited Electronic State. *J. Chem. Phys.* **1984**, *80*, 4403–4409.

Brus, L. E.; Szajowski, P. F.; Wilson, W. L.; Harris, T. D.; Schuppler, S.; Citrin, P. H. Electronic Spectroscopy and Photophysics of Si Nanocrystals: Relationship to Bulk c-Si and Porous Si. *J. Am. Chem. Soc*. **1995**, *117*, 2915–2922.

Cabrera, I.; Elizondo, E.; Esteban, O.; Corchero, J. L.; Melgarejo, M.; Pulido, D.; Córdoba, A.; Moreno, E.; Unzueta, U.; Vazquez, E.; Abasolo, I.; Schwartz, S.; Villaverde, A.; Albericio, F.; Royo, M.; Garcia-Parajo, M. F.; Ventosa, N.; Veciana, J. Multifunctional Nanovesicle-Bioactive Conjugates Prepared by a One-Step Scalable Method Using CO2-Expanded Solvents. *Nano Lett*. **2013**, *13*, 3766–3774.

Cai, W.; Shin, D.-W.; Chen, K.; Gheysens, O.; Cao, Q.; Wang, S. X.; Gambhir, S. S.; Chen, X. Peptide-Labeled Near-Infrared Quantum Dots for Imaging Tumor Vasculature in Living Subjects. *Nano Lett.* **2006**, *6*, 669–676.

Canham, L. T. Silicon Quantum Wire Array Fabrication by Electrochemical and Chemical Dissolution of Wafers. *Appl. Phys. Lett*. **1990**, *57*, 1046–1048.

Cannon, W. r.; Danforth, S. c.; Flint, J. h.; Haggerty, J. s.; Marra, R. a. Sinterable Ceramic Powders from Laser-Driven Reactions: I, Process Description and Modeling. *J. Am. Ceram. Soc*. **1982**, *65*, 324–330.

Carlini, L.; Nadeau, J. L. Uptake and Processing of Semiconductor Quantum Dots in Living Cells Studied by Fluorescence Lifetime Imaging Microscopy (FLIM). *Chem. Commun.* **2013**, *49*, 1714–1716.

Cartiera, M. S.; Johnson, K. M.; Rajendran, V.; Caplan, M. J.; Saltzman, W. M. The Uptake and Intracellular Fate of PLGA Nanoparticles in Epithelial Cells. *Biomaterials* **2009**, *30*, 2790–2798.

Casey, K. G.; Quitevis, E. L. Effect of Solvent Polarity on Nonradiative Processes in Xanthene Dyes: Rhodamine B in Normal Alcohols. *J. Phys. Chem*. **1988**, *92*, 6590–6594.

Chan, J.; Dodani, S. C.; Chang, C. J. Reaction-Based Small-Molecule Fluorescent Probes for Chemoselective Bioimaging. *Nat. Chem.* **2012**, *4*, 973–984.

Chandler, D. Interfaces and the Driving Force of Hydrophobic Assembly. *Nature* **2005**, *437*, 640–647.

Chang, H.-I.; Yeh, M.-K. Clinical Development of Liposome-Based Drugs: Formulation, Characterization, and Therapeutic Efficacy. *Int. J. Nanomedicine* **2012**, *7*, 49–60.

Chen, G.; Shen, J.; Ohulchanskyy, T. Y.; Patel, N. J.; Kutikov, A.; Li, Z.; Song, J.; Pandey, R. K.; Ågren, H.; Prasad, P. N.; Han, G. (α-NaYbF4:Tm3+)/CaF2 Core/Shell Nanoparticles with Efficient Near-Infrared to Near-Infrared Upconversion for High-Contrast Deep Tissue Bioimaging. *ACS Nano* **2012**, *6*, 8280–8287.

Choi, H. S.; Ipe, B. I.; Misra, P.; Lee, J. H.; Bawendi, M. G.; Frangioni, J. V. Tissue- and Organ-Selective Biodistribution of NIR Fluorescent Quantum Dots. *Nano Lett.* **2009**, *9*, 2354–2359.

Choi, H. S.; Liu, W.; Misra, P.; Tanaka, E.; Zimmer, J. P.; Itty Ipe, B.; Bawendi, M. G.; Frangioni, J. V. Renal Clearance of Quantum Dots. *Nat. Biotechnol*. **2007**, *25*, 1165–1170.

Choi, J.; Wang, N. S.; Reipa, V. Conjugation of the Photoluminescent Silicon Nanoparticles to Streptavidin. *Bioconjug. Chem.* **2008**, *19*, 680–685.

Clark, R. J.; Aghajamali, M.; Gonzalez, C. M.; Hadidi, L.; Islam, M. A.; Javadi, M.; Mobarok, M. H.; Purkait, T. K.; Robidillo, C. J. T.; Sinelnikov, R.; Thiessen, A. N.; Washington, J.; Yu, H.; Veinot, J. G. C. From Hydrogen Silsesquioxane to Functionalized Silicon Nanocrystals. *Chem. Mater*. **2017**, *29*, 80–89.

Clark, R. J.; Dang, M. K. M.; Veinot, J. G. C. Exploration of Organic Acid Chain Length on Water-Soluble Silicon Quantum Dot Surfaces. *Langmuir* **2010**, *26*, 15657–15664.

Colloid Science: Principles, Methods and Applications; Cosgrove, T., Ed.; 2nd ed.; John Wiley & Sons, Inc., 2010.

Colloidal Silica: Fundamentals and Applications; Bergna, H. E.; Roberts, W. O., Eds.; CRC Press, 2005.

Connor, E. E.; Mwamuka, J.; Gole, A.; Murphy, C. J.; Wyatt, M. D. Gold Nanoparticles Are Taken Up by Human Cells but Do Not Cause Acute Cytotoxicity. *Small* **2005**, *1*, 325–327.

Conroy, J.; Byrne, S. J.; Gun'ko, Y. K.; Rakovich, Y. P.; Donegan, J. F.; Davies, A.; Kelleher, D.; Volkov, Y. CdTe Nanoparticles Display Tropism to Core Histones and Histone-Rich Cell Organelles. *Small* **2008**, *4*, 2006–2015.

Cullis, A. G.; Canham, L. T.; Calcott, P. D. J. The Structural and Luminescence Properties of Porous Silicon. *J. Appl. Phys*. **1997**, *82*, 909–965.

Dahan, M.; Laurence, T.; Pinaud, F.; Chemla, D. S.; Alivisatos, A. P.; Sauer, M.; Weiss, S. Time-Gated Biological Imaging by Use of Colloidal Quantum Dots. *Opt. Lett*. **2001**, *26*, 825–827.

Damalakiene, L.; Karabanovas, V.; Bagdonas, S.; Rotomskis, R. Fluorescence-Lifetime Imaging Microscopy for Visualization of Quantum Dots' Endocytic Pathway. *Int. J. Mol. Sci.* **2016**, *17*, 473.

Dasog, M.; De los Reyes, G. B.; Titova, L. V.; Hegmann, F. A.; Veinot, J. G. C. Size vs Surface: Tuning the Photoluminescence of Freestanding Silicon Nanocrystals Across the Visible Spectrum via Surface Groups. *ACS Nano* **2014**, *8*, 9636–9648.

Dasog, M.; Yang, Z.; Regli, S.; Atkins, T. M.; Faramus, A.; Singh, M. P.; Muthuswamy, E.; Kauzlarich, S. M.; Tilley, R. D.; Veinot, J. G. C. Chemical Insight into the Origin of Red and Blue Photoluminescence Arising from Freestanding Silicon Nanocrystals. *ACS Nano* **2013**, *7*, 2676–2685.

De Leo, V.; Catucci, L.; Falqui, A.; Marotta, R.; Striccoli, M.; Agostiano, A.; Comparelli, R.; Milano, F. Hybrid Assemblies of Fluorescent Nanocrystals and Membrane Proteins in Liposomes. *Langmuir* **2014**, *30*, 1599–1608.

Dekeyser, C. M.; Buron, C. C.; Derclaye, S. R.; Jonas, A. M.; Marchand-Brynaert, J.; Rouxhet, P. G. Degradation of Bare and Silanized Silicon Wafer Surfaces by Constituents of Biological Fluids. *J. Colloid Interface Sci.* **2012**, *378*, 77–82.

Denk, W.; Strickler, J. H.; Webb, W. W. Two-Photon Laser Scanning Fluorescence Microscopy. *Science* **1990**, *248*, 73–76.

Derfus, A. M.; Chan, W. C. W.; Bhatia, S. N. Intracellular Delivery of Quantum Dots for Live Cell Labeling and Organelle Tracking. *Adv. Mater*. **2004**, *16*, 961–966.

Dhas, N. A.; Raj, C. P.; Gedanken, A. Preparation of Luminescent Silicon Nanoparticles: A Novel Sonochemical Approach. *Chem. Mater*. **1998**, *10*, 3278–3281.

Dickey, A.; Faller, R. Examining the Contributions of Lipid Shape and Headgroup Charge on Bilayer Behavior. *Biophys. J*. **2008**, *95*, 2636–2646.

Documents & Support and Media Formulations | Thermo Fisher Scientific https://www.thermofisher.com/search/supportSearch?query=&type=Media+Formulations (accessed Oct 3, 2017).

Dohnalová, K.; Gregorkiewicz, T.; Kůsová, K. Silicon Quantum Dots: Surface Matters. *J. Phys. Condens. Matter* **2014**, *26*, 173201.

Dohnalová, K.; Poddubny, A. N.; Prokofiev, A. A.; De Boer, W. D.; Umesh, C. P.; Paulusse, J. M.; Zuilhof, H.; Gregorkiewicz, T. Surface Brightens up Si Quantum Dots: Direct Bandgap-like Size-Tunable Emission. *Light Sci. Appl*. **2013**, I, e47.

dos Santos, T.; Varela, J.; Lynch, I.; Salvati, A.; Dawson, K. A. Effects of Transport Inhibitors on the Cellular Uptake of Carboxylated Polystyrene Nanoparticles in Different Cell Lines. *PLoS ONE* **2011**, *6*.

Dougherty, T. J.; Gomer, C. J.; Henderson, B. W.; Jori, G.; Kessel, D.; Korbelik, M.; Moan, J.; Peng, Q. Photodynamic Therapy. *J. Natl. Cancer Inst.* **1998**, *90*, 889–905.

Du, Z.; Munye, M. M.; Tagalakis, A. D.; Manunta, M. D. I.; Hart, S. L. The Role of the Helper Lipid on the DNA Transfection Efficiency of Lipopolyplex Formulations. *Sci. Rep*. **2014**, *4*.

Dubertret, B.; Skourides, P.; Norris, D. J.; Noireaux, V.; Brivanlou, A. H.; Libchaber, A. In Vivo Imaging of Quantum Dots Encapsulated in Phospholipid Micelles. *Science* **2002**, *298*, 1759–1762.

Dubochet, J. Cryo-Electron Microscopy of Vitrified Specimens. *Q. Rev. Biophys*. **1988**, *21*, 129–228.

Elias, D. R.; Poloukhtine, A.; Popik, V.; Tsourkas, A. Effect of Ligand Density, Receptor Density, and Nanoparticle Size on Cell Targeting. *Nanomedicine Nanotechnol. Biol. Med*. **2013**, *9*, 194–201.

Elizondo, E.; Larsen, J.; Hatzakis, N. S.; Cabrera, I.; Bjørnholm, T.; Veciana, J.; Stamou, D.; Ventosa, N. Influence of the Preparation Route on the Supramolecular Organization of Lipids in a Vesicular System. *J. Am. Chem. Soc*. **2012**, *134*, 1918–1921.

English, D. S.; Pell, L. E.; Yu, Z.; Barbara, P. F.; Korgel, B. A. Size Tunable Visible Luminescence from Individual Organic Monolayer Stabilized Silicon Nanocrystal Quantum Dots. *Nano Lett*. **2002**, *2*, 681–685.

Erogbogbo, F.; Tien, C.-A.; Chang, C.-W.; Yong, K.-T.; Law, W.-C.; Ding, H.; Roy, I.; Swihart, M. T.; Prasad, P. N. Bioconjugation of Luminescent Silicon Quantum Dots for Selective Uptake by Cancer Cells. *Bioconjug. Chem*. **2011**, *22*, 1081–1088.

Erogbogbo, F.; Yong, K.-T.; Roy, I.; Hu, R.; Law, W.-C.; Zhao, W.; Ding, H.; Wu, F.; Kumar, R.; Swihart, M. T.; Prasad, P. N. In Vivo Targeted Cancer Imaging, Sentinel Lymph Node Mapping and Multi-Channel Imaging with Biocompatible Silicon Nanocrystals. *ACS Nano* **2010**, *5*, 413–423.

Erogbogbo, F.; Yong, K.-T.; Roy, I.; Xu, G.; Prasad, P. N.; Swihart, M. T. Biocompatible Luminescent Silicon Quantum Dots for Imaging of Cancer Cells. *ACS Nano* **2008**, *2*, 873–878.

European Medicines Agency - Multidisciplinary: nanomedicines http://www.ema.europa.eu/ema/index.jsp?curl=pages/regulation/general/general_content_000564.jsp&mid=WC0b01ac05806403e0 (accessed Oct 24, 2017).Frangioni, J. V. In Vivo Near-Infrared Fluorescence Imaging. *Curr. Opin. Chem. Biol*. **2003**, *7*, 626–634.

Fernando, L. P.; Kandel, P. K.; Yu, J.; McNeill, J.; Ackroyd, P. C.; Christensen, K. A. Mechanism of Cellular Uptake of Highly Fluorescent Conjugated Polymer Nanoparticles. *Biomacromolecules* **2010**, *11*, 2675–2682.

Ferrer-Tasies, L.; Moreno-Calvo, E.; Cano-Sarabia, M.; Aguilella-Arzo, M.; Angelova, A.; Lesieur, S.; Ricart, S.; Faraudo, J.; Ventosa, N.; Veciana, J. Quatsomes: Vesicles Formed by Self-Assembly of Sterols and Quaternary Ammonium Surfactants. *Langmuir* **2013**, *29*, 6519–6528.

Fluorescence Microscopy of Living Cells in Culture, Part A: Fluorescent Analogs, Labeling Cells and Basic Microscopy; Wang, Y. L.; Taylor, D. L., Eds.; Academic Press, 1989; Vol. 29.

Frangioni, J. V. In Vivo Near-Infrared Fluorescence Imaging. *Curr. Opin. Chem. Biol.* **2003**, *7*, 626–634.

Fuzell, J.; Thibert, A.; Atkins, T. M.; Dasog, M.; Busby, E.; Veinot, J. G. C.; Kauzlarich, S. M.; Larsen, D. S. Red States versus Blue States in Colloidal Silicon Nanocrystals: Exciton Sequestration into Low-Density Traps. *J. Phys. Chem. Lett*. **2013**, *4*, 3806–3812.

Gallová, J.; Uhríková, D.; Islamov, A.; Kuklin, A.; Balgavý, P. Effect of Cholesterol on the Bilayer Thickness in Unilamellar Extruded DLPC and DOPC Liposomes: SANS Contrast Variation Study. *Gen. Physiol. Biophys*. **2004**, *23*, 113–128.

Gao, J.; Bender, C. M.; Murphy, C. J. Dependence of the Gold Nanorod Aspect Ratio on the Nature of the Directing Surfactant in Aqueous Solution. *Langmuir* **2003**, *19*, 9065–9070.

Gao, X.; Cui, Y.; Levenson, R. M.; Chung, L. W. K.; Nie, S. In Vivo Cancer Targeting and Imaging with Semiconductor Quantum Dots. *Nat. Biotechnol*. **2004**, *22*, 969–976.

Giraud, G.; Schulze, H.; Bachmann, T. T.; Campbell, C. J.; Mount, A. R.; Ghazal, P.; Khondoker, M. R.; Ross, A. J.; Ember, S. W. J.; Ciani, I.; Tlili, C.; Walton, A. J.; Terry, J. G.; Crain, J. Fluorescence Lifetime Imaging of Quantum Dot Labeled DNA Microarrays. *Int. J. Mol. Sci.* **2009**, *10*, 1930–1941.

Glendinning, A. B.; Russel, W. B. The Electrostatic Repulsion between Charged Spheres from Exact Solutions to the Linearized Poisson-Boltzmann Equation. *J. Colloid Interface Sci*. **1983**, *93*, 95–104.

Grimaldi, N.; Andrade, F.; Segovia, N.; Ferrer-Tasies, L.; Sala, S.; Veciana, J.; Ventosa, N. Lipid-Based Nanovesicles for Nanomedicine. *Chem. Soc. Rev*. **2016**, *45*, 6520–6545.

Grecco, H. e.; Lidke, K. a.; Heintzmann, R.; Lidke, D. s.; Spagnuolo, C.; Martinez, O. e.; Jares-Erijman, E. a.; Jovin, T. m. Ensemble and Single Particle Photophysical Properties (Two-Photon Excitation, Anisotropy, FRET, Lifetime, Spectral Conversion) of Commercial Quantum Dots in Solution and in Live Cells. *Microsc. Res. Tech.* **2004**, *65*, 169–179.

Gref, R.; Lück, M.; Quellec, P.; Marchand, M.; Dellacherie, E.; Harnisch, S.; Blunk, T.; Müller, R. H. 'Stealth' Corona-Core Nanoparticles Surface Modified by Polyethylene Glycol (PEG): Influences of the Corona (PEG Chain Length and Surface Density) and of the Core Composition on Phagocytic Uptake and Plasma Protein Adsorption. *Colloids Surf. B Biointerfaces* **2000**, *18*, 301–313.

Gupta, A.; Swihart, M. T.; Wiggers, H. Luminescent Colloidal Dispersion of Silicon Quantum Dots from Microwave Plasma Synthesis: Exploring the Photoluminescence Behavior Across the Visible Spectrum. *Adv. Funct. Mater*. **2009**, *19*, 696–703.

Gu, L.; Hall, D. J.; Qin, Z.; Anglin, E.; Joo, J.; Mooney, D. J.; Howell, S. B.; Sailor, M. J. In Vivo Time-Gated Fluorescence Imaging with Biodegradable Luminescent Porous Silicon Nanoparticles. *Nat. Commun*. **2013**, 4.

Guo, Y.; Terazzi, E.; Seemann, R.; Fleury, J. B.; Baulin, V. A. Direct Proof of Spontaneous Translocation of Lipid-Covered Hydrophobic Nanoparticles through a Phospholipid Bilayer. *Sci. Adv*. **2016**, *2*, e1600261.

Handbook of Biological Confocal Microscopy; Pawley, J. B., Ed.; 3rd ed.; Springer US: Boston, MA, 2006.

Hayashi, S.; Nagareda, T.; Kanzawa, Y.; Yamamoto, K. Photoluminescence of Si-Rich SiO2 Films: Si Clusters as Luminescent Centers. *Jpn. J. Appl. Phys*. **1993**, *32*, 3840.

He, G. S.; Zheng, Q.; Yong, K.-T.; Erogbogbo, F.; Swihart, M. T.; Prasad, P. N. Two- and Three-Photon Absorption and Frequency Upconverted Emission of Silicon Quantum Dots. *Nano Lett*. **2008**, *8*, 2688–2692.

He, Y.; Zhong, Y.; Peng, F.; Wei, X.; Su, Y.; Lu, Y.; Su, S.; Gu, W.; Liao, L.; Lee, S.-T. One-Pot Microwave Synthesis of Water-Dispersible, Ultraphoto- and PH-Stable, and Highly Fluorescent Silicon Quantum Dots. *J. Am. Chem. Soc*. **2011**, *133*, 14192–14195.

Heath, J. R. A Liquid-Solution-Phase Synthesis of Crystalline Silicon. *Science* **1992**, *258*, 1131.

Henderson, E. J.; Kelly, J. A.; Veinot, J. G. C. Influence of HSiO1.5 Sol−Gel Polymer Structure and Composition on the Size and Luminescent Properties of Silicon Nanocrystals. *Chem. Mater*. **2009**, *21*, 5426–5434.

Henderson, E. J.; Shuhendler, A. J.; Prasad, P.; Baumann, V.; Maier-Flaig, F.; Faulkner, D. O.; Lemmer, U.; Wu, X. Y.; Ozin, G. A. Colloidally Stable Silicon Nanocrystals with Near-Infrared Photoluminescence for Biological Fluorescence Imaging. *Small* **2011**, *7*, 2507–2516.

Hermanson, G. T. *Bioconjugate Techniques*; 2nd ed.; Elsevier Science: Burlington, 2010.

Hessel, C. M.; Henderson, E. J.; Veinot, J. G. C. Hydrogen Silsesquioxane: A Molecular Precursor for Nanocrystalline Si−SiO2 Composites and Freestanding Hydride-Surface-Terminated Silicon Nanoparticles. *Chem. Mater*. **2006**, *18*, 6139–6146.

Hessel, C. M.; Rasch, M. R.; Hueso, J. L.; Goodfellow, B. W.; Akhavan, V. A.; Puvanakrishnan, P.; Tunnel, J. W.; Korgel, B. A. Alkyl Passivation and Amphiphilic Polymer Coating of Silicon Nanocrystals for Diagnostic Imaging. *Small* **2010**, *6*, 2026–2034.

Hessel, C. M.; Reid, D.; Panthani, M. G.; Rasch, M. R.; Goodfellow, B. W.; Wei, J.; Fujii, H.; Akhavan, V.; Korgel, B. A. Synthesis of Ligand-Stabilized Silicon Nanocrystals with Size-Dependent Photoluminescence Spanning Visible to Near-Infrared Wavelengths. *Chem. Mater*. **2012**, *24*, 393–401.

Hilderbrand, S. A.; Weissleder, R. Near-Infrared Fluorescence: Application to in Vivo Molecular Imaging. *Curr. Opin. Chem. Biol.* **2010**, *14*, 71–79.

Holmes, J. D.; Ziegler, K. J.; Doty, R. C.; Pell, L. E.; Johnston, K. P.; Korgel, B. A. Highly Luminescent Silicon Nanocrystals with Discrete Optical Transitions. *J. Am. Chem. Soc*. **2001**, *123*, 3743–3748.

Hsu, M. J.; Juliano, R. L. Interactions of Liposomes with the Reticuloendothelial System: II. Nonspecific and Receptor-Mediated Uptake of Liposomes by Mouse

Peritoneal Macrophages. *Biochim. Biophys. Acta BBA - Mol. Cell Res*. **1982**, *720*, 411–419

Hu, M.; Chen, J.; Li, Z.-Y.; Au, L.; Hartland, G. V.; Li, X.; Marquez, M.; Xia, Y. Gold Nanostructures: Engineering Their Plasmonic Properties for Biomedical Applications. *Chem. Soc. Rev*. **2006**, *35*, 1084–1094.

Iler, R. K. *The Chemistry of Silica: Solubility, Polymerization, Colloid and Surface Properties, and Biochemistry*; Wiley: New York, 1979.

International Organization for Standardization. *ISO 14887:2000. Sample Preparation -- Dispersing Procedures for Powders in Liquids*; 2000.

Jaiswal, J. K.; Mattoussi, H.; Mauro, J. M.; Simon, S. M. Long-Term Multiple Color Imaging of Live Cells Using Quantum Dot Bioconjugates. *Nat. Biotechnol*. **2003**, *21*, 47–51.

Jang, H.; Pell, L. E.; Korgel, B. A.; English, D. S. Photoluminescence Quenching of Silicon Nanoparticles in Phospholipid Vesicle Bilayers. *J. Photochem. Photobiol. Chem*. **2003**, *158*, 111–117.

Jiang, X.; Miclăuş, T.; Wang, L.; Foldbjerg, R.; Sutherland, D. S.; Autrup, H.; Chen, C.; Beer, C. Fast Intracellular Dissolution and Persistent Cellular Uptake of Silver Nanoparticles in CHO-K1 Cells: Implication for Cytotoxicity. *Nanotoxicology* **2015**, *9*, 181–189.

Jokerst, J. V.; Lobovkina, T.; Zare, R. N.; Gambhir, S. S. Nanoparticle PEGylation for Imaging and Therapy. *Nanomed*. **2011**, *6*, 715–728.

Joo, J.; Liu, X.; Kotamraju, V. R.; Ruoslahti, E.; Nam, Y.; Sailor, M. J. Gated Luminescence Imaging of Silicon Nanoparticles. *ACS Nano* **2015**, *9*, 6233–6241.

Kang, W. J.; Chae, J. R.; Cho, Y. L.; Lee, J. D.; Kim, S. Multiplex Imaging of Single Tumor Cells Using Quantum-Dot-Conjugated Aptamers. *Small* **2009**, *5*, 2519–2522.

Kazmi, S. M. S.; Salvaggio, A. J.; Estrada, A. D.; Hemati, M. A.; Shaydyuk, N. K.; Roussakis, E.; Jones, T. A.; Vinogradov, S. A.; Dunn, A. K. Three-Dimensional Mapping of Oxygen Tension in Cortical Arterioles before and after Occlusion. *Biomed. Opt. Express* **2013**, *4*, 1061–1073.

Kim, D.; Kang, J.; Wang, T.; Ryu, H. G.; Zuidema, J. M.; Joo, J.; Kim, M.; Huh, Y.; Jung, J.; Ahn, K. H.; Kim, K. H.; Sailor, M. J. Two-Photon In Vivo Imaging with Porous Silicon Nanoparticles. *Adv. Mater*. **2017**, 1703309.

Kim, S.; Choi, I.-H. Phagocytosis and Endocytosis of Silver Nanoparticles Induce Interleukin-8 Production in Human Macrophages. *Yonsei Med. J.* **2012**, *53*, 654–657.

Kim, S.; Lim, Y. T.; Soltesz, E. G.; De Grand, A. M.; Lee, J.; Nakayama, A.; Parker, J. A.; Mihaljevic, T.; Laurence, R. G.; Dor, D. M.; Cohn, L. H.; Bawendi, M. G.; Frangioni, J. V. Near-Infrared Fluorescent Type II Quantum Dots for Sentinel Lymph Node Mapping. *Nat. Biotechnol.* **2004**, *22*, 93–97.

Klein, D. *Organic Chemistry*; John Wiley & Sons, Inc., 2012.

Kobayashi, H.; Ogawa, M.; Alford, R.; Choyke, P. L.; Urano, Y. New Strategies for Fluorescent Probe Design in Medical Diagnostic Imaging. *Chem. Rev*. **2010**, *110*, 2620–2640.

Kosaka, N.; Ogawa, M.; Choyke, P. L.; Kobayashi, H. Clinical Implications of Near-Infrared Fluorescence Imaging in Cancer. *Future Oncol. Lond. Engl.* **2009**, *5*, 1501–1511.

Kovalenko, M. V.; Manna, L.; Cabot, A.; Hens, Z.; Talapin, D. V.; Kagan, C. R.; Klimov, V. I.; Rogach, A. L.; Reiss, P.; Milliron, D. J.; Guyot-Sionnest, P.; Konstantatos, G.; Park, W. J.; Hyeon, T.; Korgel, B. A.; Murray, C. B.; Heiss, W. Prospects of Nanoscience with Nanocrystals. *ACS Nano* **2015**, *9*, 1012–1057.

Kulkarni, S. B.; Betageri, G. V.; Singh, M. Factors Affecting Microencapsulation of Drugs in Liposomes. *J. Microencapsul*. **1995**, *12*, 229–246.

Laaksonen, T.; Ahonen, P.; Johans, C.; Kontturi, K. Stability and Electrostatics of Mercaptoundecanoic Acid-Capped Gold Nanoparticles with Varying Counterion Size. *ChemPhysChem* **2006**, *7*, 2143–2149.

Lamaze, C.; Fujimoto, L. M.; Yin, H. L.; Schmid, S. L. The Actin Cytoskeleton Is Required for Receptor-Mediated Endocytosis in Mammalian Cells. *J. Biol. Chem.* **1997**, *272*, 20332–20335.

Lee, K. D.; Nir, S.; Papahadjopoulos, D. Quantitative Analysis of Liposome-Cell Interactions in Vitro: Rate Constants of Binding and Endocytosis with Suspension and Adherent J774 Cells and Human Monocytes. *Biochemistry* **1993**, *32*, 889–899.

Li, L.; Daou, T. J.; Texier, I.; Kim Chi, T. T.; Liem, N. Q.; Reiss, P. Highly Luminescent CuInS2/ZnS Core/Shell Nanocrystals: Cadmium-Free Quantum Dots for In Vivo Imaging. *Chem. Mater.* **2009**, *21*, 2422–2429.

Li, X.; He, Y.; Talukdar, S. S.; Swihart, M. T. Process for Preparing Macroscopic Quantities of Brightly Photoluminescent Silicon Nanoparticles with Emission Spanning the Visible Spectrum. *Langmuir* **2003**, *19*, 8490–8496.

Li, Z. F.; Ruckenstein, E. Water-Soluble Poly(Acrylic Acid) Grafted Luminescent Silicon Nanoparticles and Their Use as Fluorescent Biological Staining Labels. *Nano Lett*. **2004**, *4*, 1463–1467.

Lingerfelt, B. M.; Mattoussi, H.; Goldman, E. R.; Mauro, J. M.; Anderson, G. P. Preparation of Quantum Dot−Biotin Conjugates and Their Use in Immunochromatography Assays. *Anal. Chem*. **2003**, *75*, 4043–4049.

Liu, J.; Erogbogbo, F.; Yong, K.-T.; Ye, L.; Liu, J.; Hu, R.; Chen, H.; Hu, Y.; Yang, Y.; Yang, J.; Roy, I.; Karker, N. A.; Swihart, M. T.; Prasad, P. N. Assessing Clinical Prospects of Silicon Quantum Dots: Studies in Mice and Monkeys. *ACS Nano* **2013**, *7*, 7303–7310.

Liu, X.; Ardizzone, A.; Sui, B.; Anzola, M.; Ventosa, N.; Liu, T.; Veciana, J.; Belfield, K. D. Fluorenyl-Loaded Quatsome Nanostructured Fluorescent Probes. *ACS Omega* **2017**, *2*, 4112–4122.

Lu, Y.; Zhao, J.; Zhang, R.; Liu, Y.; Liu, D.; Goldys, E. M.; Yang, X.; Xi, P.; Sunna, A.; Lu, J.; Shi, Y.; Leif, R. C.; Huo, Y.; Shen, J.; Piper, J. A.; Robinson, J. P.; Jin, D. Tunable Lifetime Multiplexing Using Luminescent Nanocrystals. *Nat. Photonics* **2014**, *8*, 32–36.

Luo, X.; Morrin, A.; Killard, A. J.; Smyth, M. R. Application of Nanoparticles in Electrochemical Sensors and Biosensors. *Electroanalysis* **2006**, *18*, 319–326.

Macrophages; Kloc, M., Ed.; Springer International Publishing: Cham, 2017; Vol. 62.

Mandal, G.; Darragh, M.; Andrew Wang, Y.; D. Heyes, C. Cadmium-Free Quantum Dots as Time-Gated Bioimaging Probes in Highly-Autofluorescent Human Breast Cancer Cells. *Chem. Commun.* **2013**, *49*, 624–626.

Mangolini, L.; Thimsen, E.; Kortshagen, U. High-Yield Plasma Synthesis of Luminescent Silicon Nanocrystals. *Nano Lett*. **2005**, *5*, 655–659.

Manzoor, A. A.; Lindner, L. H.; Landon, C. D.; Park, J.-Y.; Simnick, A. J.; Dreher, M. R.; Das, S.; Hanna, G.; Park, W.; Chilkoti, A.; Koning, G. A.; Hagen, T. L. M. T.; Needham, D.; Dewhirst, M. W. Overcoming Limitations in Nanoparticle Drug Delivery: Triggered, Intravascular Release to Improve Drug Penetration into Tumors. *Cancer Res*. **2012**, *72*, 5566–5575.

Marques, E. F. Size and Stability of Catanionic Vesicles: Effects of Formation Path, Sonication, and Aging. *Langmuir* **2000**, *16*, 4798–4807.

Marsh, D. *Handbook of Lipid Bilayers*, Second Edition; CRC Press, 2013.

Medina, S. H.; Tekumalla, V.; Chevliakov, M. V.; Shewach, D. S.; Ensminger, W. D.; El-Sayed, M. E. H. N-Acetylgalactosamine-Functionalized Dendrimers as Hepatic Cancer Cell-Targeted Carriers. *Biomaterials* **2011**, *32*, 4118–4129.

Medintz, I. L.; Uyeda, H. T.; Goldman, E. R.; Mattoussi, H. Quantum Dot Bioconjugates for Imaging, Labelling and Sensing. *Nat. Mater*. **2005**, *4*, 435–446.

Michalet, X.; Pinaud, F. F.; Bentolila, L. A.; Tsay, J. M.; Doose, S.; Li, J. J.; Sundaresan, G.; Wu, A. M.; Gambhir, S. S.; Weiss, S. Quantum Dots for Live Cells, in Vivo Imaging, and Diagnostics. *Science* **2005**, *307*, 538–544.

Miller, C. R.; Bondurant, B.; McLean, S. D.; McGovern, K. A.; O'Brien, D. F. Liposome−Cell Interactions in Vitro: Effect of Liposome Surface Charge on the Binding and Endocytosis of Conventional and Sterically Stabilized Liposomes. *Biochemistry* **1998**, *37*, 12875–12883.

Monopoli, M. P.; Walczyk, D.; Campbell, A.; Elia, G.; Lynch, I.; Baldelli Bombelli, F.; Dawson, K. A. Physical−Chemical Aspects of Protein Corona: Relevance to in Vitro and in Vivo Biological Impacts of Nanoparticles. *J. Am. Chem. Soc.* **2011**, *133*, 2525–2534.

Mundy, D. I.; Machleidt, T.; Ying, Y.; Anderson, R. G. W.; Bloom, G. S. Dual Control of Caveolar Membrane Traffic by Microtubules and the Actin Cytoskeleton. *J. Cell Sci.* **2002**, *115*, 4327–4339.

Murray, C. B.; Norris, D. J.; Bawendi, M. G. Synthesis and Characterization of Nearly Monodisperse CdE (E = Sulfur, Selenium, Tellurium) Semiconductor Nanocrystallites. *J. Am. Chem. Soc*. **1993**, *115*, 8706–8715.

Nakajima, N.; Ikada, Y. Mechanism of Amide Formation by Carbodiimide for Bioconjugation in Aqueous Media. *Bioconjug. Chem*. **1995**, *6*, 123–130.

Niehörster, T.; Löschberger, A.; Gregor, I.; Krämer, B.; Rahn, H.; Patting, M.; Koberling, F.; Enderlein, J.; Sauer, M. Multi-Target Spectrally Resolved Fluorescence Lifetime Imaging Microscopy. *Nat. Methods* **2016**, *13*, 257–262.

Ntziachristos, V.; Bremer, C.; Weissleder, R. Fluorescence Imaging with Near-Infrared Light: New Technological Advances That Enable in Vivo Molecular Imaging. *Eur. Radiol.* **2003**, *13*, 195–208.

Nyk, M.; Kumar, R.; Ohulchanskyy, T. Y.; Bergey, E. J.; Prasad, P. N. High Contrast In Vitro and In Vivo Photoluminescence Bioimaging Using Near Infrared to Near Infrared Up-Conversion in Tm3+ and Yb3+ Doped Fluoride Nanophosphors. *Nano Lett.* **2008**, *8*, 3834–3838.

O'Farrell, N.; Houlton, A.; Horrocks, B. R. Silicon Nanoparticles: Applications in Cell Biology and Medicine. *Int. J. Nanomedicine* **2006**, *1*, 451–472.

Oh, N.; Park, J.-H. Endocytosis and Exocytosis of Nanoparticles in Mammalian Cells. *Int. J. Nanomedicine* **2014**, *9*, 51–63.

Orte, A.; Alvarez-Pez, J. M.; Ruedas-Rama, M. J. Fluorescence Lifetime Imaging Microscopy for the Detection of Intracellular PH with Quantum Dot Nanosensors. *ACS Nano* **2013**, *7*, 6387–6395.

Paasonen, L.; Laaksonen, T.; Johans, C.; Yliperttula, M.; Kontturi, K.; Urtti, A. Gold Nanoparticles Enable Selective Light-Induced Contents Release from Liposomes. *J. Controlled Release* **2007**, *122*, 86–93.

Paasonen, L.; Sipilä, T.; Subrizi, A.; Laurinmäki, P.; Butcher, S. J.; Rappolt, M.; Yaghmur, A.; Urtti, A.; Yliperttula, M. Gold-Embedded Photosensitive Liposomes for Drug Delivery: Triggering Mechanism and Intracellular Release. *J. Controlled Release* **2010**, *147*, 136–143.

Pankhurst, Q. A.; Connolly, J.; Jones, S. K.; Dobson, J. Applications of Magnetic Nanoparticles in Biomedicine. *J. Phys. Appl. Phys.* **2003**, *36*, R167.

Panthani, M. G.; Khan, T. A.; Reid, D. K.; Hellebusch, D. J.; Rasch, M. R.; Maynard, J. A.; Korgel, B. A. In Vivo Whole Animal Fluorescence Imaging of a Microparticle-Based Oral Vaccine Containing (CuInSexS2–x)/ZnS Core/Shell Quantum Dots. *Nano Lett*. **2013**, *13*, 4294–4298.

Papahadjopoulos, D.; Allen, T. M.; Gabizon, A.; Mayhew, E.; Matthay, K.; Huang, S. K.; Lee, K. D.; Woodle, M. C.; Lasic, D. D.; Redemann, C. Sterically Stabilized Liposomes: Improvements in Pharmacokinetics and Antitumor Therapeutic Efficacy. *Proc. Natl. Acad. Sci*. **1991**, *88*, 11460–11464.

Park, J.-H.; Gu, L.; Maltzahn, G. von; Ruoslahti, E.; Bhatia, S. N.; Sailor, M. J. Biodegradable Luminescent Porous Silicon Nanoparticles for in Vivo Applications. *Nat. Mater*. **2009**, *8*, 331–336.

Patterson, A. L. The Scherrer Formula for X-Ray Particle Size Determination. *Phys. Rev.* **1939**, *56*, 978–982.

Pavesi, L.; Negro, L. D.; Mazzoleni, C.; Franzo, G.; Priolo, F. Optical Gain in Silicon Nanocrystals. *Nature* **2000**, *408*, 440–444.

Pinaud, F.; Michalet, X.; Bentolila, L. A.; Tsay, J. M.; Doose, S.; Li, J. J.; Iyer, G.; Weiss, S. Advances in Fluorescence Imaging with Quantum Dot Bio-Probes. *Biomaterials* **2006**, *27*, 1679–1687.

Popplewell, J. F.; King, S. J.; Day, J. P.; Ackrill, P.; Fifield, L. K.; Cresswell, R. G.; di Tada, M. L.; Liu, K. Kinetics of Uptake and Elimination of Silicic Acid by a Human Subject: A Novel Application of 32Si and Accelerator Mass Spectrometry. *J. Inorg. Biochem*. **1998**, *69*, 177–180.

Prabhu, A.; Shelburne, C. E.; Gibbons, D. F. Cellular Proliferation and Cytokine Responses of Murine Macrophage Cell Line J774A.1 to Polymethylmethacrylate and Cobalt-Chrome Alloy Particles. *J. Biomed. Mater. Res.* **1998**, *42*, 655–663.

Pulkkinen, M.; Pikkarainen, J.; Wirth, T.; Tarvainen, T.; Haapa-aho, V.; Korhonen, H.; Seppälä, J.; Järvinen, K. Three-Step Tumor Targeting of Paclitaxel Using Biotinylated PLA-PEG Nanoparticles and Avidin–biotin Technology:

Formulation Development and in Vitro Anticancer Activity. *Eur. J. Pharm. Biopharm*. **2008**, *70*, 66–74.

Rahman, M.; Laurent, S.; Tawil, N.; Yahia, L.; Mahmoudi, M. *Protein-Nanoparticle Interactions : The Bio-Nano Interface*; 1st ed.; Springer: Dordrecht, 2013.

Rasch, M. R.; Rossinyol, E.; Hueso, J. L.; Goodfellow, B. W.; Arbiol, J.; Korgel, B. A. Hydrophobic Gold Nanoparticle Self-Assembly with Phosphatidylcholine Lipid: Membrane-Loaded and Janus Vesicles. *Nano Lett*. **2010**, *10*, 3733–3739.

Rasch, M. R.; Yu, Y.; Bosoy, C.; Goodfellow, B. W.; Korgel, B. A. Chloroform-Enhanced Incorporation of Hydrophobic Gold Nanocrystals into Dioleoylphosphatidylcholine (DOPC) Vesicle Membranes. *Langmuir* **2012**, *28*, 12971–12981.

Resch-Genger, U.; Grabolle, M.; Cavaliere-Jaricot, S.; Nitschke, R.; Nann, T. Quantum Dots versus Organic Dyes as Fluorescent Labels. *Nat. Methods* **2008**, *5*, 763–775.

Robinson, J. T.; Hong, G.; Liang, Y.; Zhang, B.; Yaghi, O. K.; Dai, H. In-Vivo Fluorescence Imaging in the NIR-II with Long Circulating Carbon Nanotubes Capable of Ultra-High Tumor Uptake. *J. Am. Chem. Soc.* **2012**, *134*, 10664–10669.

Roger, E.; Kalscheuer, S.; Kirtane, A.; Guru, B. R.; Grill, A. E.; Whittum-Hudson, J.; Panyam, J. Folic Acid Functionalized Nanoparticles for Enhanced Oral Drug Delivery. *Mol. Pharm*. **2012**, *9*, 2103–2110.

Ruedas-Rama, M. J.; Orte, A.; Hall, E. A. H.; Alvarez-Pez, J. M.; Talavera, E. M. Quantum Dot Photoluminescence Lifetime-Based PH Nanosensor. *Chem. Commun.* **2011**, *47*, 2898–2900.

Salata, O. Applications of Nanoparticles in Biology and Medicine. *J. Nanobiotechnology* **2004**, *2*, 3.

Salatin, S.; Yari Khosroushahi, A. Overviews on the Cellular Uptake Mechanism of Polysaccharide Colloidal Nanoparticles. *J. Cell. Mol. Med.* **2017**, *21*, 1668–1686.

Sánchez-Iglesias, A.; Grzelczak, M.; Altantzis, T.; Goris, B.; Pérez-Juste, J.; Bals, S.; Van Tendeloo, G.; Donaldson, S. H.; Chmelka, B. F.; Israelachvili, J. N.; Liz-Marzan, L. M. Hydrophobic Interactions Modulate Self-Assembly of Nanoparticles. *ACS Nano* **2012**, *6*, 11059–11065.

Sato, S.; Swihart, M. T. Propionic-Acid-Terminated Silicon Nanoparticles: Synthesis and Optical Characterization. *Chem. Mater*. **2006**, *18*, 4083–4088.

Sau, T. K.; Murphy, C. J. Room Temperature, High-Yield Synthesis of Multiple Shapes of Gold Nanoparticles in Aqueous Solution. *J. Am. Chem. Soc*. **2004**, *126*, 8648–8649.

Sawant, R. M.; Hurley, J. P.; Salmaso, S.; Kale, A.; Tolcheva, E.; Levchenko, T. S.; Torchilin, V. P. "SMART" Drug Delivery Systems: Double-Targeted PH-Responsive Pharmaceutical Nanocarriers. *Bioconjug. Chem*. **2006**, *17*, 943–949.

Schmid, S. L.; Fuchs, R.; Male, P.; Mellman, I. Two Distinct Subpopulations of Endosomes Involved in Membrane Recycling and Transport to Lysosomes. *Cell* **1988**, *52*, 73–83.

Schwartz, A. L.; Fridovich, S. E.; Lodish, H. F. Kinetics of Internalization and Recycling of the Asialoglycoprotein Receptor in a Hepatoma Cell Line. *J. Biol. Chem.* **1982**, *257*, 4230–4237.

Shin, J.-S.; Abraham, S. N. Caveolae--Not Just Craters in the Cellular Landscape. *Science* **2001**, *293*, 1447–1448.

Sinelnikov, R.; Dasog, M.; Beamish, J.; Meldrum, A.; Veinot, J. G. C. Revisiting an Ongoing Debate: What Role Do Surface Groups Play in Silicon Nanocrystal Photoluminescence? *ACS Photonics* **2017**, *4*, 1920–1929.

Smith, D. K.; Korgel, B. A. The Importance of the CTAB Surfactant on the Colloidal Seed-Mediated Synthesis of Gold Nanorods. *Langmuir* **2008**, *24*, 644–649.

Stetefeld, J.; McKenna, S. A.; Patel, T. R. Dynamic Light Scattering: A Practical Guide and Applications in Biomedical Sciences. *Biophys. Rev*. **2016**, *8*, 409–427.

Stolik, S.; Delgado, J. A.; Pérez, A.; Anasagasti, L. Measurement of the Penetration Depths of Red and near Infrared Light in Human "Ex Vivo" Tissues. *J. Photochem. Photobiol. B* **2000**, *57*, 90–93.

Sutter, J. U.; Birch, D. J. S.; Rolinski, O. J. CdSe/ZnS Core/Shell Quantum Dots as Luminescence Lifetime Sensors for Cu 2+. *Meas. Sci. Technol.* **2012**, *23*, 055103.

Szoka, F.; Papahadjopoulos, D. Comparative Properties and Methods of Preparation of Lipid Vesicles (Liposomes). *Annu. Rev. Biophys. Bioeng*. **1980**, *9*, 467–508.

Tahara, K.; Fujimoto, S.; Fujii, F.; Tozuka, Y.; Jin, T.; Takeuchi, H. Quantum Dot-Loaded Liposomes to Evaluate the Behavior of Drug Carriers after Oral Administration. *J. Pharm*. **2013**, *2013*.

Takagahara, T.; Takeda, K. Theory of the Quantum Confinement Effect on Excitons in Quantum Dots of Indirect-Gap Materials. *Phys. Rev. B* **1992**, *46*, 15578–15581.

Tang, R.; Lee, H.; Achilefu, S. Induction of PH Sensitivity on the Fluorescence Lifetime of Quantum Dots by NIR Fluorescent Dyes. *J. Am. Chem. Soc.* **2012**, *134*, 4545–4548.

Terai, T.; Nagano, T. Fluorescent Probes for Bioimaging Applications. *Curr. Opin. Chem. Biol.* **2008**, *12*, 515–521.

Thomas, N.; Dong, D.; Richter, K.; Ramezanpour, M.; Vreugde, S.; Thierry, B.; Wormald, P.-J.; Prestidge, C. A. Quatsomes for the Treatment of Staphylococcus Aureus Biofilm. *J. Mater. Chem. B* **2015**, *3*, 2770–2777.

Tu, C.; Ma, X.; Pantazis, P.; Kauzlarich, S. M.; Louie, A. Y. Paramagnetic, Silicon Quantum Dots for Magnetic Resonance and Two-Photon Imaging of Macrophages. *J. Am. Chem. Soc*. **2010**, *132*, 2016–2023.

Tu, C.-C.; Awasthi, K.; Chen, K.-P.; Lin, C.-H.; Hamada, M.; Ohta, N.; Li, Y.-K. Time-Gated Imaging on Live Cancer Cells Using Silicon Quantum Dot Nanoparticles with Long-Lived Fluorescence. *ACS Photonics* **2017**, *4*, 1306–1315.

U.S. Department of Health and Human Services, Food and Drug Administration, Center for Drug Evaluation and Research (CDER). *Liposome Drug Products: Guidance for Industry, Rev 1*; 2015; pp. 1–13.

van Steensel, B.; van Binnendijk, E. P.; Hornsby, C. D.; van der Voort, H. T.; Krozowski, Z. S.; de Kloet, E. R.; van Driel, R. Partial Colocalization of Glucocorticoid and Mineralocorticoid Receptors in Discrete Compartments in Nuclei of Rat Hippocampus Neurons. *J. Cell Sci.* **1996**, *109*, 787–792.

van Veggel, F. C. J. M. Near-Infrared Quantum Dots and Their Delicate Synthesis, Challenging Characterization, and Exciting Potential Applications. *Chem. Mater.* **2014**, *26*, 111–122.

Ventosa, N.; Cabrera, I.; Veciana, J.; Santana, H.; Martinez, E.; Berlanga, J. A. Vesicles Comprising Epidermal Growth Factor and Compositions That Contain Them. CU2012-0112, 2012.

Walkey, C. D.; Olsen, J. B.; Guo, H.; Emili, A.; Chan, W. C. W. Nanoparticle Size and Surface Chemistry Determine Serum Protein Adsorption and Macrophage Uptake. *J. Am. Chem. Soc.* **2012**, *134*, 2139–2147.

Wang, G.; Petzke, M. M.; Iyer, R.; Wu, H.; Schwartz, I. Pattern of Proinflammatory Cytokine Induction in RAW264.7 Mouse Macrophages Is Identical for Virulent and Attenuated Borrelia Burgdorferi. *J. Immunol.* **2008**, *180*, 8306–8315.

Wang, L.; Reipa, V.; Blasic, J. Silicon Nanoparticles as a Luminescent Label to DNA. *Bioconjug. Chem.* **2004**, *15*, 409–412.

Wang, M.; Thanou, M. Targeting Nanoparticles to Cancer. *Pharmacol. Res*. **2010**, *62*, 90–99.

Warner, J. H.; Hoshino, A.; Yamamoto, K.; Tilley, R. D. Water-Soluble Photoluminescent Silicon Quantum Dots. *Angew. Chem*. **2005**, *117*, 4626–4630.

Weissleder, R. A Clearer Vision for in Vivo Imaging. *Nat. Biotechnol*. **2001**, *19*, 316–317.

Wegner, K. D.; Hildebrandt, N. Quantum Dots: Bright and Versatile in Vitro and in Vivo Fluorescence Imaging Biosensors. *Chem. Soc. Rev*. **2015**, *44*, 4792–4834.

Welsher, K.; Liu, Z.; Sherlock, S. P.; Robinson, J. T.; Chen, Z.; Daranciang, D.; Dai, H. A Route to Brightly Fluorescent Carbon Nanotubes for Near-Infrared Imaging in Mice. *Nat. Nanotechnol.* **2009**, *4*, 773-780.

Win, K. Y.; Feng, S.-S. Effects of Particle Size and Surface Coating on Cellular Uptake of Polymeric Nanoparticles for Oral Delivery of Anticancer Drugs. *Biomaterials* **2005**, *26*, 2713–2722.

Wu, X.; Liu, H.; Liu, J.; Haley, K. N.; Treadway, J. A.; Larson, J. P.; Ge, N.; Peale, F.; Bruchez, M. P. Immunofluorescent Labeling of Cancer Marker Her2 and Other Cellular Targets with Semiconductor Quantum Dots. *Nat. Biotechnol*. **2003**, *21*, 41–46.

Xiao, L.; Gu, L.; Howell, S. B.; Sailor, M. J. Porous Silicon Nanoparticle Photosensitizers for Singlet Oxygen and Their Phototoxicity against Cancer Cells. *ACS Nano* **2011**, *5*, 3651–3659.

Xu, C. T.; Svensson, N.; Axelsson, J.; Svenmarker, P.; Somesfalean, G.; Chen, G.; Liang, H.; Liu, H.; Zhang, Z.; Andersson-Engels, S. Autofluorescence Insensitive Imaging Using Upconverting Nanocrystals in Scattering Media. *Appl. Phys. Lett.* **2008**, *93*, 171103.

Yang, C.-S.; Bley, R. A.; Kauzlarich, S. M.; Lee, H. W. H.; Delgado, G. R. Synthesis of Alkyl-Terminated Silicon Nanoclusters by a Solution Route. *J. Am. Chem. Soc*. **1999**, *121*, 5191–5195.

Yao, J.; Yang, M.; Duan, Y. Chemistry, Biology, and Medicine of Fluorescent Nanomaterials and Related Systems: New Insights into Biosensing, Bioimaging, Genomics, Diagnostics, and Therapy. *Chem. Rev*. **2014**, *114*, 6130–6178.

Yu, Y.; Fan, G.; Fermi, A.; Mazzaro, R.; Morandi, V.; Ceroni, P.; Smilgies, D.-M.; Korgel, B. A. Size-Dependent Photoluminescence Efficiency of Silicon Nanocrystal Quantum Dots. *J. Phys. Chem. C* **2017**, *121*, 23240-23248.

Yu, Y.; Hessel, C. M.; Bogart, T. D.; Panthani, M. G.; Rasch, M. R.; Korgel, B. A. Room Temperature Hydrosilylation of Silicon Nanocrystals with Bifunctional Terminal Alkenes. *Langmuir* **2013**, *29*, 1533–1540.

Yu, Y.; Korgel, B. A. Controlled Styrene Monolayer Capping of Silicon Nanocrystals by Room Temperature Hydrosilylation. *Langmuir* **2015**, *31*, 6532–6537.

Yu, Y.; Rowland, C. E.; Schaller, R. D.; Korgel, B. A. Synthesis and Ligand Exchange of Thiol-Capped Silicon Nanocrystals. *Langmuir* **2015**, *31*, 6886–6893.

Zaki, N. M.; Nasti, A.; Tirelli, N. Nanocarriers for Cytoplasmic Delivery: Cellular Uptake and Intracellular Fate of Chitosan and Hyaluronic Acid-Coated Chitosan

Nanoparticles in a Phagocytic Cell Model. *Macromol. Biosci.* **2011**, *11*, 1747–1760.

Zeng, X.; Zhang, Y.; Nyström, A. M. Endocytic Uptake and Intracellular Trafficking of Bis-MPA-Based Hyperbranched Copolymer Micelles in Breast Cancer Cells. *Biomacromolecules* **2012**, *13*, 3814–3822.

Zhang, L. W.; Monteiro-Riviere, N. A. Mechanisms of Quantum Dot Nanoparticle Cellular Uptake. *Toxicol. Sci.* **2009**, *110*, 138–155.

Zhao, F.; Zhao, Y.; Liu, Y.; Chang, X.; Chen, C.; Zhao, Y. Cellular Uptake, Intracellular Trafficking, and Cytotoxicity of Nanomaterials. *Small* **2011**, *7*, 1322–1337.

Zhelev, Z.; Jose, R.; Nagase, T.; Ohba, H.; Bakalova, R.; Ishikawa, M.; Baba, Y. Enhancement of the Photoluminescence of CdSe Quantum Dots during Long-Term UV-Irradiation: Privilege or Fault in Life Science Research? *J. Photochem. Photobiol. B* **2004**, *75*, 99–105.

Zipfel, W. R.; Williams, R. M.; Webb, W. W. Nonlinear Magic: Multiphoton Microscopy in the Biosciences. *Nat. Biotechnol*. **2003**, *21*, 1369–1377.

Vita

Dorothy Ann Silbaugh was born and raised in northern California. She attended the University of California, San Diego where she obtained her Bachelors of Science in Bioengineering with summa cum laude distinction in 2006. She continued her studies at the University of California, San Diego to obtain her Masters of Science in Bioengineering in 2007 after completing a thesis focused on mouse cardiomyocyte action potentials. Dorothy worked for several years in the medical device industry before renewing her interest in research and engineering and deciding to return to school. She has attended the University of Texas at Austin since August 2013 studying nanomaterials while working towards a Ph.D. in Materials Science and Engineering.

The author can be reached at dsilbaugh@utexas.edu.

This dissertation was typed by the author.